Use Authorization

In presenting this dissertation in partial fulfillment of the requirements for an advanced degree at Idaho State University, I agree that the Library shall make it freely available for inspection. I further state that permission to download and/or print my dissertation for scholarly purposes may be granted by the Dean of the Graduate School, Dean of my academic division, or by the University Librarian. It is understood that any copying or publication of this dissertation for financial gain shall not be allowed without my written permission.

Signature ______________________________

Date ______________________________

ShowerMax

An Electromagnetic Calorimeter for Independent Measurement of the Parity-Violating Asymmetry in Møller Scattering

by

Daniel Sluder

A thesis

submitted in partial fulfillment

of the requirements for the degree of

Master of Science in the Department of Physics

Idaho State University

Spring 2018

To the Graduate Faculty:

The members of the committee appointed to examine the dissertation of Daniel Sluder find it satisfactory and recommend that it be accepted.

Dr. Dustin McNulty,

Major Advisor

Dr. Daniel Dale,

Committee Member

Dr. Richard Wabrek,

Graduate Faculty Representative

Acknowledgements

First and foremost I would like to acknowledge my parents and siblings. My father is my best friend. He supports me in all my endeavors and has always pushed me to be a better person. He's also kept me active. Without him dragging me snowboarding and mountain biking every weekend I don't know where I'd be. Those things provide me happiness that I couldn't get anywhere else. My mother has also been very important to me. She's supported all of my career aspirations no matter how stupid they may have been. The evolution of my relationship with her has made me a much more understanding and tolerant person. She's provided me with perspective that has helped me see the best in others. I hope to pull my head out of the sand and call her more often. I also need to acknowledge my sisters. Though we grew up apart it's been nice having someone else like me in the world. Caitlin has always been a shining role model. Watching her success and hard work paved a trail for me. She has also been the glue that held us together all of these years. Beth is another story. She has fought her way from the bottom and has become a truly beautiful person. I deeply identify with her character. I hope she finishes her autobiography. Her preliminary writings brought me closer to my past and our family.

Next, I need to acknowledge my fiance and soon to be daughter. Trista has been my closest source of emotional support during my education. She doesn't care about money (though she wouldn't mind it) or my own character flaws. She only cares that we spend time together and love each other. Whatever happens, I know she will provide me unconditional support. What more could someone want? Shyann may have played the biggest role in shaping me into a better person. I wasn't a good enough person when I first entered a parenting role in her life. I was all too often impatient and irritable. She endured all of this and never stopped showing me love and kindness. Through her I was able to see my biggest flaws and have made a lot of ground to remedy them.

I also want to acknowledge those involved in my academic life. Seabury is a key figure here. He has shown himself to be a truly great thinker. I've been truly amazed at his willingness to consider new arguments while exercising proper skepticism. When the time comes for him to change his mind he'll do it. I wish I could say that about myself with the same confidence. Our conversations have brought me out of the dogmatic slumber that my mind used to be. I also need to thank Mike Riley. You have truly overcome hardship and made it through the highest levels of education. You've given me something to aspire to and plenty of new things to ponder. Melissa Norton also deserves a mention here. She has done truly amazing fostering our local philosophy club. It has given me something to look forward to every week.

Everyone involved in ISU's Parity Violation Group also deserves gratitude. Kevin Rhine and Carlos Bula were the real pioneers of this project. Their quality work made my life easier than it had to be. This is especially true of Carlos. He was always willing to lend me a hand when I didn't know what was going on. Brady Lowe has consistently surprised me with the breadth and uniqueness of his mind. Devi Adhikari is the hardest working guy around. He puts the rest of us to shame. Joey Mccullough is nothing less than a superstar. He is always sharp and easy to talk to. Finally, I need to thank my advisor. Dr. McNulty is the best mentor anyone could ever ask for. I truly lucked out when I got a job in his lab. He cares deeply about the well being of his students. He won't hesitate to go far beyond his obligations to help give his students a better life. McNuDust is a great person. Not to mention he exceeds the polymathic requirements for professorship and knows a strange amount about rocks.

Table of Contents

List of Figures

List of Tables

ShowerMax

An Electromagnetic Calorimeter for Independent Measurement of the Parity-Violating Asymmetry in Møller Scattering

Thesis Abstract–Idaho State University (2018)

This document outlines the design selection of an electromagnetic sampling calorimeter, deemed ShowerMax, which will make an independent measurement of the parity-violating asymmetry in electron-electron scattering in JLabs's MOLLER experiment. The physics motivation for the experiment is outlined and a justification for using such a detector is given. The theory of electromagnetic calorimetry is covered along with the challenges for using a calorimeter in order to measure a parity-violating asymmetry. Next, the testing, simulations, and general decision making process for all aspects of the detector are covered. Finally, a beam test is devised in order to benchmark the simulations and test the full scale ShowerMax prototypes.

Keywords:

Physics, Nuclear Physics, Nuclear Instrumentation, ShowerMax, Calorimeter, Electromagnetic Calorimetry, Weak Interaction, Weak Nuclear Force, Parity Violation, Moller, Moller Asymmetry, Moller Scattering, MOLLER Experiment

Chapter 1

Introduction

This thesis details the design of an electromagnetic calorimeter called ShowerMax that will be used at Jefferson Lab in the MOLLER Experiment. MOLLER[1] proposes to measure the parity-violating asymmetry (A_{PV}) in electron-electron scattering at an average Q^2 of 0.0056 GeV^2. It will be the most precise measurement of A_{PV} to date. At MOLLER's kinematics A_{PV} is expected to be approximately *36 parts per billion* and the experiment proposes to measure this value with an error of *0.7 parts per billion.* This measurement serves several purposes. It will look for evidence of yet-to-be-discovered particles and their possible interactions. It is also an attempt to find fault in the standard model of particle physics and give guidance to the future of physics as we search for a unified theory. MOLLER will push our technological boundaries; precision physics requires mankind to exert control over nature with accuracy that has never been achieved before. ShowerMax will be an integral part of this experiment. It will make an independent[2] measurement of A_{PV} while remaining more resistant to soft photon and charged hadron backgrounds than other detectors in the experiment. In addition, it will provide an extra handle on pion background identification during event—or tracking—mode calibrations.

This chapter gives a broad overview of the MOLLER experiment and the role that ShowerMax plays. Section 1.1 is a brief introduction to the motivation and physics behind the MOLLER Experiment. In Section 1.2 the experimental setup of MOLLER is explored. The last section of this chapter serves as a justification for the use of ShowerMax in this experiment. It details what the detector will contribute and how it helps the broader goals of MOLLER.

The rest of this document is a description of electromagnetic calorimetry and the Shower-

[1] MOLLER stands for Measurement Of a Lepton Lepton Electroweak Reaction. It also serves to honor the Danish physicist, Christian Møller, who first calculated relativistic electron-electron scattering [15].

[2] MOLLER will take two independent measurements of A_{PV}. The first measurement will be made by thin quartz detectors and the second will be by ShowerMax.

Max detector. In Chapter 2 the underpinnings of electromagnetic calorimetry are explored. This includes the theory of electromagnetic cascades and their development in tungsten. It also includes the subtle complications involved with using a calorimeter to measure A_{PV} (as opposed to thin quartz detectors) and the resolution of such a device. Chapter 3 details the work done to optimize all of the considerations of the ShowerMax detector, such as the detector geometry, material layout, light guides, relevant simulations, and engineering considerations. Chapter 4 details experimental methodology used to benchmark the optical and shower properties of the material used. Finally, a compact summary and conclusion is given in Chapter 5. Additional information is included in the appendices. Appendix A analyzes the structural integrity of the ShowerMax frame. Several failure analyses are performed to ensure that the detector will not undergo any structural failures during the experiment. Appendix B includes a study of lateral shower development with respect to the benchmarking apparatus. It also includes the results of several different configurations of the full-scale ShowerMax. All of the CAD drawings of the ShowerMax frame and light-guides are included in Appendix C. The final appendix, Appendix D, provides the code used to develop a model of longitudinal shower development.

1.1 Physics Motivation

The MOLLER experiment is looking to test[3] the standard model of particle physics and set bounds for hypotheses Beyond the Standard Model (BSM). When trying to find error in an existing model it is best to look where that model makes precise predictions. One such place for the standard model is the weak mixing angle, θ_W. The theoretical uncertainty in its value for Møller scattering is only 0.6%, making it a prime candidate for measurement [7]. For comparison, this uncertainty is much less than the thickness of the curve in Figure 1.1. This

[3]This is the current jargon of the field. I would prefer to say "Falsify the standard model." It's my opinion that all of our scientific endeavors should be framed in terms of falsification as Karl Popper suggested [20] to resist sliding into pseudo-science. While the standard model is extremely successful, we also know it must be incomplete. Particle physics is the endeavor to find all of the places where it's wrong so that we can usher in a better theory that fits this data and makes bold new predictions.

section covers the basics of electroweak physics and the usefulness of MOLLER in setting bounds on BSM models.

1.1.1 Electroweak Physics

In an attempt to explain beta decay, Enrico Fermi proposed a fourth force of nature [26]. This force plays a central role in modern physics and is known as the weak nuclear force. Since its initial proposal, the theoretical framework of the weak interaction has evolved significantly. Fermi originally proposed a four-fermion interaction with no range (a contact force). Today, the weak interaction and the electromagnetic interaction are unified under an $SU(2) \otimes U(1)$ gauge group. There are three bosons corresponding to $SU(2)$, W_i^μ, and one corresponding to $U(1)$, B^μ [23]. The Higgs mechanism causes spontaneous symmetry breaking of the group into $U(1)_{em}$ and makes the W_3^μ and B^μ amalgamate into the Z^0 boson and the photon (γ). This symmetry breaking is described by rotating the W_3^μ and B^μ vector boson plane by an angle θ_W (known as the 'Weinberg angle' or 'weak-mixing' angle):

$$\begin{pmatrix} \gamma \\ Z^0 \end{pmatrix} = \begin{pmatrix} \cos\theta_W & \sin\theta_W \\ -\sin\theta_W & \cos\theta_W \end{pmatrix} \begin{pmatrix} B^\mu \\ W_3^\mu \end{pmatrix} \tag{1.1}$$

Maybe the most interesting part of the weak interaction is that it violates parity. All of the other known forces of nature conserve parity. Parity transformation is described by flipping the sign of all of the spatial coordinates:

$$\mathbf{P} \begin{pmatrix} x \\ y \\ z \end{pmatrix} = \begin{pmatrix} -x \\ -y \\ -z \end{pmatrix} \tag{1.2}$$

Put simply, when an interaction associated with any of the other three forces (such as gravity) is observed through a mirror, the observer can't tell any difference between the mirror world and the real world[4].

Throughout the history of physics, parity was assumed to be conserved. In 1956 physicist Chien-Shiung Wu performed an experiment that showed this was not true [27] using beta decay of cobalt-60. In fact, it was later shown that the charged current, weak interaction *maximally* violates parity.

Today parity violation is used in many experiments. Polarized electron-electron (Møller) scattering can be used to measure the weak-mixing angle. Present measurements (such as the mass of the Higgs) combined with the standard model have put very tight constraints on the weak-mixing angle, making it a good candidate test bed of the standard model. It is also a good way to look for new particles or interactions. Some proposed dark matter candidates, such as dark photons or a dark, low mass Z boson (Z_d) [16] are predicted to violate parity enough to be detected in the MOLLER experiment. Figure 1.1 shows the predicted value of the weak-mixing angle as a function of experimental energy. As stated previously, the theoretical precision of the weak-mixing angle is much less than the thickness of the line in this figure. If the MOLLER experiment finds any statistically significant deviations from theory (greater than 2σ) it could be an indication of BSM physics.

1.1.2 Parity Violating Asymmetry

The weak-mixing angle can be extracted by measuring the parity violating asymmetry (A_{PV}) in polarized electron-electron scattering. A_{PV} is the difference in cross-section between left and right polarized incident electrons divided by their sum. More simply put, it is a measure of how many more interactions happen for right vs. left polarized electrons. The asymmetry is due to the interference terms of the electromagnetic and weak amplitudes which violate parity and thus give a non-zero result in the numerator.

$$A_{PV} = \frac{\sigma_R - \sigma_L}{\sigma_R + \sigma_L} = \frac{A_\gamma A_Z}{A_\gamma^2} = m_e E_{lab} \frac{G_F}{\sqrt{2}\pi\alpha} \frac{4\sin^2(\theta_W)}{(3+\cos^2(\theta_W))^2} Q_W^e \tag{1.3}$$

[4]This analogy breaks down because a mirror only flips the sign of one spatial coordinate.

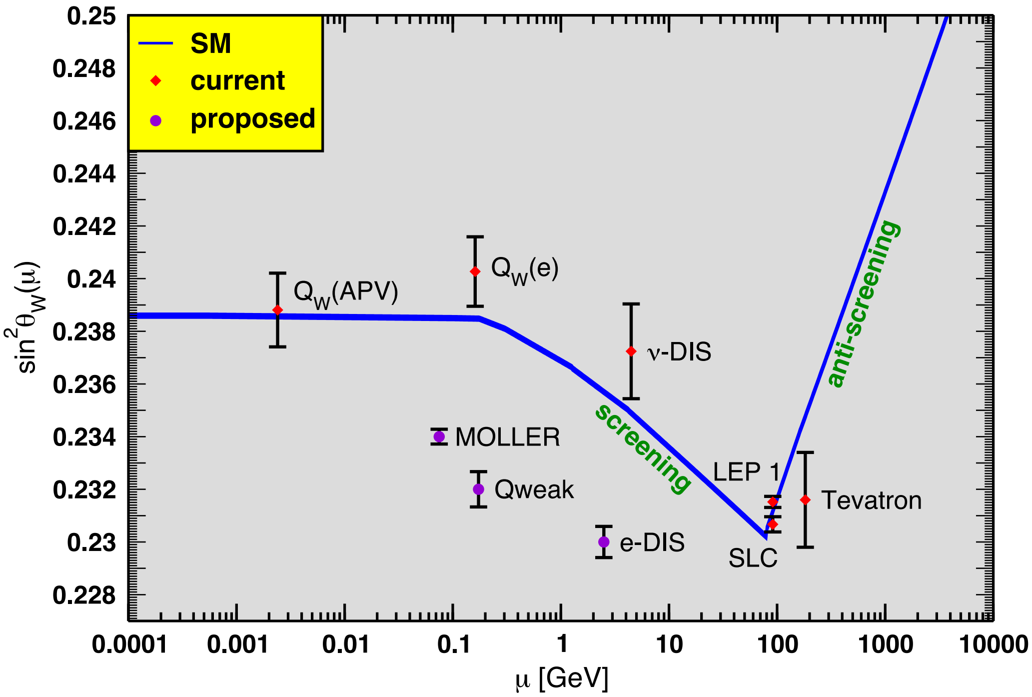

Figure 1.1: Standard model prediction of weak mixing angle as a function of measurement energy scale. The blue curve illustrates the 'running' of the weak-mixing angle. Red diamonds represent completed experiments and purple dots represent proposed experiments and are arbitrarily placed (but shown with their proposed error bars).

Because of the low Q^2 in MOLLER, the experiment will be sensitive to tree (or Born) level diagrams as well as the full set of one-loop and leading two loop radiative corrections. It is at the single loop level, shown in Figure 1.2, in which new physics could appear. That is, virtual "new" particles could be subtly coupling to radiative correction (virtual) loops of the known real particles in the experiment (the electrons).

1.2 The MOLLER Experiment

The MOLLER Experiment aims to measure A_{PV} in electron-electron (Møller) scattering with unprecedented precision. At the proposed kinematics A_{PV} is predicted to be approximately 36 part per billion (ppb) and the goal is to perform a statistics limited measurement

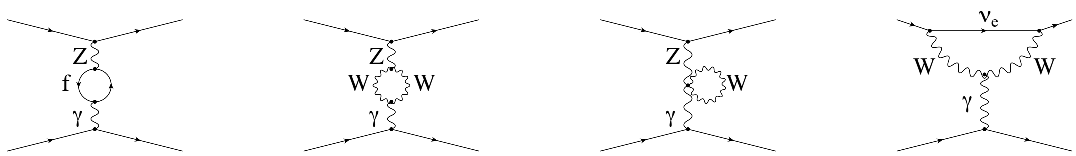

Figure 1.2: Single Loop Electroweak Diagrams in Møller Scattering.

of this quantity with a precision of 0.7 ppb. This will give the weak charge of the electron (Q_W^e) to a fractional accuracy of 2.4% at an average Q^2 of 0.0056 GeV^2 [4]. The electron's weak charge at this accuracy leads to immediate knowledge of the weak mixing angle to a precision matching the most precise previous experiments[5]. In order to achieve this goal, the MOLLER Experiment will use several novel features and an extremely detailed analysis in order to completely understand backgrounds and systematics that could drown out such a small asymmetry. Figure 1.3 illustrates the experimental setup of MOLLER.

The first component of this experiment is the polarized electron beam. The beam source and accelerator will create 11 GeV longitudinally polarized electron bunches which are uniformly polarized. The electron beam's polarization is created using circularly-polarized laser-induced photoemission from a strained, super-lattice GaAs wafer[21]. It will be flipped on a pseudo-random basis at a frequency of 1.92 kHz. The flipping of the electron polarization changes the beam helicity, thus simulating a parity operation without the need of physically rotating any of the experimental components. The beam position, trajectory, current, and energy of each helicity window will be continually monitored. Fluctuations in these values must be small in order to prevent any significant false asymmetries or other systematic errors in the measurement.

The electron beam is proposed to be incident on a 1.5 meter thick liquid hydrogen target.

[5]MOLLER precision on θ_W matches the SLC and LEP-I measurements. Notice on Figure 1.1 that the results of these experiments are incompatible. MOLLER will resolve this discrepancy.

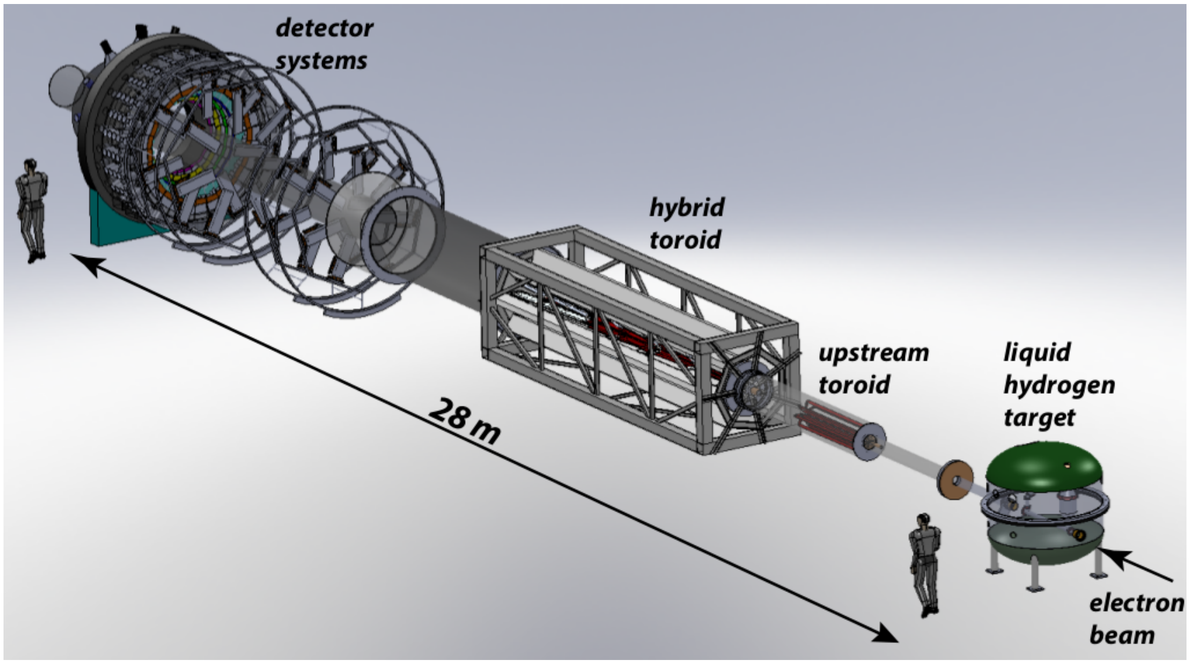

Figure 1.3: Experimental setup of MOLLER. Beam enters from lower left corner. Shower-Max is located at the rear of the detector systems.

The target will be unpolarized and should be capable of removing up to a 5 kW heat load (from the beam). The liquid hydrogen target is used because it is electron dense and provides the highest ratio of electron target thickness to radiation length. Another advantage to a liquid hydrogen target is that the radiative backgrounds are relatively well understood[6]. These backgrounds are due to electron-proton elastic and inelastic scattering. In order to decrease false asymmetries from possible target density fluctuations (boiling) special precautions must be taken. Fluctuations of the target must remain below the timescale of the helicity flip rate of the beam.

The center of mass energy of an 11 GeV electron scattering off of a fixed target electron is 106 MeV. In the laboratory frame the acceptance of these electrons is at extremely low angles. As a result the MOLLER Experiment will need to have an acceptance of scattered electrons with energies between roughly 2 GeV and 8 GeV. Additionally, since Møller scattering is coplanar scattering of identical particles, combined with an odd number of toroid

[6]Hydrogen targets also minimize false asymmetries due to the intrinsic momenta of the target electrons. This is called the Levchuk effect [17, 24].

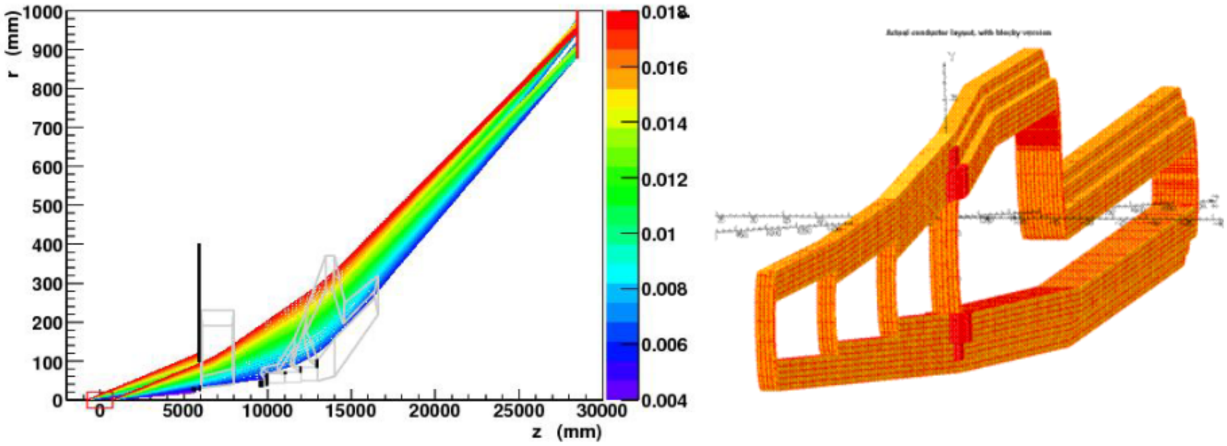

Figure 1.4: Shape and Radial Focusing of Spectrometer. Left: Radial focusing of spectrometer. Color represents energy. Note the gross scale mismatch for r (in mm) and z (in m)—this is a factor of 1000. Right: Shape of spectrometer.

coils, the experimental apparatus will accept the full range of azimuthal angles. These factors, in combination with the high event rate, require that the scattered electrons be focused to a small region with low background. In order to achieve this, a novel hybrid toroidal spectrometer design is used. The spectrometer will focus the full momentum range of scattered electrons to a ring approximately 28.5 meters downstream of the target with a radius of approximately 1 meter from the beam line. This part of the design has subtle consequences for the ShowerMax detector. Its overall resolution will be impacted by how well the magnetic field can be mapped. These considerations will be revisited throughout this thesis. Figure 1.4 illustrates the radial focusing and shape of the spectrometer. Figure 1.5 and Figure 1.6 show the rates of Møller and ep scattered electrons at the detector plane.

Many detectors will be used in the experiment to measure A_{PV} and monitor backgrounds. The main detectors will use thin quartz Cherenkov detectors operated in current mode (integrating). The advantage of using quartz is that it does not scintillate and is radiation hard. Additionally, the signal from a thin quartz detector is independent of the energy of incident particles so long as they are highly relativistic (and have charge). However, this makes the thin quartz detector more susceptible to soft photon and charged hadron backgrounds. In order to understand backgrounds and help identify any false asymmetries, calorimeters and event-mode tracking ges electron multiplier (GEM) planes will be used. They will identify charged hadrons, e.g. pions, and MIP (minimum ionizing particle) signals from muons generated in the target. Additionally, ShowerMax will be used to get a second independent measurement of A_{PV} and will also be operated in integrating mode. Given the design of ShowerMax it will be resistant to backgrounds and have the ability to identify MIP signals.

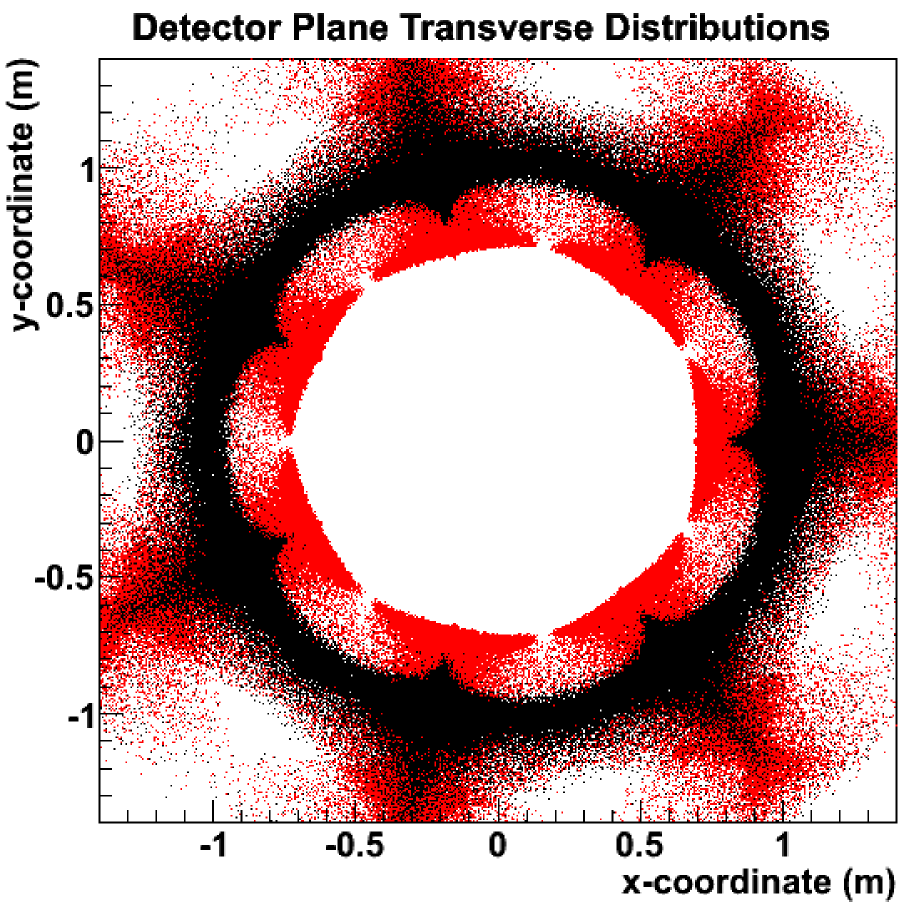

Figure 1.5: Azimuthal rate distribution at the detector plane. Black represents Møller scattered electrons while red represents elastic ep scattered electrons.

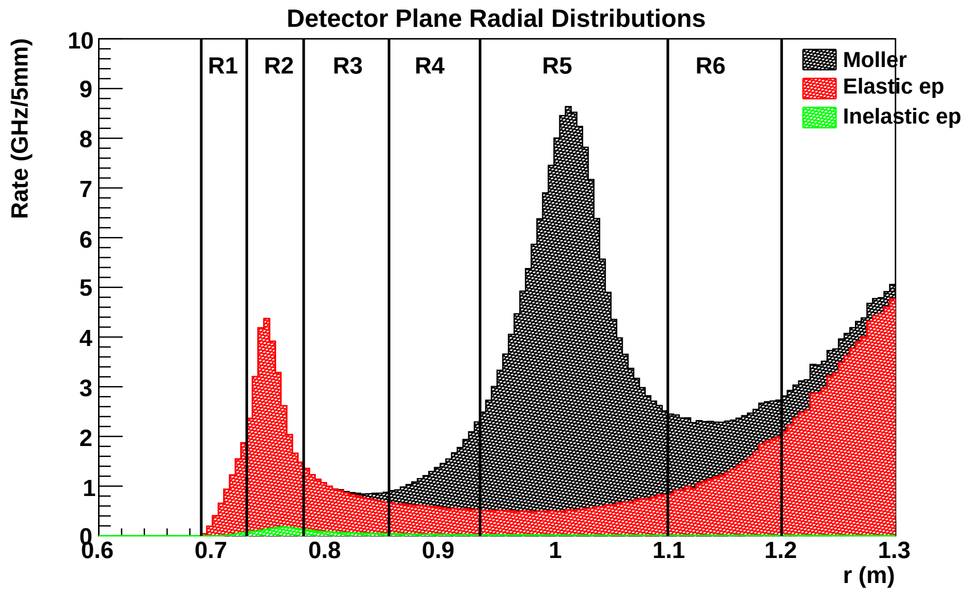

Figure 1.6: Radial rate distribution at the detector plane. Black represents Møller scattered electrons while red represents elastic ep scattered electrons. The detector ring is located at the Møller peak (1 m).

1.3 Why ShowerMax

ShowerMax is an electromagnetic sampling calorimeter. Electromagnetic sampling calorimeters use a dense metal (such as tungsten), called a radiator, to create a shower of particles. This shower grows bigger transversely, the further into the metal it travels, until the average energy of the showering particles falls below a threshold level. This threshold level is reached when the showering particle energy equals the critical energy of the radiator, at which point the transverse shower development tapers off rapidly. At several key locations along the shower's growth, an optical material (such as quartz) interrupts the metal and allows the shower to release detectable light.

ShowerMax will be located behind the thin quartz detector rings and in front of the pion detectors as shown in Figure 1.7. As shown in Figure 1.8, it will be positioned radially to intercept Møller scattered electrons so that it can make an independent measurement of A_{PV} subject to its own set of systematic errors. There are several key implications of calorimeters that will make ShowerMax a crucial detector for MOLLER.

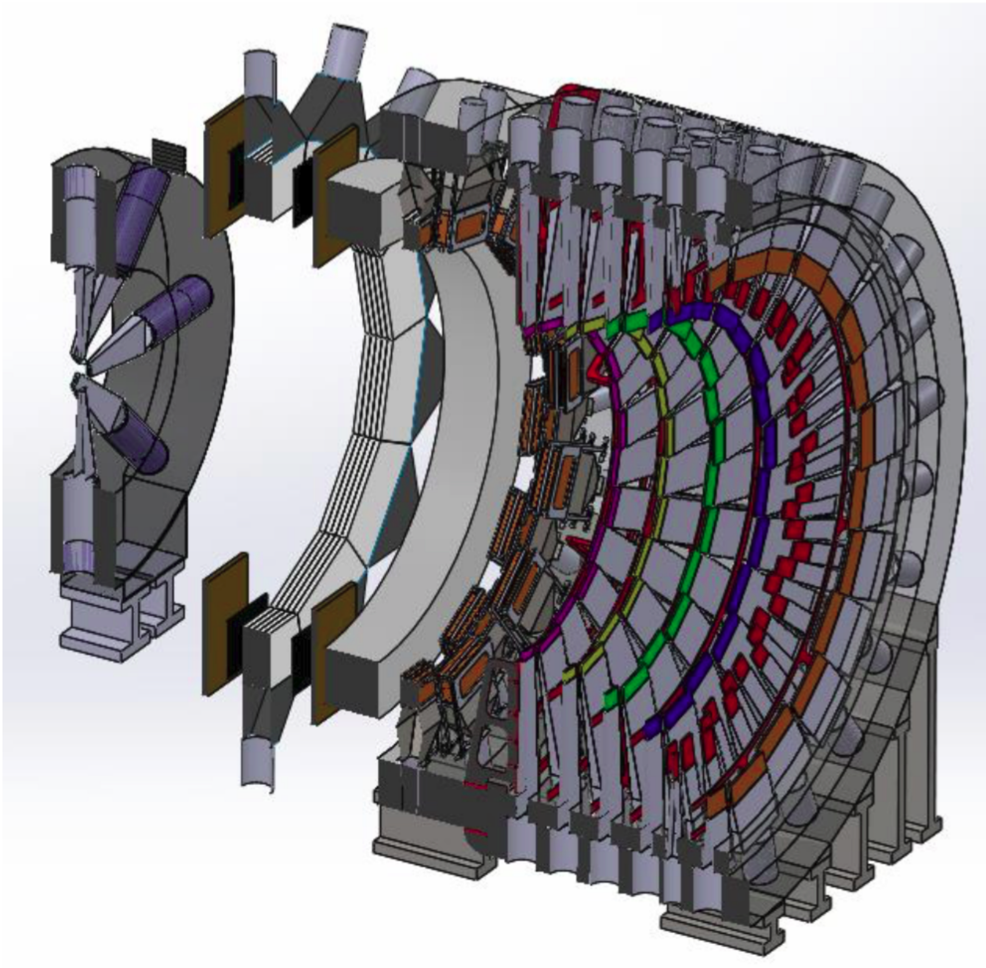

Figure 1.7: Detector ring cross-section. The first several rows of detectors are thin quartz for measuring A_{PV} and backgrounds. ShowerMax is the orange detector with its own ring. The remaining detectors are pion detectors and beam monitors.

The most important implication is that much more light is created in a calorimeter than for a thin quartz detector. Additionally, the response is linear with respect to energy. Because of this, particles with low energy (such as the backgrounds for MOLLER) make a significantly smaller signal than higher energy particles. Because of this, ShowerMax will be more resistant to backgrounds than the thin quartz detectors. Additionally, it will act as a backup to the thin quartz as it will be able to independently measure A_{PV} in the case that they have problems. This could be due to extremely high background rates, unexpected false asymmetries in the backgrounds, or other technical issues.

Another reason for the use of an electromagnetic calorimeter is to increase the statistics

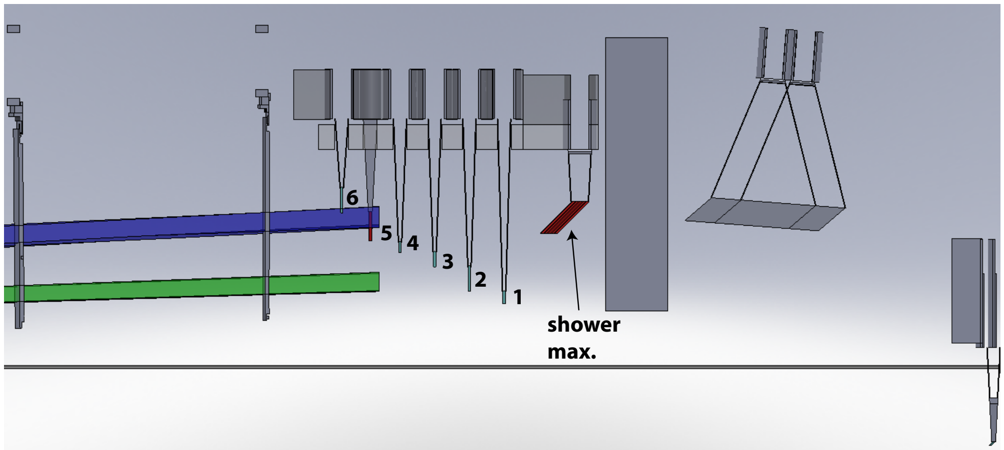

Figure 1.8: Detector ring cross-section with signal (Møller) and background (ep) electron paths. The ShowerMax sits behind ring 5 (the Moller ring). Notice that the signal electrons (blue) are separated, spatially, from the background electron-proton scattered electrons (green).

of the overall A_{PV} measurement. As previously mentioned, ShowerMax will make a measurement completely independent of the thin quartz detectors and subject to its own set of systematic errors. This will potentially enhance the statistical precision of the experiment's measurement by a factor of $\sqrt{2}$. In essence, ShowerMax will cross-check the thin quartz measurement, doubling the sample size of the experiment.

Finally, it's important to note that electromagnetic calorimeters have been the standard detectors in previous measurements of A_{PV}. Due to this, they are a well developed technology in the field. Thin quartz detectors are relatively new to the field. Having a calorimeter in the experiment will provide securities for unforeseen problems with thin quartz since it is a well tested and trusted technology.

Chapter 2

Theory

A calorimeter is a device that is used to measure the energy of a particular reaction. The most common image of a calorimeter is that of the bomb calorimeter encountered in an introductory chemistry class. However, there are a wide range of different calorimeters for a wide range of applications. This chapter will focus on the type of calorimeter ShowerMax is (an electromagnetic sampling calorimeter), its use in asymmetry measurements, and its limitations.

2.1 Electromagnetic Calorimetry

Electromagnetic calorimetry is a method of measuring the energy of an electron (or photon) through its absorption into some bulk material. In an electromagnetic sampling calorimeter, the electron first encounters the bulk material, or radiator, and begins to undergo bremsstrahlung and pair production reactions. This process leads to an exponential increase in the number of particles moving through the bulk material and is referred to as an electromagnetic cascade (or electromagnetic shower). Sampling calorimeters have alternating "detector" tiles sandwiched in between radiator plates which is referred to as a 'stack'. The quartz tiles in the stack allow a sampling of the shower at various depths along the shower's development. The longitudinal and lateral shower development are important considerations when designing such a device. Due to the properties of shower development (Section 2.1.1), the response of an electromagnetic calorimeter is linear with respect to energy. Given a redundancy of energy measurement (for calibration purposes), an electromagnetic calorimeter can be used to measure an asymmetry, and this is the purpose of ShowerMax. Throughout this chapter the properties and limitations of such a detector will be covered.

2.1.1 Electromagnetic Cascades

An electromagnetic cascade occurs when a relatively high energy electron impinges on some material and begins to lose energy [8]. The primary mode of energy loss in these energy regimes is bremsstrahlung radiation. The bremsstrahlung photons then undergo pair production, creating secondary electrons and positrons. These secondary particles will then undergo the same process which creates an exponential increase in particles, known as an electromagnetic cascade or an electromagnetic shower. Figure 2.1 gives an illustration of this process.

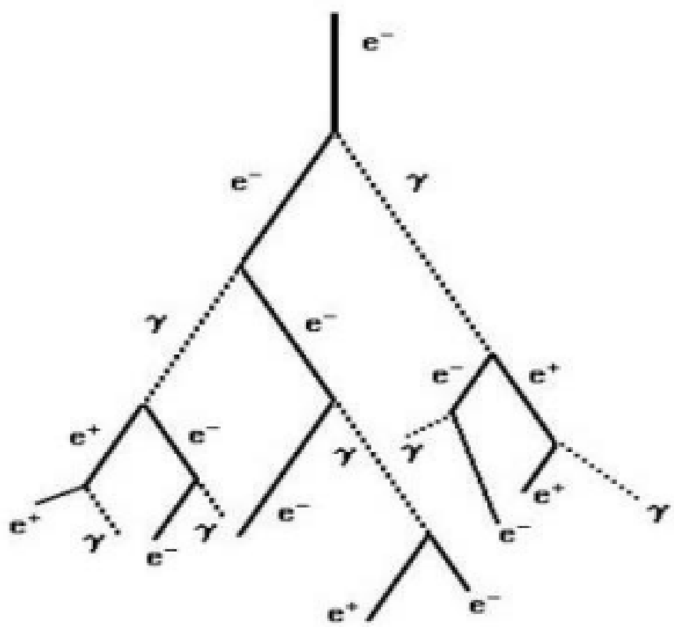

Figure 2.1: Illustration of an electromagnetic cascade [14].

The shower will continue to grow until the average particle energy is such that losses are only due to ionization processes instead of bremsstrahlung radiation. This energy is referred to as the critical energy and is described satisfactorily as [1]

$$E_c = \frac{610\ MeV}{Z + 1.24}, \tag{2.1}$$

where Z is the atomic number of the material (or radiator).

Electromagnetic cascades can be quantified through several key parameters. A simple model of these showers can be made through a thought experiment. Consider an electron of incident energy E_0 impinging on a radiator. It should be expected that the electron travels one radiation length before undergoing bremsstrahlung and creating a photon. Therefore, on average, the number of particles doubles after one radiation length. The electron will undergo the same process after the next radiation length. The photon will also pair produce upon traveling approximately another radiation length[1]. Thus, the number of particles will again double at two radiation lengths. Therefore the number of particles at a given depth is given as [9],

$$N(t) = 2^t, \tag{2.2}$$

where N is the number of particles in the shower and t is the depth in radiation lengths. With each doubling of the number of particles comes a halving of the average energy of the particles in the shower. The average energy of a shower particle is then given by,

$$E(t) = \frac{E_0}{2^t}, \tag{2.3}$$

where E_0 is the energy of the initial electron. Since the primary mode of shower production is bremsstrahlung radiation, shower growth reaches its maximum at the critical energy. Using this knowledge, Equations 2.2 and 2.3 can be rearranged to give the depth and number of particles at shower maximum. The resulting equations are

$$t_{max} = \frac{\ln(E_0/E_c)}{\ln(2)} \tag{2.4}$$

and

$$N_{max} = 2^{t_{max}} = \frac{E_0}{E_c}, \tag{2.5}$$

[1] Note that this is not as accurate as it is for the electron. The mean free path for pair production is $\frac{9}{7}X_0$, not X_0.

where t_{max} and N_{max} are the depth and number of particles, respectively, at shower-maximum.

Equations 2.4 and 2.5 are very important. They show that the number of particles created in the electromagnetic shower process is linear with energy. They also show that the depth of the shower maximum only increases logarithmically. Thus, electromagnetic calorimeters have a response that's proportional to energy. Additionally, they can remain quite compact and still accept a wide range of energies. This greater compactness provides a wide range of benefits when engineering such devices. However, it does create some unique challenges for the MOLLER experiment as will be outlined in Chapter 3.

Another important property of electromagnetic showers are their radial size. As it turns out, this is an extremely difficult value to quantify [3]. However, it is common to quantify radial size with a value known as the Molière radius (R_M). It is defined as the radius of an infinitely long cylinder that contains, on average, 90% of the shower energy deposition. A cylinder of radius $2R_M$ contains 95% of the shower energy deposition. Figure 2.2 shows the fraction of energy loss as a function of Molière radius. The Molière radius can be approximated in units of grams per square centimeter by [11]

$$R_M = \frac{21\text{MeV}}{E_c} X_0, \tag{2.6}$$

where X_0 is the radiation length of the material[2] and E_c is the critical energy. In these units, the Molière radius is approximately constant with respect to energy.

This section has provided a simplistic model for the properties of electromagnetic showers. For more advanced detector considerations, a more detailed analysis is needed. The following section provides an expanded analysis of longitudinal shower development in tungsten.

[2]If the shower passes through more than one material, the Molière radius can be found by $R_M^{-1} = \sum_j w_j / R_{Mj}$, where w_j is the weight fraction of each material.

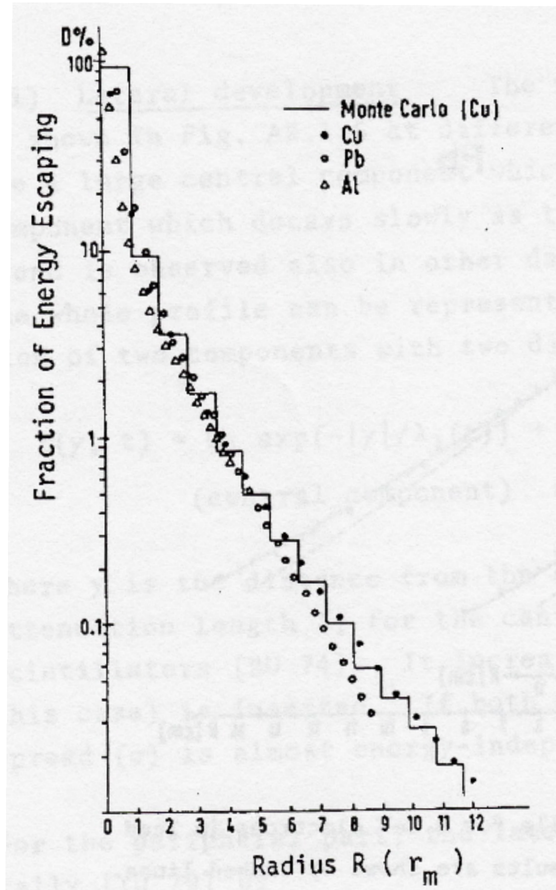

Figure 2.2: Fraction of energy escaping with respect to Molière radius [13]. Materials shown are copper, lead, and aluminum.

2.1.2 Shower Development in Tungsten

While the parameters in the previous section are sufficient for most applications, development of ShowerMax requires a more detailed understanding of electromagnetic shower development[3]. The reason for this is covered in more detail in Section 2.2, but is essentially due to the unique focusing characteristics of the spectrometer in the MOLLER experiment. This section provides a more detailed model of the longitudinal development of electromagnetic showers in tungsten and the crude model from the previous section is expanded upon. This gives a model that will be extremely useful in Chapter 3. Specifically, this section will

[3]It will also be important to understand the rate of neutron production (mostly photoneutrons) in ShowerMax because it will be a source of noise for the thin quartz detectors. The parity violation group at SBU is currently working on 'splash-back' studies of ShowerMax that will include neutron production.

examine incident energies between 2 and 8 GeV due to the fact that the MOLLER spectrometer will focus all energies in this range on to the ShowerMax ring. The model that will be developed is still only an approximation but will be extremely important in ShowerMax design considerations discussed in Chapter 3.

In the previous section it was shown that the number of particles in a shower initially grows as 2^t. However, this does not continue indefinitely throughout the material due to energy loss. As the average energy of shower particles decreases, the chance of pair production also decreases. Therefore, a slow tapering off of $N(t)$ should be expected as a function of shower depth into the material (as seen in Figure 2.3). The standard method of modeling longitudinal shower development was pioneered by Longo and Sestili in 1975 [5]. Shower growth as a function of depth (t) is represented by,

$$N(t) = At^{\alpha}e^{-\beta t} \; , \tag{2.7}$$

where A, α, and β are generally found using Monte Carlo simulations. Using data from Longo and Sestili along with the known t_{max} and N_{max} in tungsten, the best fit for these parameters was found using Matlab. Figure 2.3 shows the results of shower size with respect to depth in tungsten while Table 2.1 shows the values for the best fit. Appendix D contains the code which was used to find the fit. Notice that the shower size grows at approximately the same rate at shallow depths ($< 3X_0$) of tungsten for all incident energies; after that they begin to diverge. Lower energy showers begin to lose energy to ionization at a quicker rate than higher energy showers. Also notice the depths and magnitudes (max value of the curve) at which the peaks occur. The magnitudes are linearly separated along the vertical axis while the depth at which they occur increases very slowly (logarithmically). This is shown more clearly in Figures 2.4 and 2.5 and are manifestations of Equation 2.5.

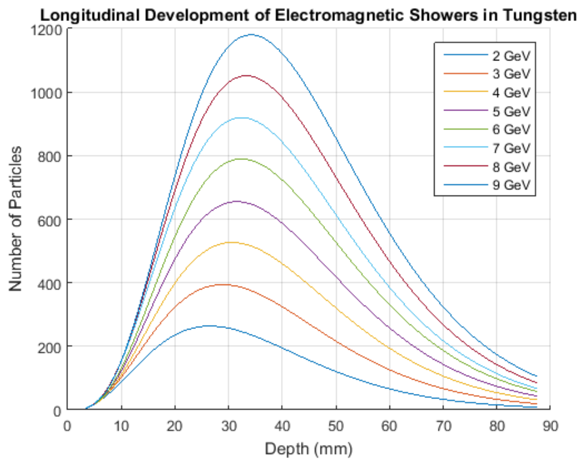

Figure 2.3: Longitudinal shower development in tungsten for incident electron energies between 2 and 9 GeV. For a larger image, see Appendix D.

E	A	α	β
2	11.05	3.1	0.41
3	10.1	3.3	0.4
4	8.8	3.5	0.4
5	8.8	3.6	0.4
6	8.5	3.7	0.4
7	9.9	3.7	0.4
8	9.05	3.8	0.4
9	8.1	3.9	0.4

Table 2.1: Fitted parameters for Figure 2.3 found using Matlab.

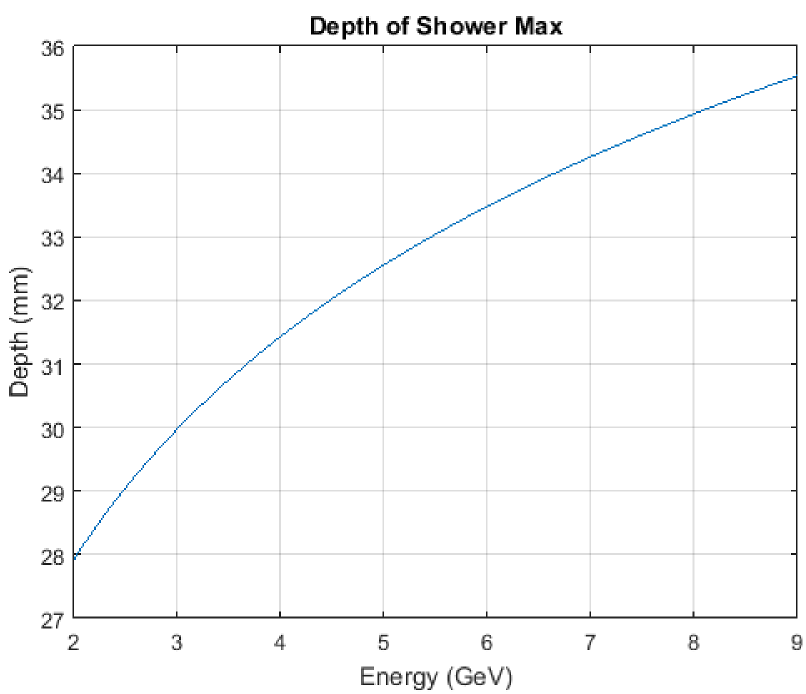

Figure 2.4: Depth at which the maximum shower size occurs in tungsten as a function of energy.

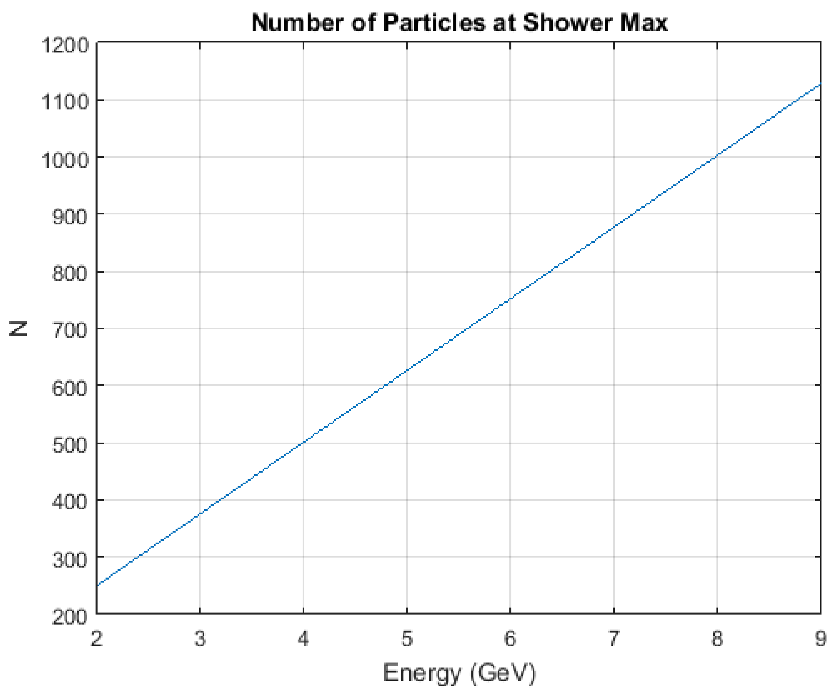

Figure 2.5: Maximum number of particles in an electromagnetic shower as a function of energy.

2.2 Calorimetry to Measure A_{PV}

Measuring an asymmetry with a calorimeter seems counter-intuitive. This is because, in essence, MOLLER is an electron counting experiment. Ideally, each electron would give the same flash of Cherenkov light. However, this is not the case in calorimetry. To understand the issues further, the logistics of asymmetry measurements are covered in this section. Then the methodology of measuring A_{PV} with a thin quartz device is contrasted with performing that same measurement with ShowerMax.

The standard parity violating asymmetry (A_{PV}) measurement is done with a highly longitudinally polarized electron beam. The beam polarization (and therefore helicity) is flipped in pseudo-random intervals. Each time interval is referred to as a gate whereas two consecutive gates of opposite helicity is considered a pair (Figure 2.6).

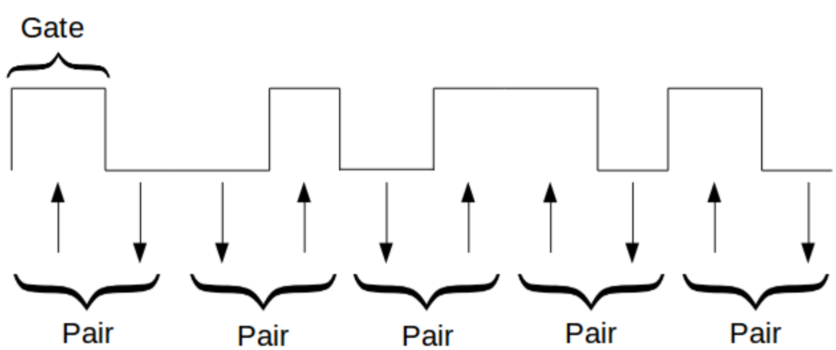

Figure 2.6: Illustration of beam helicity, gates, and pairs.

To measure A_{PV}, in essence, is to subtract the number of electrons detected from one helicity gate ($\uparrow$) from the electrons in the opposite helicity gate ($\downarrow$) of this pair; this is then divided by the sum of the electrons in the two gates.

$$A_{PV} \propto \frac{n_\uparrow - n_\downarrow}{n_\uparrow + n_\downarrow} \tag{2.8}$$

Measurement of A_{PV} is straightforward to perform with a thin quartz detector. Each electron that passes through such a detector creates the same amount of photo-electrons, on average, independent of the incident electron energy. Consider a thin quartz detector that creates x photo-electrons (PEs) per incident electron. If this detector is found to have measured N photo-electrons in a gate, then the number of incident electrons passing through the thin quartz detector is $n = N/x$. To find A_{PV}, the number of photo electrons can be used in a simple calculation given by,

$$A_{PV} \propto \frac{N_{\uparrow}/x - N_{\downarrow}/x}{N_{\uparrow}/x + N_{\downarrow}/x} = \frac{n_{\uparrow} - n_{\downarrow}}{n_{\uparrow} + n_{\downarrow}}. \tag{2.9}$$

The process of measuring A_{PV} becomes slightly more complicated when using a calorimeter. Experiments like MOLLER focus electrons with a wide range of energies on the measuring apparatus. The response of a calorimeter is linear with respect to energy. This implies that an electron incident on ShowerMax with an energy of 8 GeV makes four times more light than an incident electron with 2 GeV. Therefore, someone might conclude that the use of a calorimeter to measure A_{PV} could be problematic. How might we know the difference between one 8 GeV electron and four 2 GeV electrons? Furthermore, at the kinematics in the MOLLER experiment, only one extra electron is expected for roughly every 5 pairs [18]. Some clever analysis can be used to (mostly) overcome this challenge. As briefly mentioned earlier, the solution will come from a redundancy in energy measurement. The first "measurement" comes from the GEM planes mapping the spectrometer's fields so that the energy distributions of incident electrons will be known. This can then be used to back out the energy dependence of the calorimeter.

In order to better understand how to measure A_{PV} with ShowerMax, three separate gedanken-experiments will be discussed. The experiments take place in worlds in which the physics causing A_{PV} is only an approximation to our world. The first gedanken-experiment takes place in a world (call it 'World-A') where parity is maximally violated during a Z^0 exchange. Additionally, the electromagnetic and weak interaction energy transfer are the same in $\uparrow$ and $\downarrow$ gates. That is to say that the distributions of scattered electrons arriving at the detector are the same in both gates. The second gedanken-experiment takes place in a world ('World-B') nearly identical to World-A. In this world, however, the energy transfer in the ↑ and ↓ gates are different between the electromagnetic and weak interactions. Therefore, the energy distributions arriving from opposite helicity gates are also different (though both have the same underlying purely electromagnetic distributions). The third gedanken ('World-C') is also very similar to World-A. Parity is maximally violated during a Z^0 exchange and the energy transfer is the same in both the electromagnetic and weak interactions. The difference in this world is that there is a new, yet-to-be-discovered, interaction that can influence A_{PV} measurements. This interaction maximally violates parity as well and the Lagrangian of this interaction can be as unusual as one can imagine. Therefore, the physicists in this world do not know the probability of energy transfer in this new interaction at all and are therefore looking for deviations from known physics.

World-A

Consider now running an experiment in World-A similar to MOLLER. Recall that World-A is only an approximation to our world. In this world, parity is maximally violated during a Z^0 exchange[4]. That is to say that the Z^0 only couples to electrons of, let's say, a positive helicity gate (↑). Furthermore, the energy transfer of the electromagnetic and weak interactions are the same. This is to say that the energy distribution of electrons entering the detector are the same for positive and negative helicity gates. In this world there are no unknown interactions lurking in the background. The physicists somehow know this and are merely performing this measurement as a display of technological prowess.

The experiment in World-A is also measuring Møller scattering, and the only detector is an electromagnetic calorimeter. This experiment also has a unique spectrometer that focuses scattered electrons on the detector with energies between 2 GeV and 8 GeV (just like MOLLER). For simplicity, assume that the energy of the electrons entering the detector

[4]Note that this is not the case in our world. In our World-A Z^0 exchange mostly violates parity. The strength of this violation is determined by the weak-mixing angle

have a constant probability distribution[5], $P(E) = 1/6$. The calorimeter in this experiment has a perfect PMT and a response that is perfectly proportional to energy. This perfect response is merely given by the number of particles at shower maximum, i.e. $N_{max} = E/E_c$ (Equation 2.5). In this scenario, the total detector response for each gate in a pair is given by the equations,

$$N_\uparrow = \int_2^8 N_{max} n_\uparrow P(E) dE \tag{2.10}$$

and

$$N_\downarrow = \int_2^8 N_{max} n_\downarrow P(E) dE \tag{2.11}$$

Here, $n_\downarrow$ is the actual number of electrons that entered the detector during a negative helicity gate. Since parity is maximally violated in this world during a Z^0 exchange (i.e. only during positive helicity gates), $n_\uparrow = n_\downarrow + n_{apv}$, where n_{apv} is the scattered electrons entering the detector due to electromagnetic-weak interference. Plugging in the values of N_{max}, $P(E)$ and integrating, Equations 2.10 and 2.17 become:

$$N_\uparrow = \frac{1}{6E_c} n_\uparrow \int_2^8 E dE = \frac{5n_\uparrow}{E_c} = \frac{5}{E_c}(n_\downarrow + n_{apv}) \tag{2.12}$$

and

$$N_\downarrow = \frac{1}{6E_c} n_\downarrow \int_2^8 E dE = \frac{5n_\downarrow}{E_c} \ . \tag{2.13}$$

This is an interesting result. Notice what happens if the physicists in this world analyze their data in the same way they would with thin quartz detectors:

$$A_{PV} \propto \frac{5E_c^{-1}(n_\uparrow - n_\downarrow)}{5E_c^{-1}(n_\uparrow + n_\downarrow)} = \frac{n_\uparrow - n_\downarrow}{n_\uparrow + n_\downarrow} \tag{2.14}$$

It reproduces Equation 2.9 exactly! No fancy analysis has to be done to get A_{PV}. They just have to perform a subtraction of two gates and divide by the sum in the exact same way

[5] This is normalized for energy between 2 GeV and 8 GeV.

they would with thin quartz. A calorimeter can measure A_{PV} just as good (or better) than a thin quartz detector in this world since the energy dependence of the response cancels out.

This expression can be reduced further by recalling that $n_{\uparrow} = n_{\downarrow} + n_{apv}$. This expression will become useful when contrasting this world with World-B.

$$A_{PV} \propto \frac{n_{apv}}{2n_{\downarrow} + n_{apv}} \tag{2.15}$$

World-B

Now consider World-B. World-B is identical in almost every way to World-A. The exchange of a Z^0 maximally violates parity ($n_{\uparrow} = n_{\downarrow} + n_{apv}$). The difference between the two worlds occurs within the energy distributions of the excess electrons in a positive helicity gate. The energy distribution of the scattered electrons from Z^0 exchanges are different from the electromagnetic interactions. For this example the energy distribution of electrons scattered by the electromagnetic interaction will be $P_{\downarrow}(E)$ and will be the same function as it was in World-A ($P_{\downarrow}(E) = 1/6$). The electrons scattered by a Z^0 exchange will be $P_w(E)$. In this example, we don't need to know the functional form of $P_w(E)$. However, we will assume that the physicists in this world know all about these distributions as they did in World-A.

The experimental set up for this world is also identical to World-A. They have the same perfect calorimeter ($N_{max} = E/E_c$) and, as before, the spectrometer focuses scattered electrons to the detector with energies ranging between 2 GeV and 8 GeV. In World-B, the total detector response for each gate in a pair is given by the following equations:

$$N_{\uparrow} = \int_2^8 N_{max}\big[n_{\downarrow}P_{\downarrow}(E) + n_{apv}P_w(E)\big]dE \tag{2.16}$$

and

$$N_{\downarrow} = \int_2^8 N_{max}n_{\downarrow}P_{\downarrow}(E)dE. \tag{2.17}$$

Notice that Equation 2.16 is essentially the same as Equation 2.10 except that different probability distributions must be applied to the electromagnetic and weak scattered electrons. Substituting the known values of N_{max} and $P_{\downarrow}$ into Equations 2.16 and 2.17 and integrating, we get:

$$N_{\uparrow} = \frac{5n_{\downarrow}}{E_c} + \frac{n_{apv}}{E_c}\int_2^8 EP_w(E)dE \tag{2.18}$$

and

$$N_{\downarrow} = \frac{5n_{\downarrow}}{E_c} \tag{2.19}$$

Using these values in the same way the physicists in World-A results in:

$$\frac{N_{\uparrow} - N_{\downarrow}}{N_{\uparrow} + N_{\downarrow}} = \frac{n_{apv}\int_2^8 EP_w(E)dE}{10n_{\downarrow} + n_{apv}\int_2^8 EP_w(E)dE} \not\propto A_{PV} \tag{2.20}$$

Notice the difference between Equation 2.12 and Equation 2.18. If the physicists in World-B do the same analysis as in World-A they will get the wrong result! To see this compare Equation 2.15 and Equation 2.20. The only way that these equations could be equivalent would be if $P_w(E) = P_{\downarrow}(E)$. As stated earlier, this is not the case in World-B.

Fortunately, the physicists in this world know the energy distributions and they can do a different analysis that will give the correct A_{PV}. They have to use their knowledge of the incident electron energy distributions and the calorimeter (Equation 2.5) to convert $N_{\uparrow}$ and $N_{\downarrow}$ to $n_{\uparrow}$ and $n_{\downarrow}$. The solution is:

$$n = \int_2^8 \frac{N}{N_{max}(E)} P(E)dE\ . \tag{2.21}$$

To understand this equation, first consider a given energy E_i. The quantity $NP(E_i)$ gives the amount of the signal in the gate from that energy. Then to divide $NP(E_i)$ by $N_{max}(E_i)$ is to get the number of incident electrons, $n(E_i)$, at that energy (just as was done in Equation 2.9). Integrating over all of the energies gives the total number of incident electrons. Now the physicists in this world can apply this equation to find A_{PV}. Recall that $n_{\uparrow} = n_{\downarrow} + n_{apv}$ and, therefore, $n_\uparrow - n_\downarrow = n_{apv}$ and $n_\uparrow + n_\downarrow = n_{apv} + 2n_\downarrow$. The physicists of World-B will then find:

$$A_{PV} \propto \frac{n_{apv}}{n_{apv} + 2n_\downarrow} = \frac{\int_2^8 \frac{N_{apv}}{N_{max}(E)} P_w(E)dE}{\int_2^8 \frac{N_{apv}}{N_{max}(E)} P_w(E)dE + 2\int_2^8 \frac{N_\downarrow}{N_{max}(E)} P_\downarrow(E)dE}. \tag{2.22}$$

Equation 2.22 can be written in a form that is more useful. This is done by combining and normalizing the probability distributions of the electromagnetic and weak interactions ($P_\downarrow$ and P_w) into $P_\uparrow(E)$. Then A_{PV} can be written as follows:

$$A_{PV} \propto \frac{n_\uparrow - n_\downarrow}{n_\uparrow + n_\downarrow} = \frac{\int_2^8 \frac{N_\uparrow}{N_{max}(E)} P_\uparrow(E)dE - \int_2^8 \frac{N_\downarrow}{N_{max}(E)} P_\downarrow(E)dE}{\int_2^8 \frac{N_\uparrow}{N_{max}(E)} P_\uparrow(E)dE + \int_2^8 \frac{N_\downarrow}{N_{max}(E)} P_\downarrow(E)dE}. \tag{2.23}$$

Equation 2.23 is a more useful form for the real world as will be discussed at the end of this section. The lesson to be learned here is that the physicists in World-B can not blindly subtract the integrated response from their calorimeters and divide it by their sum in order to get A_{PV}. They must be aware of the incident electron's energy distributions[6] ($P_\uparrow$ and $P_\downarrow$) and their calorimeter's response ($N_{max}(E)$). They can then use this knowledge to extract $n_\uparrow$ and $n_\downarrow$. Once they have these values they can accurately calculate A_{PV}.

World-C

Now for the final gedanken-experiment. World-C is almost identical to World-A and the energy transfer of the electromagnetic and weak interactions are the same. Just as in World-A, assume that the energy of the electrons entering the detector have a constant probability distribution ($P(E) = 1/6$). The physicists use the same calorimeter and the same spectrometer as before; this time there is new physics to be discovered. The electrons that scatter due to this interaction have an unknown energy distribution when they are incident on the detector (P_{new}). Assume for simplicity that this new interaction also maximally violates parity. Therefore, $n_\uparrow = n_\downarrow + n_{apv} + n_{new}$. Here, $n_\downarrow$ are electrons scattered due to the electromagnetic interaction, n_{apv} are electrons scattered due to the weak interaction, and n_{new} are

[6]It is very important to note that this requires a good mapping of the spectrometer's fields.

electrons scattered due to the undiscovered interaction. Of course, for this interaction to be undiscovered, it must be that $n_{new} << n_{apv}$. In this world, the total detector response for each gate in a pair is:

$$N_{\uparrow} = \int_{2}^{8} N_{max}\left[n_{\downarrow}P(E) + n_{apv}P(E) + n_{new}P_{new}(E)\right]dE \tag{2.24}$$

and

$$N_{\downarrow} = \int_{2}^{8} N_{max}n_{\downarrow}P(E)dE\ . \tag{2.25}$$

Substituting the known values of N_{max}, $P(E)$, and integrating, Equations 2.24 and 2.25 become:

$$N_{\uparrow} = \frac{5}{E_c}(n_{\downarrow} + n_{apv}) + \frac{n_{new}}{E_c}\int_{2}^{8} EP_{new}(E)dE \tag{2.26}$$

and

$$N_{\downarrow} = \frac{5n_{\downarrow}}{E_c}\ . \tag{2.27}$$

Notice that Equation 2.13 and Equation 2.27 are the same expression. Also, the first term in Equation 2.26 is equivalent to Equation 2.12. Most importantly, $P_{new}(E)$ is not known. The best that the physicists in World-C can do is use the analysis of World-A to approximate A_{PV}. They won't get the same result as World-A but, as we saw from World-B, neither will they get the correct result of their world. Given that n_{new} is small, they will have a result very close to the correct A_{PV}. Notice, however, that the physicists from World-C could use a thin quartz detector *and* a calorimeter. If they perform a good experiment their thin quartz detector will give them the correct[7] A_{PV}. They should not be surprised to see that their calorimeter gives them a slightly different A_{PV} compared with the thin quartz detector. In fact, this difference can be used to glean some information about $P_{new}(E)$ and

[7]Given that the thin quartz has approximately the same response for all particles it always gives the correct value for A_{PV}. No fancy analysis is needed. However, these quartz detectors are more susceptible to false asymmetries from background noise.

thus the Lagrangian of the new interaction.

MOLLER A_{PV}

The real world is quite different than the worlds of the previous gedanken-experiments. In the real world, parity is not maximally violated during a Z^0 exchange. The Z^0 couples more strongly to helicity electrons of one gate than another and the strength of the violation is determined by the weak-mixing angle. However, the three worlds discussed can still provide insight into how calorimetry can be used to measure A_{PV}. The standard model predicts A_{PV} very precisely. In the same way it also predicts precisely the expected energy distributions of the scattered electrons arriving at the ShowerMax in each gate. We can use these distributions, and insight gained from the gedanken-experiments, to back out the energy dependence of ShowerMax and extract A_{PV} more precisely to connect to theory.

A large part of the motivation for MOLLER is to try to probe physics beyond the standard model. One might ask, "Wasn't it already shown that an accurate measurement of A_{PV} can not be done when we don't know what the energy distribution from the unknown reaction will be?" Not exactly. Almost all of A_{PV} is going to be from known processes and the probabilities from the known physics can be used in the analysis to help understand any deviations that could result from unknown physics. If the result has any significant deviation from the standard model prediction, that will be an indication of possible new physics. Furthermore, in this situation a comparison between the A_{PV} from the thin quartz and A_{PV} from ShowerMax can be used to glean information about the new interaction's Lagrangian. In the case that there is no deviation from the standard model, that will be telling too. It will further the success of the standard model and will also put further restrictions (bounds) on BSM models that contribute to parity violation. However, it must be noted that there could be Lagrangians from new physics that MOLLER still may not be sensitive to. As discussed previously, designing ShowerMax to have a low energy-linearity[8] can greatly mitigate any

[8]To clarify any confusion: what is meant here is that the detector will have some response that is dependent on energy. Something of the form $N = mE + b$. Low energy-linearity is referring to a small m

concerns. In any case, lower energy-linearity will provide a more accurate measurement of A_{PV} so long as good detector resolution and resistance to backgrounds are not compromised.

In order to measure A_{PV} with ShowerMax, a method needs to be constructed that uses the energy distribution of incident electrons to back out the energy dependence of the signal. This is contrasted from World-A and World-C in that $n_\uparrow$ and $n_\downarrow$ are trying to be extracted from $N_\uparrow$ and $N_\downarrow$ instead of being assumed. Additionally, the known physics is more complicated than the physics of the gedankens. Asymmetry electrons can be in both gates of a pair, making the analysis slightly more complicated. However, the energy distributions of each gate are well known[9] and will be measured during the experiment's calibration. These distributions will be referred to as $P_\uparrow(E)$ and $P_\downarrow(E)$.

Consider first a single gate in which ShowerMax has a total response of N, i.e. the PMT sees N photo-electrons[10]. If nothing was known about the energy distribution of incident electrons, N could only be used to find A_{PV} to within a factor of four. However, two tools can be used to cope with this. First, Equation 2.5 gives us a value for the amount of shower particles $N_{max}(E)$ created by a single incident electron. Second, $P(E)$ gives the energy distribution of incident electrons. Therefore, the number of incident electrons required to make a signal of N is

$$n = \int_0^\infty \frac{N}{N_{max}(E)} P(E) dE \; . \tag{2.28}$$

Now it is straight forward to calculate A_{PV} for a pair using Equation 2.8. In this instance $n_\uparrow$ and $n_\downarrow$ are found using Equation 2.28 where the energy distributions for each gate are used. Here we find

$$A_{PV} \propto \frac{\int_0^\infty \frac{N_\uparrow}{N_{max}(E)} P_\uparrow(E) dE - \int_0^\infty \frac{N_\downarrow}{N_{max}(E)} P_\downarrow(E) dE}{\int_0^\infty \frac{N_\uparrow}{N_{max}(E)} P_\uparrow(E) dE + \int_0^\infty \frac{N_\downarrow}{N_{max}(E)} P_\downarrow(E) dE} \; . \tag{2.29}$$

(slope).

[9] This, of course, does not include effects from potentially new physics

[10] This number is directly proportional to the total number of shower particles throughout a gate. For simplicity, these two values can be assumed to be the same here.

Equation 2.29 will give a completely accurate result for A_{PV} within the standard model. Note, however, that the final MOLLER analyses must be cognizant that the space of potential Lagrangians for new interactions is infinite. As World-B and World-C illustrated, this can result in a measurement of A_{PV} that is good, but not exact. Fortunately, the contribution to A_{PV} from known interactions will be the overwhelming majority. Given this, Equation 2.29 will result in an acceptable and useful measurement of A_{PV}, especially when combined with the thin quartz measurement.

2.3 Detector Resolution

In this text, the resolution is defined as the rms of the detected and digitized signal divided by the mean of that signal. In essence, it is the relative width of the signal. In the ideal detector, the resolution would be 0% and the signal would be a delta function. The resolution of ShowerMax also needs to be known well because it determines the excess statistical noise contribution to its A_{PV} measurement. Excess noise is the error inflation in the nominal statistical error due to the fact that the experiment must be performed in "integration-mode" as opposed to the more traditional "event-mode". It is given by

$$\text{Excess Noise} = \sqrt{1 + \left\langle \frac{rms}{mean} \right\rangle} - 1 \; . \tag{2.30}$$

ShowerMax will have many different incident electron energies and each one has their own resolution. Naively, one might expect that the total resolution is just the total $rms/mean$ of a standard helicity gate, however, this is not true. Given that the analysis of A_{PV} uses knowledge of the gate energy distributions, so must the resolution. To do this, the energy distribution of the incident electrons and the resolution as a function of energy are convoluted as in Equation 2.31. An example of this convolution, for an early ShowerMax prototype, is shown in Figure 2.7.

$$\left\langle \frac{rms}{mean} \right\rangle = \int_0^\infty R(E)P(E)dE \qquad (2.31)$$

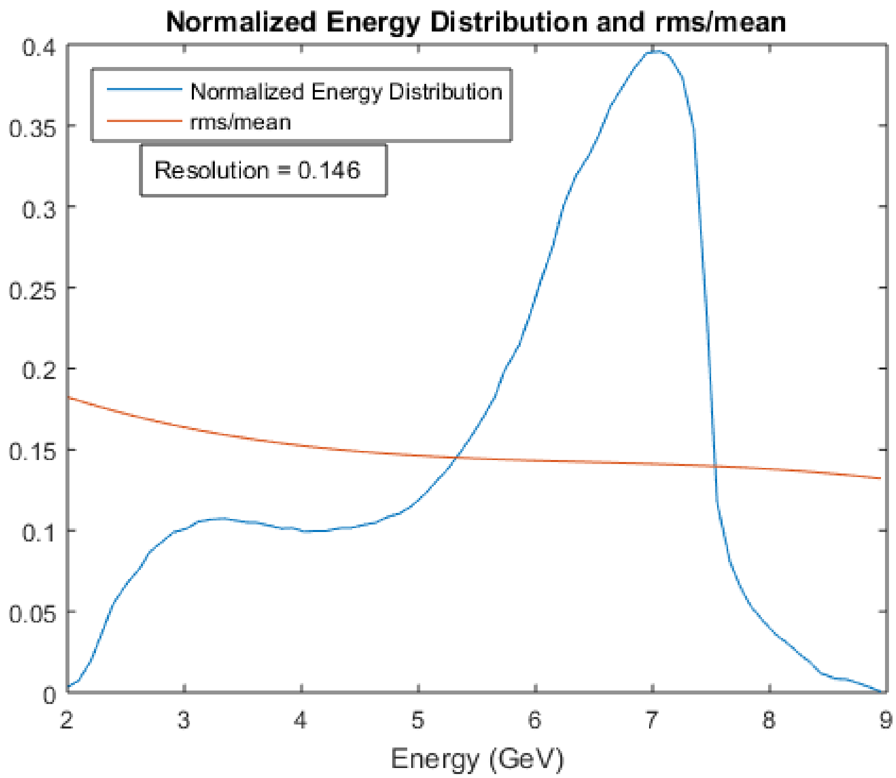

Figure 2.7: Sample resolution analysis. Resolution and normalized energy distribution are convoluted using Equation 2.31 to find a resolution of 0.146.

This chapter has documented the theory of electromagnetic calorimeters for A_{PV} measurement. This included the development of electromagnetic showers, specifically for showers initiated by 2 GeV to 8 GeV incident electrons in tungsten. It also discussed how the energy dependence of a calorimeter needs to be backed out in order to accurately calculate A_{PV}. The resolution of such a detector was also covered. In the following chapter, this knowledge will be used in order to design a calorimeter (ShowerMax) that will suit the needs of MOLLER.

Chapter 3

ShowerMax

3.1 Design Parameters

When designing the ShowerMax detector there are four considerations at the forefront: the first is the radial size of the detector ring, second is the detector resilience to backgrounds, third is the detector linearity with respect to energy, and the final is the resolution. This section covers the importance of each of these topics.

The size of the ShowerMax detector ring is fixed by the optics of the spectrometer[1]. The inner most edge of the detector ring is at a radius of 93.5 centimeters from the beam line while the outer edge of the detectors vary slightly depending on the azimuthal location. The detectors directly in the shadow of the coil are the largest radially while those out of the shadow are the smallest (the azimuthal extent of each detector is the same). This is due to the Møller electrons having lower energies and thus greater radial dispersion in the shadow. The detectors can not be any closer to the beam line due to Mott backgrounds; Mott Scattering is elastic electron proton scattering (or ep). Due to the larger mass of the proton, Mott scattered electrons typically have more energy than Møller scattered electrons and are therefore bent less through the spectrometer. Placing the ring in this position optimizes the ratio of signal to background in the detectors. Figure 3.1 shows a cross section of electron positions at the detector ring. Red dots are Mott scattered electrons and black are Møller scattered electrons. The second image shows the same plot with an overlay schematic of the ShowerMax detector ring.

Another feature of the detector ring placement is that the energy distribution seen by the detectors will be determined by this placement. Recall that the spectrometer not only focuses electrons radially but it also smears (or defocuses) them azimuthally. Figure 3.2 shows this focusing and smearing in a progression of transverse "cut-outs" of the scattered Møller

[1]The optics of the spectrometer have been tuned to give the sharpest radial focus with the largest separation from the main ep background peak.

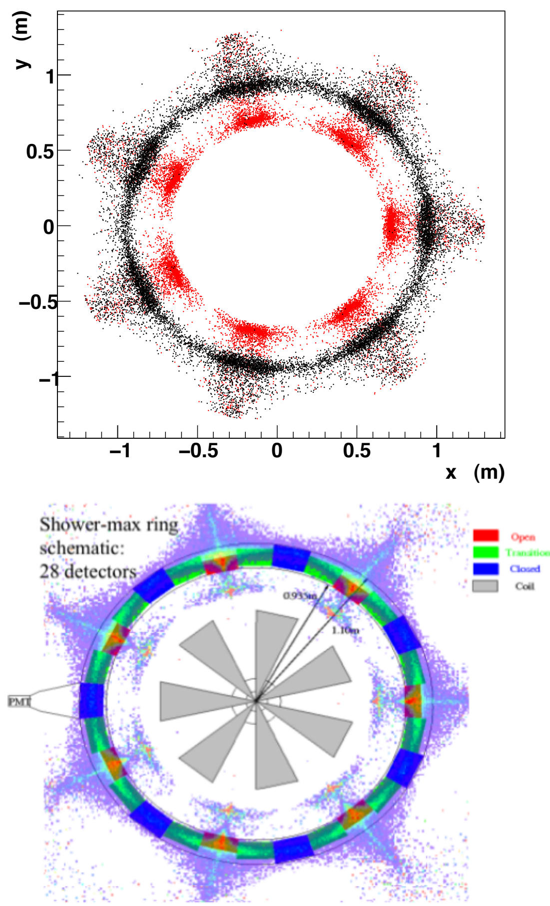

Figure 3.1: Above plot shows the transverse (relative to beam direction) distributions of electron positions at the detector ring. Red dots are Mott scattered and black dots are Møller scattered electrons. The image below is an overlay of the above plot onto a schematic of the ShowerMax detector ring. The electron rates are indicated by dot color: red is the highest and blue is the lowest.

electron envelopes as they progress through the spectrometer to the detector plane. Each cutout is an illustration of the radial position combined with angle (or energy) information at a certain location downstream of the target. Initially (upper left pane) the energies are well segmented by radius and azimuth according to the seven-fold symmetry of the toroidal spectrometer coils. As they move downstream they begin to focus radially and smear more and more azimuthally, with lower energy (higher angle) electrons experiencing more azimuthal smearing. By the time the electrons reach the location of the detector ring (lower right pane) all but the highest energies are fully smeared around the ring. This has serious consequences for the ShowerMax detector design and cannot be mitigated by selectively choosing the detector segmentation schemes as will be discussed in Section 3.2.3.

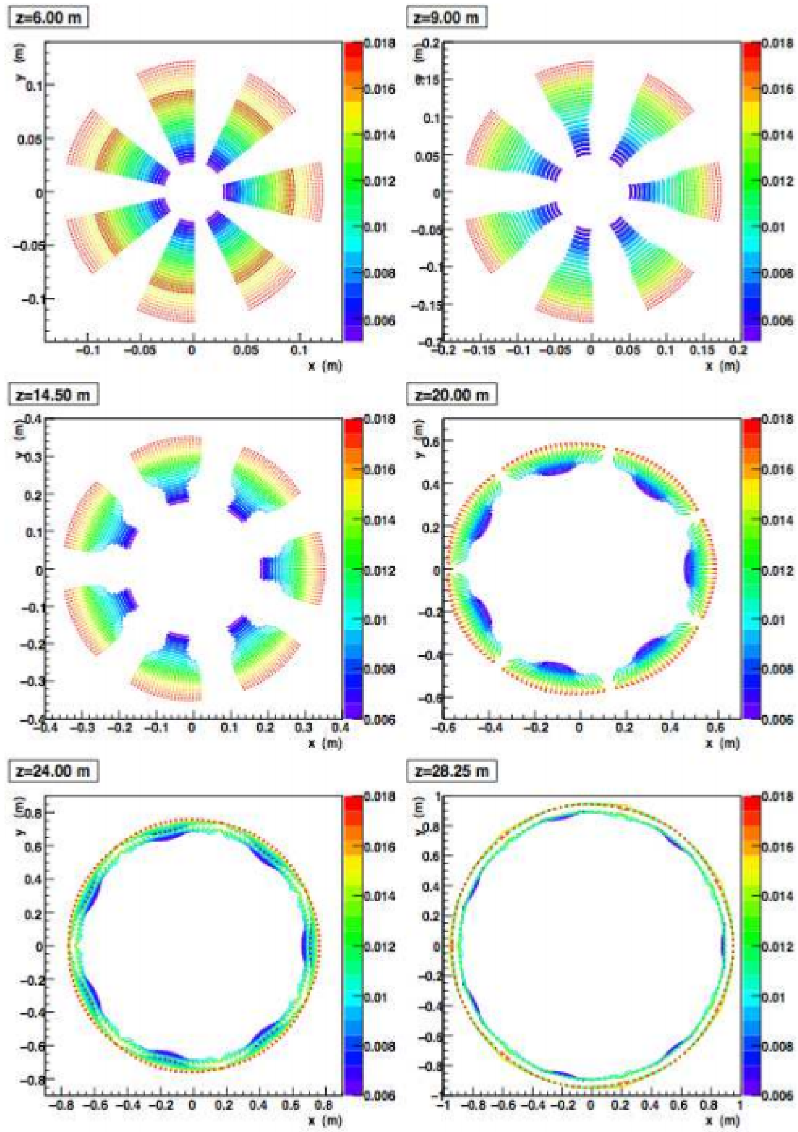

Figure 3.2: This progression of figures shows the radial focusing and azimuthal smearing of electrons by the spectrometer. Each image gives information about electrons at certain locations downstream of the target. Here blue represents higher energy (lower angle) electrons while red represents lower energy (higher angle) electrons.

In addition to the radial size and location of the detector ring being fixed, the radial location of the PMT is also fixed. To help minimize background noise, the PMT must be encased/shielded in a lead annulus. The annulus has an inner radius of ~ 135 centimeters which determines the overall length of the light guides for each detector. The light guides are discussed in Section 3.3.

ShowerMax must be resilient to soft photon and charged hadron backgrounds. The sensitivity of the main detectors in MOLLER make this extremely important[2]. It is possible that when the experiment is run, the anticipated suppression of photon and monitoring of pion backgrounds from the target hampers the efficient use of the bare, thin quartz detectors. In this case ShowerMax must be able to make the measurement at a reasonable precision on its own. In order to reduce the possibility that soft photons can make a sizeable signal, ShowerMax must be sufficiently thick such that only 2–8 GeV electrons make a significant signal. To test if this is the case, pion and photon beam simulations will be explored later in Section 3.5.

Another parameter is the detector's energy-linearity. The signal strength of an electromagnetic calorimeter is linear with respect to energy. As previously stated, the spectrometer focuses electrons between 2 GeV and 8 GeV in an inseparable smear at the detector ring. Since the experiment is 'counting' electrons, it is best if an 8 GeV electron makes, as close as possible, the same signal as a 2 GeV electron as possible. This will be studied using integer beam energies (2–8 GeV) incident on potential detector designs and fitting a linear curve to the resulting PE means. The slope of the fit will be referred to as the energy-linearity. The energy-linearity results are detailed at the end of Section 3.2.4.

The final parameter is the detector resolution. This may be the most important parameter. Detector resolution is defined as the rms of the signal divided by the mean of the signal. A perfect ShowerMax (0% resolution) would give the same delta function signal for any electron that passes through it and, therefore, it is desirable to 'minimize' the resolution. This will be studied using the same mono-energetic simulations as was used for the energy-linearity studies.

[2]This is due to the fact that they are thin quartz detectors. The response of these detectors is highly sensitive to photons and charged particles as compared with ShowerMax.

3.2 Stack Selection

3.2.1 Material

There are two materials in the stack of an electromagnetic calorimeter. The first is the radiator which is responsible for initiating and growing the shower. The second is the optical material which is used to release light from the shower in order to create a signal that can be digitized by a photo-sensitive device (i.e. PMT). It is not uncommon to use a single material for the stack which acts as both the optical material and the radiator. Generally, optical materials have larger radiation lengths (X_0) than radiators. As a result, the showers can grow more slowly and therefore require larger or physically thicker detectors. Given the space constraints imposed on the experiment apparatus, ShowerMax will be a compact sampling calorimeter. A sampling calorimeter consists of alternating radiator and optical materials.

There are many commonly used radiator materials for calorimeters. E158 at SLAC, the parent experiment of MOLLER, used copper [2] while other experiments often use lead. Table 3.1 gives the radiation length and Molière radii of commonly used calorimeter materials. ShowerMax must also be compact due to the positioning of the other detectors in the experiment. Therefore, tungsten was chosen as the radiator because it has a very low radiation length. It has a lower radiation length than lead and is much easier to handle in the lab [10].

Material	Use	X_0 (cm)	Molière Radius (cm)
Tungsten	Radiator	0.3504	0.9327
Lead	Radiator	0.5612	1.602
Copper	Radiator	1.436	1.568
Quartz	Optical	12.29	5.154
Acrylic	Optical	34.07	8.422
Lead glass	Radiator/optical	1.265	2.578
Lead tungstate	Radiator/optical	0.8903	1.959

Table 3.1: Properties of commonly used calorimeter materials [10].

Given that the energy of the incident electrons on ShowerMax is relatively high, Cherenkov radiation will be its main source of generated light. Cherenkov light is radiation emitted when a particle travels faster than the speed of light in that medium. The preferred optical material for transmitting Cherenkov radiation is fused silica (quartz for short) because it has been well tested and is known to be radiation hard, have low response to hadronic backgrounds, and have negligible scintillation [4]. Quartz also has remarkably good material properties such as high melting point and low thermal expansion coefficient [18]. The quartz to be used in ShowerMax will be optically polished Spectrosil-2000.

3.2.2 Quartz Geometry

The earliest ShowerMax designs were modelled after a calorimeter designed by Piotr Decowski. This design used ten pieces of tungsten interleaved with ten pieces of quartz. Scattered electrons traversed this 'stack' of material at a 45° angle. One end of the quartz was bevelled to prevent electrons from passing through different thicknesses of quartz while the other end was square allowing light to exit the quartz towards a PMT as shown in Figure 3.3.

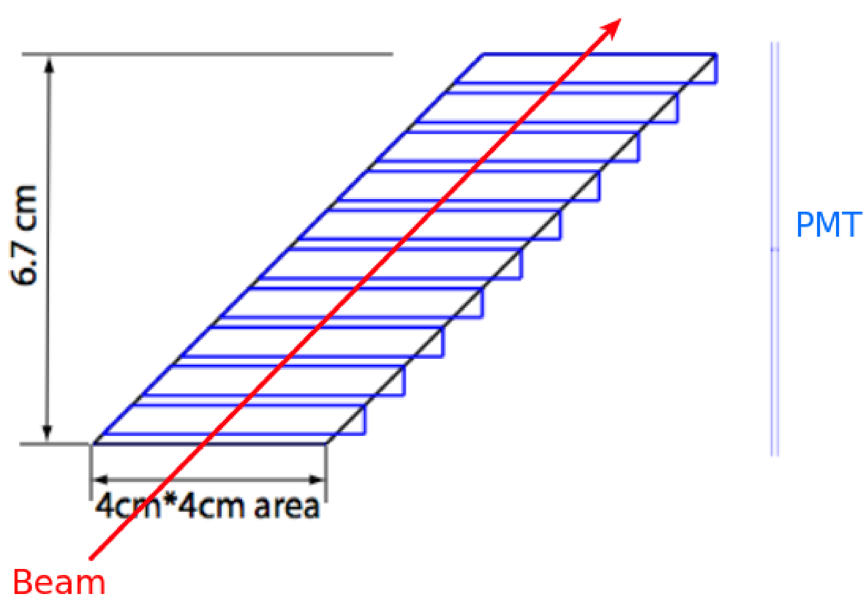

Figure 3.3: Original calorimeter design by Piotr Decowski.

Beam tests at the Mainz Microtron (MAMI), and simulations performed by the UMass (now SBU) and ISU Parity Violation Groups, led to a change in the design. Having the beam at a 45° angle to the quartz face causes half the generated Cherenkov light cone to be lost due to the angle in which it encounters the quartz-air boundary as shown on the left side of Figure 3.4. This can be fixed by rotating the quartz such that the incident electrons pass perpendicularly through the quartz face as shown on the right side of Figure 3.4. The electron emits a Cherenkov cone that experiences total internal reflection on all quartz faces except for at the bevel where the light exits. The only potential downside of the new design is that the light output is much more sensitive to small deviations in the incident electron angle. Fortunately, this is not a serious concern for ShowerMax because the electromagnetic shower process washes out the sensitivity of this dependence (see Appendix B). MAMI test beam data had good agreement with simulation—showing that the new quartz orientation resulted in higher photo-electron yields (or means) and lower resolution[3]. As a direct result, the excess noise is also reduced. Given that the new design outperforms the old in nearly all aspects, the quartz geometry for ShowerMax will use rectangular pieces with a 45° bevel at the outer edge and be positioned such that electrons are perpendicularly incident on the front face.

3.2.3 Azimuthal Width

A major consideration for stack selection is the stack azimuthal width (which directly corresponds to detector width and segmentation). As previously stated, there are regions inside and out of the shadow of the spectrometer coils. It is desirable to have a detector in the center of the region not in the shadow of a coil due to the high rate densities in these regions of the ring. This phi-region is referred to as the 'Open' region. The region directly in the shadow of a coil is referred to as the 'Closed' region while the region half in the shadow are

[3] A lower resolution is attained because incident electrons pass through a factor of $\sqrt{2}$ less material. As a result, there is a smaller chance of producing secondary particles, known as delta rays, which produce an asymmetric light tail in the signal which blows-up the rms and the resolution.

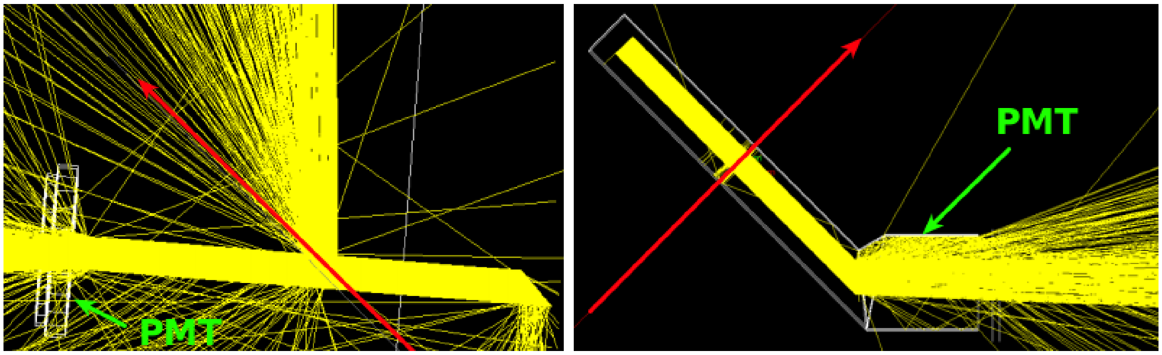

Figure 3.4: Red arrow indicates the direction and position of the electron while the yellow rays are optical (Cherenkov) photons. Left:Geant4 simulation visualization of a single electron event for the Original design. Note that half the light escapes the quartz and is lost. Right: Visualization of the updated design which uses total internal reflection to capture the entire Cherenkov light cone.

referred to as the 'Transition' region. These phi-regions are illustrated in Figure 3.5.

The question of how wide (azimuthally) and how many detectors there should be can now be addressed. The ideal layout would make it such that each detector region receives an energy distribution with the smallest spread possible. Six different phi-segmentation configurations were examined and are shown in Figure 3.6 along with their accepted energy distributions. As is shown, varying the stack width has little effect on reducing the energy spread within an individual detector, therefore the original (baseline) layout was chosen as the preferred one. This layout results in 28 detectors, each with an azimuthal width of 246 millimeters. It was selected as the best compromise between energy resolution and cost. Figure 3.6 reveals that varying the detector widths unfortunately does not effectively change the shapes or relative widths of the accepted energy distributions. While there are layouts that do improve the energy distribution relative widths, the change is not significant enough to warrant the increased cost and complexity of more and different sized detectors.

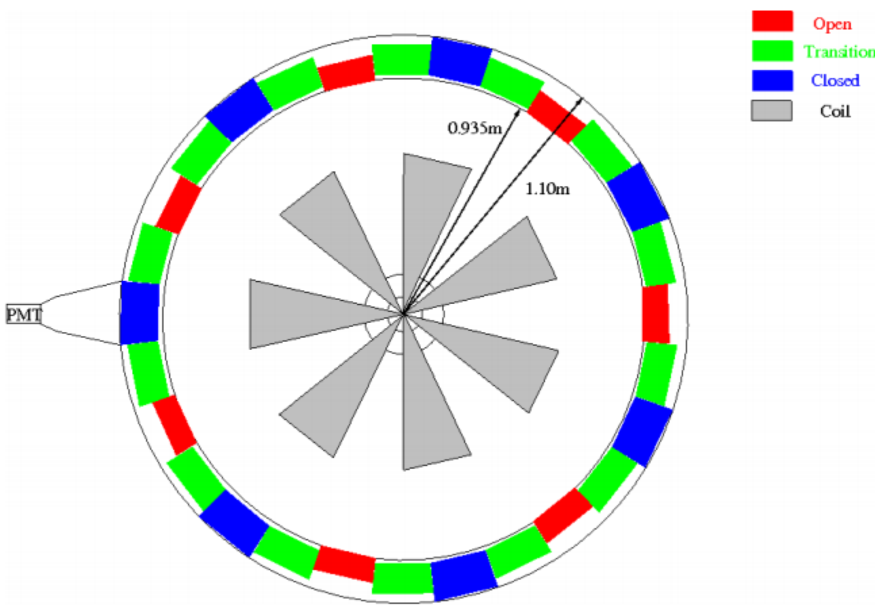

Figure 3.5: An illustration of the ShowerMax detector ring and azimuthal detector segmentations. The grey triangles protruding from the center represent the coils. The red, green, and blue parallelograms represent open, transition, and closed detector regions respectively.

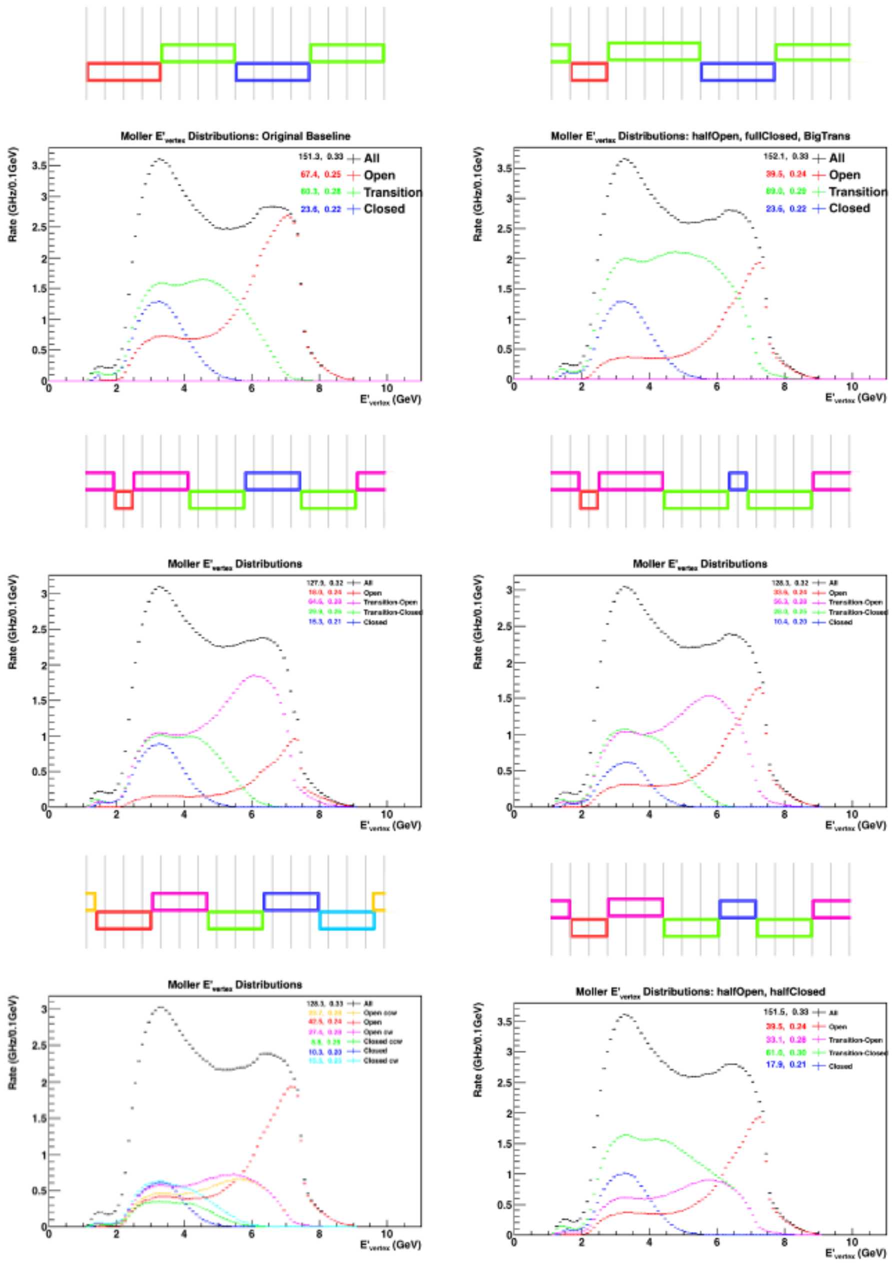

Figure 3.6: Azimuthal stack width and segmentation study with associated energy distributions. The cartoon above each plot shows the detector layout (looking radially) within one septant, or one seventh, of the entire ring. The light hash marks depict 61.5 millimeters of detector width. Starting in the upper left is the preferred detector layout (labeled original baseline) and five other configurations that were studied. The integral rates (in GHz) and relative widths are given in the legends.

3.2.4 Configuration

This section is concerned with the layout of tungsten and quartz in the calorimeter stack. It deals with parameters such as how many layers of tungsten and quartz and what their individual thicknesses should be.

The first thing we will consider is how many layers of tungsten and quartz to use in the detector stack. We first considered choosing this parameter based upon balancing resolution and cost. The cost is important here because the detector ring has an estimated budget of $250k that should not be overshot. Additionally, the quartz used is optically polished (to the nanometer scale) and such polish comes at a significant expense. The number of layers we considered varied between one and ten while keeping the total radiation length, total quartz thickness, and total tungsten thickness of each design permutation constant. It was found that six layers was best as shown in Figure 3.7. However, there was not a great advantage over four layers and given the cost of polished quartz, the four layer option was chosen.

Next, we can consider choosing the thicknesses of the tungsten and quartz to minimize the energy-linearity of the detector. To keep energy-linearity low, it would be best to sample the shower where the ratio of particle numbers between 2 GeV and 8 GeV electrons are closest to one. This is a challenge as shower size dies off much quicker for lower energy particles. Plotting the shower development model on a semi-log scale makes this apparent This is shown in the upper plot of Figure 3.8, where the shower development model is plotted on a semi-log scale. As the shower development progresses, the ratios grow worse and worse (farther from unity). This is especially apparent when considering the ratio between 2 GeV and 8 GeV shower sizes. The result is a near exponential decay as shown in the lower plot of Figure 3.8.

Figure 3.8 leads to the conclusion that the stack thickness should not proceed past the depth at which shower-max occurs (thus, the name ShowerMax) due to the worsening ratios of the high and low energies shown by the blue curve in the lower plot. Near the beginning of the shower development the ratios are near unity but the total radiation length of the detector is too low at this depth to be resistant to backgrounds. Also, the detector resolution in this region is poor as will be shown later in Figure 3.10. Ideally, the final piece of quartz in the shower development will occur somewhere near the shower-max of the 2 GeV shower.

Next, we can imagine sampling the shower at various depths while holding quartz thickness constant. Given that the radiation length of quartz is much larger than that of tungsten, the quartz pieces can be assumed to play a negligible role in the growth of the shower. Figure 3.9 shows one possible sampling where the quartz pieces are evenly spaced. In order to get an idea of how different configurations affect the detector response Geant4/Qsim simulations were performed on several different configurations. These configurations were chosen in order to keep the ratios between 2 GeV and 8 GeV shower sizes as low as possible. Appendix B has tabulated many of the configurations that were tested and their results.

Figure 3.10 shows the effect of varying tungsten thickness while keeping the quartz thickness constant. Here it can be seen that the resolution is dominated by total tungsten thickness and is less driven by quartz thickness. Thicker tungsten plates result in lower resolution but differences in light levels are not significant in this range of tungsten thicknesses. From the right side of Figure 3.9, it can be seen that 6 mm and 8 mm tungsten offer good resolution and energy-linearity.

Next, tungsten thickness can be held constant while the quartz thickness is varied. Figure 3.11 shows that quartz thickness primarily affects light levels and energy-linearity. The plots show a direct trade off between energy-linearity and resolution. Configuration 1A[4] offers the best resolution while configuration 4B has the lowest energy-linearity. Configuration 1B may be the best of both worlds as it has low energy-linearity and decent resolution. Given the trade-off, both of these detector configurations were chosen to build-full scale prototypes for testing (the prototype test beam experiment is discussed in Chapter 4).

[4]The 'A' in the configuration title refers to 10 mm thick quartz tiles while 'B' indicates 6 mm thick quartz.

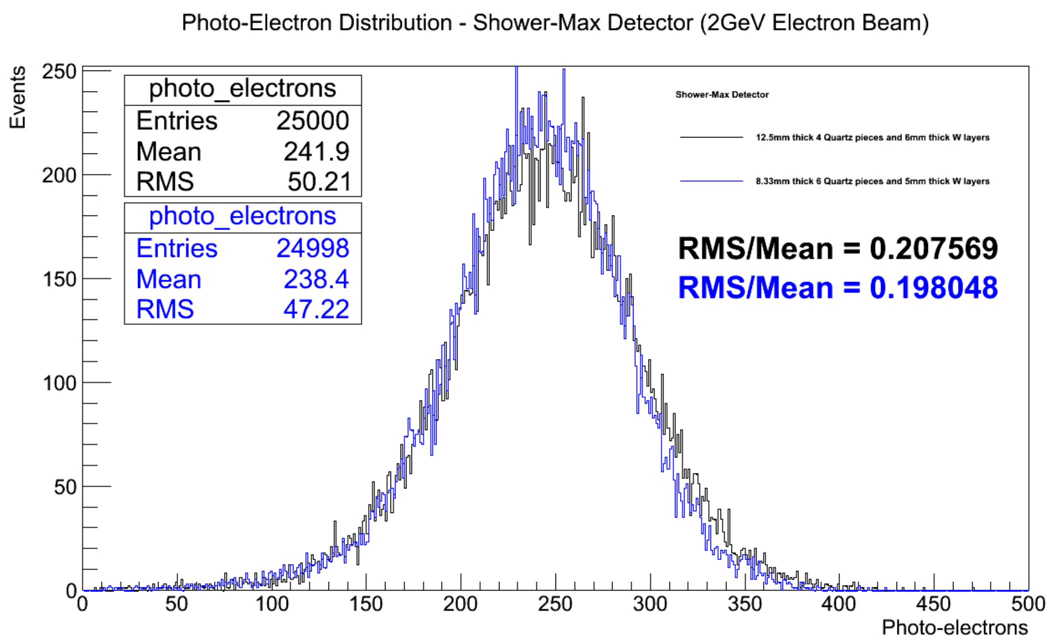

Figure 3.7: Four and six layer PE distributions. The black line shows 4-layer and the blue shows 6-layer PE response to 2 GeV electrons. Notice only marginal improvement in resolution going from 4 to 6 layers. Also note that the overall radiation lengths, quartz thickness, and tungsten thickness are the same.

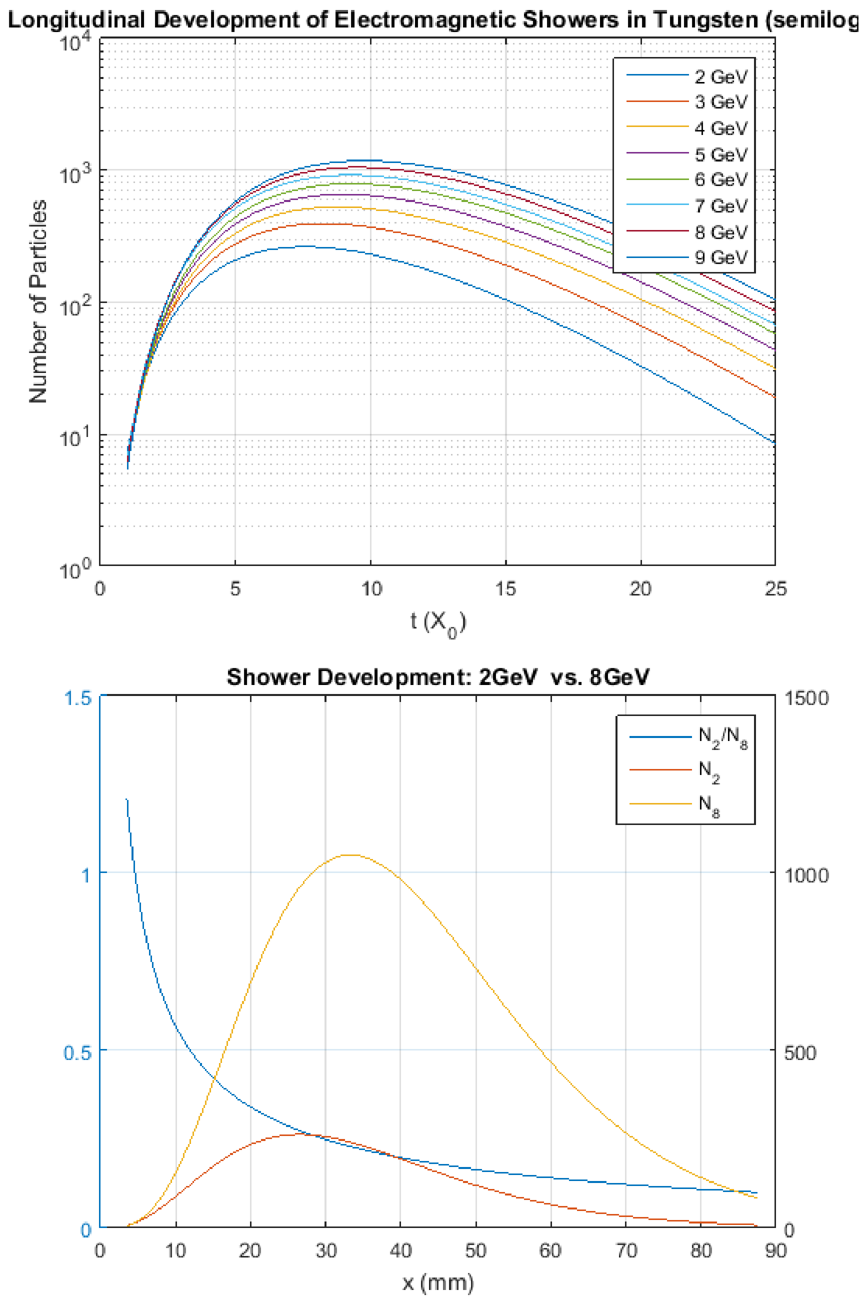

Figure 3.8: Top: Longitudinal shower development with respect to depth in tungsten on a logarithmic scale. Bottom: Shower development with respect to depth in tungsten at 2 GeV (red curve) and 8 GeV (orange curve). The ratio of 2 GeV to 8 GeV is also shown as a blue curve. Notice that the numbers of showering particles is given on the right side y-axis while the ratios are given on the left.

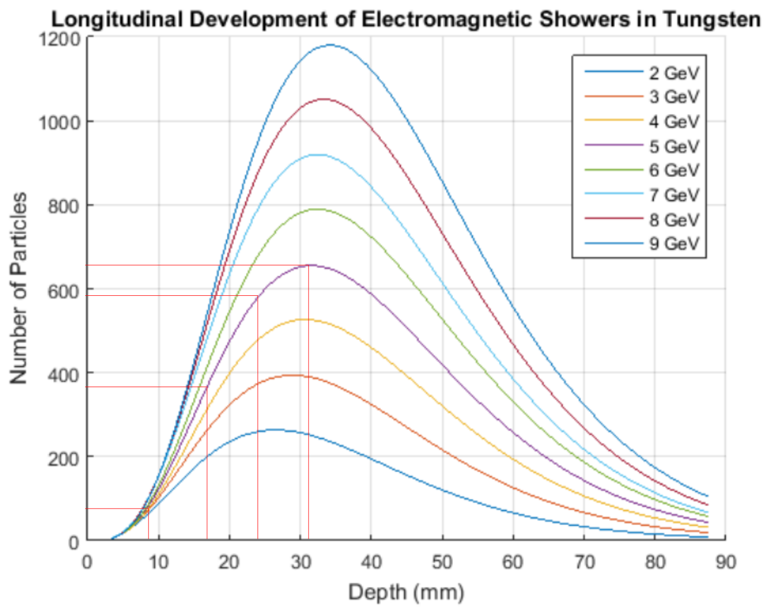

Figure 3.9: One possible shower sampling scheme. Vertical red lines indicate the position of quartz while the gaps between them represent the tungsten.

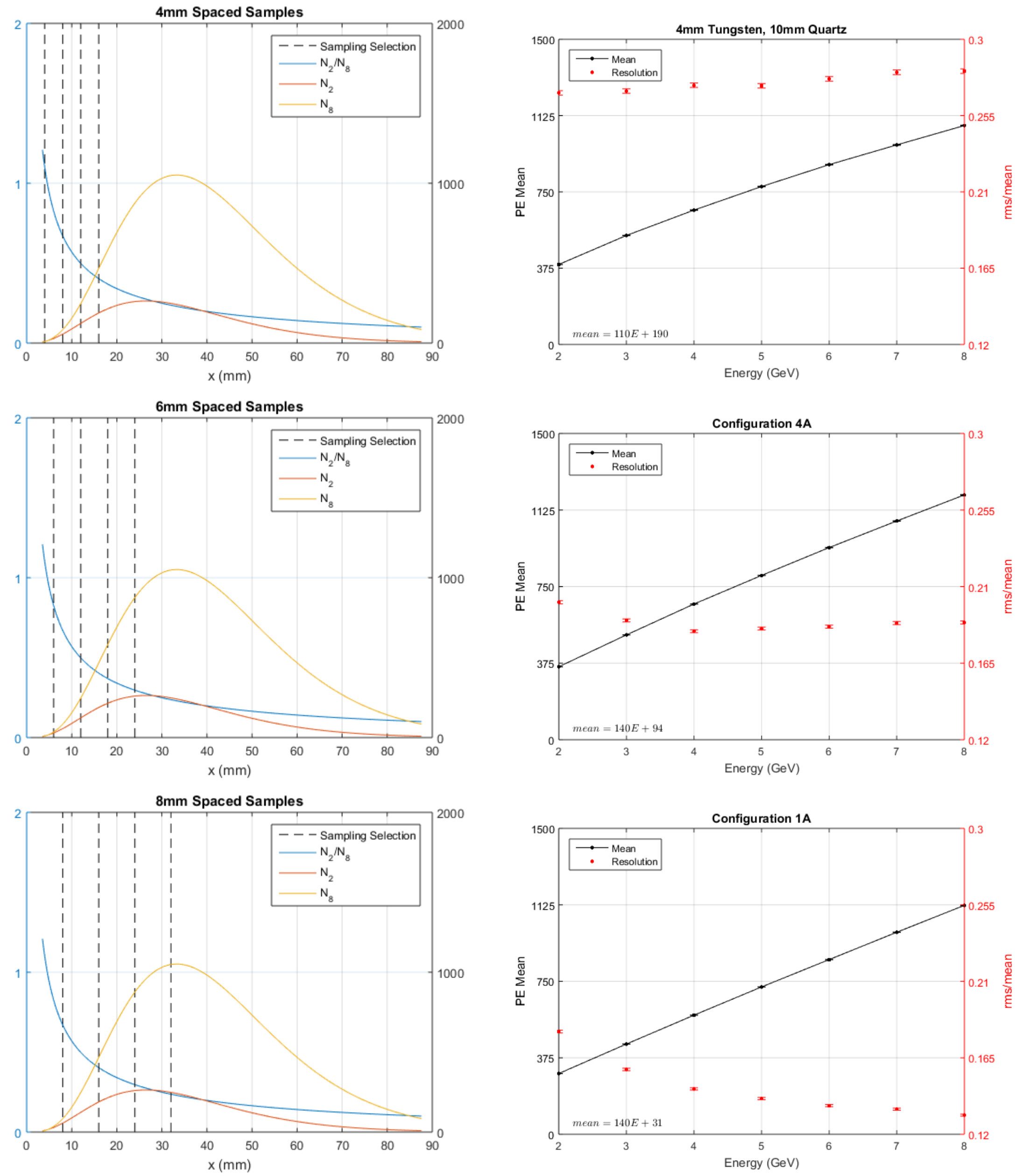

Figure 3.10: Left side: Figures show 2 GeV and 8 GeV shower development (right y-axis) and their ratios (left y-axis) as a function of shower depth. The dashed lines indicate quartz placement (10 mm thick). Right side: Results of the corresponding sampling scheme. The black lines are PE means and the red dots are the resolution with respect to energy. Note that the slope of the black line is the energy-linearity and is given by a fit at the bottom left of each plot. From top to bottom tungsten thicknesses are 4 mm, 6 mm, and 8 mm.

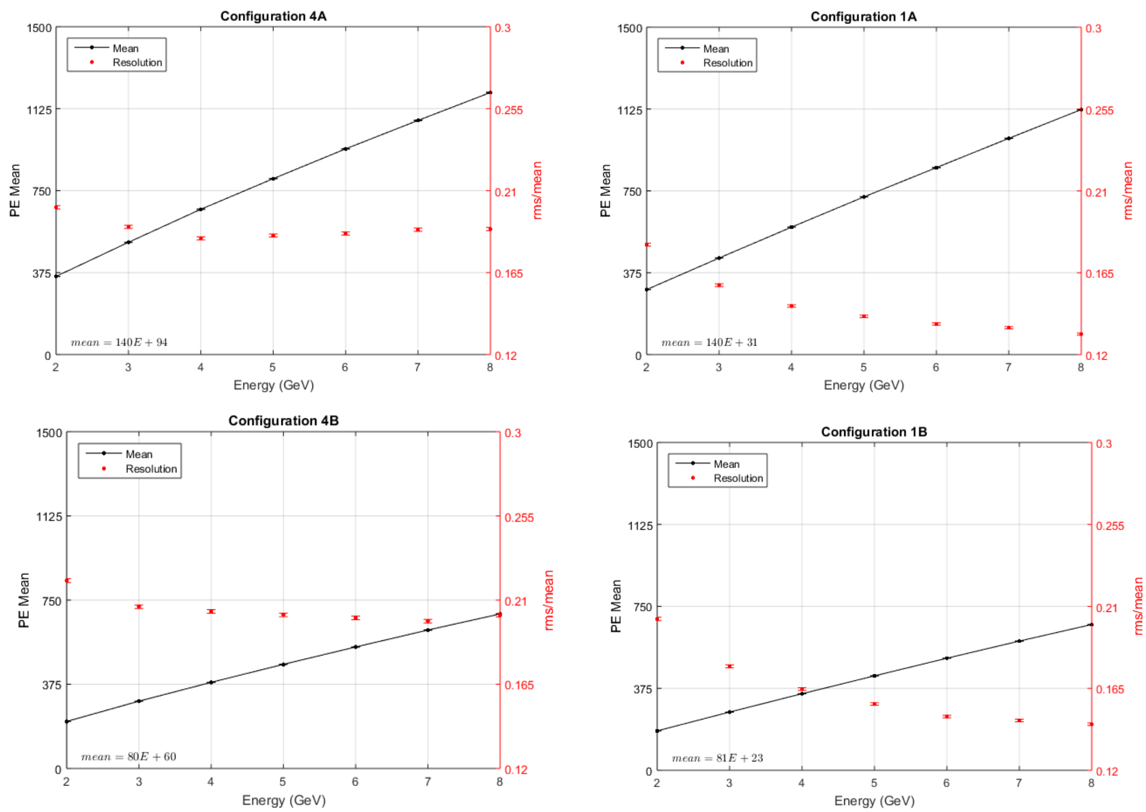

(a) 6mm Tungsten (b) 8mm Tungsten

Figure 3.11: Effects on PE yield and resolution as a function of energy while holding tungsten thickness constant and varying quartz thickness. Left side: 6 mm Tungsten with 10 mm (top) and 6 mm (bottom) quartz. Right side: 8 mm Tungsten with 10 mm (top) and 6 mm (bottom) quartz

3.3 Light Guide

ShowerMax will use an aluminum-mirror, air core light guide design that can efficiently direct the Cherenkov light from the stack to the PMT while being relatively immune to the high flux of charged particles passing through it. These light guides are known to be radiation-hard and will produce negligible background light (Cherenkov and scintillation) compared with ShowerMax's light.

3.3.1 Geometry

It is well known that the optimal shaped mirror for focusing incoming plane waves is a paraboloid. This was the guiding principle for developing the geometry of the ShowerMax light guide. There are two planes to be considered when designing the geometry. The first is the plane parallel to the beam line and the radial direction of the ring; this will be called the "side-plane" and is illustrated in Figure 3.12. The second plane is perpendicular to the beam line and parallel to the radial direction of the ring; this will be called the "front-plane" and is illustrated in Figure 3.13. This paper will discuss light guide design by first focusing on the side-plane then moving on to the front-plane. A constraining design parameter of the light guide is due to the distance between the outer edge of the stack the lead annulus that will be used to shield the electronics. For the Open detector, the light guide must have a length of $\sim$ 25 cm in order to connect the outer edge of the quartz to the PMT. Additionally, in order to minimize light losses, it is desirable that photons leaving the quartz only experience a single bounce before reaching the PMT.

When observing the stack from the side-plane, the quartz 45° bevel orientations alternate as shown in Figure 3.12. The reason for this design choice is primarily to keep the detector compact. It also provides a symmetry to the detector which allows for more straightforward structural design. The bevels of the outside quartz tiles point to the center of the PMT. This is a necessity for light guide compactness because light exits perpendicular to the bevel's face.

In order to determine the best geometry for the light guide cross section in the side-plane, an application was written in order to test the space of parabolas with the correct concavity[5]. Once the best parabola was determined, it was approximated to a straight line extending to the point where it intersects with the furthest light ray (point 'P' in Figure 3.12). The angle of the straight line approximation is found to be 15.5° degrees off of the vertical. From point 'P' the light guide is bent to return to the outer edge of the PMT at the shallowest possible angle. Figure 3.12 shows the best parabola and the straight line approximation to it.

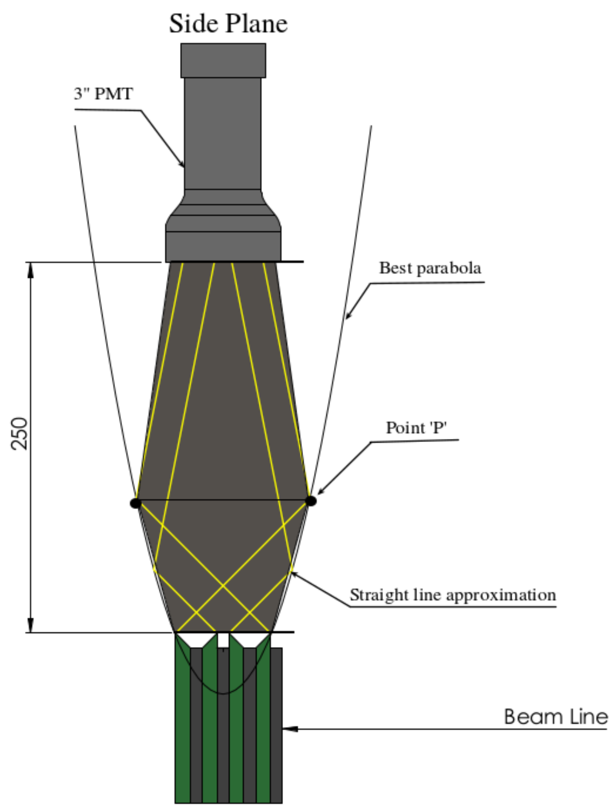

Figure 3.12: This is the side-plane view. Yellow lines represent light rays and green represents quartz. Dimensions are in millimeters.

Next, we can consider the front-plane. When viewing a cross-section of the detector from the front-plane, light rays appear to be exiting the quartz in the direction of the PMT

[5]This work was pioneered by Kevin Rhine using Wolfram Mathematica.

as illustrated in Figure 3.13. In order to find the optimal shape of the light guide in this plane the same procedure that was used for the side-plane was followed. An application was made to test the space of parabolas for optimal focus at the PMT. Notice in the top image of Figure 3.13 that the width of the quartz is much more than that of the PMT and two straight lines had to be used to best approximate the parabola. Construction of this light guide is very complex and, as will be discussed later in Section 3.5, too much light is incident on the PMT which could damage the electronics. To mitigate these concerns, a simpler light guide geometry was chosen and is shown in the bottom image of Figure 3.13. This design will allow for simpler construction, which will also help prevent light leaks[6].

[6] Due to the fact that they will be bent from flat sheets, the more bends that are present the more seams there will be. Each seam has a potential to leak light.

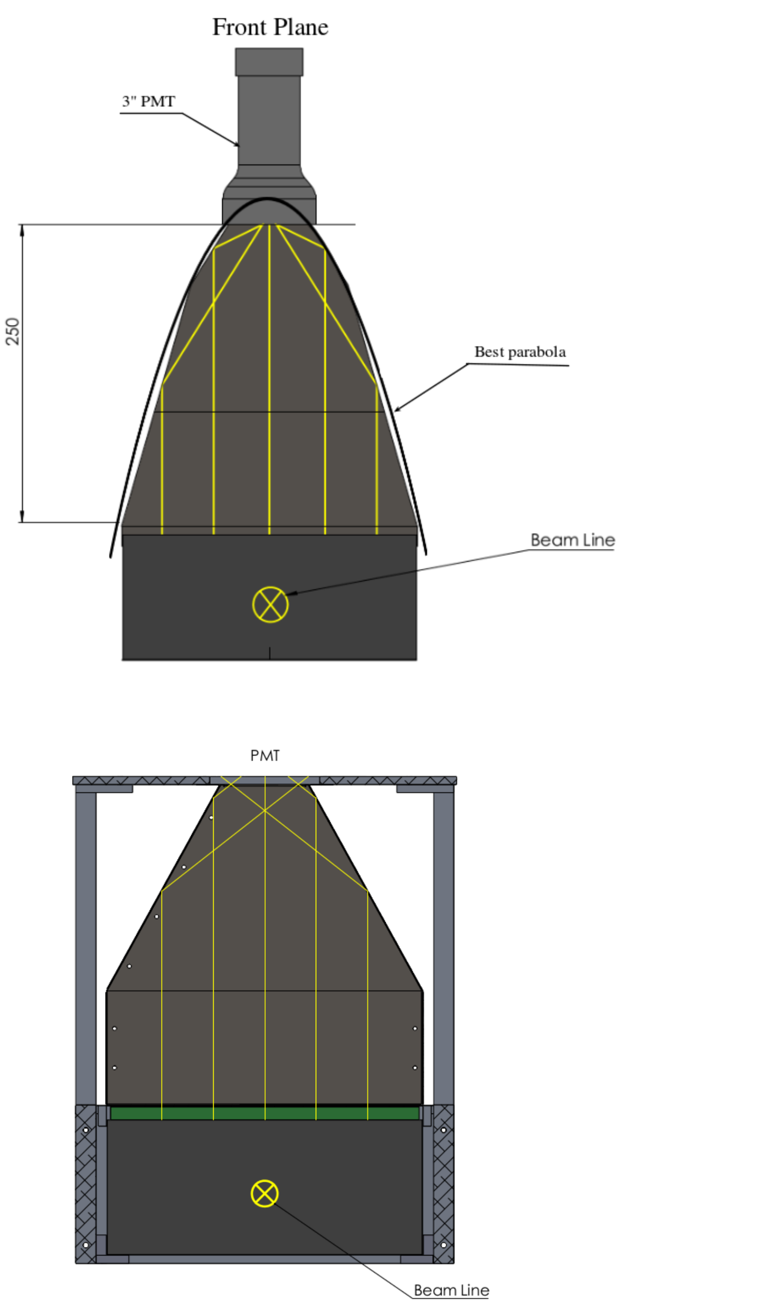

Figure 3.13: This is the front-plane view. The top image is the best fit to the optimal parabola using two straight lines. The bottom image is a simplified light guide that will make construction more repeatable and reduce light leaks.

3.3.2 Material

ShowerMax will be in a high radiation environment for about five years. Given this, precautions need to be taken that ensure the light guide will be able to perform throughout the experiment's lifetime. To ensure this, ISU's parity violation group (of whom the author is a member) took measurements of light guide reflectivity at the Idaho Accelerator Center (IAC). Several candidate light guide materials were exposed to an 8 MeV electron beam with 4 μs pulse width at 250 Hz repetition rate[7]. The peak current of the beam ranged between 65-110 mA. Given this, the materials were exposed to approximately 5 kRad/s during the irradiation.

Light guide reflectivity measurements were performed using an Ocean Optics light source and spectrometer. To calibrate the equipment, NIST calibration standards for a high reflectivity aluminum mirror were used. Measurements were taken before and after exposure at 90° (or normal incidence) to the light guide surface for wavelengths between 180 nm and 900 nm.

The conclusion of the irradiation reflectivity study was that all of the light guide materials were quite robust (including aluminized mylar). Materials with silver were found to be poor reflectors of deep UV light; however, the silvered mirror performed better in the MAMI beam-tests. Due to this, miro-silver 27 was chosen for the light guide material. It should be noted that more experimentation on the radiation hardness of reflective materials will be done in the future with more advanced techniques. However, Figure 3.14 shows the results of our initial radiation hardness study of ShowerMax light guide materials.

[7] Quartz will also be irradiated at the IAC in the near future to see how light transmission is effected.

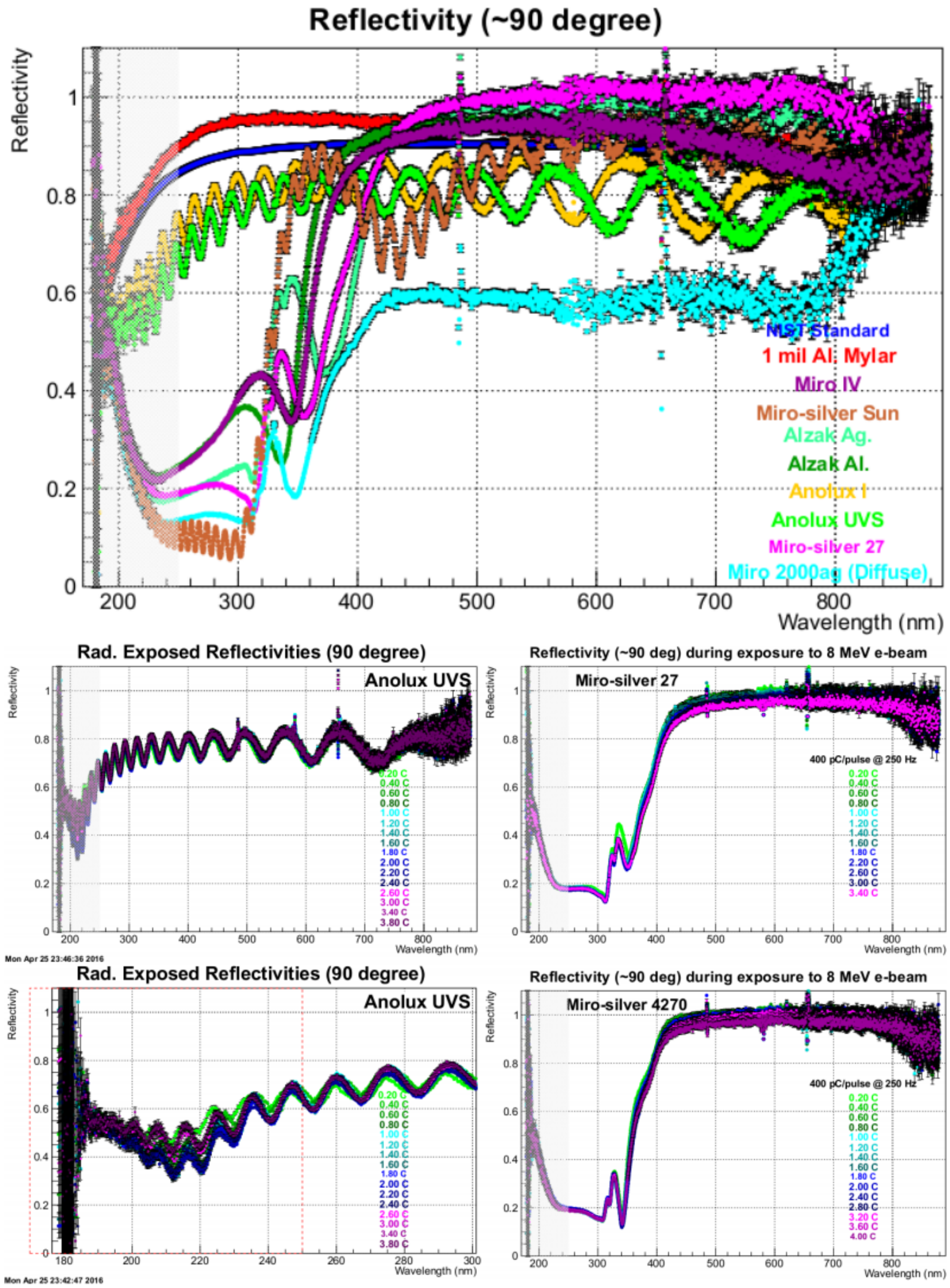

Figure 3.14: Results from reflectivity measurements of various light guide materials considered for ShowerMax. Top: Reflectivity of materials before irradiation. Bottom four: Reflectivity measurements after irradiation for anolux UVS and Miro-silver 27. The progression of numbers give the color encoding for the plots with corresponding dose exposures.

3.4 Engineering Considerations

There are two key engineering challenges for ShowerMax. The first is that the design must be able to support its own weight in any position on the detector ring and the second is that there must be a low profile way to suspend the tungsten and quartz without blocking light. This section covers our solutions to these problems.

3.4.1 Structural Support

The ShowerMax stack and light guide must be securely suspended from the lead annulus in a reproducible manner. We considered a number of potential different designs to fulfill this requirement. In the end, we chose to build a frame for each stack and light guide in the ring that can independently support its own weight. The quartz-tungsten stack is supported by four $\frac{1}{4} \times \frac{5}{8}$ inch aluminum flat bars that have a gusseted 'T' for bolting onto the annulus as shown in Figure 3.15. To ensure the bars will be load bearing, a failure analysis was performed using standard failure theories. The analysis was conservative and assumed a worst case scenario in which only two of the four columns support the entire load. In this scenario, it was found that the columns would have a factor of safety[8] of approximately 2.5. This analysis is included in Appendix A.

[8] A factor of safety of 2.5 means that 250% more weight could be supported before failure in that situation.

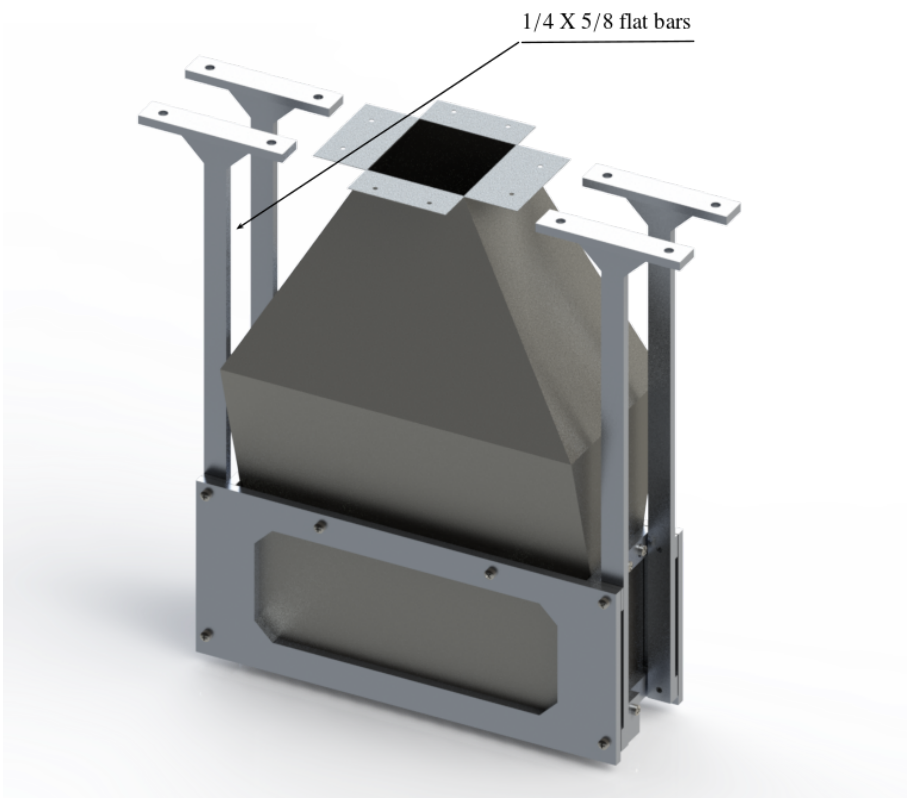

Figure 3.15: ShowerMax frame. The frame includes load bearing columns that bolt to the lead annulus.

3.4.2 Stack Stabilization

Supporting the tungsten and quartz stack against its own weight for all possible ring positions and without blocking much light is challenging. Additionally, the design must not contribute to stress concentrations on the strong but brittle quartz. The chosen solution is to use structural support bars with specially machined ledges that hold the stack in place. Renders of the machined ledges are shown in Figure 3.16. The square ledges shown in the right image provide support for the first and third tungsten pieces. The other two ledges provide support for the remaining tungsten and quartz pieces and have multiple shallow corners to be forgiving on the quartz. Each ledge protrudes an eighth of an inch from the support bar. This is enough to support the stack while remaining small enough not to block too much light. Additionally, the machined ledges anchor to the frame in such a way as to allow pressure on the stack to be increased or decreased as needed.

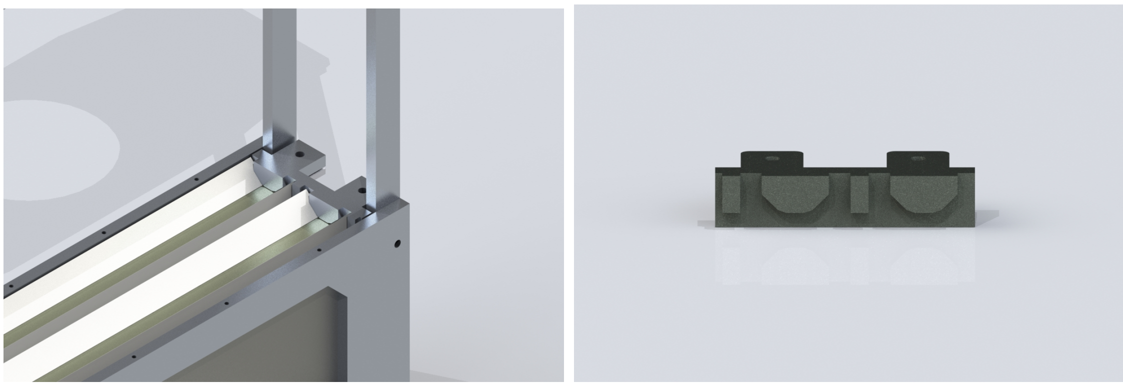

Figure 3.16: Stack stabilization method. Left: Aluminum ledge supporting stack. Note that the ledge has bolts that can be used to apply a controlled amount of pressure to the stack. Right: Front view of the ledge geometry.

3.5 Final Designs

Two ShowerMax detector configurations have been chosen to be constructed. The first is called config 1A. This consists of four tungsten radiators. The radiators are each 8 mm thick with dimensions, perpendicular to the beam line, of 246 mm (azimuthally) by 105 mm (radially). The optical material is 10 mm thick, optically polished Spectrosil 2000 with a 45° bevel on one edge. The quartz dimensions perpendicular to the beam, not including the bevel, are the same as the tungsten. The second detector is called config 1B. This detector is made of the same radiator and optical material as config 1A. It has the same dimensions perpendicular to the beam line and the thickness of the tungsten is also 8 mm. The only difference is that the thickness of the quartz is 6 mm for config 1B. The final light guide is a straight line approximation to the optimal parabola on the side-plane. On the front-plane, a simple design was chosen to minimize light leaks and simplify construction. The light guides are made from water-jet cut 0.02 inch thick miro-silver aluminum sheets. The detectors are also designed with a load bearing frame that can support the weight of the stack in any position in the detector ring and the stack is supported with specially machined ledges.

The simulations for the detector configurations show a trade off between energy-linearity and resolution as was shown in Figure 3.11. Config 1A shows great resolution and reasonable energy-linearity (140 PE's/GeV). Config 1B shows good resolution and better energy-linearity (80 PE's/GeV). Simulations also show that PE means are too high. For higher energy electrons in config 1A, over a thousand PE's are generated on average by the PMT, thus neutral density filters will need to be used on both detectors in order to reduce the number of PE's per electron to less than 200. This is necessary to protect the PMT. Table 3.2 shows the expected performance of the detectors for mono-energetic incident electrons of 2, 5, and 8 GeV.

Configuration	Energy (GeV)	RMS	Mean	Resolution	Energy-linearity
1A	2	63.36	315.9	0.20	140
1A	5	123.7	768.5	0.16	140
1A	8	183.2	1197	0.15	140
1B	2	45.46	197.7	0.23	81
1B	5	87.82	473.6	0.19	81
1B	8	129.1	732.3	0.18	81

Table 3.2: Performance of final ShowerMax designs for mono-energetic incident electrons.

The ShowerMax detectors are expected to be resistant to the photon and charged hadron backgrounds present during the experiment. In order to guage the response of ShowerMax to pions, a Geant4 simulated beam incident on the detector was studied. Figure 3.17 shows that a 5 GeV pion incident on config 1A will have a response that is only 22% of that of a 2 GeV electron; for config 1B it is 15%. This response is quite good and thus when the experiment is run in event-mode, pions will be easily distinguishable from the desired channel. The detectors were also simulated using Geant4 to incident photon beams. Figure 3.18 shows the results for incident photons between 10 MeV and 100 Mev.

Once the detector is fully built, it will be tested in the ISU parity violation group's cosmic ray stand. This will serve as an additional benchmarking procedure and is described in Chapter 4. A Geant4 simulated beam, incident on the detector, was studied in preparation for the first prototypes. 1 GeV muons are predicted to generate 36 PE's in the PMT on

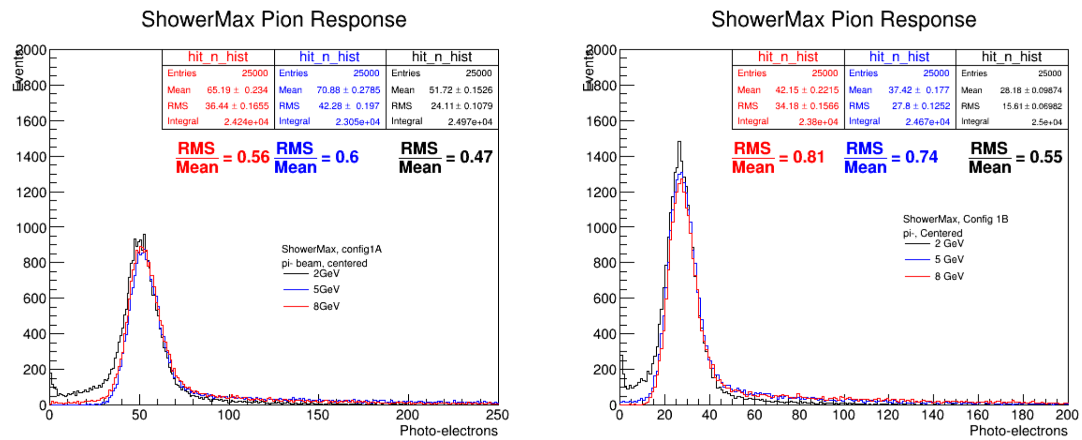

Figure 3.17: ShowerMax response to mono-energetic π^- beams. Red, blue, and black represent 2, 5, and 8 GeV pions respectively. Left and right hand plots are configurations 1A and 1B respectively.

average for config 1A and approximately 19 for config 1B as is shown in Figure 3.19.

Geant4 simulations have also been conducted in order to gauge our expectations for the full-scale ShowerMax prototypes in the future test beam studies (further detailed in Chapter 4). Figure 3.20 shows the expectations for configurations 1A and 1B. Config 1A is expected to make much more light and have better resolution than config 1B. At the high end of the energy scale, config 1A is expected to produce more than 1000 photo-electrons, on average, at the PMT for each incident electron. Config 1B gives a significantly lower yield at around 700 photo-electrons per incident electron. As mentioned earlier, the average mean PE yield across different energies should be closer together (lower linearity) for config 1B compared with config 1A, according to simulations.

It is also of interest to look at the total resolution of the detector. This is the overall resolution of the entire energy spectrum, of a single helicity gate, convoluted with the probability distribution of the incident electrons as discussed in Section 2.3. In order to find the detector resolution as a function of energy the resolution data shown in Figure 3.11 was fit to a cubic function. Next, this function was convoluted with the normalized energy distribution according to Equation 2.31. Surprisingly, the difference in resolution between the different configurations makes very little difference in the final result as shown in Figure 3.21. The

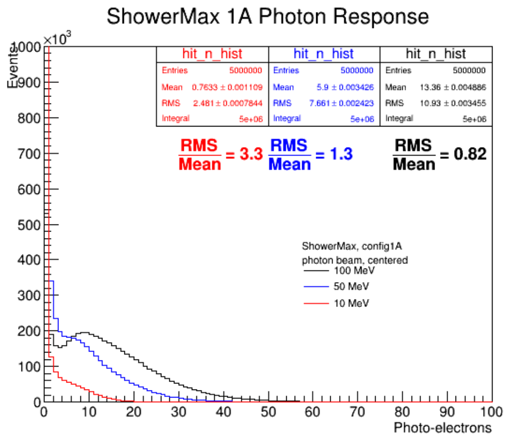

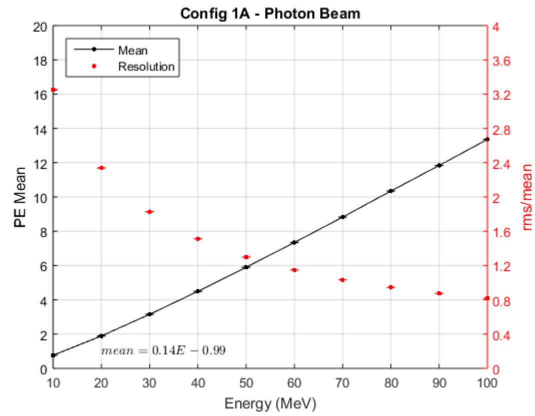

Figure 3.18: ShowerMax response to mono-energetic photon beams. Left image: Red, blue, and black represent 10, 50, and 100 MeV photons respectively. Right image: Black represents PE means and red represents resolution with respect to energy. Notice the low energy-linearity for the PE means (0.14 MeV^{-1}).

convoluted resolution for both detectors is expected to be 0.146 which equates to an excess noise of 1.06%.

Up to this point, the simulations discussed have had particles incident on the center of the detector face (a center sampled beam). In addition to a center sampled beam, the detector response can be studied for particles incident on different parts of the detector face. This will be helpful for MOLLER analysis since there will be electrons incident at all points on the face of the detector.

First, we'll consider how the PE yields and resolution are effected when electrons are incident at different positions azimuthally on the detector face. To study this, electrons were simulated in Geant4 to be incident on any part of the detector face with an equal probability. Then, PE yields and resolution were extracted from electrons that had been incident on certain azimuthal slices of the detector face. Figure 3.22 shows the result of these slices in the azimuthal dimension for 5 GeV incident electrons. There is a very distinct "M" in the shape of the PE yield across this dimension. Simulations have shown that light is emitted approximately uniformly across the quartz in the azimuthal direction. Thus, the "M" shape is entirely due to light guide effects.

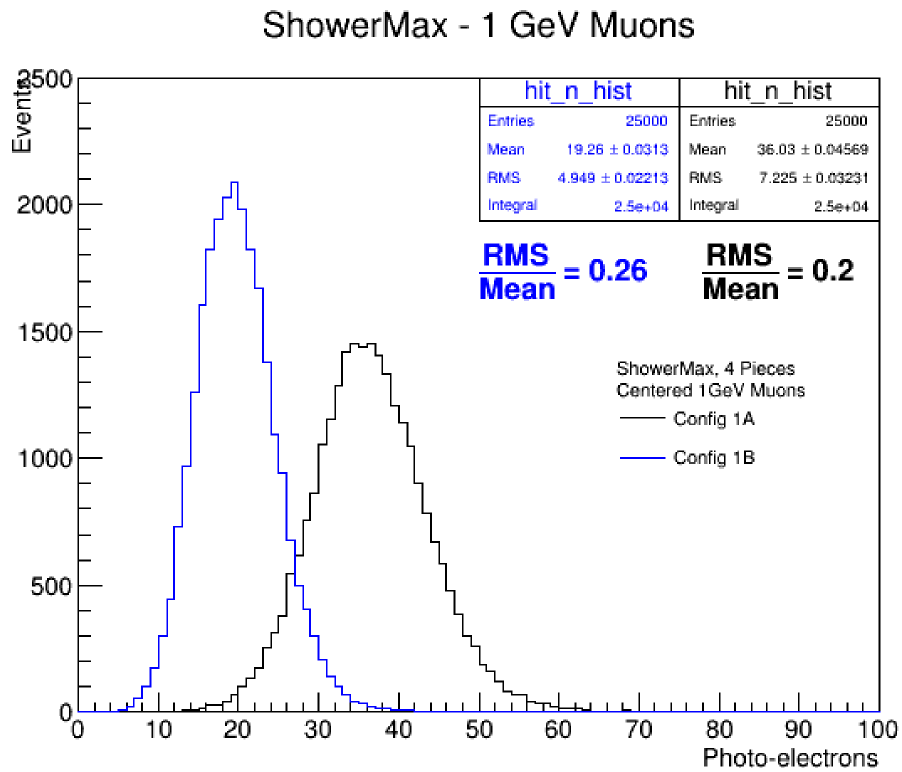

Figure 3.19: ShowerMax response to 1 GeV muon beams. Black and blue represent configurations 1A and 1B respectively.

Next, we'll consider how the PE yields and resolution are effected when electrons are incident at different positions radially on the detector face. The same data from the azimuthal segmentation study will be used again, however, this time PE yields and resolution were extracted from electrons that had been incident on certain *radial* slices of the detector face. Figure 3.22 shows the result of slices in the radial dimension for 5 GeV incident electrons. For most of the detector, the results for the signal are quite flat, however, there is interesting behavior at the inner and outer edges. Electrons incident near the bottom/inner edge of the detector (the slice furthest from the PMT) create a lower signal than the average, while electrons incident near the top/outer edge create a higher one. It is suspected that this could be due to at least two factors: first, at the inner edge of the detector a fraction of the shower is lost due to the lateral size of the shower escaping the stack and second, there is more attenuation through the quartz for light produced at the inner edge of the detector

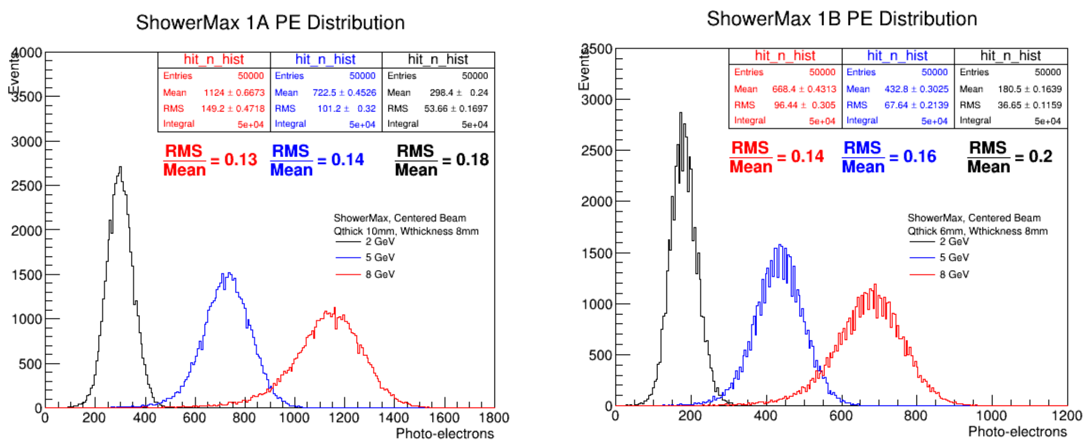

Figure 3.20: Full Scale ShowerMax Response. Red, blue, and black represent 2, 5, and 8 GeV electrons respectively. Left and right are configurations 1A and 1B respectively.

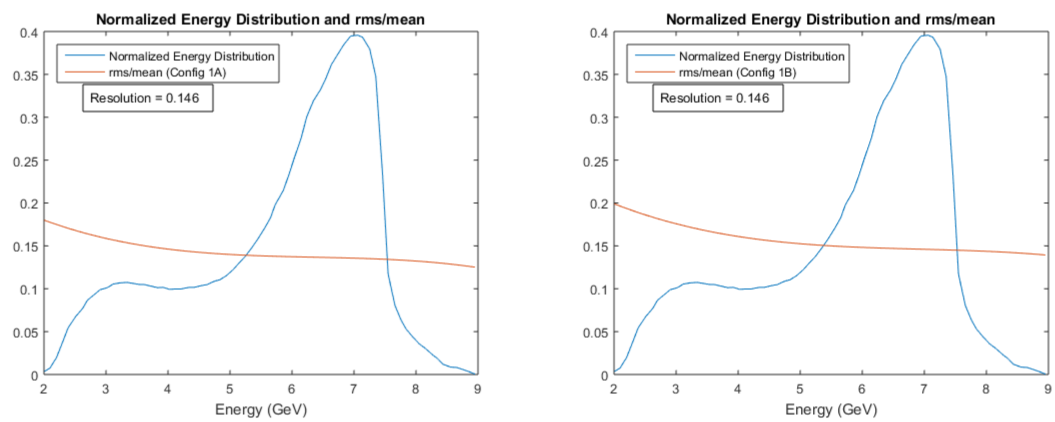

Figure 3.21: Convoluted resolution for config 1A (left) and config 1B (right). Blue represents the normalized energy distribution while red represents the resolution. Integrating according to Equation 2.31 gives the total (convoluted) resolution.

than light produced at the outer edge. A similar argument can be made for the top of the detector. Here, there is lateral shower leakage but there is nearly no attenuation which results in the peak in the PE mean at large r (or positive x) as illustrated in Figure 3.23. The resolution is flat for most of the detector, however, it gets worse at the edges.

The ShowerMax detectors chosen for construction perform well in simulations. They are expected to have low energy-linearity and good resolution. The resolution is good enough that the excess noise is acceptably low. Additionally, ShowerMax will be sufficiently immune to any large backgrounds encountered during the experiment. They are designed with an

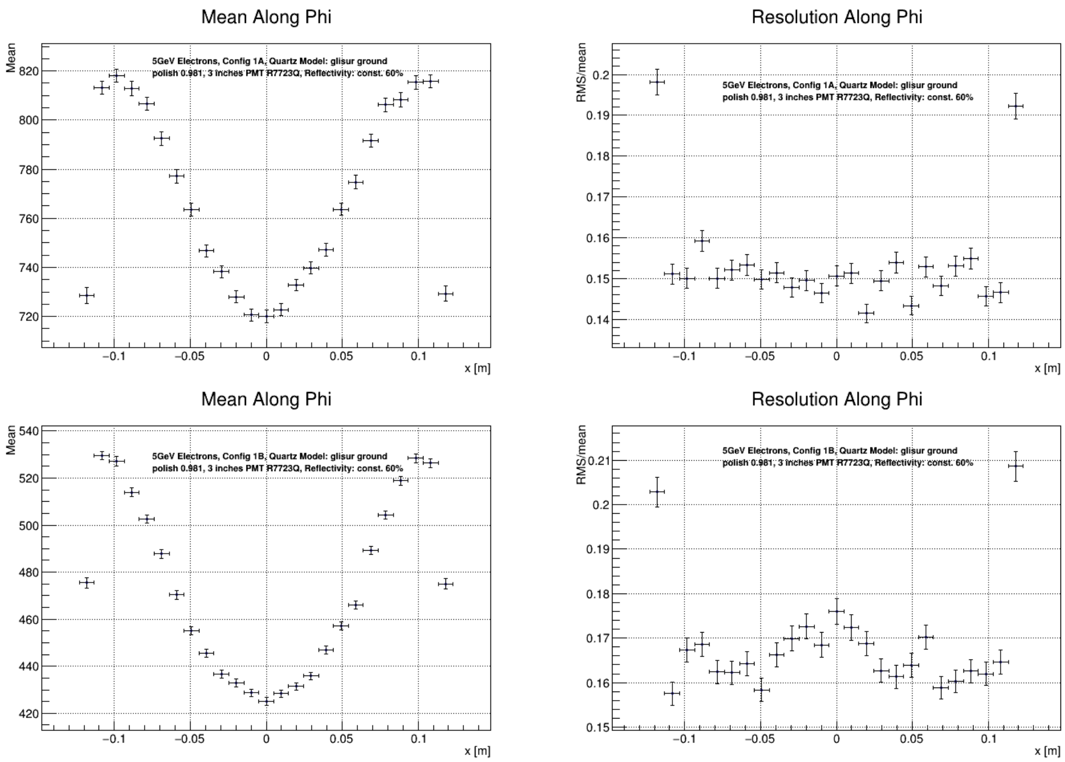

Figure 3.22: ShowerMax azimuthal segmentation study. Top: Config 1A. Bottom: Config 1B. Note the scale of the vertical axis. While the light yeild changes by more than 10% the resolution remains flat.

aluminum frame which is able to support the stack in any position on the detector ring. In order to ensure the expected performance of the detector, a test beam experiment will be performed to benchmark the simulations, which is discussed in Chapter 4

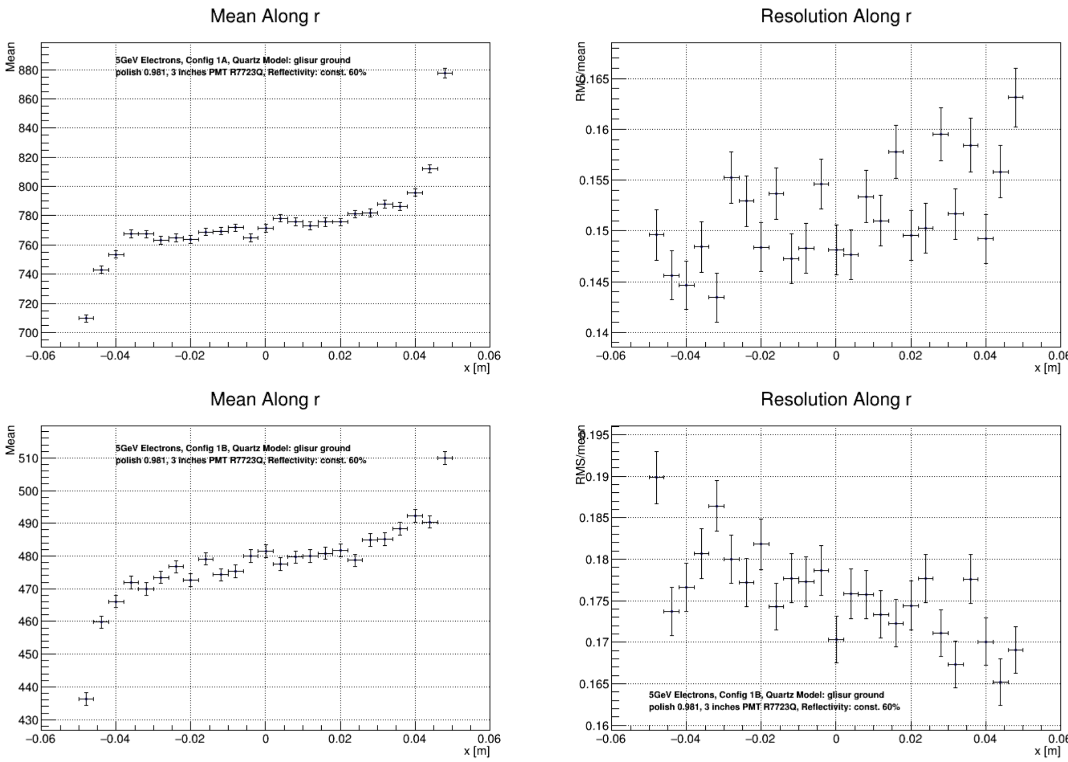

Figure 3.23: ShowerMax radial segmentation study. Top: Config 1A. Bottom: Config 1B. Note the scales of the vertical axis. The resolution remains very flat.

Chapter 4

Future Test Beam Studies

In order to achieve the precision goal of the MOLLER experiment, the response of ShowerMax needs to be very well understood. There are several parameters that need to be tuned in Geant4 (G4) simulations for the ShowerMax analysis. These include the optical properties of the quartz such as polish, reflectivity, refractive index, etc. They also include shower properties of the tungsten such as step size, density, and absorption constant. Properties of the light guide and PMT photo-cathode, such as reflectivity, must also be well known. In order to gain a better understanding of these properties for the ShowerMax detector, a beam test will be performed.

A benchmarking detector has been designed for ShowerMax that will have the ability to test most of the parameters needed for the G4 simulations mentioned above. The optical properties of the quartz will be studied by placing a single quartz piece in a well controlled beam (without using a light guide). The shower properties can then be studied by adding stack components one at a time during the measurement process. Additionally, the "full-scale" ShowerMax will be placed in the beam in order to test its response and light guide properties. Note that the full-scale prototype stack configurations match those of the benchmarking prototypes.

This chapter describes the experimental setup to be used during the beam test. It also describes the experimental procedures that will be used. Finally, the predictions of what we expect to see are outlined based on the current G4 simulations that have been performed.

4.1 Experimental Apparatus

The beam test consists of two main parts, each with various stages. The first part is the optical and shower benchmarking tests. The second is testing the full-scale prototypes. The beam test is to be performed at the SLAC End Station Test Beam (ESTB) facility with mono-energetic electrons between 2 GeV and 8 GeV with a nominal bunch length and spot size.

4.1.1 Benchmarking Prototype

A fully 3-D printed benchmarking detector apparatus has been made using 100% ABS plastic for the first part of the beam test. The apparatus consists of a light-tight enclosure with the ability to encapsulate the entire stack. The radiation hardness of ABS plastic is unknown. Thus, in order to avoid having the beam pass through the plastic, sliding doors are designed that attach to the body with inset Kapton windows for the beam to pass through. Each stack configuration has its own interior support frame (deemed 'elevators') used to hold the stack layers in place. The elevators are constructed so that the leading piece of quartz always remains at the same position relative to the PMT for each iteration of a configuration measurement. The PMT (which will be shielded from the beam) sits atop the whole configuration inside a PVC pipe and encapsulates the entire stack within its circular window. Figure 4.1 shows an exploded view of two configurations (a single piece of quartz and the full stack).

The biggest concern in designing the benchmarking apparatus was the stack width (transverse to the beam line). Stacks with insufficient width could lose a significant portion of the shower due to the transverse development. The minimum acceptable width the stack can have, without significant transverse light leakage, was determined using G4/qsim simulations and the Molière radius. Various overall stack widths—that could be circumscribed within a 3 inch PMT to avoid the use of a light guide—were compared against a "wide" stack in which there would be no loss due to shower size[1]. These simulations and a spreadsheet of the results are given in Appendix B. Due to this study, it was determined that the stack width should be 40 mm. This is enough to comfortably circumscribe config 1A (the thickest configuration) in a 3 inch PMT window with nominal losses (less than 0.09%) as discussed

[1] Although the wider stacks did have more losses due to attenuation of internally reflected light, this was not a significant contributor to any differences seen in the PE distributions in Appendix B.

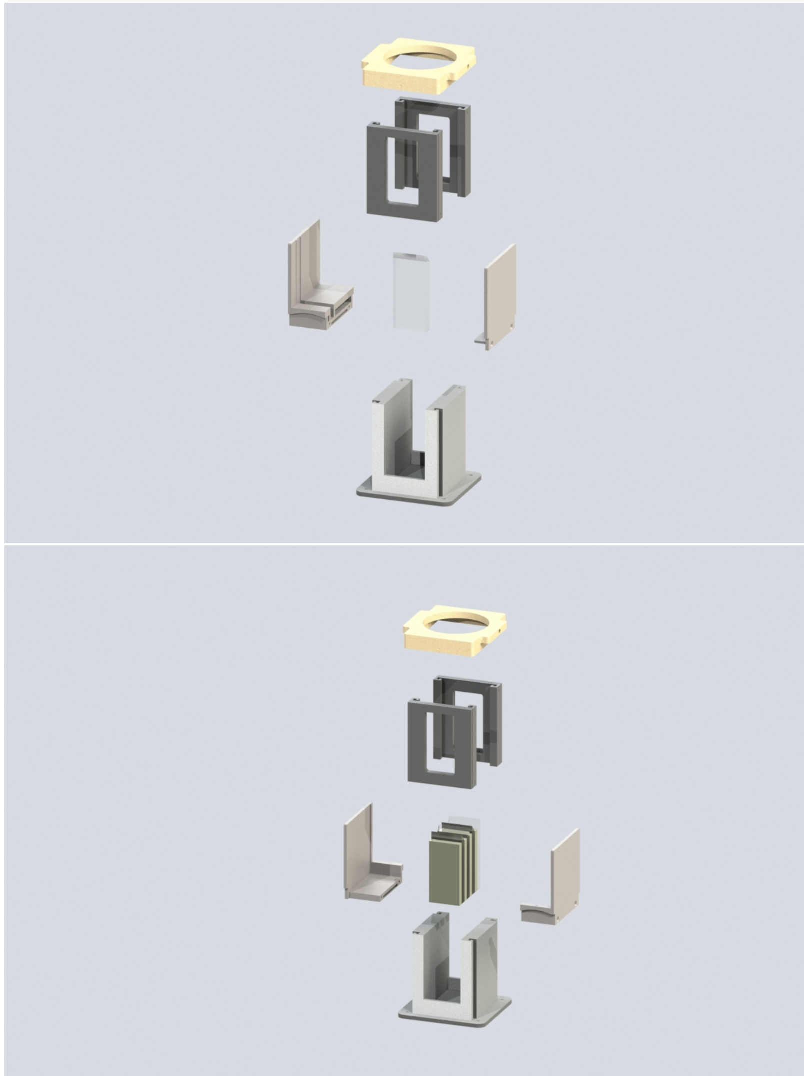

Figure 4.1: Exploded view of Config 1A benchmarking apparatus for the single quartz configuration (top) and the full stack (bottom).

in Appendix B.

Past test beam studies from our group have shown that incident electron angle has a large effect on thin quartz detector PE yields as shown in Figure 4.2. This data was obtained in 2015 at the Mainz Microtron (MAMI) in Germany during preliminary tests of the CREX and PREX II detectors. It is apparent that angular dependence will be important to control, especially for stack configurations with only one piece of quartz (with or without one radiator). We are also interested in quantifying the effect of angle on the full stack configuration.

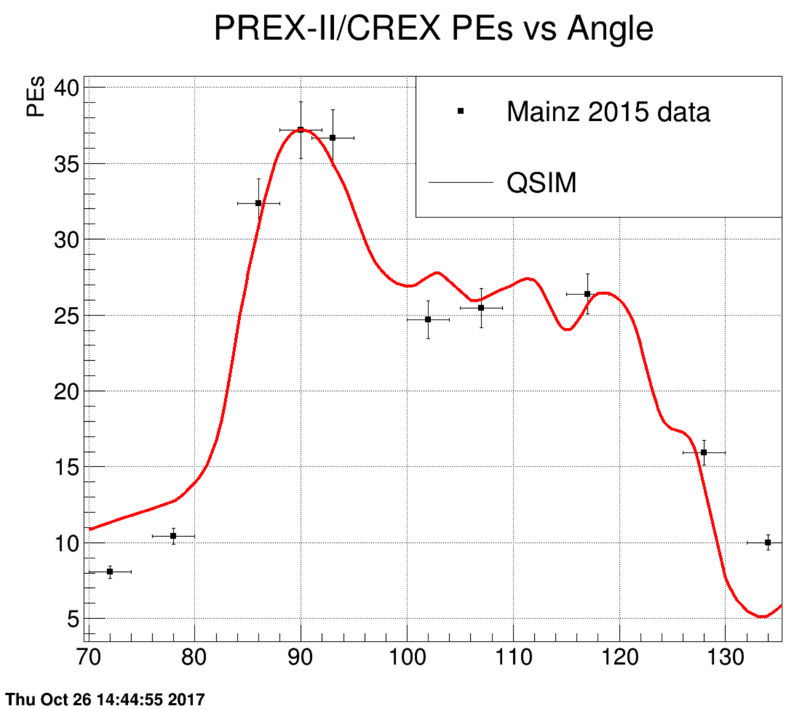

Figure 4.2: Dependence of signal with respect to incident beam angle for thin quartz. Data collected from 2015 MAMI testbeam.

In order to control the position and angle of the incident beam, the apparatus will be fastened to a linear and rotary stage. The linear stage will have the ability to move the apparatus entirely out of the beam path if desirable. The entire assembly will be controllable from outside the beam area which will allow for more efficient testing—without having to continually re-enter zones that may still be radioactive and have time-intensive entry procedures. The upper plot of Figure 4.3 shows a graphic of the completed benchmarking assembly and the size constraints of the device. The entire apparatus (linear and rotary stages included) is under a meter in each dimension allowing for easy setup at the ESTB facility.

4.1.2 Full-Scale Prototype

The second part of the beam test is for testing the full-scale ShowerMax prototypes. As was the case for the benchmarking assembly, the full-scale device will sit atop computer controlled linear and rotary stages. This will enable control over the beam position and

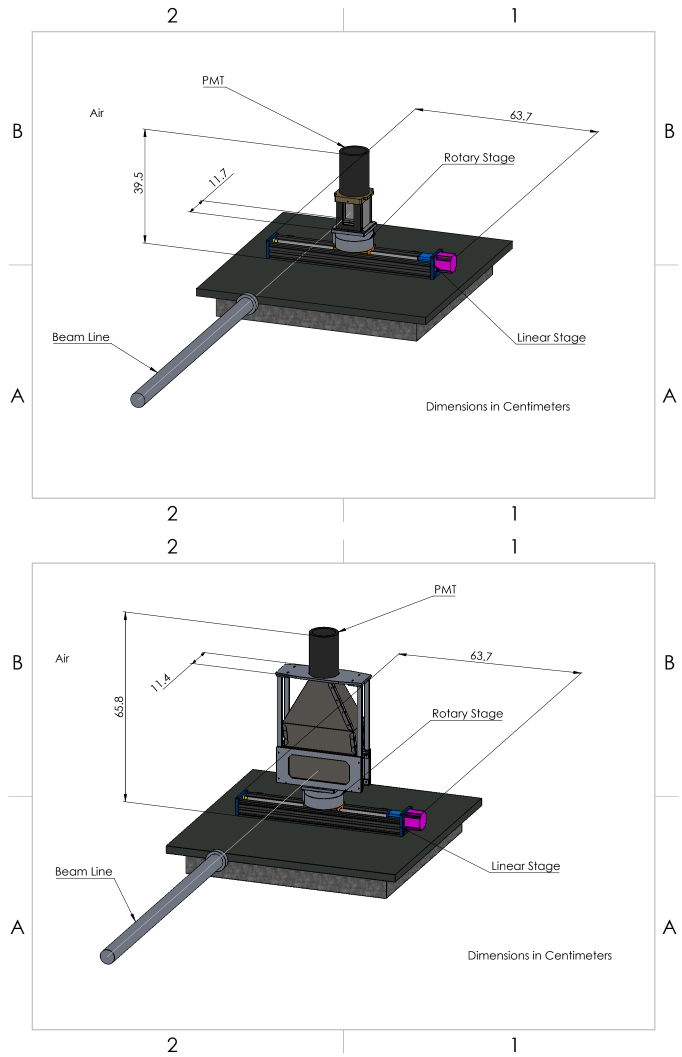

Figure 4.3: Experimental test beam set up for the benchmarking apparatus (top) and full-scale prototype (bottom). Notice the linear and rotary stages they are mounted to.

angle. Shielding may be placed around the detector in order to keep the PMT and light guide from having any potential backgrounds but is not likely to be necessary given the clean, low current beam of the ESTB. As with the benchmarking assembly, the entire apparatus is again under a meter in any direction—making it easy to install and work around in the ESTB. This detector will also have the ability to be moved entirely out of the beam line from a remote location providing more flexibility and beam time. A graphic of this assembly is shown in the lower plot of Figure 4.3.

4.2 General Run Plan and Procedures

The desired beam for the benchmarking experiment is a single particle electron beam with energies ranging from 2 GeV to 8 GeV. The beam should have a nominal bunch size, meaning only one electron is delivered to the detector at a time. It should also have the smallest possible spot size (how precisely the electrons can be focused on the target). The ESTB facility boasts a sufficiently small spot size of approximately 1 mm [6].

Simulations have shown that, when testing the fully loaded stack, the position of the beam should be centered on the stack with precision under 2 mm[2]. The apparatus should also be perpendicular to the beam with precision of less than 2 degrees[3] (this needs to be more precise when testing a single piece of quartz). Figure 4.4 shows the beam position sensitivity of the fully loaded config 1A benchmarking apparatus. The response of the detector will only be minimally perturbed if the spatial beam parameters are kept within 2mm of stack center and with $\leq 2^{\circ}$ angular deviation from the normal incidence.

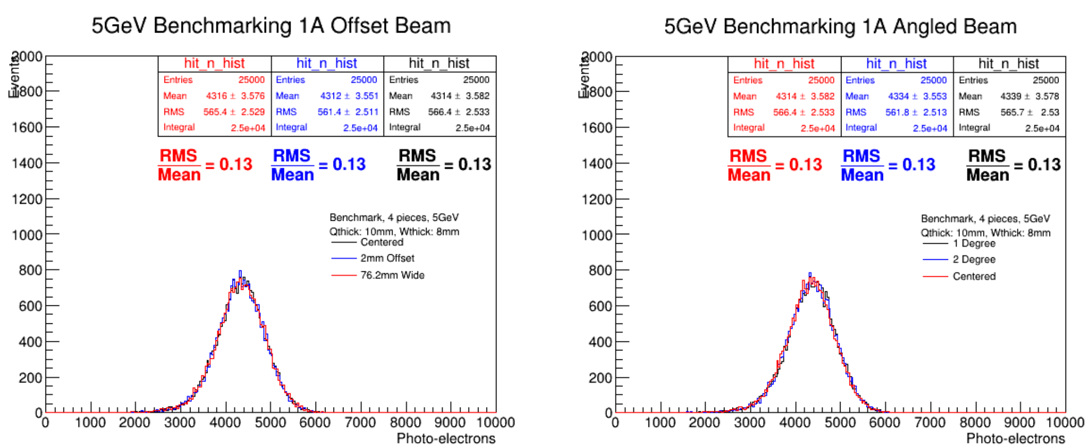

Figure 4.4: Expected spacial sensitivity of benchmarking apparatus from simulation. Left: Effects of offsetting the beam spatially. Right: Effects of rotating the apparatus.

Once the spatial parameters of the beam have been calibrated, a single piece of quartz (config 1A) should first be subjected to the beam and at least three energies should be

[2] This is to ensure that less than 1% of the shower is lost due to its transverse size. Appendix B contains the results simulations showing this for various stack configurations.

[3] Interestingly, more light is created with the full stack when an incident electron has a small angle. This is because more of the shower can develop. Appendix B shows this for various stack configurations.

subjected to the apparatus. Once this is complete, a single radiator should be placed in front of the quartz and then repeat the measurement. After this, another radiator should be added downstream of the first piece of quartz along with another piece of quartz; the measurement will then be repeated. This procedure should continue until the full stack configuration has been tested. This entire procedure should then be repeated for config 1B. Once this is done, each full-scale prototype should be subjected to the beam.

During each data collection run with the accelerator, enough particles should be sent through the apparatus to get the appropriate statistics. Given that the standard error goes as $n^{-0.5}$, it's recommended that n be as large as possible. The author of this text recommends that the statistical precision of the data collected exceed that of the G4 simulations discussed throughout this text by a factor of ten. This is a recommended n of $250,000$ for each configuration tested.

4.3 Simulated Results and Expectations

As has been discussed throughout this thesis, the PE response for a single piece of quartz is essentially energy independent. Given incident electron energies of 2 GeV, 5 GeV, and 8 GeV their individual PE responses should be nearly indistinguishable, as shown in Figure 4.5. The relative width (or resolution) of the signal responses are expected to be around 19%.

Once a single radiator is added to the apparatus, the mean, rms, and rms/mean of the signal significantly increases. This is due to the under-developed shower that forms before the quartz. An under-developed shower creates fluctuations in the number of charged particles that traverse the quartz for each electron, and the rms increases more than the mean increases. As more radiators are added to the apparatus, the Gaussian-like responses should become more separated for the different energies due to the further developed shower and thus more consistent numbers of shower particles produced per electron. While the rms of the PE distribution progressively increases as more stack layers are progressively added, the rms/mean of the distribution improves with each added set of tungsten and quartz to the

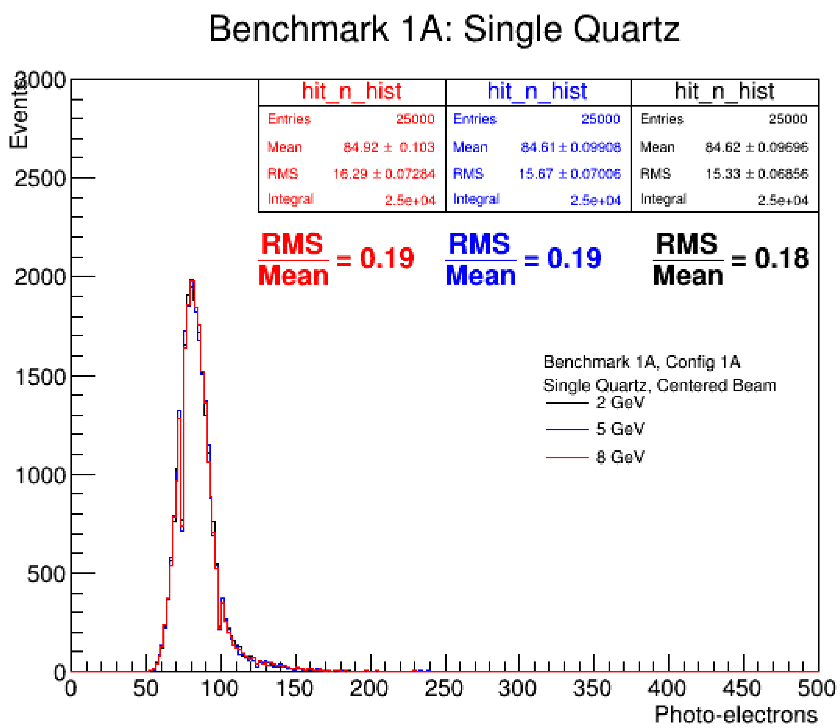

Figure 4.5: Response of benchmarking apparatus configured with a single piece of quartz. Notice that the responses are the same for 2, 5, and 8 GeV.

configuration. This result is simply a consequence of a more fully-developed and predictable shower[4]. Figure 4.6 Shows the increasing mean and decreasing rms/mean for successively adding more layers with 2 GeV, 5 GeV, and 8 GeV electron beams.

[4]This is merely statistics. As the number of shower particles (N) increases, the fluctuation in that number goes as $1/\sqrt{N}$

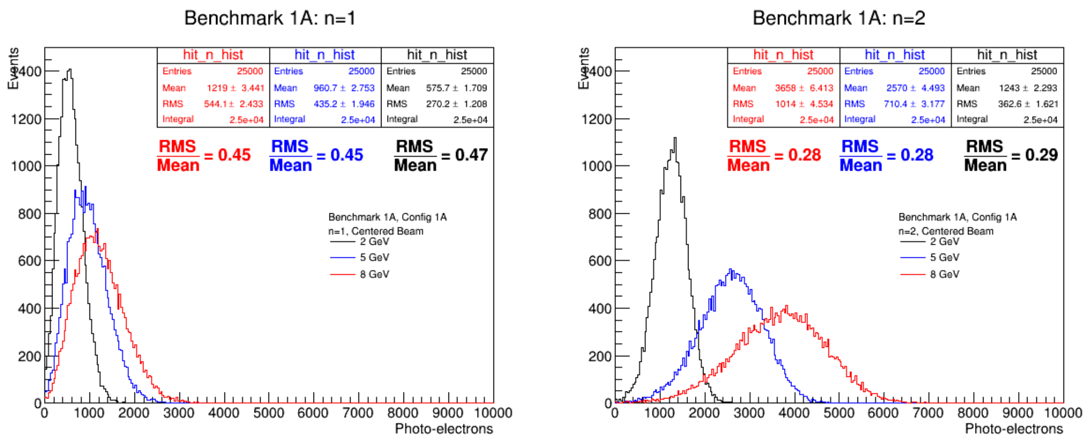

Figure 4.6: Expected response for various benchmarking configurations. Notice that the resolution gets better and the signals for different energies separate as more layers are added to the stack. Also note the huge numbers of mean PE's—this will require the use of 1–10% transmission ND filters to keep the mean PE's below 200.

Chapter 5

Conclusion

This document has given an overview of the work done to design and test the ShowerMax detector for the MOLLER Experiment. The purpose of MOLLER is to measure the parity violating asymmetry in Møller scattering with unprecedented precision (0.7 ppb). At the very least it will set limits on possible BSM physics and at the most could discover potential interactions or particles—such as dark photons or heavy Z's. In addition, MOLLER will serve to push the limits of technology. The extreme precision of the experiment will advance our technological capabilities and sharpen our knowledge.

ShowerMax will be a key component of MOLLER. It will make an independent measurement of A_{PV} subject to its own set of systematic errors—different than those of the main thin quartz detectors. In conjunction with the thin quartz detectors, this will increase the statistical precision of the experiment by a factor of $\sqrt{2}$. ShowerMax will also be resistant to backgrounds from photons, charged hadrons (mainly pions), and muons produced in the target. This is especially important given that the response of the thin quartz detectors is independent of energy—resulting in each type of background making a similar signal. While the pions and muons make a much smaller signal than any of the scattered electrons in ShowerMax, it is still detectable, giving it the added benefit of cross-checking the pion detectors[1].

While ShowerMax is crucial to Møller, it has its own hurdles to overcome. Given that a large range (factor of 4) of scattered electron energies are incident on the detector, special care needs to be taken because the response of a calorimeter is energy dependent. This means that 8 GeV electrons make four times as much light as 2 GeV electrons, thus an 8 GeV electron is indistinguishable from four 2 GeV electrons. Because of this, the data analysis of ShowerMax will rely on a redundant measurement of energy. The spectrometer will need to be well mapped-out and track detecting GEM planes can then be used to

[1]These detectors are in the experiment solely to monitor backgrounds.

determine the energy distribution of scattered electrons on ShowerMax; this serves as the first energy "measurement." For an accurate measurement of A_{PV} with ShowerMax, the energy distribution of the incident electrons will then need to be used to cancel out the energy dependence in the signal[2]. Therefore, it will be important to fully understand the errors associated with the field-maps and GEM tracking event reconstruction as they will carry over to the ShowerMax analysis in a non-trivial manner.

ShowerMax consists of four plates of tungsten interleaving with four tiles of optically polished quartz. Two different detectors will be built with different tungsten thicknesses for preliminary testing. In order to detect the signal from the quartz, a specially designed light guide has been designed. The light guide was first designed to optically transmit light to the PMT by only a single-bounce using a parabolic funnel mirror. Then the design was simplified to a flat funnel mirror such that it could be easily and consistently built. In MOLLER, 28 ShowerMax detectors will be arranged in a ring with an approximately 1 m radius around the beam line as in Figure 5.1. A frame was designed that can support the weight of the detector from any orientation on the ring. The weakest structural members have a factor of safety of 2.5 in the worst case scenario[3]. Specially machined supports were designed to hold the tungsten and quartz in place around the ring (without inflicting damage to the material) and only blocking a very small amount of light.

Finally, a beam test was designed to benchmark the optical quartz and showering parameters of the Geant4 simulation parameters and to test the full-scale ShowerMax prototypes. The beam test will require an electron beam and a range of energies (approximately 2 GeV to 8 GeV). An apparatus was designed with the ability to first test a single piece of quartz and

[2] I am not sure if this was not done in legacy experiments such as SLAC's E158[2]. This is equivalent to assuming that scattered electrons from the electromagnetic and weak interactions have the same energy probability distribution. For most cases it is OK to make this assumption as any deviation is probably quite small. Additionally, the rates and ranges of energies have been more favorable (a factor of two instead of four) in these experiments and first order QED corrections were not considered[28]. This said, we do not know how strange "yet-to-be-discovered" physics might be and MOLLER is a BSM search. For this reason it will be important to cancel out the energy dependence as accurately as possible in order to attain as precise a measurement as possible.

[3] It should be noted that the frame was not analyzed for fatigue under dynamic or cyclic loading. The detector should be handled with care during transportation and installation.

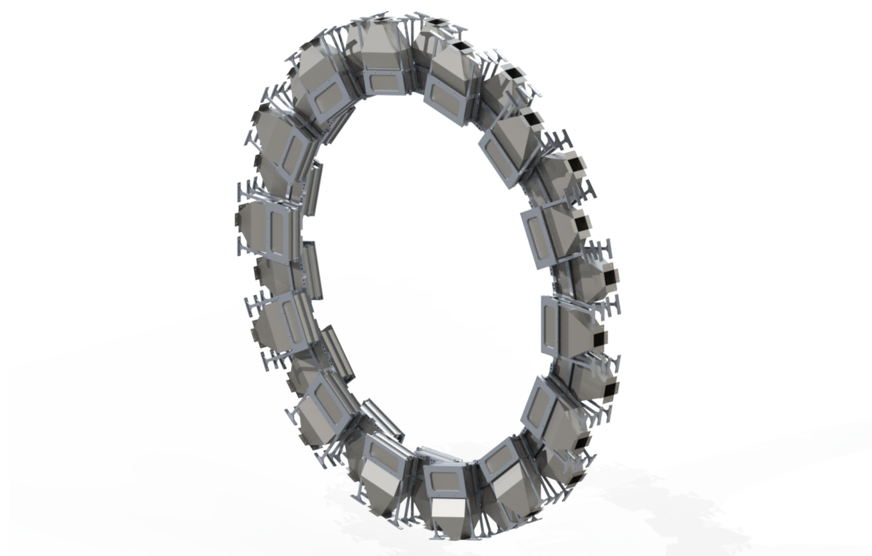

Figure 5.1: ShowerMax detectors in final ring geometry.

then progressively add stack pieces until the full configuration is reached. As in Figure 5.2, the apparatus will sit atop a linear and rotary stage that will enable precision positioning abilities. Full-scale ShowerMax prototypes will also be tested; they will also be fastened to the linear and rotary stage as shown in Figure 5.3

ShowerMax is expected to meet all the experimental requirements and even exceed some. If the actual resolution of the detector is close to the simulations, its excess noise will only minimally affect its measurement error. While making an independent measurement of A_{PV} that is resistant to the experiment's backgrounds, ShowerMax will greatly boost MOLLER's statistics and provide a safety net against any unexpected complications. As a whole, MOLLER will make the most precise measurement of A_{PV} to date. It will take precision physics to a new level and expand our technological capabilities. It also has the potential to probe physics beyond the standard model with unprecedented sensitivity and to identify as yet discovered interactions. The measurement will provide guidance for the future of physics as we search for a more complete or unifying theory. In the end, MOLLER will expand our knowledge and provide a telling glimpse into the inner workings of the universe. ShowerMax will play a crucial role in this endeavor.

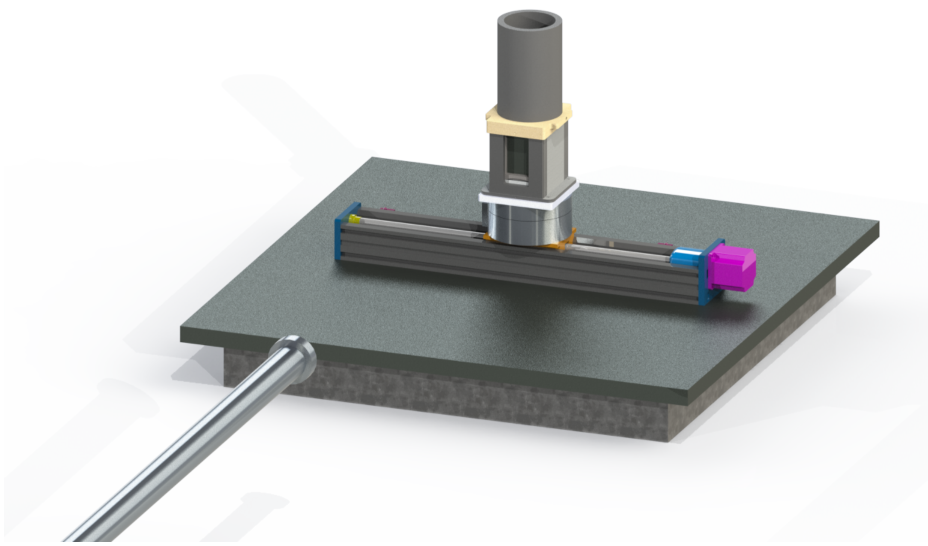

Figure 5.2: Experimental setup for benchmarking apparatus.

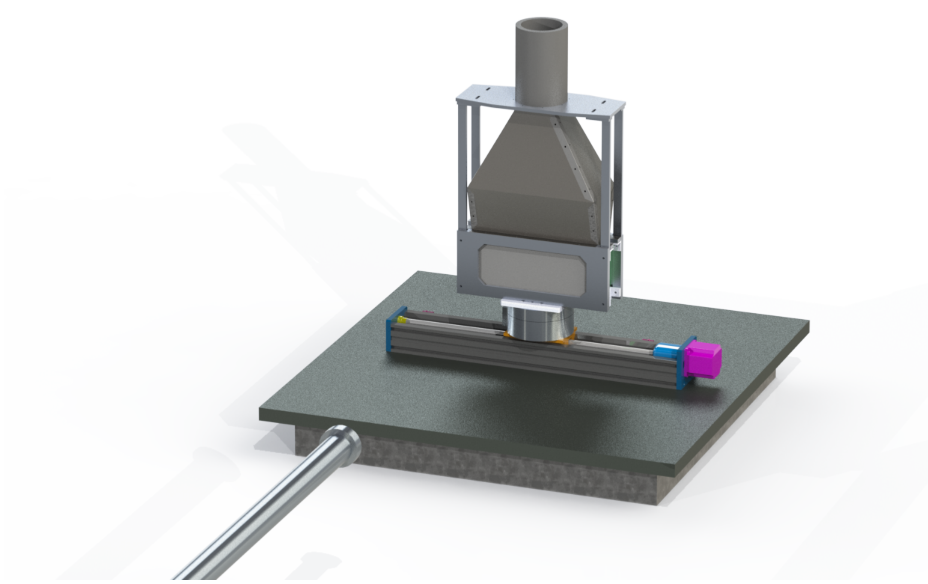

Figure 5.3: Experimental setup for the full-scale ShowerMax prototype.

Bibliography

[1] U. Amaldi. “Fluctuations in Calorimetric Measurements”. In: *Phys. Scripta* 24.409 (1981).

[2] P. L. Anthony et al. “Precision Measurement of the Weak Mixing Angle in Møller Scattering”. In: *Phys. Rev. Lett.* 95 (8 Aug. 2005), p. 081601. DOI: 10.1103/PhysRevLett.95.081601. URL: https://link.aps.org/doi/10.1103/PhysRevLett.95.081601.

[3] H.A. Bethe. “Moliere’s Theory of Multiple Scattering”. In: *Phys. Rev.* 89.6 (1953), pp. 1256–1266.

[4] Moller Collaboration. “The Moller Experiment”. In: *DOE Proposal* (2014).

[5] I. Sestili E. Longo. “Monte Carlo Calculation of Photon-Initiated Electromagnetic Showers in Lead Glass”. In: *Nucl. Instrum. Meth.* 128.2 (1975), pp. 283–307.

[6] R. Erikson *et al. ESTB End Station Test Beam*. July 2009. URL: https://portal.slac.stanford.edu/sites/ard_public/tfd/esa/Documents/ESTB_Proposal%5C%20080309.pdf.

[7] J. Erler *et al.* “Weak Polarized Electron Scattering”. In: *ANNU REV NUCL PART S* 64 (2014). DOI: 10.1146.

[8] C.W. Fabjan and F. Gianotti. “Calorimetry for Particle Physics”. In: *Rev. Mod. Phys.* 75 (4 Oct. 2003), pp. 1243–1286. DOI: 10.1103/RevModPhys.75.1243. URL: https://link.aps.org/doi/10.1103/RevModPhys.75.1243.

[9] D. Green. *The Physics of Particle Detectors*. Cambridge, UK: Cambridge University Press, 2000.

[10] Particle Data Group. “Review of Particle Physics”. In: *Chinese Physics C* 40.10 (2018).

[11] C. Grupen and B. Shwartz. *Particle Detectors*. Cambridge, UK: Cambridge University Press, 2008.

[12] R. Hibbeler. *Mechanics of Materials*. New York, NY: Prentice Hall, 2010.

[13] S. Iwata. “Calorimeter”. In: *Nagoya University Preprint* (1980). DOI: DPNU-13-80.

[14] V.S. Kaushik. *Electromagnetic Showers and Shower Detectors*. 2002. URL: http://www-hep.uta.edu/hep_notes/general/general_0001.pdf.

[15] K.S. Kumar. “The Physics of Electron-Electron (Møller) Scattering”. In: JLab Moller Seminar, Jan. 2009. URL: https://www.jlab.org/intralab/calendar/phys_seminar/2009/mollerseminar_short.pdf.

[16] K.S. Kumar et al. “Low Energy Measurements of the Weak Mixing Angle”. In: *ANNU REV NUCL PART S* 63 (2013), pp. 237–267. DOI: 0.1146/annurev-nucl-102212-170556.

[17] J. A. Magee et al. “A novel comparison of Møller and Compton electron-beam polarimeters”. In: *Phys. Lett.* B766 (2017), pp. 339–344. DOI: 10.1016/j.physletb.2017.01.026. arXiv: 1610.06083 [physics.ins-det].

[18] D. McNulty. personal communication. 2017.

[19] MechaniCalc. *Stress Transformations & Mohr’s Circle*. 2018. URL: https://mechanicalc.com/calculators/mohrs-circle/.

[20] K. Popper. *Conjectures and Refutations*. New York, NY: Basic Books, 1965.

[21] C.Y. Prescott *et al.* “Parity non-conservation in inelastic electron scattering”. In: *Phys. Lett. B* 77.347 (1978).

[22] J. Nisbett R. Budynas. *Shigley’s Mechanical Engineering Design*. New York, NY: McGraw Hill, 2015.

[23] P. Renton. *Electroweak Interactions*. Cambridge, UK: Cambridge University Press, 1990.

[24] M. Swartz et al. "Observation of target electron momentum effects in single arm Moller polarimetry". In: *Nucl. Instrum. Meth.* A363 (1995), pp. 526–537. DOI: 10.1016/0168-9002(95)00384-3. arXiv: hep-ex/9412006 [hep-ex].

[25] Engineering ToolBox. *Young's Modulus - Tensile and Yield Strength for common Materials*. 2018. URL: https://www.engineeringtoolbox.com/young-modulus-d_417.html.

[26] Fred L. Wilson. "Fermi's Theory of Beta Decay". In: *American Journal of Physics* 36.12 (1968), pp. 1150–1160. DOI: 10.1119/1.1974382. URL: https://doi.org/10.1119/1.1974382.

[27] C. S. Wu et al. "Experimental Test of Parity Conservation in Beta Decay". In: *Phys. Rev.* 105 (4 1957), pp. 1413–1415. DOI: 10.1103/PhysRev.105.1413. URL: https://link.aps.org/doi/10.1103/PhysRev.105.1413.

[28] V.A Zykunov *et al.* "First order QED corrections to the parity-violating asymmetry in Moller scattering". In: *SLAC-PUB-11378* (). DOI: hep-ph/0507287. URL: https://arxiv.org/pdf/hep-ph/0507287.pdf.

Appendix A

Structural Analysis

Consider the worst case scenario that the ShowerMax detector will be in. This is where the detector is at 90 degrees to the vertical and the supporting struts are subject to the largest possible moment. Figure A.1 shows a detector in this configuration and a free-body diagram of a structural member.

For a conservative estimate, it is assumed that only two of the beams support the load of the detector. The weight of the stack and the frame is approximately 50 pounds. Given this configuration we find that the maximum shear in the beams is 22.5 lb and the maximum moment is 23 ft-lb. Figure A.2 illustrates the shear and moment the beams are subject to.

In this model we are most likely to have failure at $x = 14.5$ in. First, we must find the stresses due to the shear and moment at this point. The transverse shear stress is given by [12]:

$$\tau = \frac{vQ}{It} \ , \tag{A.1}$$

where v is the shear force, Q is statical moment of area, I is the moment of inertia, and t is the thickness of the beam. The values of each are:

- $v = 22.5$ lb
- $Q = \bar{y}A = 0.0122\text{in}^3$
- $I = \frac{1}{12}tb^3 = 0.00509\text{in}^4$

Plugging these values in we find the following:

$$\tau = 215.7\text{psi}. \tag{A.2}$$

The stress due to the moment is given by the well known equation [12]:

$$\sigma = \frac{My}{I} \,, \tag{A.3}$$

where M is the moment, and y is a distance from the center of the beam. The max stress due to the moment is, therefore, at the edge of the beam ($y = \frac{5}{16}$ in). Plugging in the known values we find,

$$\sigma_x = 17000\text{psi}. \tag{A.4}$$

Next, Mohr's circle is used to find the max and principle stresses in the beams. Since there is no σ_y, the max normal stress is σ_x at $\theta = 0$. The max shear is the radius of Mohr's circle, which is given by [12]:

$$R = \sqrt{\left(\frac{\sigma_x - \sigma_y}{2}\right)^2 + \tau^2} = \tau_{max}. \tag{A.5}$$

The max stresses are approximately:

$$\tau_{max} = 8500\text{psi} \tag{A.6}$$

and

$$\sigma_{max} = 17000\text{psi}. \tag{A.7}$$

Given that σ_y is zero, he principle stresses are found to be:

$$\sigma_A = \frac{\sigma_x}{2} + \sqrt{\frac{\sigma_x^2}{4} + \tau^2}$$

$$\boxed{\sigma_A = 17000\text{psi.}} \tag{A.8}$$

and

$$\sigma_B = \frac{\sigma_x}{2} - \sqrt{\frac{\sigma_x^2}{4} + \tau^2}$$

$$\boxed{\sigma_B = -3\text{psi}} \tag{A.9}$$

Figure A.3 illustrates Mohr's circle for this particular case. The principle stresses are now ready to be used in various failure models. This appendix covers three such models.

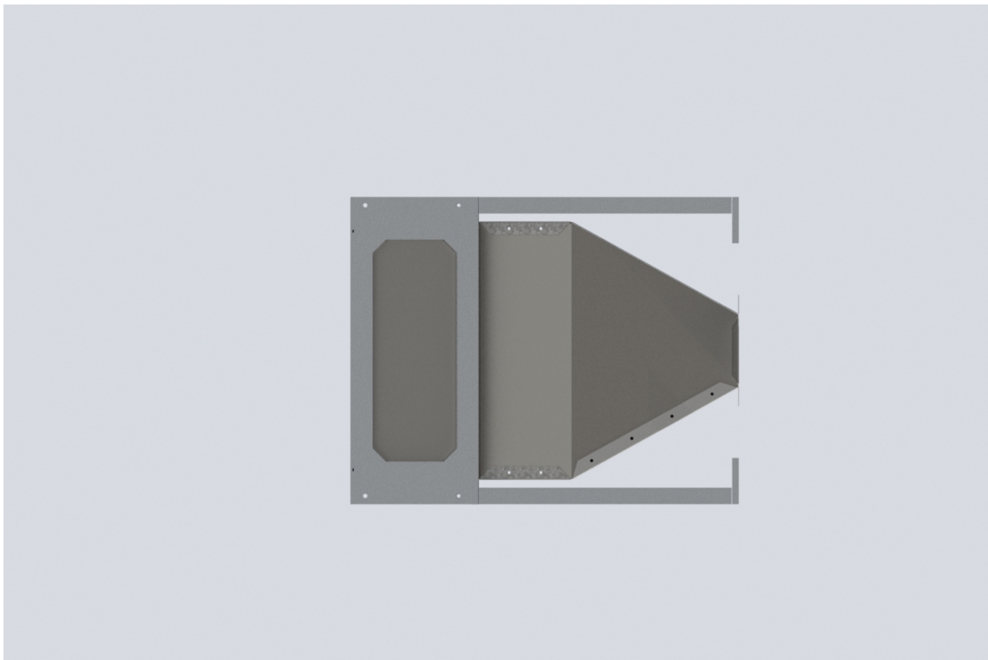

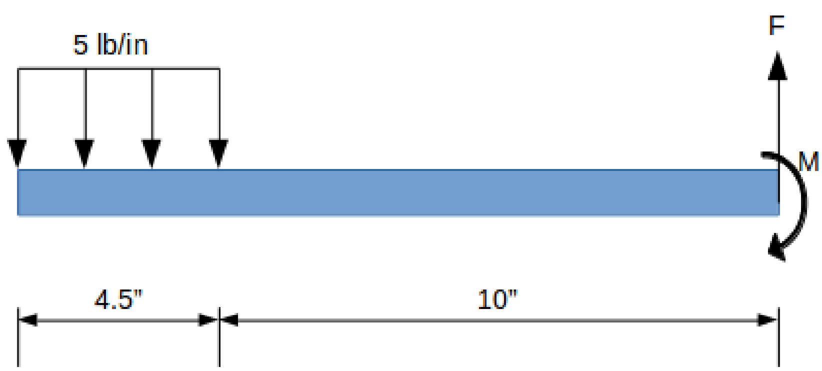

Figure A.1: Structural worst case scenario. The top image shows a ShowerMax detector in this position. The bottom image shows a free-body diagram of the structural members being analyzed.

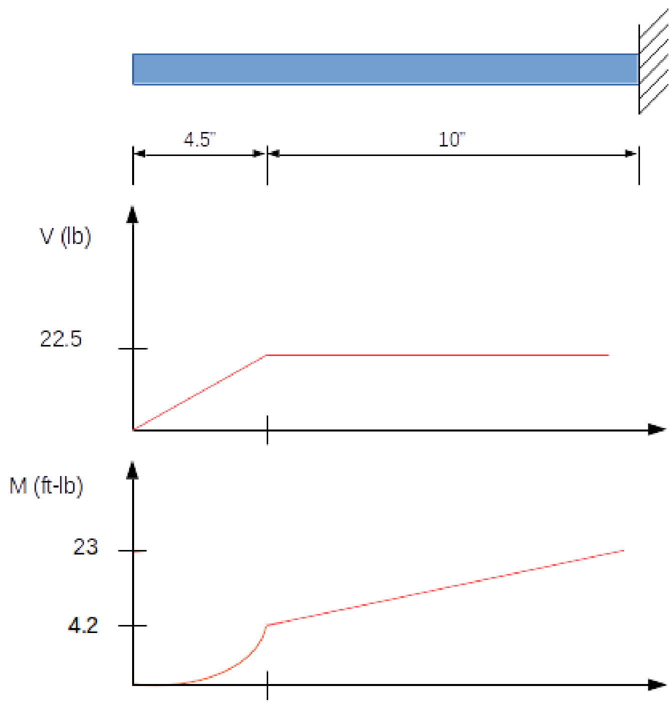

Figure A.2: Shear and Moment Diagrams.

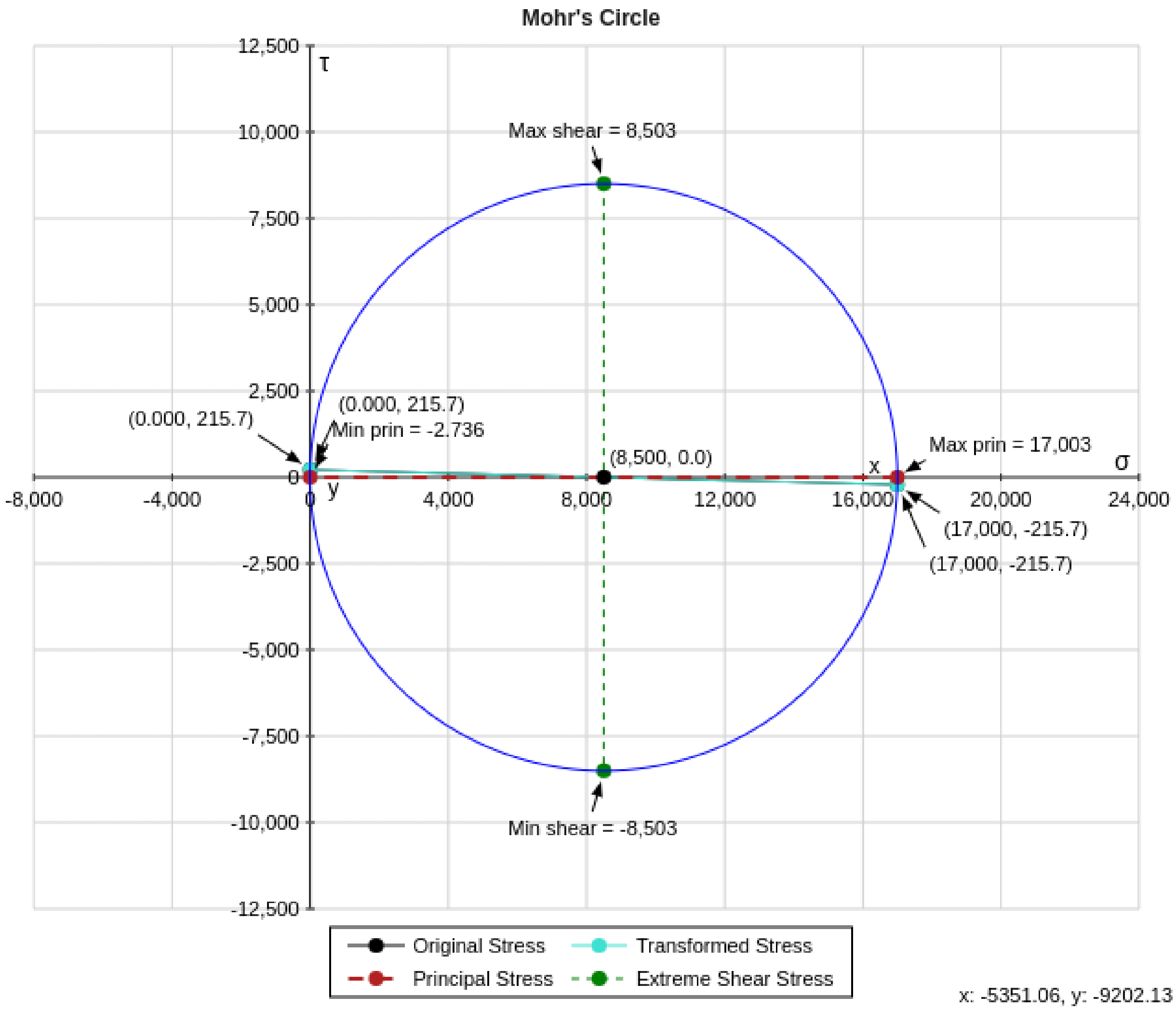

Figure A.3: Mohr's circle for the structural members in ShowerMax [19].

A.1 Von Mises Criterion

The factor of safety (n) in the Von Mises Failure criterion is given by the yield strength over the Von Mises stress [22]:

$$n_{VM} = \frac{S_y}{\sigma_{VM}} \tag{A.10}$$

Where,

$$\sigma_{VM} = \sqrt{\frac{1}{2}\left((\sigma_x - \sigma_y)^2 + (\sigma_y - \sigma_z)^2 + (\sigma_z - \sigma_x)^2 + 6\tau^2\right)} = \sqrt{\sigma_x^2 + 3\tau^2}. \tag{A.11}$$

For 2024 T4 Aluminum the following values are known [22]:

- Ultimate Tensile Strength: $S_{ut} = 64.8$ kip.
- Yield Strength: $S_y = 43$ kip.
- Compressive Yield Strength: $S_c = 43$ kip.

Plugging these values in we find:

$$n_{VM} = 2.52 \tag{A.12}$$

A.2 Standard Coulomb-Mohr

Another failure theory to check is the standard Coulomb-Mohr model. The equation for the factor of safety in this model is [22]:

$$\frac{1}{n} = \frac{\sigma_A}{S_y} - \frac{\sigma_B}{S_c} \tag{A.13}$$

Plugging in the known values and solving for n:

$$n_{SCM} = 2.5 \tag{A.14}$$

For a conservative estimate of the total factor of safety the lowest value is taken.

$$\boxed{n = 2.5} \tag{A.15}$$

A.3 Critical Load

Another structural concern is the critical load. This is the maximum load a column can bear without buckling. The critical load is given by the following formula [12].

$$P_{cr} = \frac{\pi^2 EI}{K^2 L^2} \tag{A.16}$$

For aluminum, the modulus of elasticity (E) is 10^7 psi [25]. The structural members are fixed on both ends making the shape factor, K, equal to 1. Using the values calculated previously for the moment of inertia and length, the critical is found to be well above the 50 pounds the members will have to support.

$$P_{cr} = 2390 \text{ lb} \tag{A.17}$$

Appendix B

Molière Radius Study

A major reason for performing the beam test outlined in Chapter 4 is to benchmark the optical and shower properties of tungsten and quartz used in Geant4/Qsim simulations. To achieve this, a scaled down version of the ShowerMax stack will be used. The stack must have a width such that it can be circumscribed by a 3 inch PMT (which is the size of PMT that will be used in MOLLER). The stack must also be wide enough that most of the transverse size of the shower is contained with in the stack. These parameters come from the fact that a light guide can not be used with the benchmarking apparatus because it would add a layer of uncertainty to the data. The beam test is designed to accept light directly from the quartz so that the data reflects the desired physics as well as possible.

The spreadsheet on the following pages is a summary of the simulations that were performed to determine the design of the benchmarking apparatus[1]. Figure B.1 defines the variables that were used to describe the stack geometry. Note that the thickness of the first layer of tungsten is not necessarily the same as the others. Due to this study, it was determined that the stack width should be 40 mm. This is enough to comfortably circumscribe config 1A in a 3 inch PMT with nominal losses (less than 0.09%).

Following the spreadsheet are selected PE distributions from the study. The first four plots show the change in signal for configuration 1 while increasing the number of layers (starting with one radiator and one optical tile). Stack widths of 1 in, 2 in, and 3 in are shown. Notice that there is a significant decrease in the signal (3.5%) for the full 1 inch wide stack. Such losses are what these simulations were used to avoid. The next two PE distributions show the result of a beam that is not perfectly centered on the benchmarking apparatus. The final two show the result of a beam coming in at a slight angle. Notice that configurations A and B have no significant losses from offset or angled beams[2].

[1] These simulations also played a major role in selecting the full–scale stack components.

[2] In fact, angled beams make more light. This is due to a further developed shower.

Results Spreadsheet

	Material Values (Particle Data Group)					
	R (g/cm/cm)	R (cm)	X (g/cm/cm)	X (mm)	Z	Density (g/cc)
Tungsten	18.00	0.93	6.76	3.50	74.00	19.25
Copper	14.05	1.57	12.86	14.36	29.00	8.96
Quartz	11.34	5.15	27.05	122.90	~11	2.65

PMT Radius (mm)	Gravity (m/s/s)
39	9.81

Moliere Radius:

$$\frac{1}{R_M} = \frac{1}{E_s}\sum\frac{w_j E_{cj}}{X_j} = \sum\frac{w_j}{R_{Mj}}$$

W_j = relative weight

Config #	t_f (mm)	t_q (mm)	t_w (mm)	b (mm)	a (mm)	X	Tungsten Weight (N)	Quartz Weight (N)	Total Weight (N)	Moliere R_m (mm)
1	8	12.5	8	74	24.66	9.54	156.09	35.57	191.66	11.00
2	17	12.5	5	65	43.12	9.54	156.09	35.57	191.66	11.00
3	14	12.5	6	68	38.21	9.54	156.09	35.57	191.66	11.00
4	6	12.5	6	68	38.21	7.26	117.07	35.57	152.64	11.53

	Benchmark - 2GeV			
Config #	RMS/Mean	Leakage (%)	Leakage 1mm offset (%)	Leakage 2mm offset (%)
1	0.17	2.97	3.13	3.29
2	0.19	0	0	0
3	0.2	0.52	0.63	0.84
4	0.19	0	0	0

	Full Scale ShowerMax – 2GeV		
Config #	RMS	Mean	RMS/Mean
1	74.37	369.5	0.20
2	99.1	382.4	0.26
3	88.43	393.2	0.22
4	99.82	468.7	0.21

	Benchmark - 5GeV			
Config #	RMS/Mean	Leakage (%)	Leakage 1mm offset (%)	Leakage 2mm offset (%)
1	0.13	3.5	3.6	3.8
2	0.15	0	0	0
3	0.13	0.25	0.35	0.52
4	0.17	0	0	0

	Full Scale ShowerMax – 5GeV		
Config #	RMS	Mean	RMS/Mean
1	146.4	905.8	0.16
2	195.5	1075	0.18
3	174.9	1052	0.17
4	212.1	1067	0.20

	Benchmark – 8GeV			
Config #	RMS/Mean	Leakage (%)	Leakage 1mm offset (%)	Leakage 2mm offset (%)
1				
2				
3				
4				

	Full Scale ShowerMax – 8GeV		
Config #	RMS	Mean	RMS/Mean
1	218.8	1414	0.15
2	290.9	1772	0.16
3	261	1696	0.15
4	319.7	1603	0.20

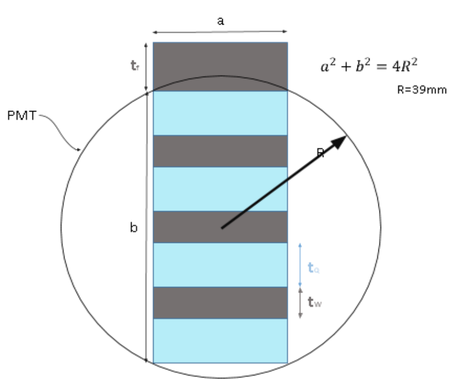

	Material Values (Particle Data Group)					
	R (g/cm/cm)	R (cm)	X (g/cm/cm)	X (mm)	Z	Density (g/cc)
Tungsten	18.00	0.93	6.76	3.50	74.00	19.25
Copper	14.05	1.57	12.86	14.36	29.00	8.96
Quartz	11.34	5.15	27.05	122.90	~11	2.65

PMT Radius (mm)	Gravity (m/s/s)
39	9.81

Moliere Radius:

$$\frac{1}{R_M} = \frac{1}{E_s}\sum \frac{w_j E_{cj}}{X_j} = \sum \frac{w_j}{R_{Mj}}$$

W_j = relative weight

Config #	t_f (mm)	t_q (mm)	t_w (mm)	b (mm)	Max A (mm)	X	Tungsten Weight (N)	Quartz Weight (N)	Total Weight (N)	Moliere R_m (mm)
1A	8	10	8	64	44.59	9.46	156.09	35.57	191.66	11.00
1B	8	6	8	48	61.48	9.33	156.09	35.57	191.66	11.00
4A	6	10	8	64	44.59	8.89	146.33	35.57	181.91	11.11
4B	6	6	6	42	65.73	7.04	117.07	35.57	152.64	11.53

	Benchmark - 2GeV			
Config #	RMS/Mean	Leakage (%)	Leakage 2mm offset (%)	Leakage 2° angle (%)
1A	0.17	0	0	-0.1
1B	0.19	0	0	0.2
4A	0.19	0	0	-
4B	0.21	0	0	-

	Full Scale ShowerMax – 2GeV		
Config #	RMS	Mean	RMS/Mean
1A	63.36	315.9	0.20
1B	45.46	197.7	0.23
4A**	60.16	300.2	0.20
4B**	39.67	179.3	0.22

	Benchmark - 5GeV			
Config #	RMS/Mean	Leakage (%)	Leakage 2mm offset (%)	Leakage 2° angle (%)
1A	0.13	0.04	0.09	-0.4
1B	0.14	0	0	0.2
4A	0.17	0.06	0.3	-
4B	0.19	0	0	-

	Full Scale ShowerMax – 5GeV		
Config #	RMS	Mean	RMS/Mean
1A	123.7	768.5	0.16
1B	87.82	473.6	0.19
4A**	126.8	677.4	0.19
4B**	80.61	397.4	0.20

	Benchmark – 8GeV			
Config #	RMS/Mean	Leakage (%)	Leakage 2mm offset (%)	Leakage 2° angle (%)
1A	0.12	0	0	-
1B	0.13	0	0	-
4A*	0.18	0	0	-
4B	0.19	0	0	-

	Full Scale ShowerMax – 8GeV		
Config #	RMS	Mean	RMS/Mean
1A	183.2	1197	0.15
1B	129.1	732.3	0.18
4A**	187.9	1012	0.19
4B**	118.8	591.3	0.20

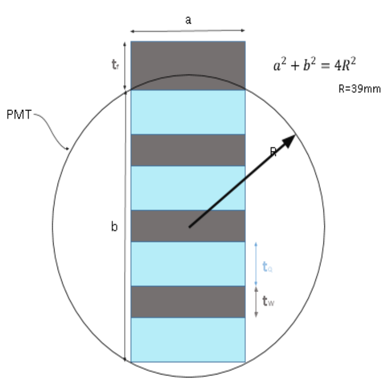

* Small bump from 10,000 PE limit

** Center Sampled Beam

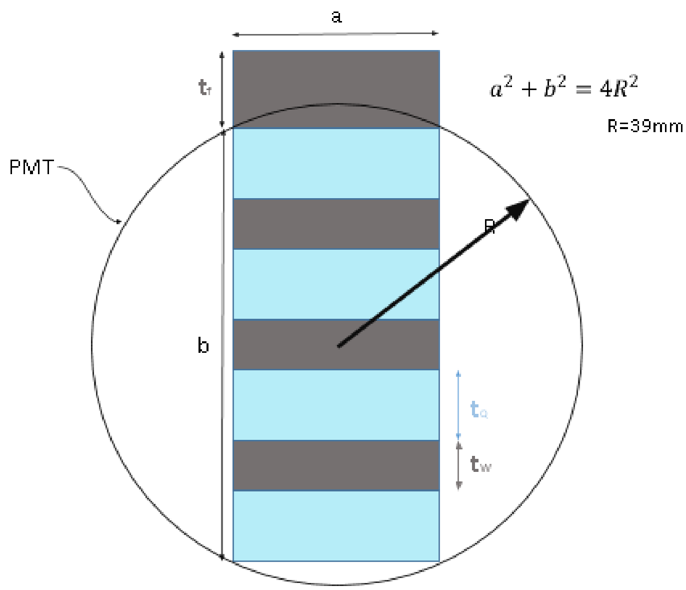

Figure B.1: Depiction of a generic stack that is being viewed from above. The circle represents a 3 inch PMT. The blue represent quartz pieces and the grey represents tungsten. Notice that all of the quartz pieces are circumscribed by the PMT.

Benchmarking Apparatus: Molière Radius Study

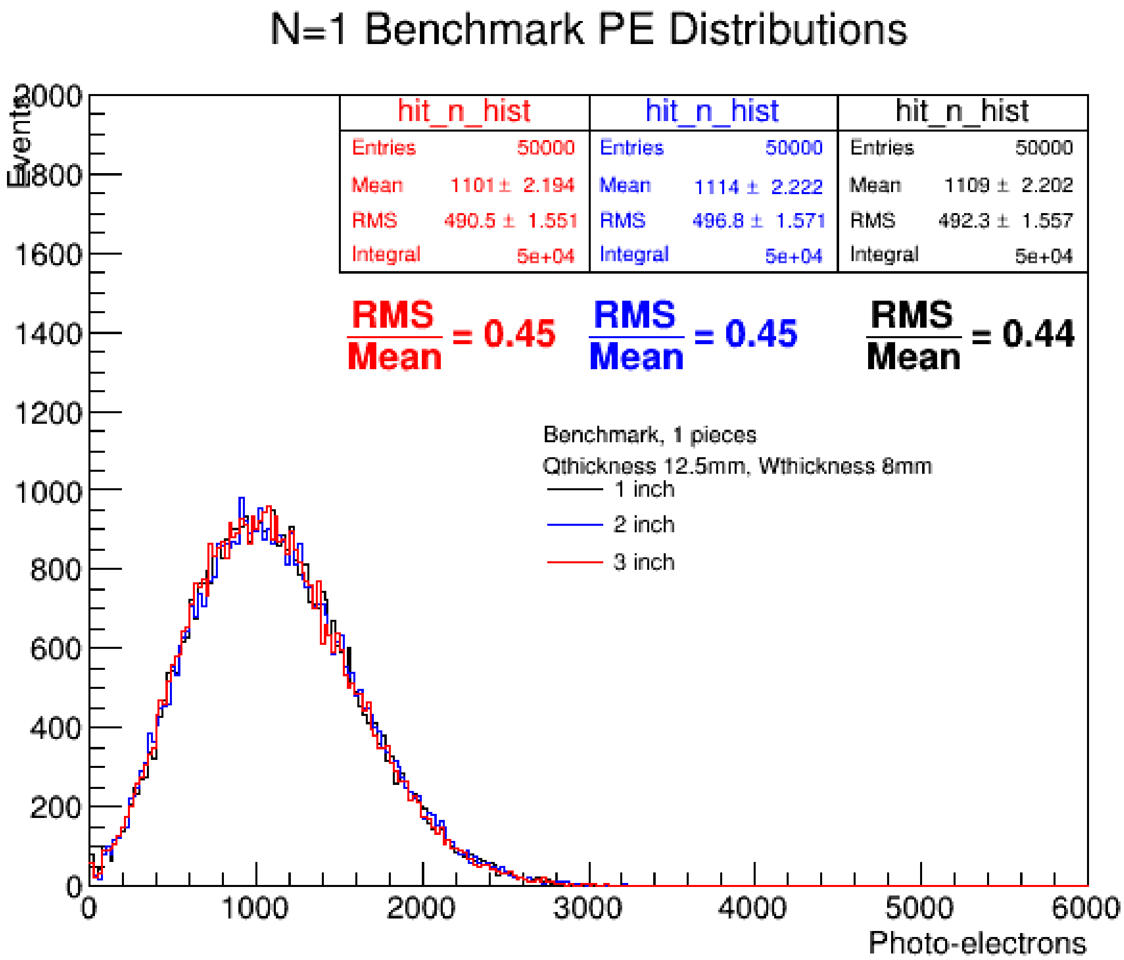

Figure B.2: PE distribution of configuration 1 benchmarking apparatus with one tungsten plate and one quartz tile. Three different stack widths are shown to compare relative losses due to transverse shower size. Black, blue, and red represent 1 in, 2 in, and 3 in stack widths consecutively.

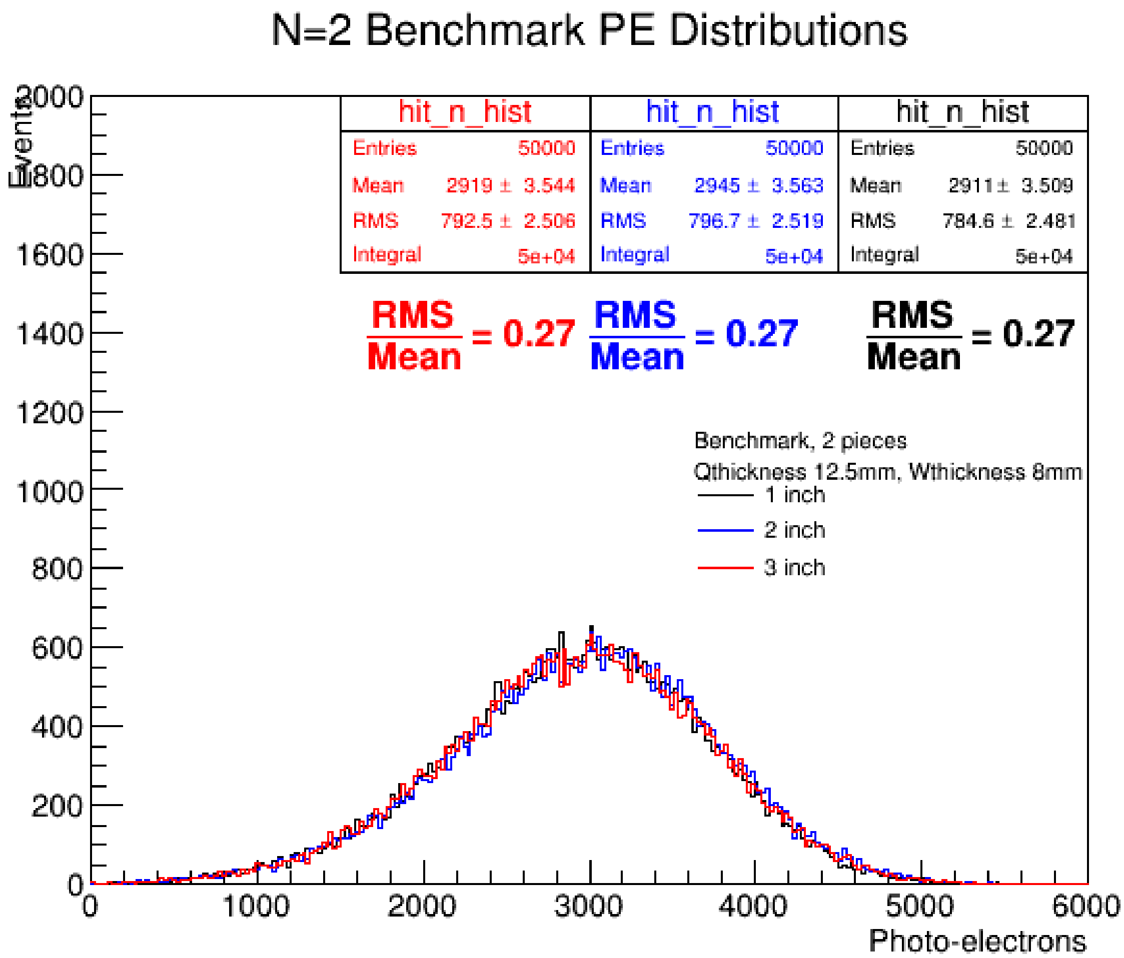

Figure B.3: PE distribution of configuration 1 benchmarking apparatus with two tungsten plates and two quartz tiles. Three different stack widths are shown to compare relative losses due to transverse shower size. Black, blue, and red represent 1 in, 2 in, and 3 in stack widths consecutively.

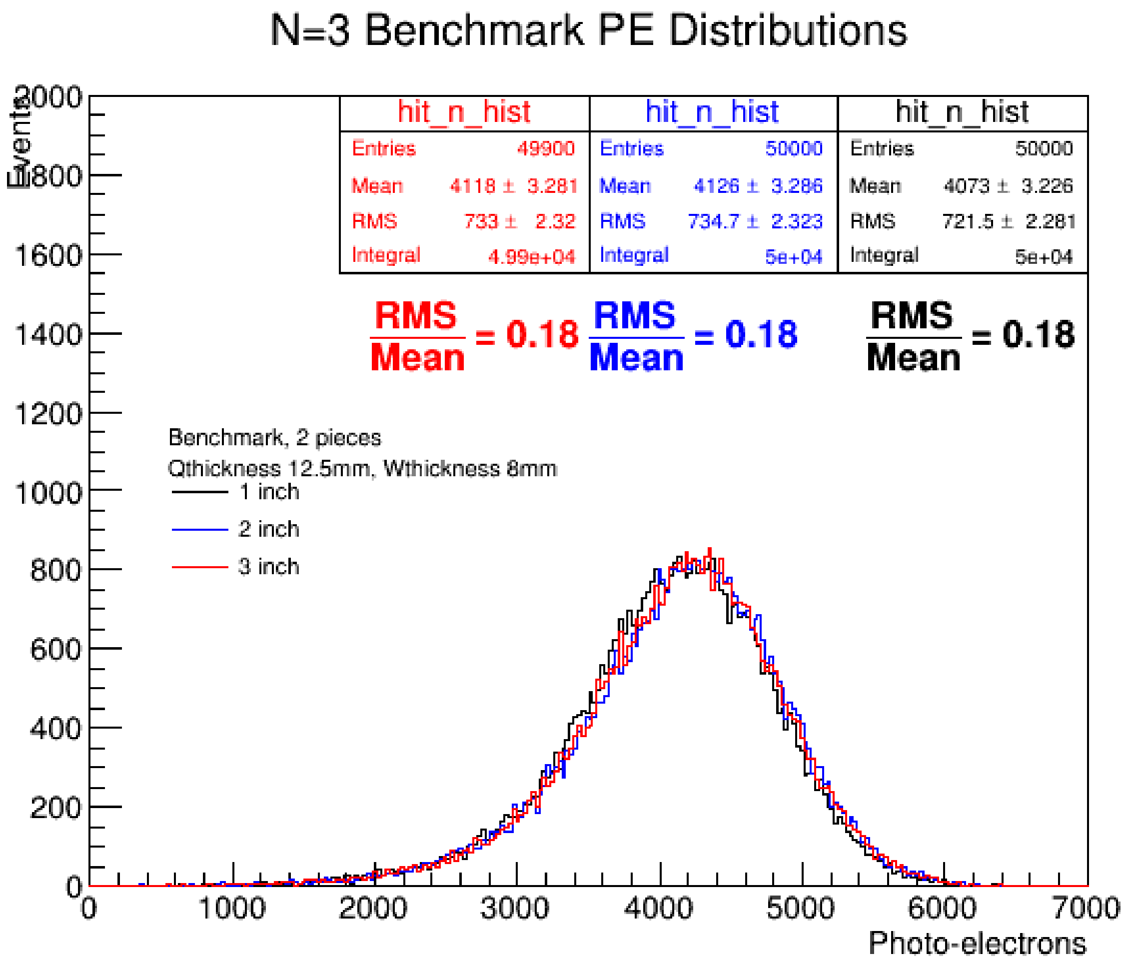

Figure B.4: PE distribution of configuration 1 benchmarking apparatus with three tungsten plates and three quartz tiles. Three different stack widths are shown to compare relative losses due to transverse shower size. Black, blue, and red represent 1 in, 2 in, and 3 in stack widths consecutively.

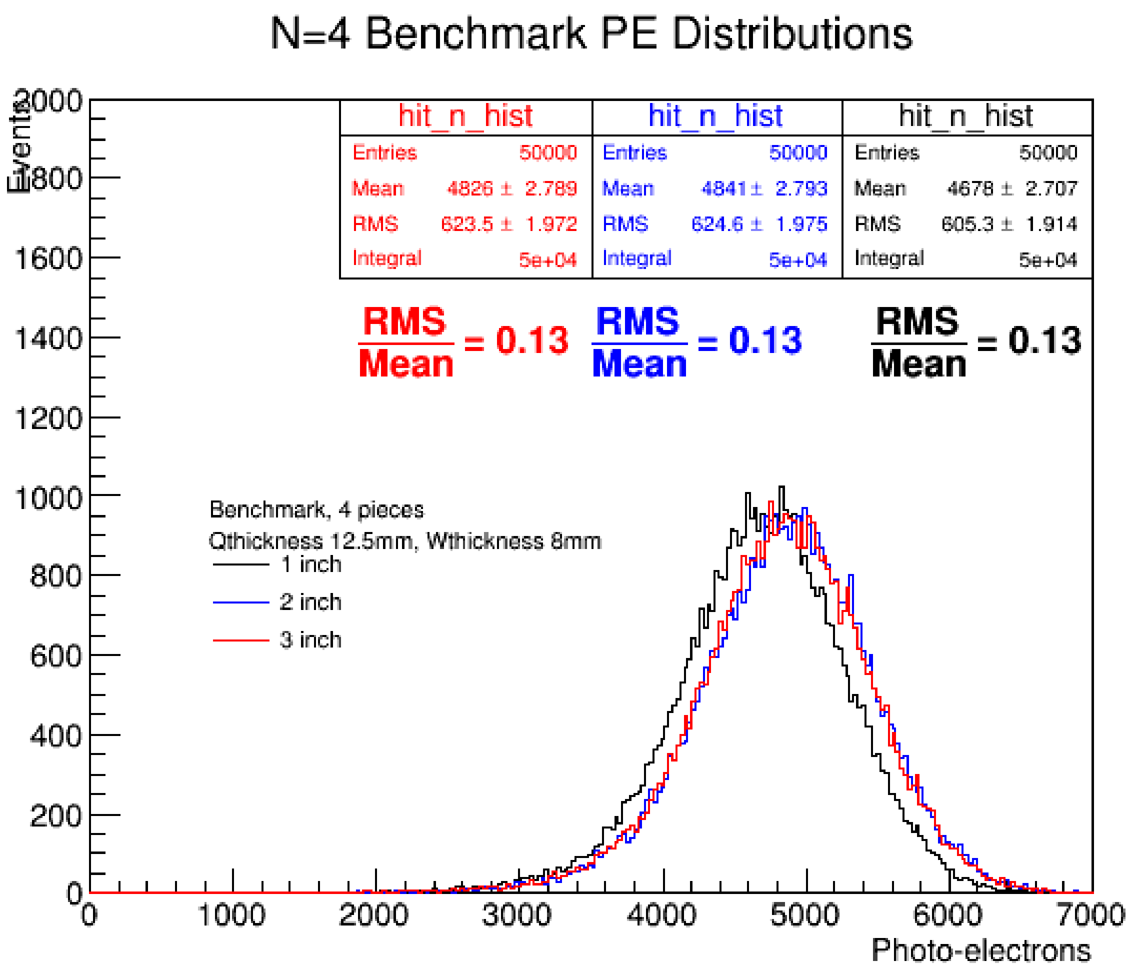

Figure B.5: PE distribution of configuration 1 benchmarking apparatus with four tungsten plates and four quartz tiles. Three different stack widths are shown to compare relative losses due to transverse shower size. Black, blue, and red represent 1 in, 2 in, and 3 in stack widths consecutively.

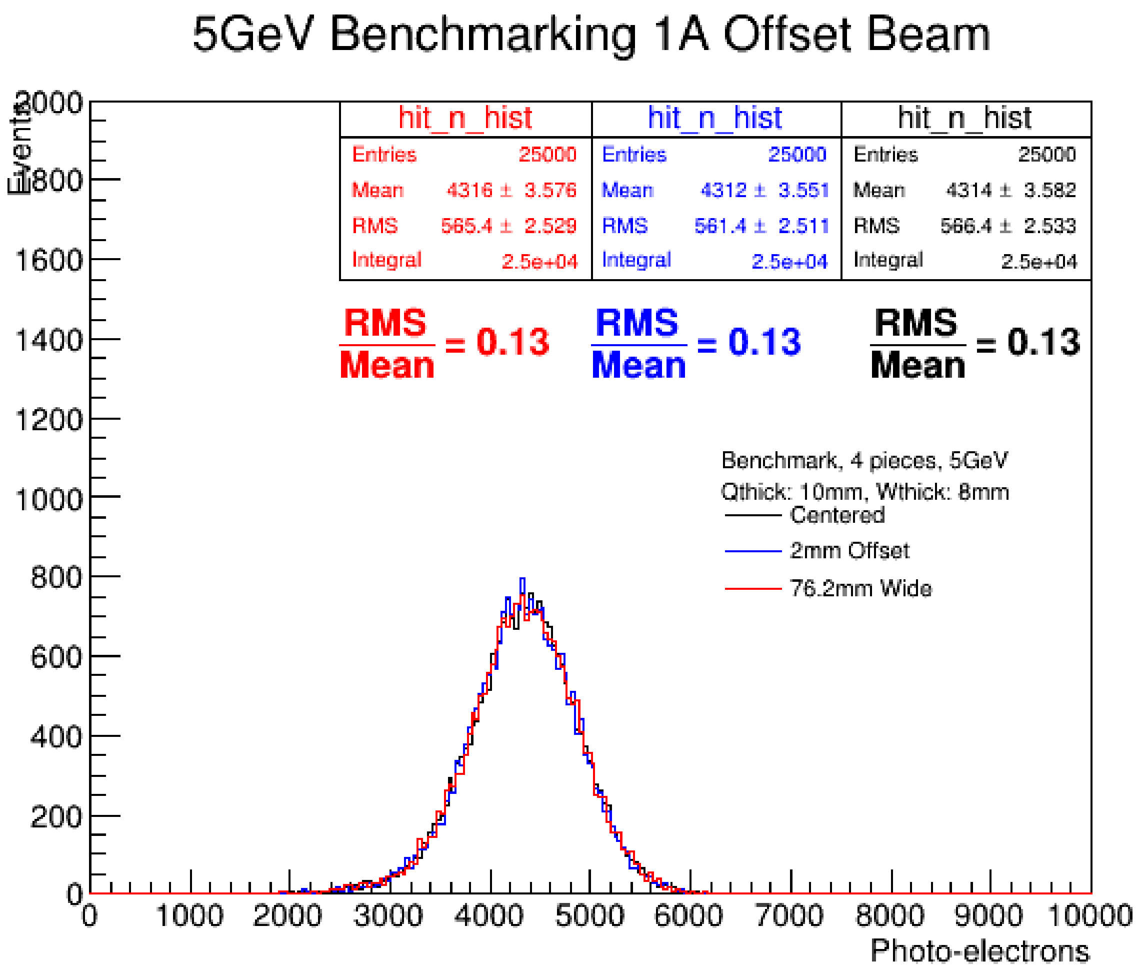

Figure B.6: PE distribution for 5 GeV beam incident on configuration 1A benchmarking apparatus. Black and blue are for a 40 mm wide stack. Black is a perfectly centered beam and blue is a beam that has been offset by 2 mm. Red represents a 76.2 mm wide stack with a centered beam. Notice that the losses are negligible.

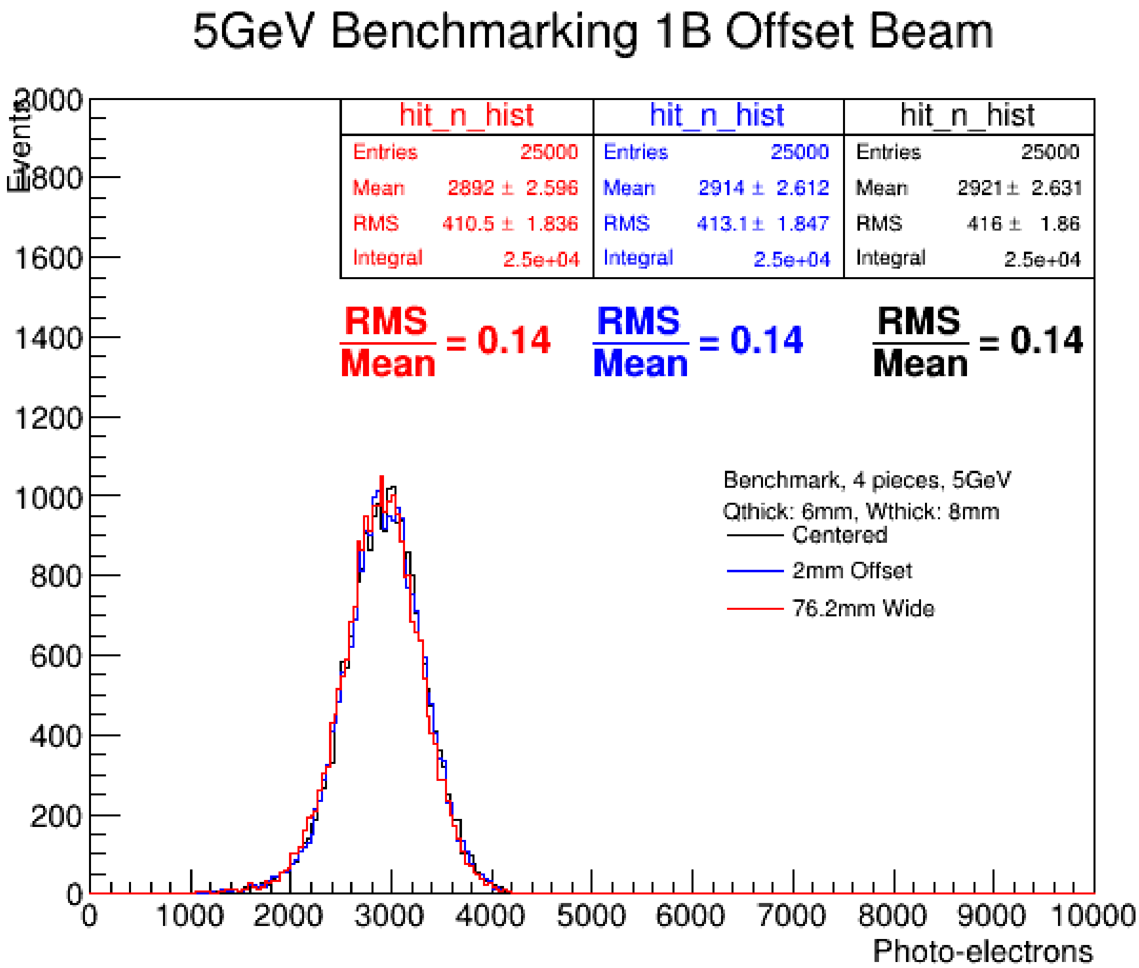

Figure B.7: PE distribution for 5 GeV beam incident on configuration 1B benchmarking apparatus. Black and blue are for a 40 mm wide stack. Black is a perfectly centered beam and blue is a beam that has been offset by 2 mm. Red represents a 76.2 mm wide stack with a centered beam. Notice that the losses are negligible.

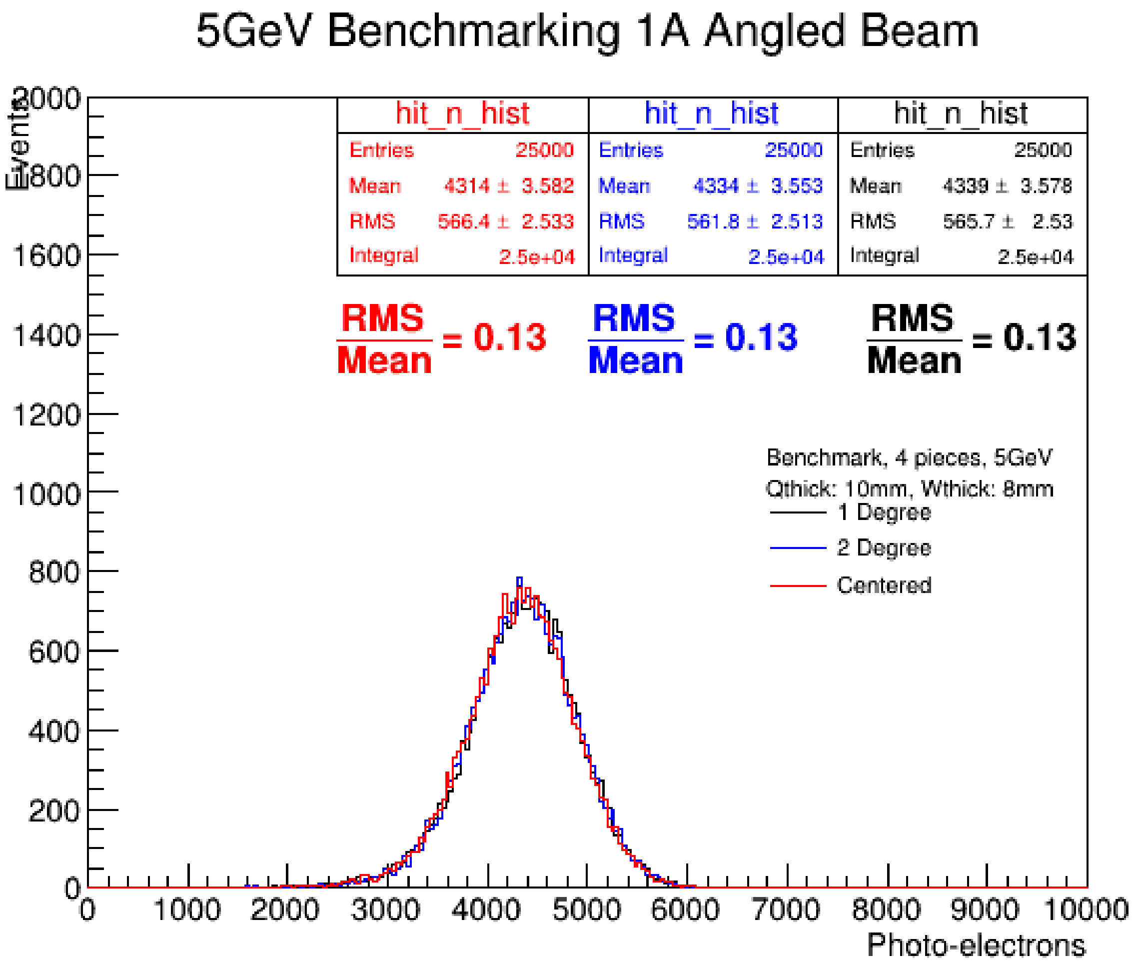

Figure B.8: PE distribution for 5 GeV beam incident on configuration 1A benchmarking apparatus with a 40 mm wide stack. Black and blue represent 1° and 2° angled (and centered) beams. Red represents a centered and perpendicular beam. Notice that there is more light created for the angled beams. This is because more material is traversed and therefore the shower becomes more developed.

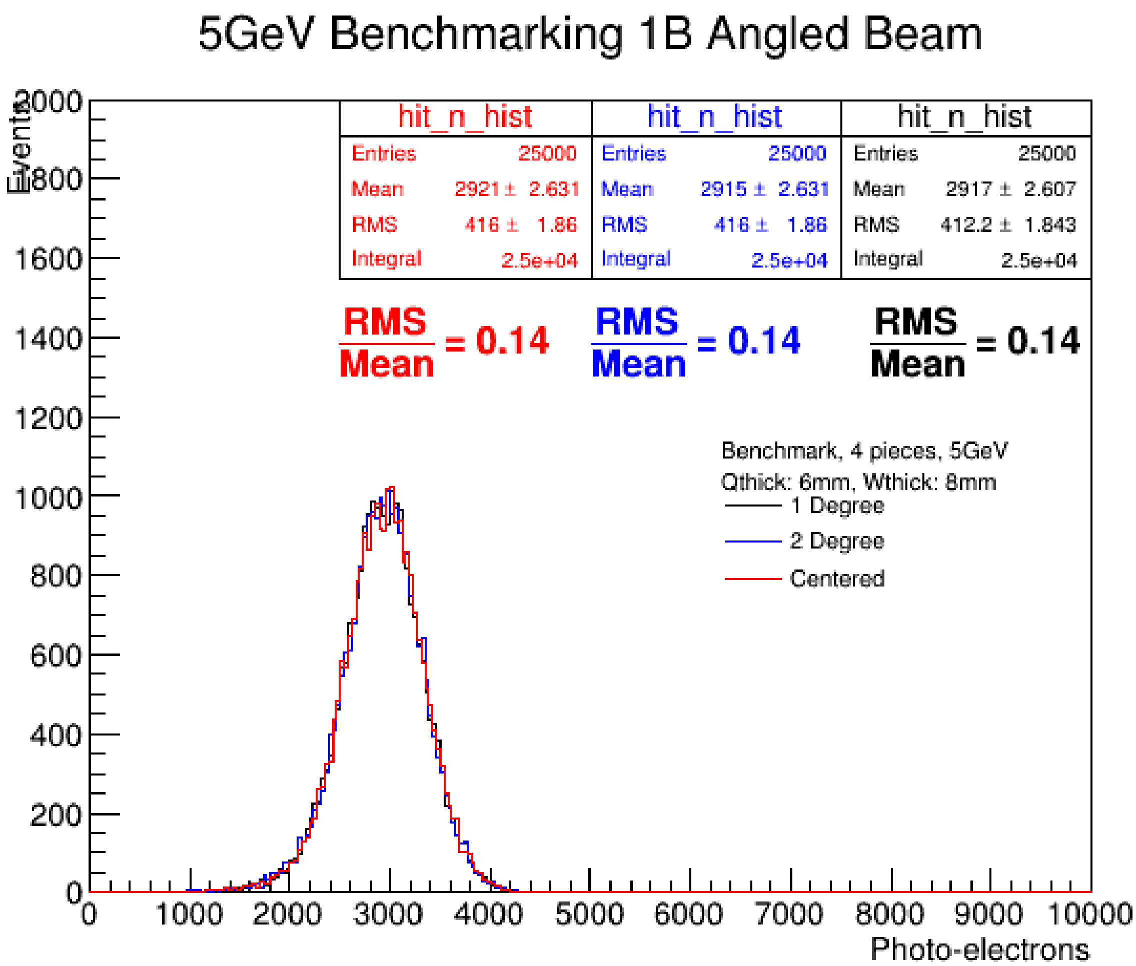

Figure B.9: PE distribution for 5 GeV beam incident on configuration 1B benchmarking apparatus with a 40 mm wide stack. Black and blue represent 1° and 2° angled (and centered) beams. Red represents a centered and perpendicular beam. Notice that the losses are negligible.

Appendix C
CAD Drawings

This appendix contains the CAD drawings created using SolidWorks for the ShowerMax frame and light guides. Configurations 1A and 1B are included. Notice that the machined ledges that support the tungsten and quartz are not included. This is because they have been 3-D printed for the first prototypes in order to test the designs effectiveness.

Configuration 1A Frame

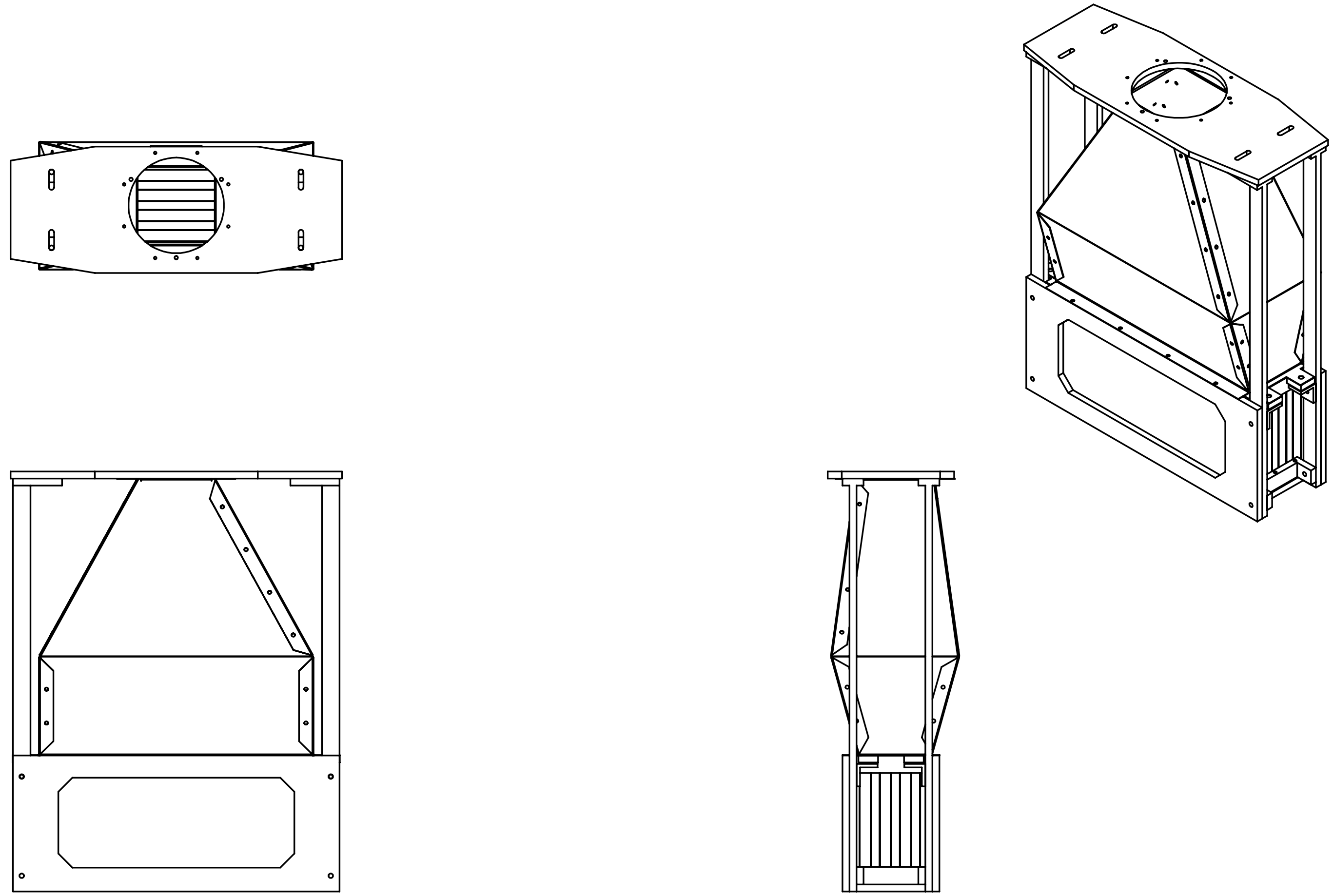

UNLESS OTHERWISE SPECIFIED:		NAME	DATE
DIMENSIONS ARE IN INCHES TOLERANCES: FRACTIONAL± ANGULAR: MACH± BEND ± TWO PLACE DECIMAL ± THREE PLACE DECIMAL ±	DRAWN	DKS	1/13/2018
	CHECKED		
	ENG APPR.		
	MFG APPR.		
INTERPRET GEOMETRIC TOLERANCING PER:	Q.A.		
MATERIAL	COMMENTS:		
FINISH			
DO NOT SCALE DRAWING			

Moller Collaboration

TITLE:

ShowerMax Frame 1A

SIZE	DWG. NO.	REV
A	1	0

SCALE: 1:6	WEIGHT:	SHEET 1 OF 11

2 1

B B

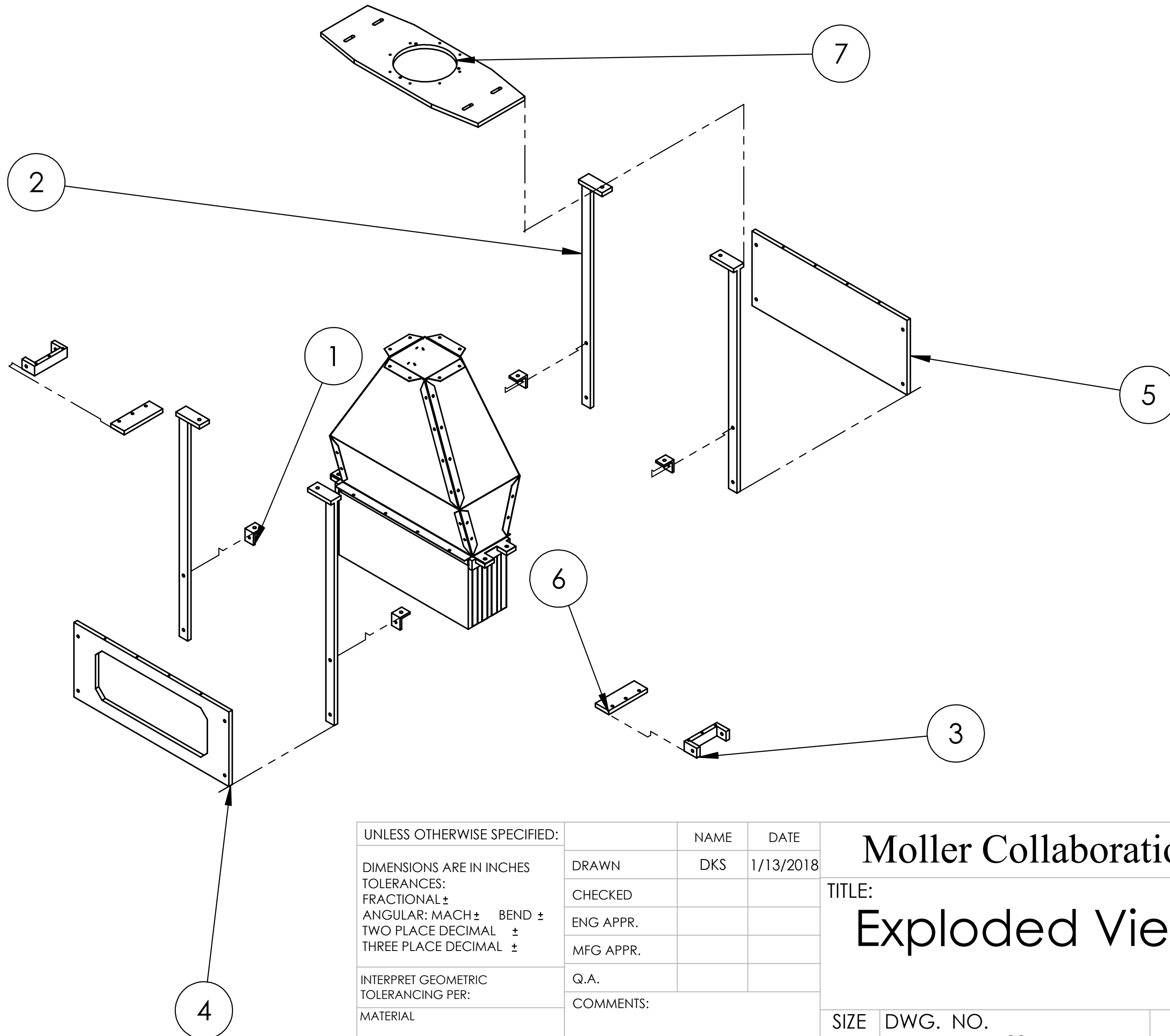

A A

UNLESS OTHERWISE SPECIFIED:		NAME	DATE	Moller Collaboration
DIMENSIONS ARE IN INCHES TOLERANCES: FRACTIONAL± ANGULAR: MACH± BEND ± TWO PLACE DECIMAL ± THREE PLACE DECIMAL ±	DRAWN	DKS	1/13/2018	TITLE:
	CHECKED			Exploded View
	ENG APPR.			
	MFG APPR.			
INTERPRET GEOMETRIC TOLERANCING PER:	Q.A.			
MATERIAL	COMMENTS:			SIZE **A** DWG. NO. II REV 0
FINISH				
DO NOT SCALE DRAWING				SCALE: 1:8 WEIGHT: SHEET 2 OF 11

2 1

ITEM NO.	PART NUMBER	Material	QTY.
1	clamp-adapter	6061 Aluminum	4
2	Struts	1/4 x 5/8 6061 Aluminum Flat Bar	4
3	U-Channel	0.25 (1/4) thick 6061-T651 Aluminum Plate	2
4	Front Plate	0.25 (1/4) thick 6061-T651 Aluminum Plate	1
5	Back Plate	0.25 (1/4) thick 6061-T651 Aluminum Plate	1
6	The Floor	0.25 (1/4) thick 6061-T651 Aluminum Plate	2
7	Top Plate	0.25 (1/4) thick 6061-T651 Aluminum Plate	1

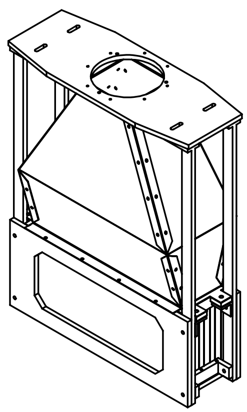

UNLESS OTHERWISE SPECIFIED:		NAME	DATE
DIMENSIONS ARE IN INCHES TOLERANCES: FRACTIONAL ± ANGULAR: MACH ± BEND ± TWO PLACE DECIMAL ± THREE PLACE DECIMAL ±	DRAWN	DKS	1/13/2018
	CHECKED		
	ENG APPR.		
	MFG APPR.		
INTERPRET GEOMETRIC TOLERANCING PER:	Q.A.		
MATERIAL	COMMENTS:		
FINISH			
DO NOT SCALE DRAWING			

Moller Collaboration

TITLE:
Bill of Materials

SIZE	DWG. NO.	REV
A	III	0
SCALE: 1:8	WEIGHT:	SHEET 3 OF 11

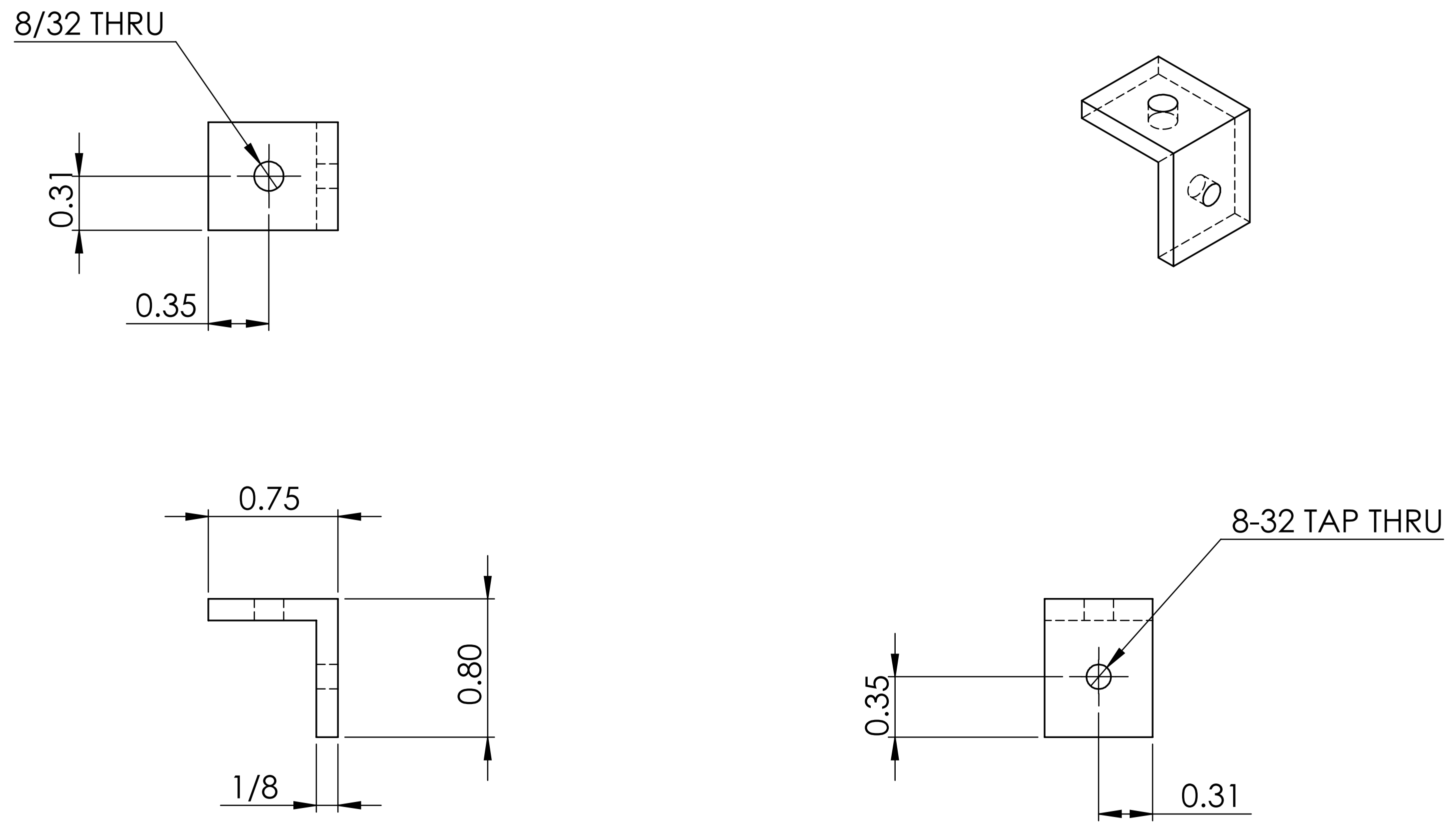

UNLESS OTHERWISE SPECIFIED:

DIMENSIONS ARE IN INCHES
TOLERANCES:
FRACTIONAL ±
ANGULAR: MACH ± BEND ±
TWO PLACE DECIMAL ±
THREE PLACE DECIMAL ±

INTERPRET GEOMETRIC TOLERANCING PER:

MATERIAL
6061 Aluminum

FINISH

DO NOT SCALE DRAWING

	NAME	DATE
DRAWN	DKS	1/11/2018
CHECKED		
ENG APPR.		
MFG APPR.		
Q.A.		

COMMENTS:

Moller Collaboration

TITLE:
Clamp Adapter

SIZE	DWG. NO.	REV
A	1	0

SCALE: 1:1 WEIGHT: SHEET 4 OF 11

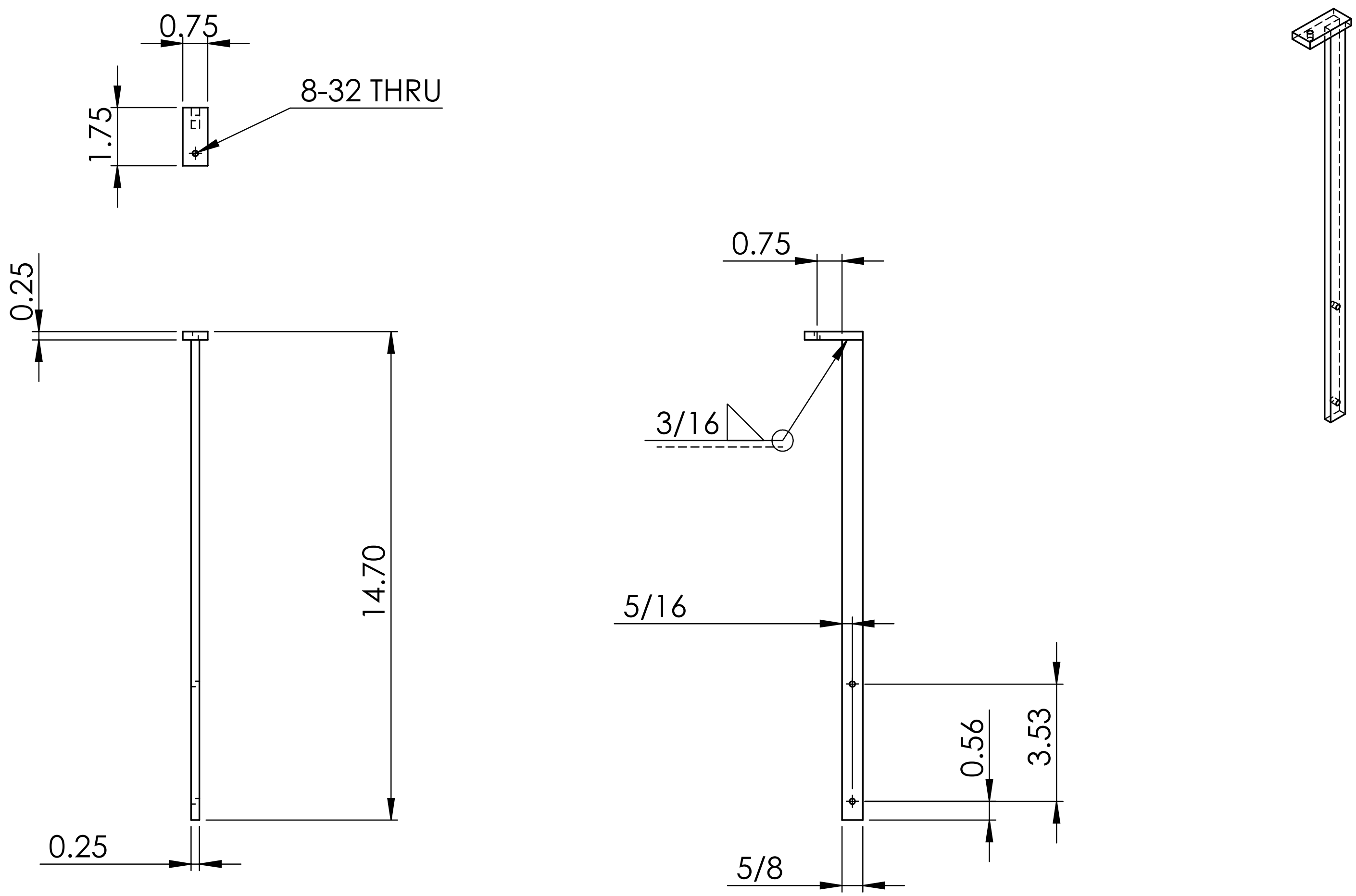

UNLESS OTHERWISE SPECIFIED:		NAME	DATE	Moller Collaboration
DIMENSIONS ARE IN INCHES TOLERANCES: FRACTIONAL ± ANGULAR: MACH ± BEND ± TWO PLACE DECIMAL ± THREE PLACE DECIMAL ±	DRAWN	DKS	1/10/2018	TITLE: Struts
	CHECKED			
	ENG APPR.			
	MFG APPR.			
INTERPRET GEOMETRIC TOLERANCING PER:	Q.A.			
MATERIAL 6061 Aluminum Flat	COMMENTS:			SIZE A DWG. NO. 2 REV 0
FINISH DO NOT SCALE DRAWING				SCALE: 1:5 WEIGHT: SHEET 5 OF 11

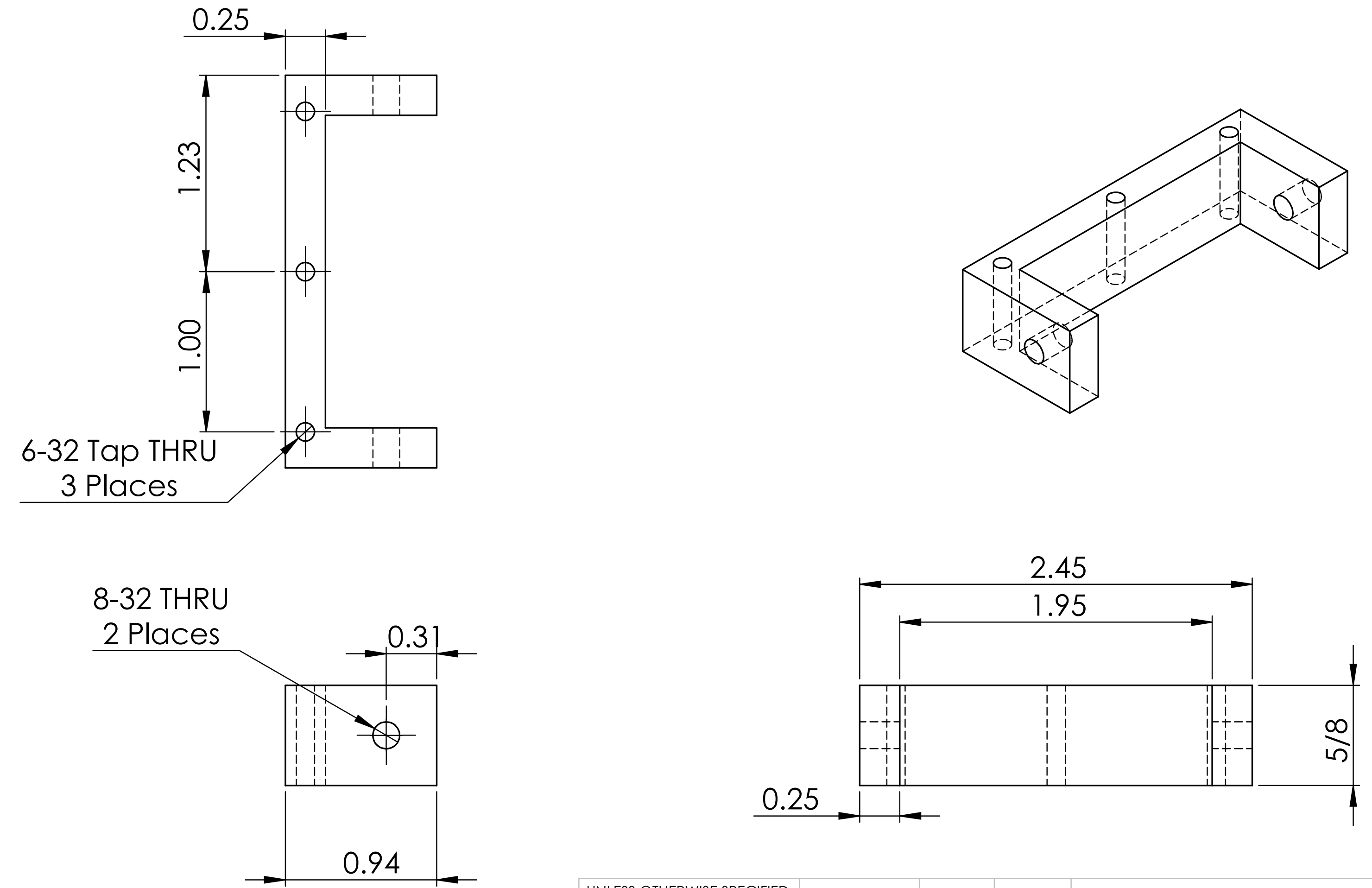

UNLESS OTHERWISE SPECIFIED:		NAME	DATE	Moller Collaboration
DIMENSIONS ARE IN INCHES TOLERANCES: FRACTIONAL ± ANGULAR: MACH ± BEND ± TWO PLACE DECIMAL ± THREE PLACE DECIMAL ±	DRAWN	DKS	1/11/2018	TITLE:
	CHECKED			U - Channel
	ENG APPR.			
	MFG APPR.			
INTERPRET GEOMETRIC TOLERANCING PER:	Q.A.			
MATERIAL 6061-T651 Aluminum Plate	COMMENTS:			SIZE A | DWG. NO. 3 | REV 0
FINISH DO NOT SCALE DRAWING				SCALE: 1:1 | WEIGHT: | SHEET 6 OF 11

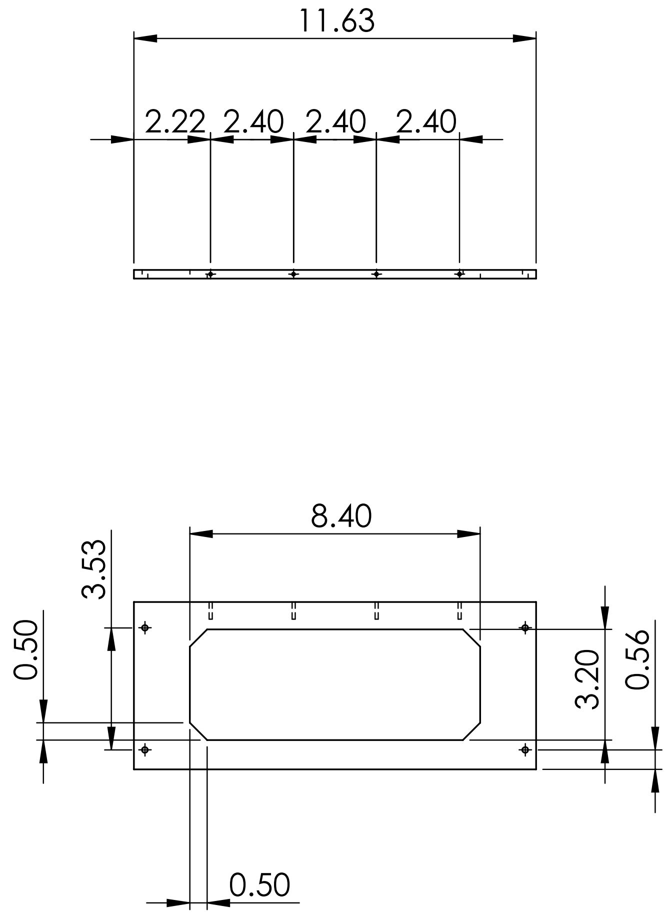

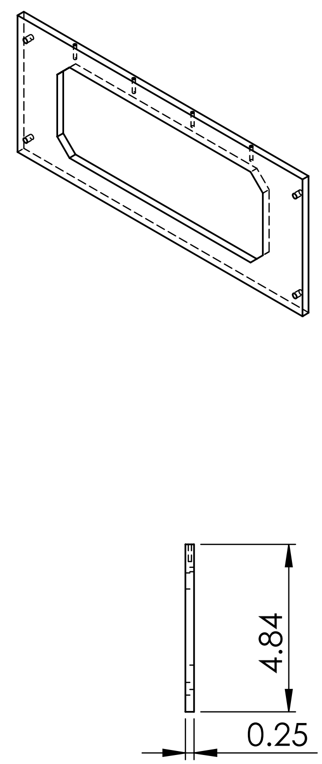

UNLESS OTHERWISE SPECIFIED:		NAME	DATE	Moller Collaboration
DIMENSIONS ARE IN INCHES TOLERANCES: FRACTIONAL ± ANGULAR: MACH ± BEND ± TWO PLACE DECIMAL ± THREE PLACE DECIMAL ±	DRAWN	DKS	1/10/2018	TITLE: Front Plate
	CHECKED			
	ENG APPR.			
	MFG APPR.			
INTERPRET GEOMETRIC TOLERANCING PER:	Q.A.			
MATERIAL 6061-T651 Aluminum Plate	COMMENTS:			SIZE A · DWG. NO. 4 · REV 0
FINISH				
DO NOT SCALE DRAWING				SCALE: 1:5 · WEIGHT: · SHEET 7 OF 11

2 1

B B

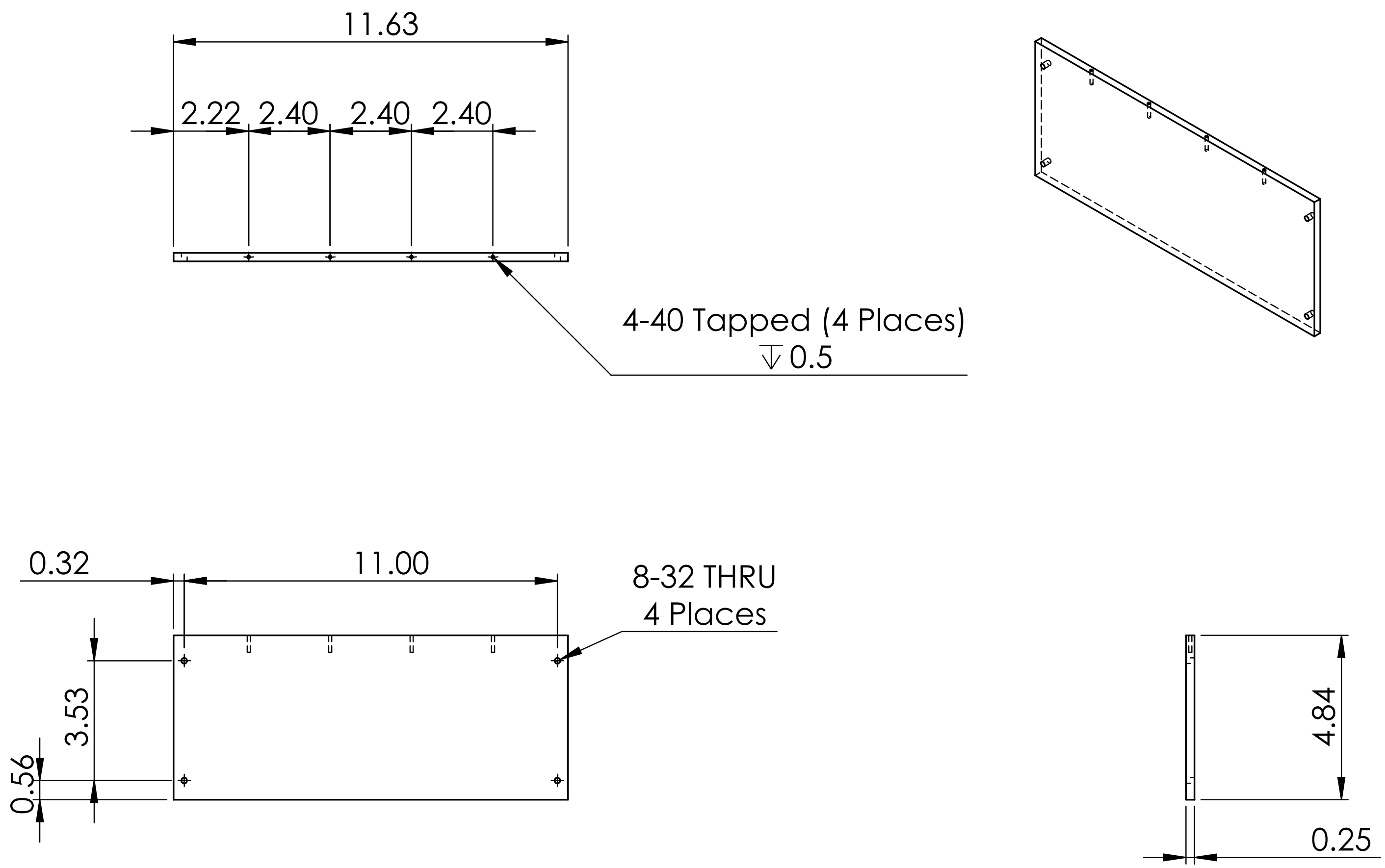

110

A A

UNLESS OTHERWISE SPECIFIED:		NAME	DATE	Moller Collaboration
DIMENSIONS ARE IN INCHES TOLERANCES: FRACTIONAL ± ANGULAR: MACH ± BEND ± TWO PLACE DECIMAL ± THREE PLACE DECIMAL ±	DRAWN	DKS	1/18/2018	TITLE:
	CHECKED			Back Plate
	ENG APPR.			
	MFG APPR.			
INTERPRET GEOMETRIC TOLERANCING PER:	Q.A.			
MATERIAL 6061-T651 Aluminum Plate	COMMENTS:			SIZE A · DWG. NO. 5 · REV 0
FINISH DO NOT SCALE DRAWING				SCALE: 1:5 · WEIGHT: · SHEET 8 OF 11

2 1

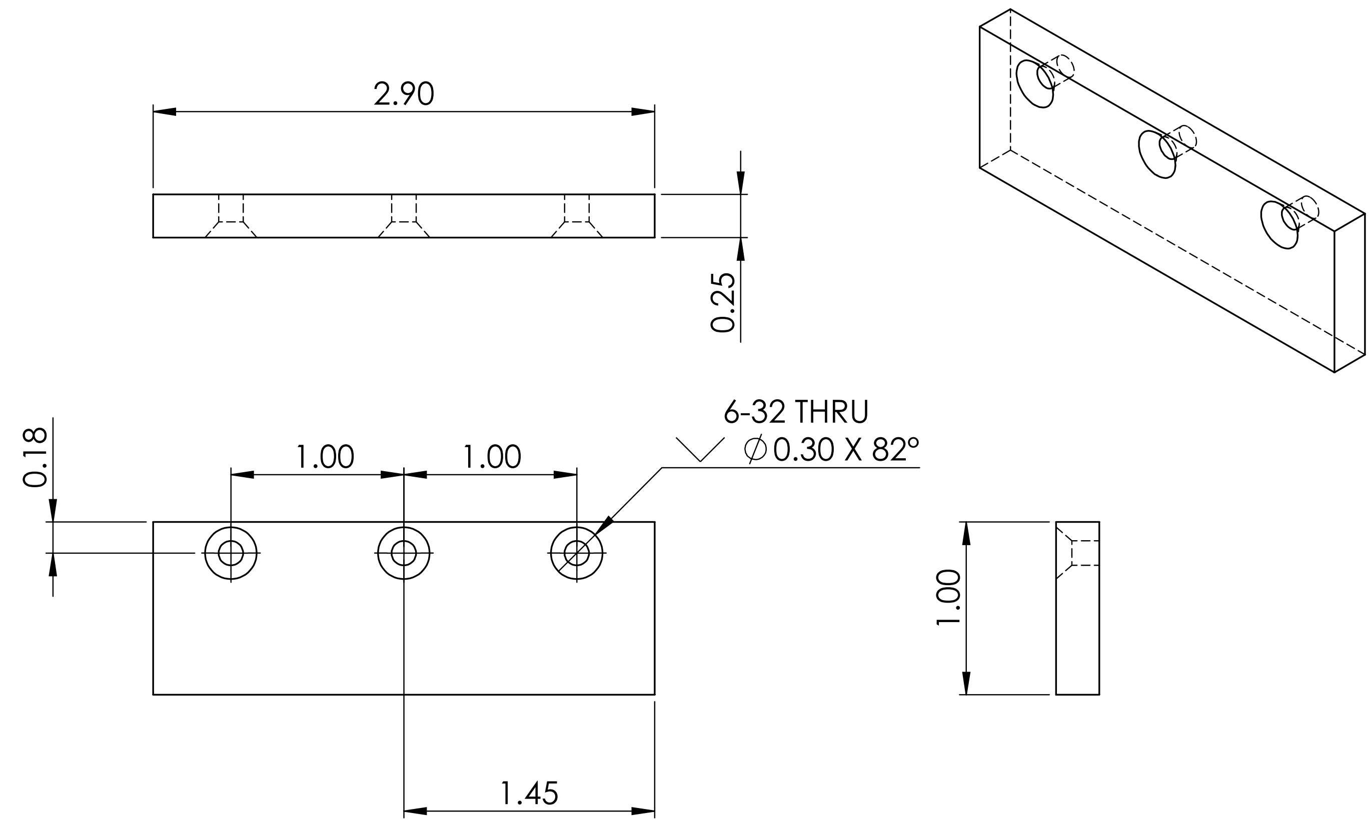

UNLESS OTHERWISE SPECIFIED:		NAME	DATE
DIMENSIONS ARE IN INCHES TOLERANCES: FRACTIONAL ± ANGULAR: MACH ± BEND ± TWO PLACE DECIMAL ± THREE PLACE DECIMAL ±	DRAWN	DKS	1/10/2018
	CHECKED		
	ENG APPR.		
	MFG APPR.		
INTERPRET GEOMETRIC TOLERANCING PER:	Q.A.		
MATERIAL 6061-T651 Aluminum Plate	COMMENTS:		
FINISH			
DO NOT SCALE DRAWING			

Moller Collaboration

TITLE:

The Floor

SIZE	DWG. NO.	REV
A	6	0
SCALE: 1:1	WEIGHT:	SHEET 9 OF 11

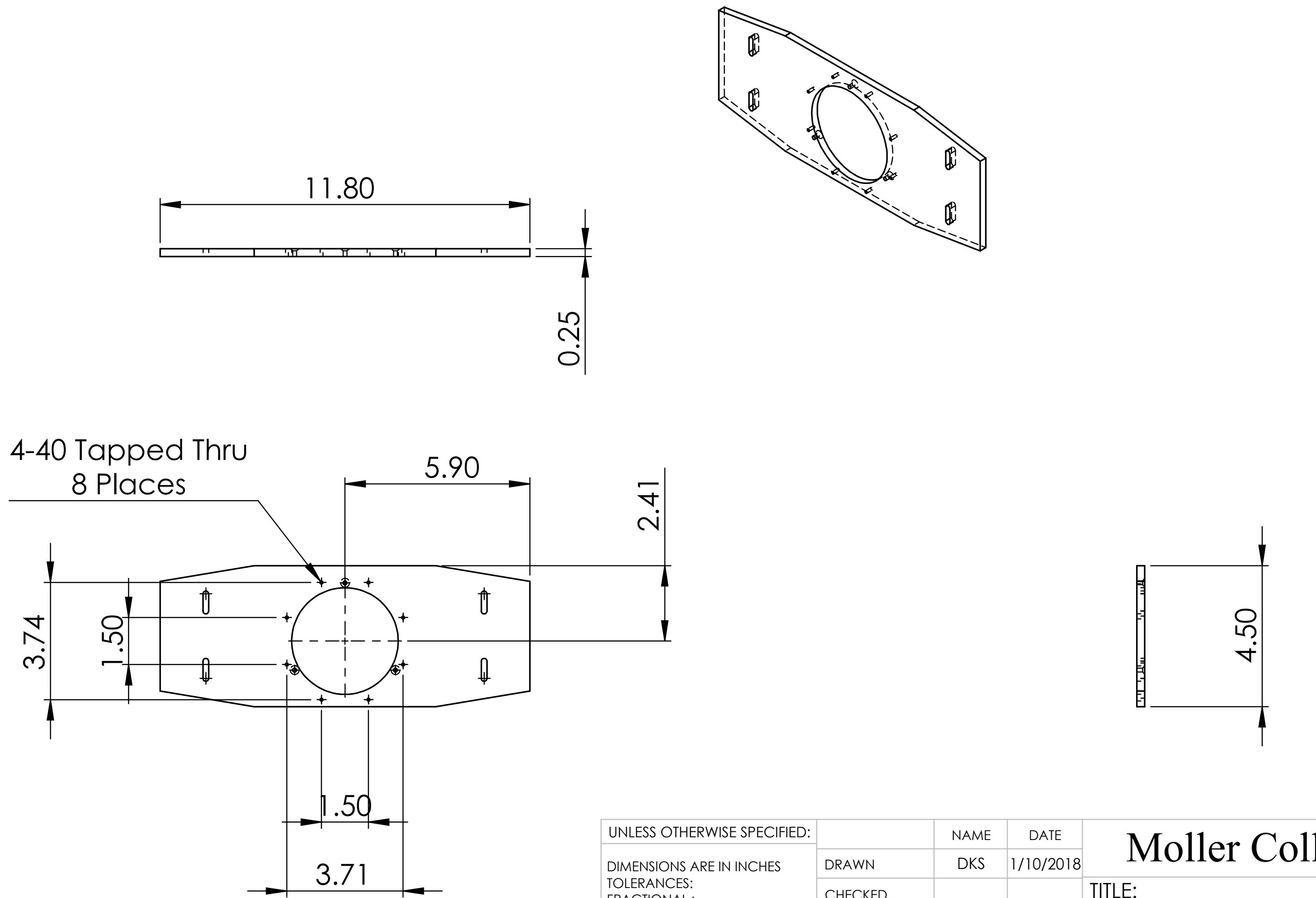

UNLESS OTHERWISE SPECIFIED:		NAME	DATE
DIMENSIONS ARE IN INCHES TOLERANCES: FRACTIONAL ± ANGULAR: MACH ± BEND ± TWO PLACE DECIMAL ± THREE PLACE DECIMAL ±	DRAWN	DKS	1/10/2018
	CHECKED		
	ENG APPR.		
	MFG APPR.		
INTERPRET GEOMETRIC TOLERANCING PER:	Q.A.		
MATERIAL 6061-T651 Aluminum Plate	COMMENTS:		
FINISH DO NOT SCALE DRAWING			

Moller Collaboration

TITLE:

Top Plate

SIZE	DWG. NO.	REV
A	7A	0
SCALE: 1:5	WEIGHT:	SHEET 10 OF 1

Top Bottom

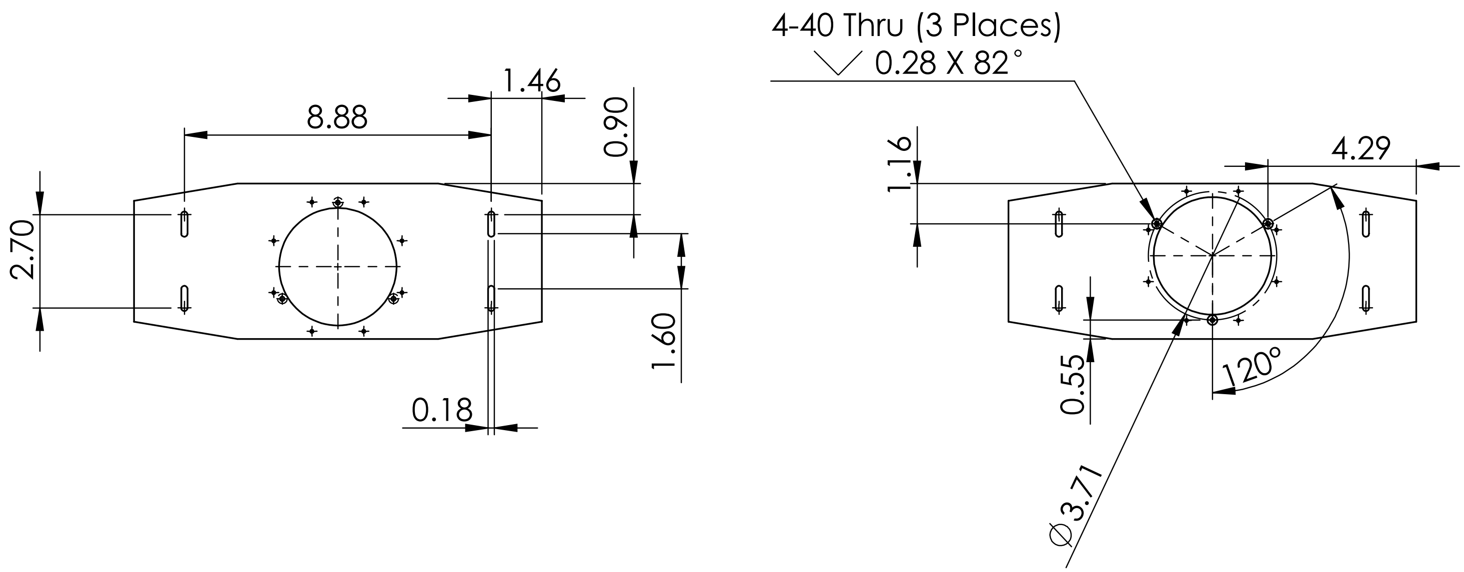

UNLESS OTHERWISE SPECIFIED:		NAME	DATE
DIMENSIONS ARE IN INCHES TOLERANCES: FRACTIONAL ± ANGULAR: MACH ± BEND ± TWO PLACE DECIMAL ± THREE PLACE DECIMAL ±	DRAWN	DKS	1/10/2018
	CHECKED		
	ENG APPR.		
	MFG APPR.		
INTERPRET GEOMETRIC TOLERANCING PER:	Q.A.		
MATERIAL 6061-T651 Aluminum Plate	COMMENTS:		
FINISH DO NOT SCALE DRAWING			

Moller Collaboration

TITLE:

Top Plate

SIZE	DWG. NO.	REV
A	7B	0
SCALE: 1:5	WEIGHT:	SHEET 11 OF 1

2 | 1

B

Configuration 1B Frame

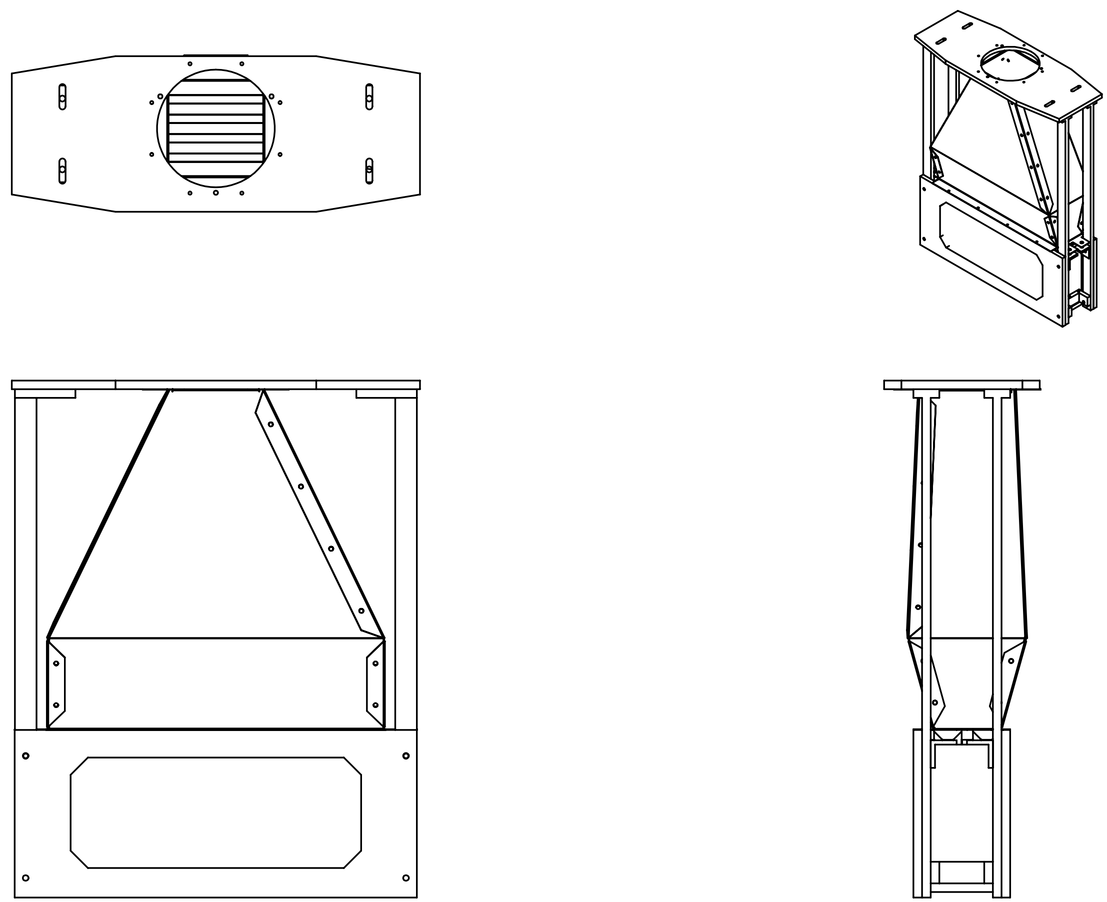

A

UNLESS OTHERWISE SPECIFIED:		NAME	DATE	Moller Collaboration
DIMENSIONS ARE IN INCHES TOLERANCES: FRACTIONAL ± ANGULAR: MACH ± BEND ± TWO PLACE DECIMAL ± THREE PLACE DECIMAL ±	DRAWN	DKS	1/24/18	TITLE:
	CHECKED			ShowerMax Config1B
	ENG APPR.			
	MFG APPR.			
	Q.A.			
INTERPRET GEOMETRIC TOLERANCING PER:	COMMENTS:			SIZE **A** DWG. NO. 1 REV 0
MATERIAL				
FINISH				
DO NOT SCALE DRAWING				SCALE: 1:5 WEIGHT: SHEET 1 OF 10

2 | 1

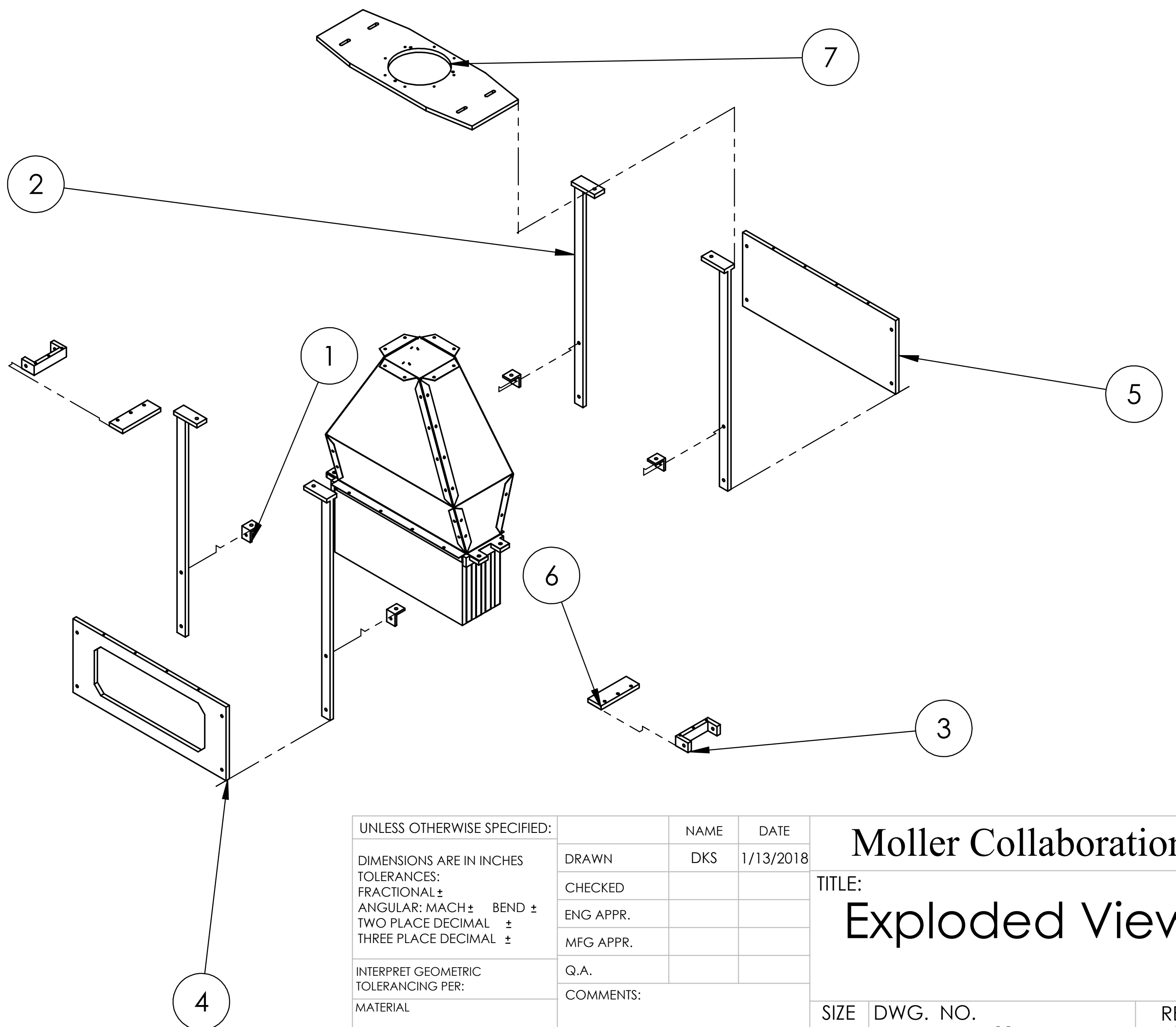

UNLESS OTHERWISE SPECIFIED:		NAME	DATE	Moller Collaboration
DIMENSIONS ARE IN INCHES TOLERANCES: FRACTIONAL ± ANGULAR: MACH ± BEND ± TWO PLACE DECIMAL ± THREE PLACE DECIMAL ±	DRAWN	DKS	1/13/2018	TITLE: Exploded View
	CHECKED			
	ENG APPR.			
	MFG APPR.			
INTERPRET GEOMETRIC TOLERANCING PER:	Q.A.			
MATERIAL	COMMENTS:			SIZE A · DWG. NO. II · REV 0
FINISH				
DO NOT SCALE DRAWING				SCALE: 1:8 · WEIGHT: · SHEET 2 OF 11

ITEM NO.	PART NUMBER	Material	QTY.
1	clamp-adapter	6061 Aluminum	4
2	Struts	1/4 x 5/8 6061 Aluminum Flat Bar	4
3	U-Channel	0.25 (1/4) thick 6061-T651 Aluminum Plate	2
4	Front Plate	0.25 (1/4) thick 6061-T651 Aluminum Plate	1
5	Back Plate	0.25 (1/4) thick 6061-T651 Aluminum Plate	1
6	The Floor	0.25 (1/4) thick 6061-T651 Aluminum Plate	2
7	Top Plate	0.25 (1/4) thick 6061-T651 Aluminum Plate	1

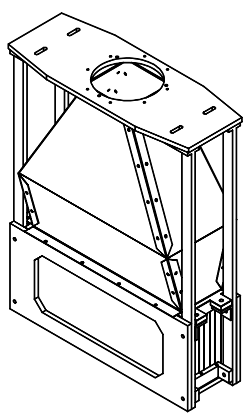

UNLESS OTHERWISE SPECIFIED:
DIMENSIONS ARE IN INCHES
TOLERANCES:
FRACTIONAL ±
ANGULAR: MACH ± BEND ±
TWO PLACE DECIMAL ±
THREE PLACE DECIMAL ±

INTERPRET GEOMETRIC TOLERANCING PER:

MATERIAL

FINISH

DO NOT SCALE DRAWING

	NAME	DATE
DRAWN	DKS	1/13/2018
CHECKED		
ENG APPR.		
MFG APPR.		
Q.A.		

COMMENTS:

Moller Collaboration

TITLE:

Bill of Materials

SIZE A | DWG. NO. III | REV 0

SCALE: 1:8 | WEIGHT: | SHEET 3 OF 11

2 1

B B

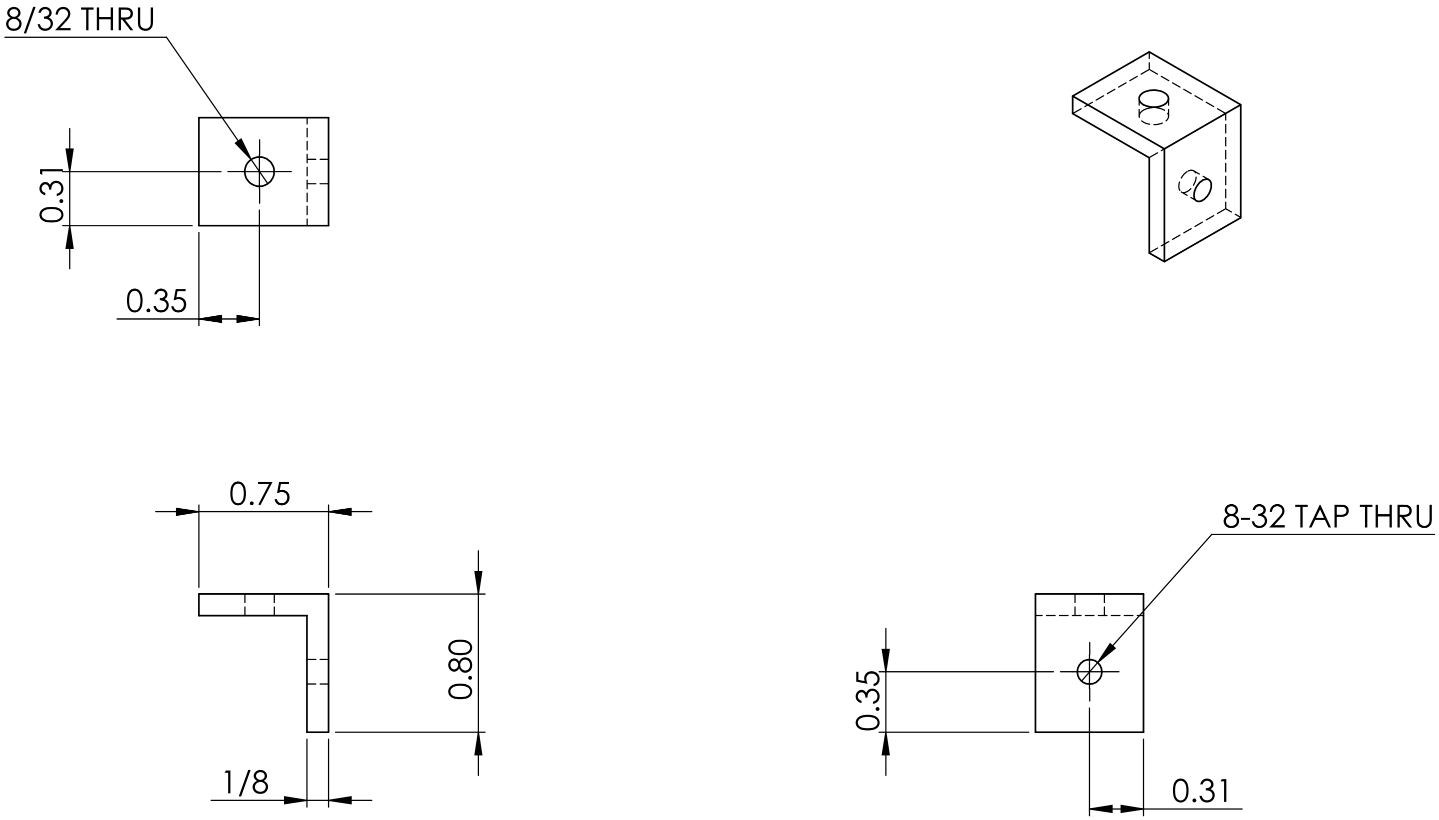

A A

UNLESS OTHERWISE SPECIFIED:		NAME	DATE	Moller Collaboration		
DIMENSIONS ARE IN INCHES TOLERANCES: FRACTIONAL ± ANGULAR: MACH ± BEND ± TWO PLACE DECIMAL ± THREE PLACE DECIMAL ±	DRAWN	DKS	1/11/2018	TITLE: Clamp Adapter		
	CHECKED					
	ENG APPR.					
	MFG APPR.					
INTERPRET GEOMETRIC TOLERANCING PER:	Q.A.					
MATERIAL 6061 Aluminum	COMMENTS:			SIZE A	DWG. NO. 1	REV 0
FINISH DO NOT SCALE DRAWING				SCALE: 1:1	WEIGHT:	SHEET 4 OF 11

2 1

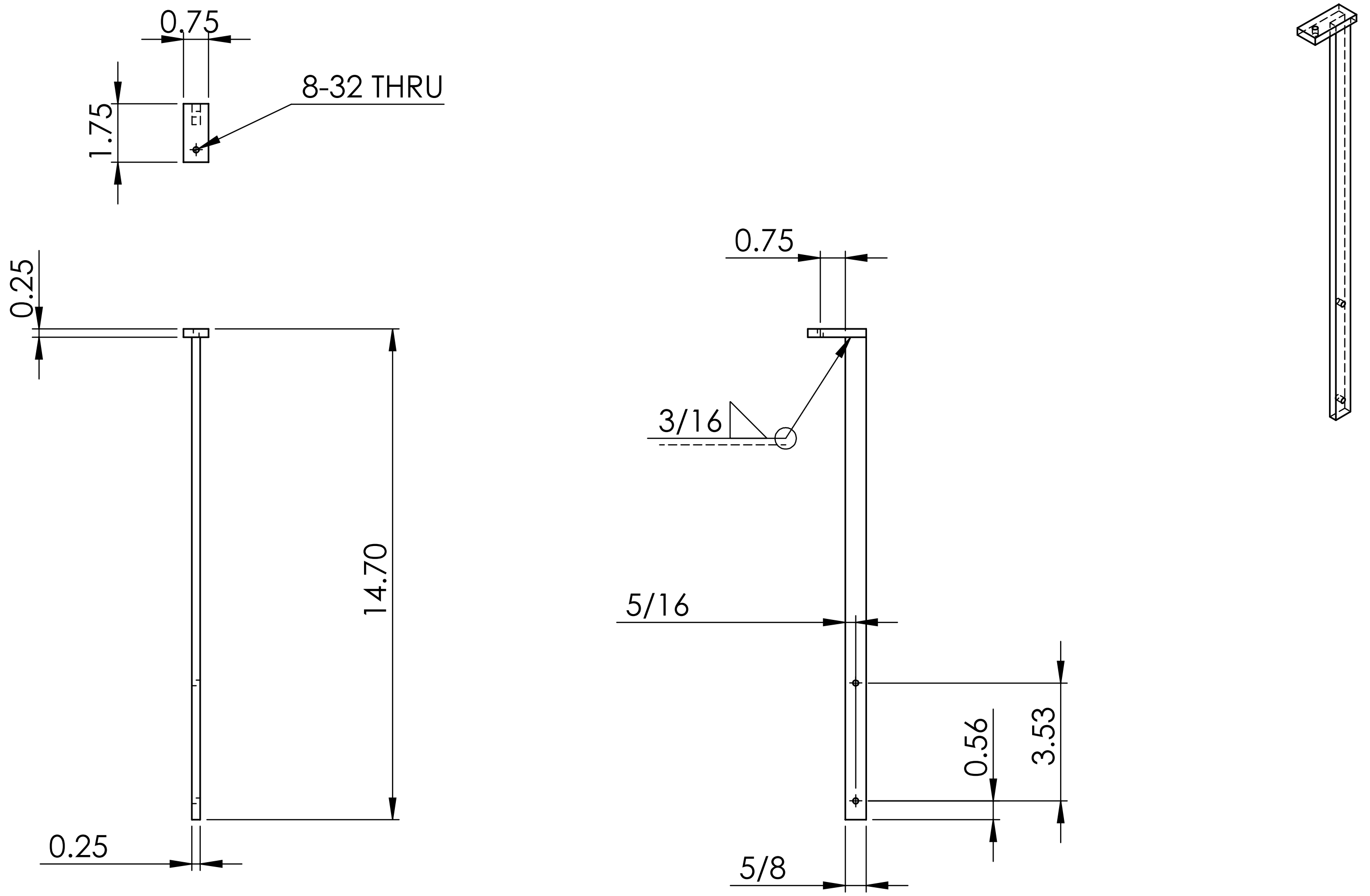

UNLESS OTHERWISE SPECIFIED:		NAME	DATE	Moller Collaboration
DIMENSIONS ARE IN INCHES TOLERANCES: FRACTIONAL ± ANGULAR: MACH ± BEND ± TWO PLACE DECIMAL ± THREE PLACE DECIMAL ±	DRAWN	DKS	1/10/2018	TITLE: Struts
	CHECKED			
	ENG APPR.			
	MFG APPR.			
INTERPRET GEOMETRIC TOLERANCING PER:	Q.A.			
MATERIAL 6061 Aluminum Flat	COMMENTS:			SIZE A · DWG. NO. 2 · REV 0
FINISH DO NOT SCALE DRAWING				SCALE: 1:5 · WEIGHT: · SHEET 5 OF 11

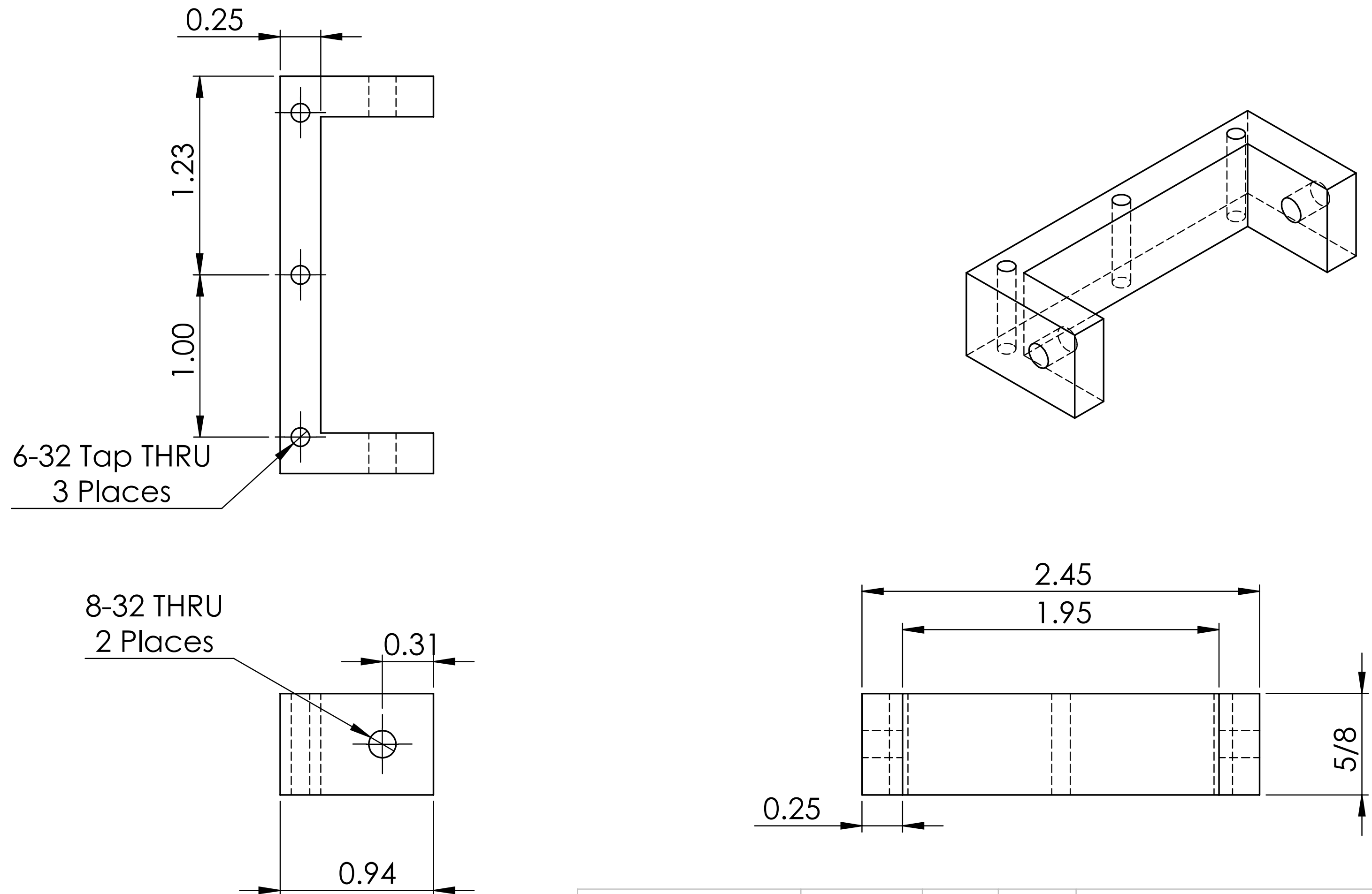

UNLESS OTHERWISE SPECIFIED:		NAME	DATE
DIMENSIONS ARE IN INCHES TOLERANCES: FRACTIONAL ± ANGULAR: MACH ± BEND ± TWO PLACE DECIMAL ± THREE PLACE DECIMAL ±	DRAWN	DKS	1/11/2018
	CHECKED		
	ENG APPR.		
	MFG APPR.		
INTERPRET GEOMETRIC TOLERANCING PER:	Q.A.		
MATERIAL 6061-T651 Aluminum Plate	COMMENTS:		
FINISH			
DO NOT SCALE DRAWING			

Moller Collaboration

TITLE:

U - Channel

SIZE	DWG. NO.	REV
A	3	0
SCALE: 1:1	WEIGHT:	SHEET 6 OF 11

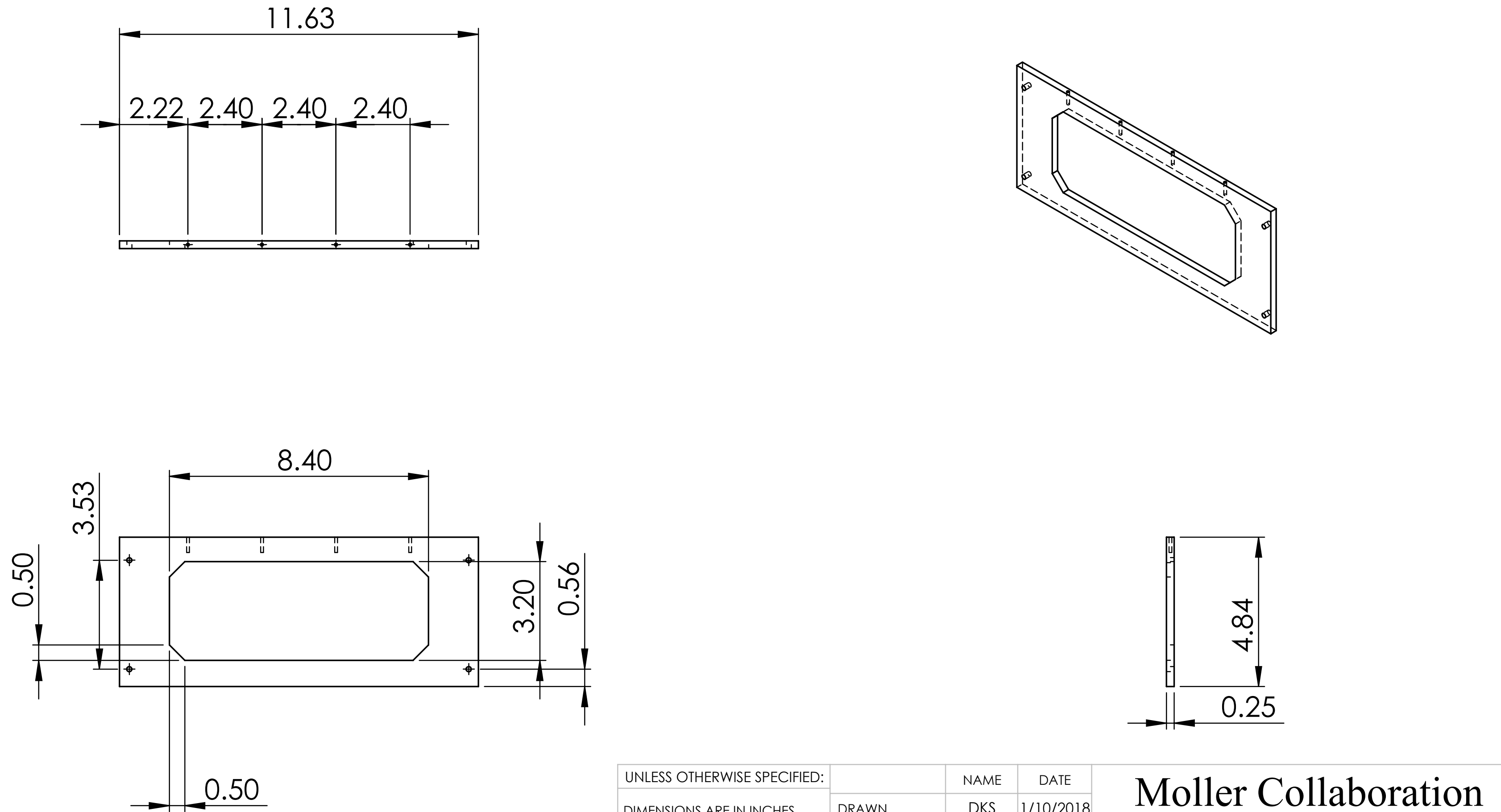

UNLESS OTHERWISE SPECIFIED:		NAME	DATE	Moller Collaboration
DIMENSIONS ARE IN INCHES TOLERANCES: FRACTIONAL ± ANGULAR: MACH ± BEND ± TWO PLACE DECIMAL ± THREE PLACE DECIMAL ±	DRAWN	DKS	1/10/2018	TITLE:
	CHECKED			Front Plate
	ENG APPR.			
	MFG APPR.			
INTERPRET GEOMETRIC TOLERANCING PER:	Q.A.			
MATERIAL 6061-T651 Aluminum Plate	COMMENTS:			SIZE A — DWG. NO. 4 — REV 0
FINISH				
DO NOT SCALE DRAWING				SCALE: 1:5 — WEIGHT: — SHEET 7 OF 11

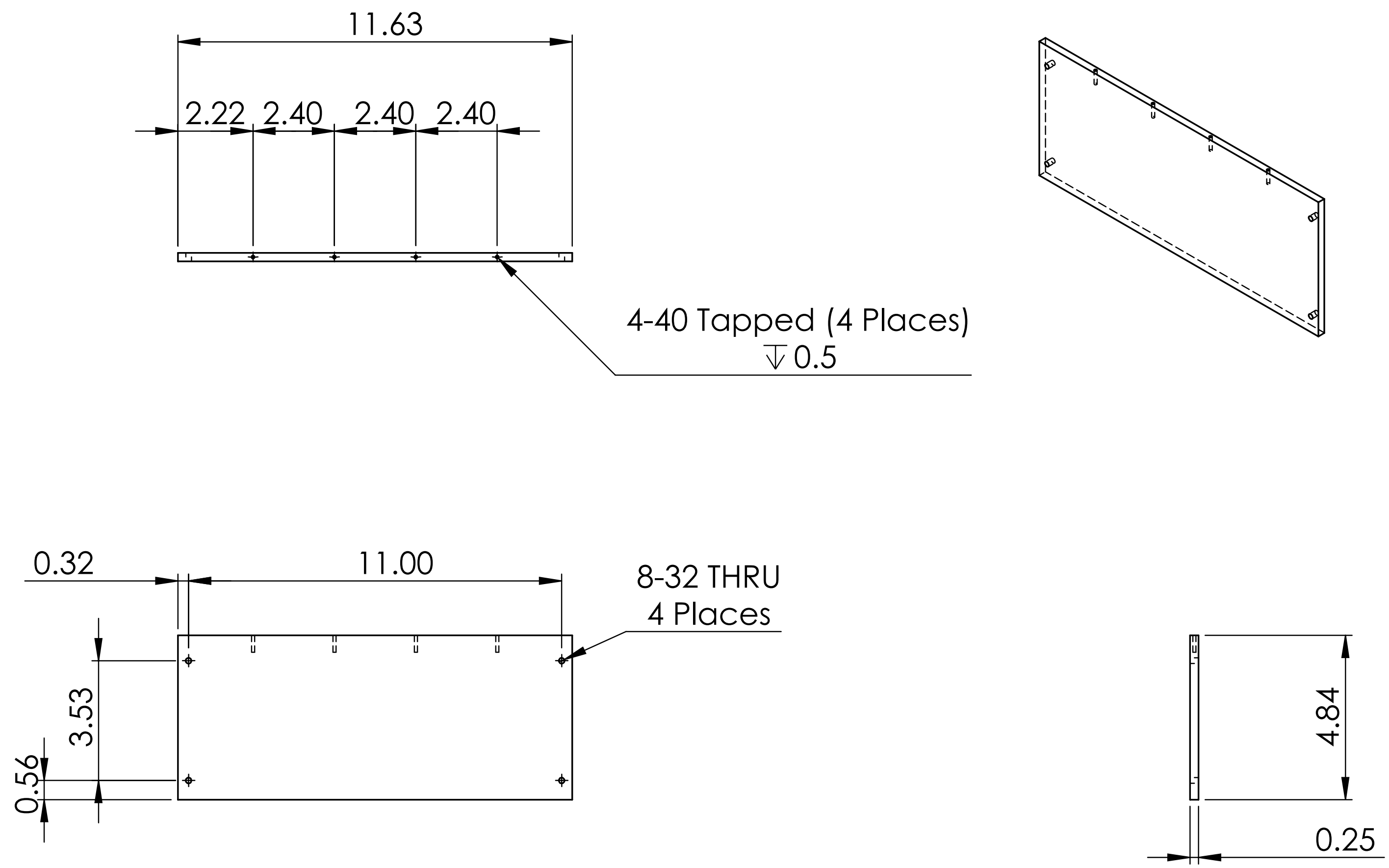

UNLESS OTHERWISE SPECIFIED:		NAME	DATE	Moller Collaboration
DIMENSIONS ARE IN INCHES TOLERANCES: FRACTIONAL ± ANGULAR: MACH ± BEND ± TWO PLACE DECIMAL ± THREE PLACE DECIMAL ±	DRAWN	DKS	1/18/2018	TITLE:
	CHECKED			Back Plate
	ENG APPR.			
	MFG APPR.			
INTERPRET GEOMETRIC TOLERANCING PER:	Q.A.			
MATERIAL 6061-T651 Aluminum Plate	COMMENTS:			SIZE A DWG. NO. 5 REV 0
FINISH DO NOT SCALE DRAWING				SCALE: 1:5 WEIGHT: SHEET 8 OF 11

2 1

B B

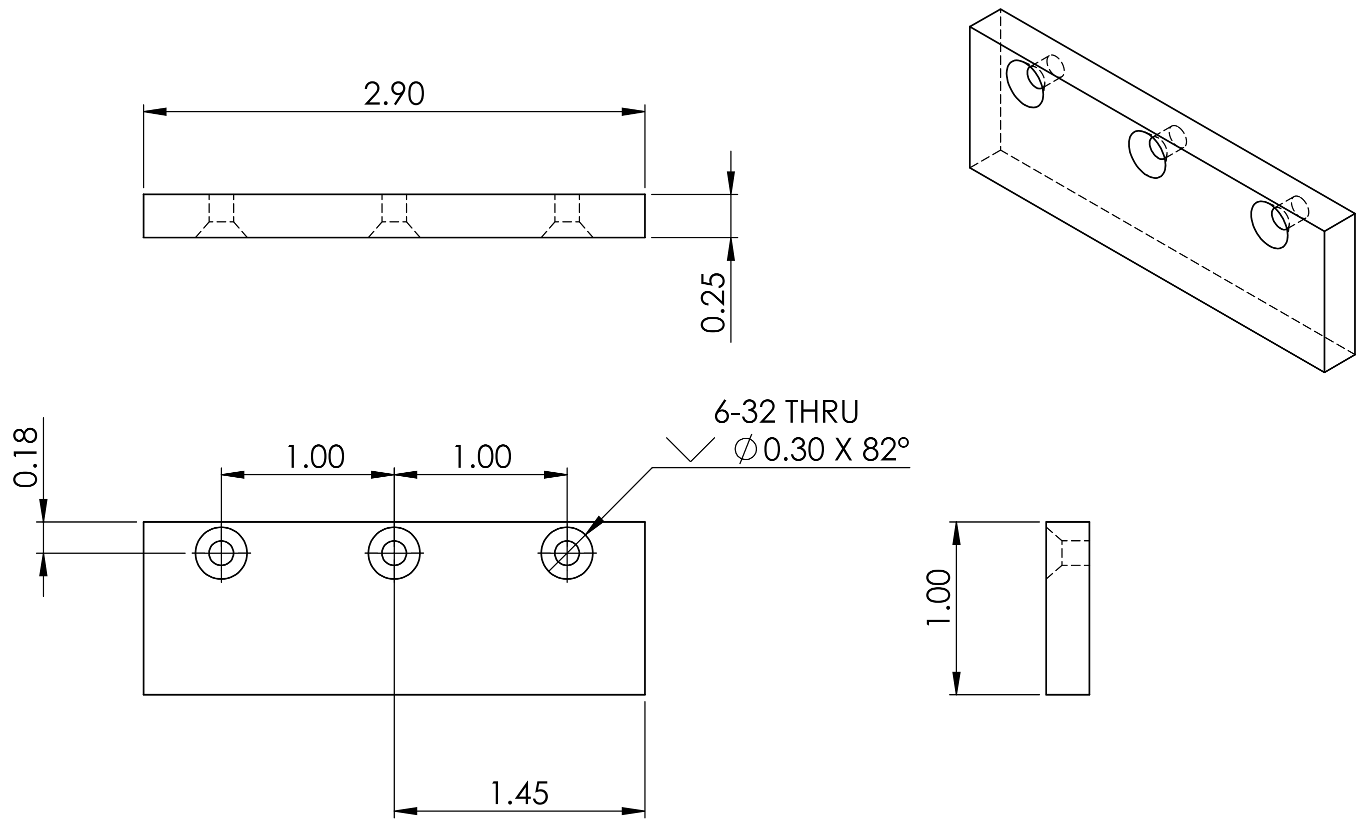

A A

UNLESS OTHERWISE SPECIFIED:		NAME	DATE	Moller Collaboration
DIMENSIONS ARE IN INCHES TOLERANCES: FRACTIONAL ± ANGULAR: MACH ± BEND ± TWO PLACE DECIMAL ± THREE PLACE DECIMAL ±	DRAWN	DKS	1/10/2018	TITLE:
	CHECKED			The Floor
	ENG APPR.			
	MFG APPR.			
	Q.A.			
INTERPRET GEOMETRIC TOLERANCING PER:	COMMENTS:			
MATERIAL 6061-T651 Aluminum Plate				SIZE A — DWG. NO. 6 — REV 0
FINISH				
DO NOT SCALE DRAWING				SCALE: 1:1 — WEIGHT: — SHEET 9 OF 11

2 1

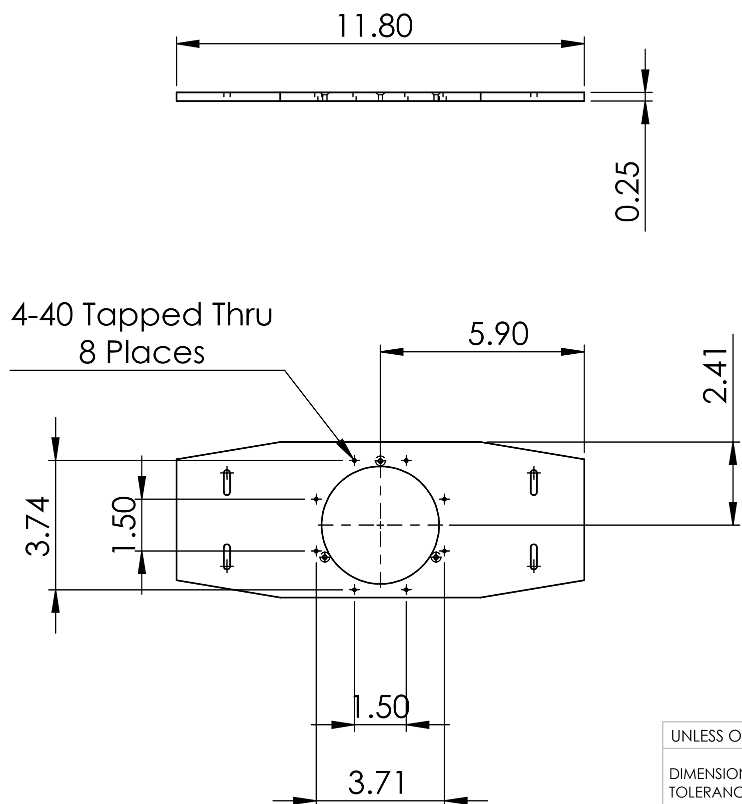

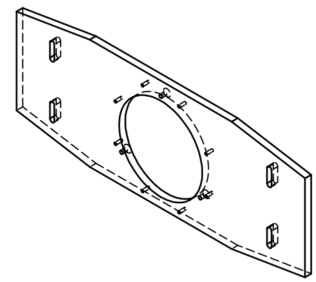

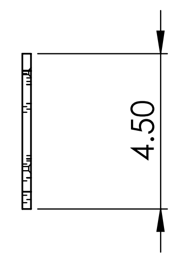

UNLESS OTHERWISE SPECIFIED:		NAME	DATE	Moller Collaboration
DIMENSIONS ARE IN INCHES TOLERANCES: FRACTIONAL ± ANGULAR: MACH ± BEND ± TWO PLACE DECIMAL ± THREE PLACE DECIMAL ±	DRAWN	DKS	1/10/2018	TITLE:
	CHECKED			Top Plate
	ENG APPR.			
	MFG APPR.			
INTERPRET GEOMETRIC TOLERANCING PER:	Q.A.			
MATERIAL 6061-T651 Aluminum Plate	COMMENTS:			SIZE A / DWG. NO. 7A / REV 0
FINISH DO NOT SCALE DRAWING				SCALE: 1:5 / WEIGHT: / SHEET 10 OF 1

Top   Bottom

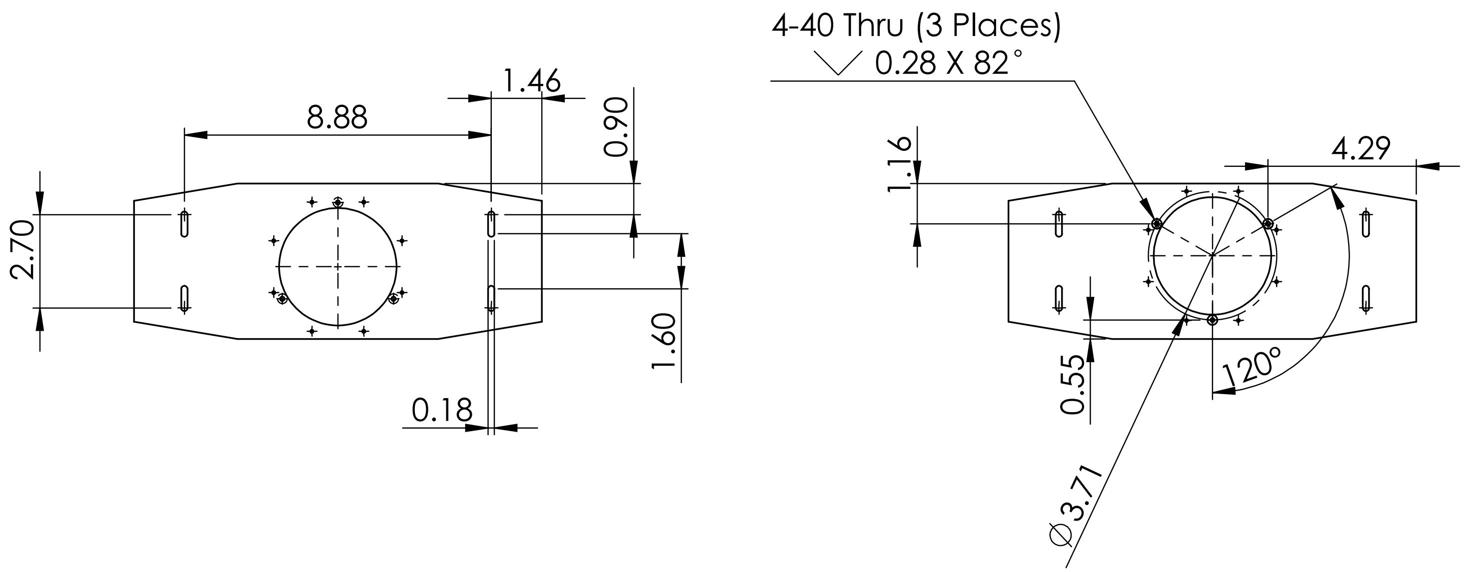

UNLESS OTHERWISE SPECIFIED:		NAME	DATE	Moller Collaboration
DIMENSIONS ARE IN INCHES TOLERANCES: FRACTIONAL ± ANGULAR: MACH ± BEND ± TWO PLACE DECIMAL ± THREE PLACE DECIMAL ±	DRAWN	DKS	1/10/2018	TITLE:
	CHECKED			Top Plate
	ENG APPR.			
	MFG APPR.			
INTERPRET GEOMETRIC TOLERANCING PER:	Q.A.			
MATERIAL 6061-T651 Aluminum Plate	COMMENTS:			SIZE A · DWG. NO. 7B · REV 0
FINISH DO NOT SCALE DRAWING				SCALE: 1:5 · WEIGHT: · SHEET 11 OF 1

2 1

B B

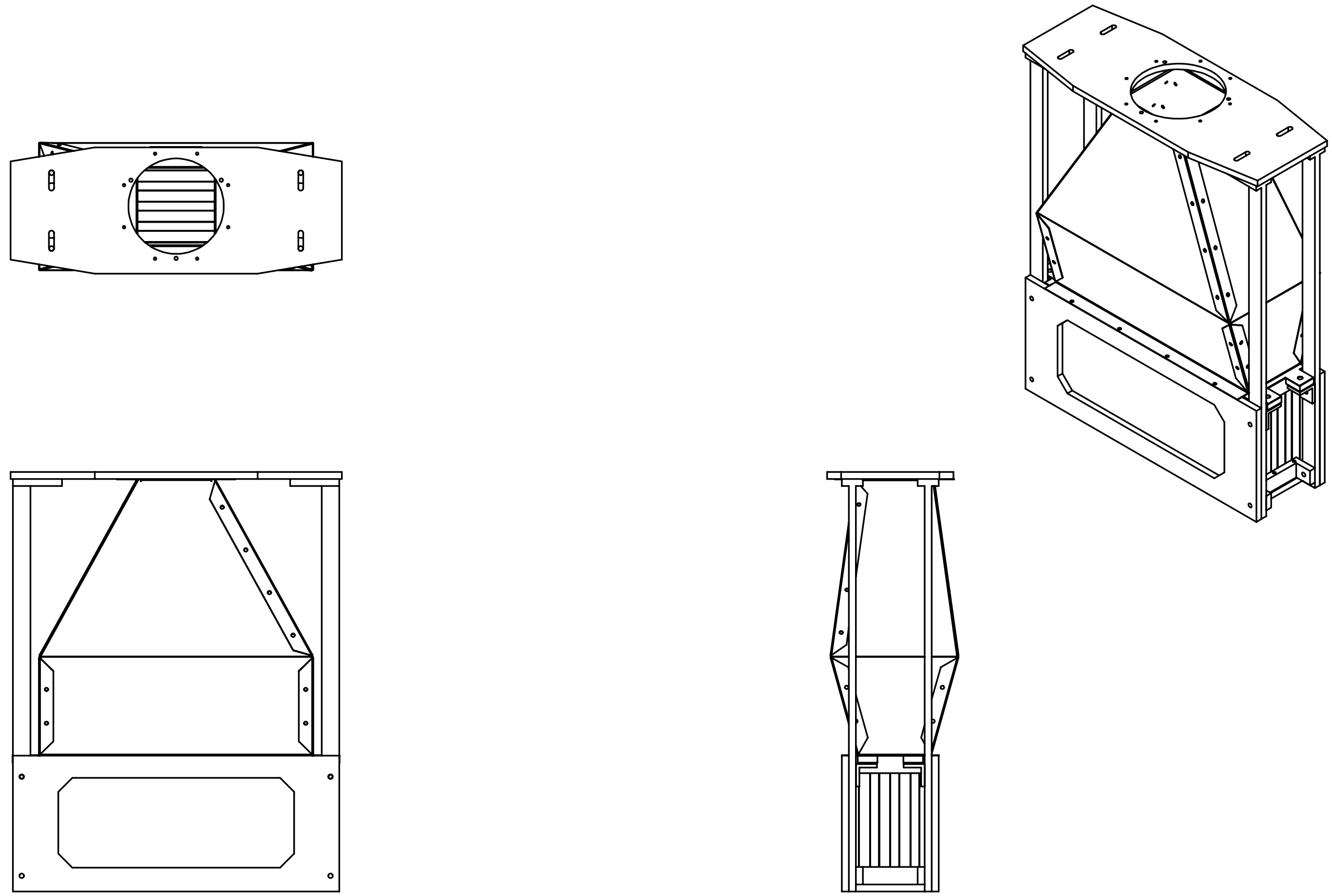

A A

UNLESS OTHERWISE SPECIFIED:		NAME	DATE
DIMENSIONS ARE IN INCHES TOLERANCES: FRACTIONAL ± ANGULAR: MACH ± BEND ± TWO PLACE DECIMAL ± THREE PLACE DECIMAL ±	DRAWN	DKS	1/13/2018
	CHECKED		
	ENG APPR.		
	MFG APPR.		
INTERPRET GEOMETRIC TOLERANCING PER:	Q.A.		
MATERIAL	COMMENTS:		
FINISH			
DO NOT SCALE DRAWING			

Moller Collaboration

TITLE:

ShowerMax Frame 1A

SIZE	DWG. NO.	REV
A	1	0

SCALE: 1:6 WEIGHT: SHEET 1 OF 11

2 1

2 | 1

ITEM NO.	PART	MATERIAL	QTY.
1	Light Guide - Back	0.020 ANOLUX MIRO-SILVER REFLECTIVE ALUMINIUM SHEET	1
2	Light Guide - Front	0.020 ANOLUX MIRO-SILVER REFLECTIVE ALUMINIUM SHEET	1
3	Long Flap	0.020 ANOLUX MIRO-SILVER REFLECTIVE ALUMINIUM SHEET	2
4	Short Flap	0.020 ANOLUX MIRO-SILVER REFLECTIVE ALUMINIUM SHEET	4
5	Suitcase	0.020 ANOLUX MIRO-SILVER REFLECTIVE ALUMINIUM SHEET	2
6	LG Back - Config 1B	0.020 ANOLUX MIRO-SILVER REFLECTIVE ALUMINIUM SHEET	1
7	LG Front - Config 1B	0.020 ANOLUX MIRO-SILVER REFLECTIVE ALUMINIUM SHEET	1
8	Long Flap - Config 1B	0.020 ANOLUX MIRO-SILVER REFLECTIVE ALUMINIUM SHEET	2
9	Short Flap - Config 1B	0.020 ANOLUX MIRO-SILVER REFLECTIVE ALUMINIUM SHEET	4
10	Suitcase - Config 1B	0.020 ANOLUX MIRO-SILVER REFLECTIVE ALUMINIUM SHEET	2

B | B

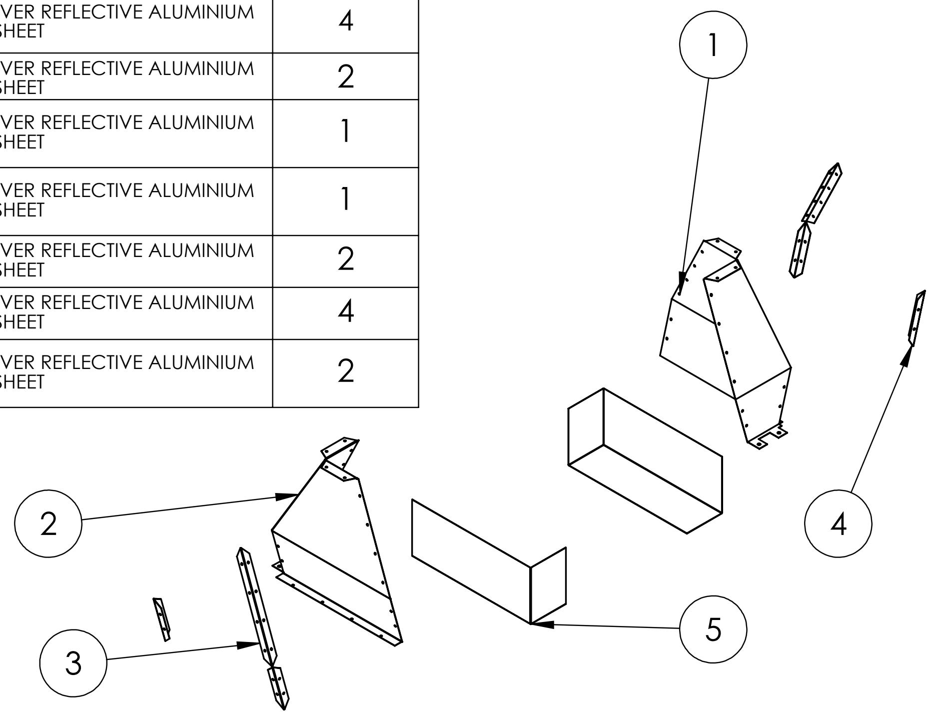

A | A

UNLESS OTHERWISE SPECIFIED:		NAME	DATE
DIMENSIONS ARE IN INCHES TOLERANCES: FRACTIONAL ± ANGULAR: MACH ± BEND ± TWO PLACE DECIMAL ± THREE PLACE DECIMAL ±	DRAWN	DKS	1/16/18
	CHECKED		
	ENG APPR.		
	MFG APPR.		
INTERPRET GEOMETRIC TOLERANCING PER:	Q.A.		
MATERIAL 0.020 ANOLUX MIRO-SILVER REFLECTIVE ALUMINIUM SHEET	COMMENTS:		

Moller Collaboration

TITLE:

Exploded View

SIZE	DWG. NO.	REV
A	II	0

SCALE: 1:10 WEIGHT: SHEET 2 OF 16

2 | 1

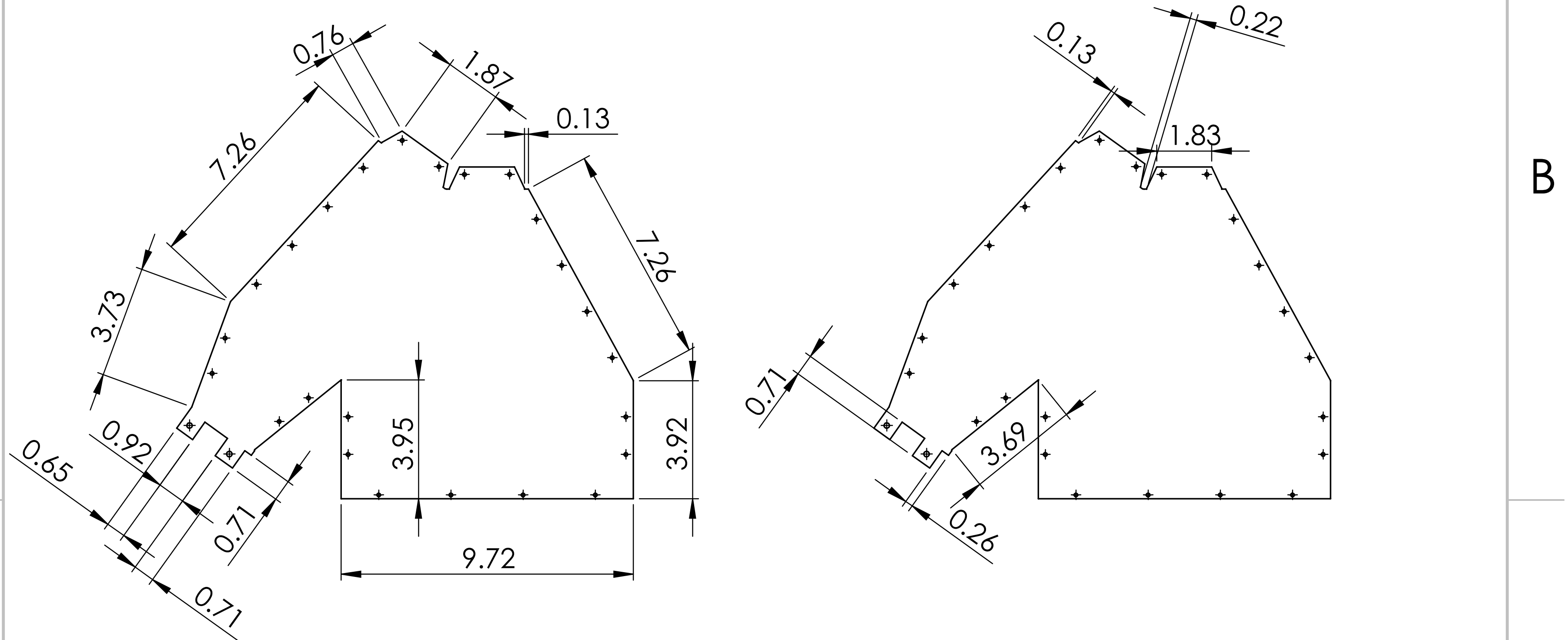

UNLESS OTHERWISE SPECIFIED:

DIMENSIONS ARE IN INCHES
TOLERANCES:
FRACTIONAL ±
ANGULAR: MACH ± BEND ±
TWO PLACE DECIMAL ±
THREE PLACE DECIMAL ±

INTERPRET GEOMETRIC TOLERANCING PER:

MATERIAL
0.020 ANOLUX
MIRO-SILVER REFLECTIVE
ALUMINIUM SHEET

	NAME	DATE
DRAWN	DKS	1/16/18
CHECKED		
ENG APPR.		
MFG APPR.		
Q.A.		
COMMENTS:		

Moller Collaboration

TITLE:
Light Guide Back

SIZE A | DWG. NO. 1A | REV 0

SCALE: 1:5 | WEIGHT: | SHEET 3 OF 16

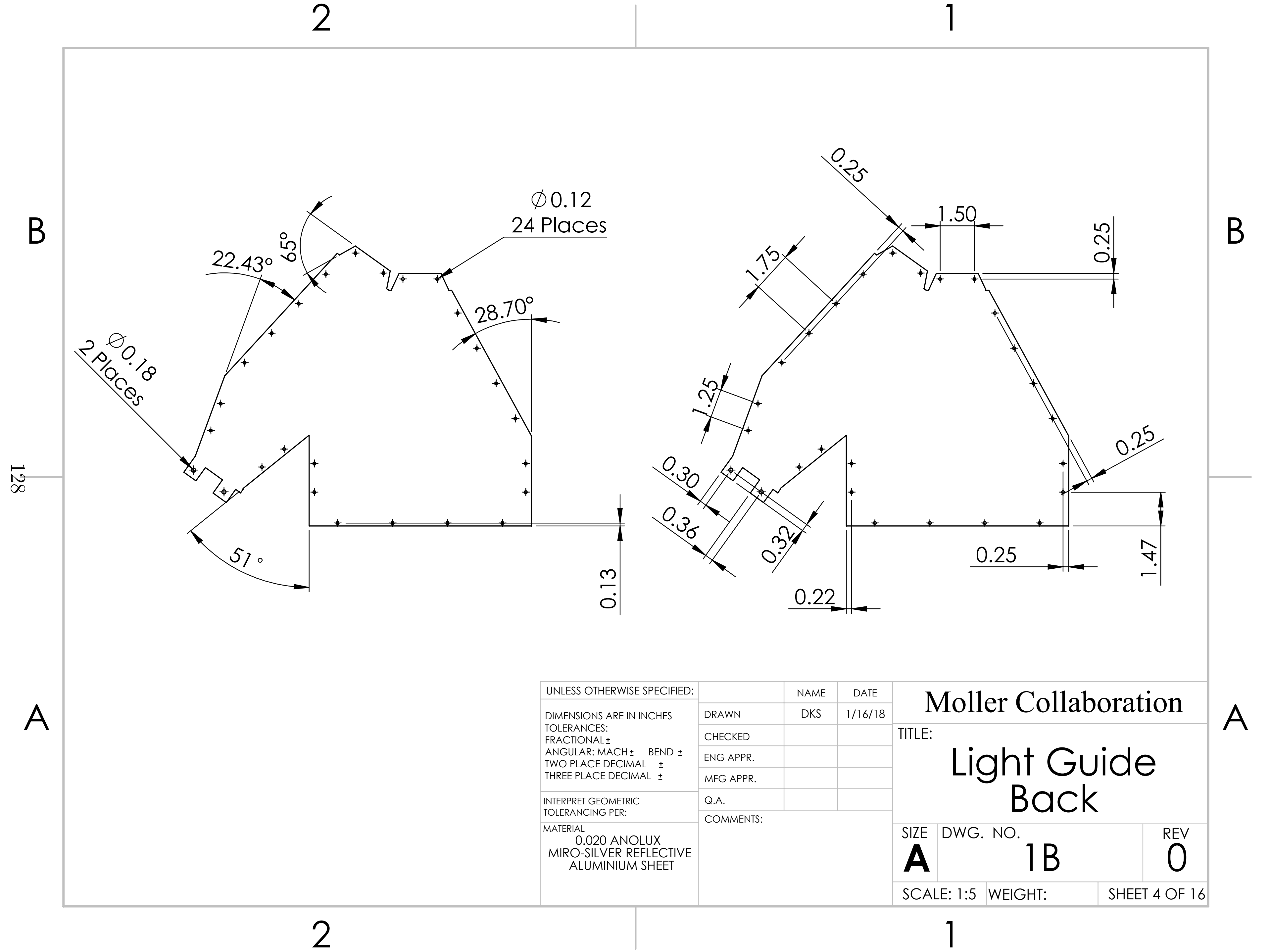

128

UNLESS OTHERWISE SPECIFIED:		NAME	DATE
DIMENSIONS ARE IN INCHES TOLERANCES: FRACTIONAL ± ANGULAR: MACH ± BEND ± TWO PLACE DECIMAL ± THREE PLACE DECIMAL ±	DRAWN	DKS	1/16/18
	CHECKED		
	ENG APPR.		
	MFG APPR.		
INTERPRET GEOMETRIC TOLERANCING PER:	Q.A.		
MATERIAL 0.020 ANOLUX MIRO-SILVER REFLECTIVE ALUMINIUM SHEET	COMMENTS:		

Moller Collaboration

TITLE:

Light Guide Back

SIZE	DWG. NO.	REV
A	1B	0
SCALE: 1:5	WEIGHT:	SHEET 4 OF 16

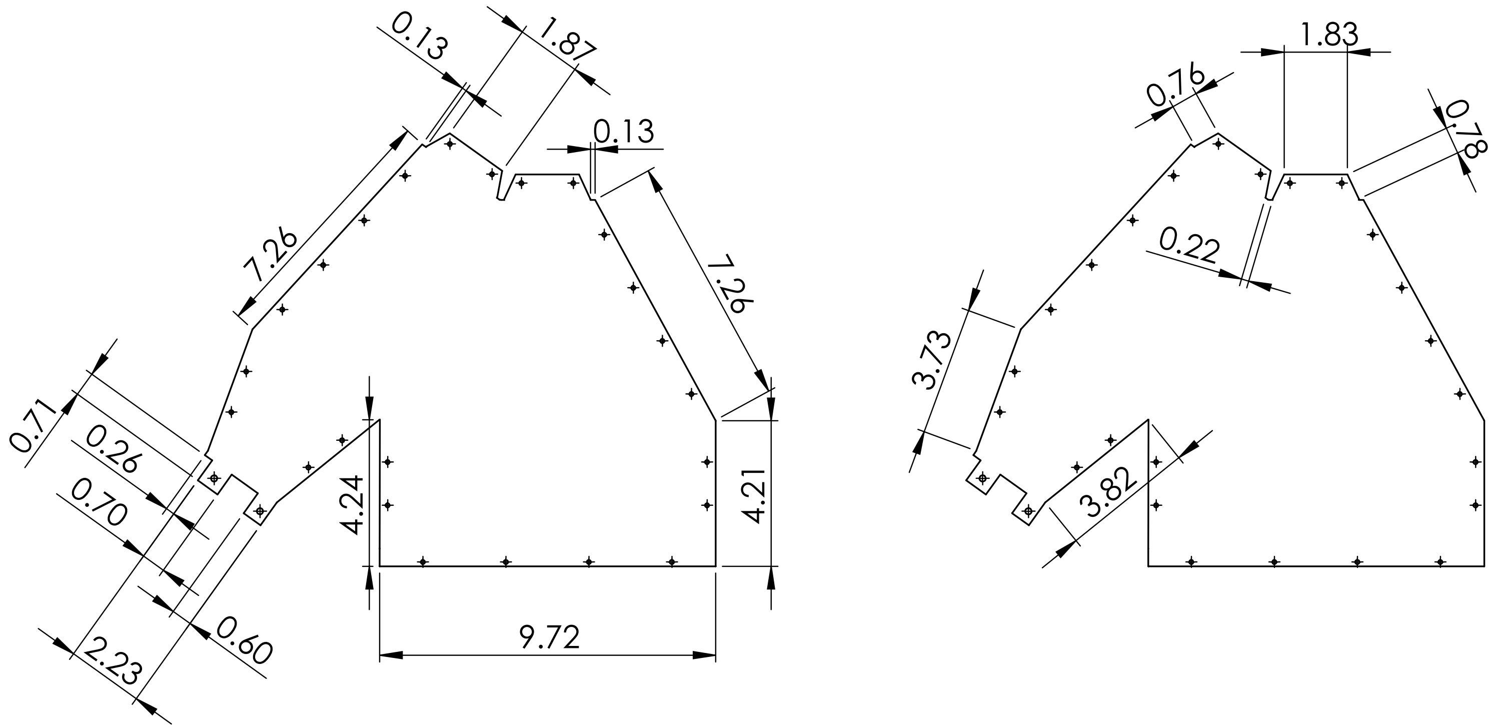

UNLESS OTHERWISE SPECIFIED:		NAME	DATE	Moller Collaboration
DIMENSIONS ARE IN INCHES TOLERANCES: FRACTIONAL± ANGULAR: MACH± BEND ± TWO PLACE DECIMAL ± THREE PLACE DECIMAL ±	DRAWN	DKS	1/14/2018	TITLE:
	CHECKED			Light Guide Front
	ENG APPR.			
	MFG APPR.			
INTERPRET GEOMETRIC TOLERANCING PER:	Q.A.			
MATERIAL 0.020 ANOLUX MIRO-SILVER REFLECTIVE ALUMINIUM SHEET	COMMENTS:			SIZE A · DWG. NO. 2A · REV 0
				SCALE: 1:5 · WEIGHT: · SHEET 5 OF 16

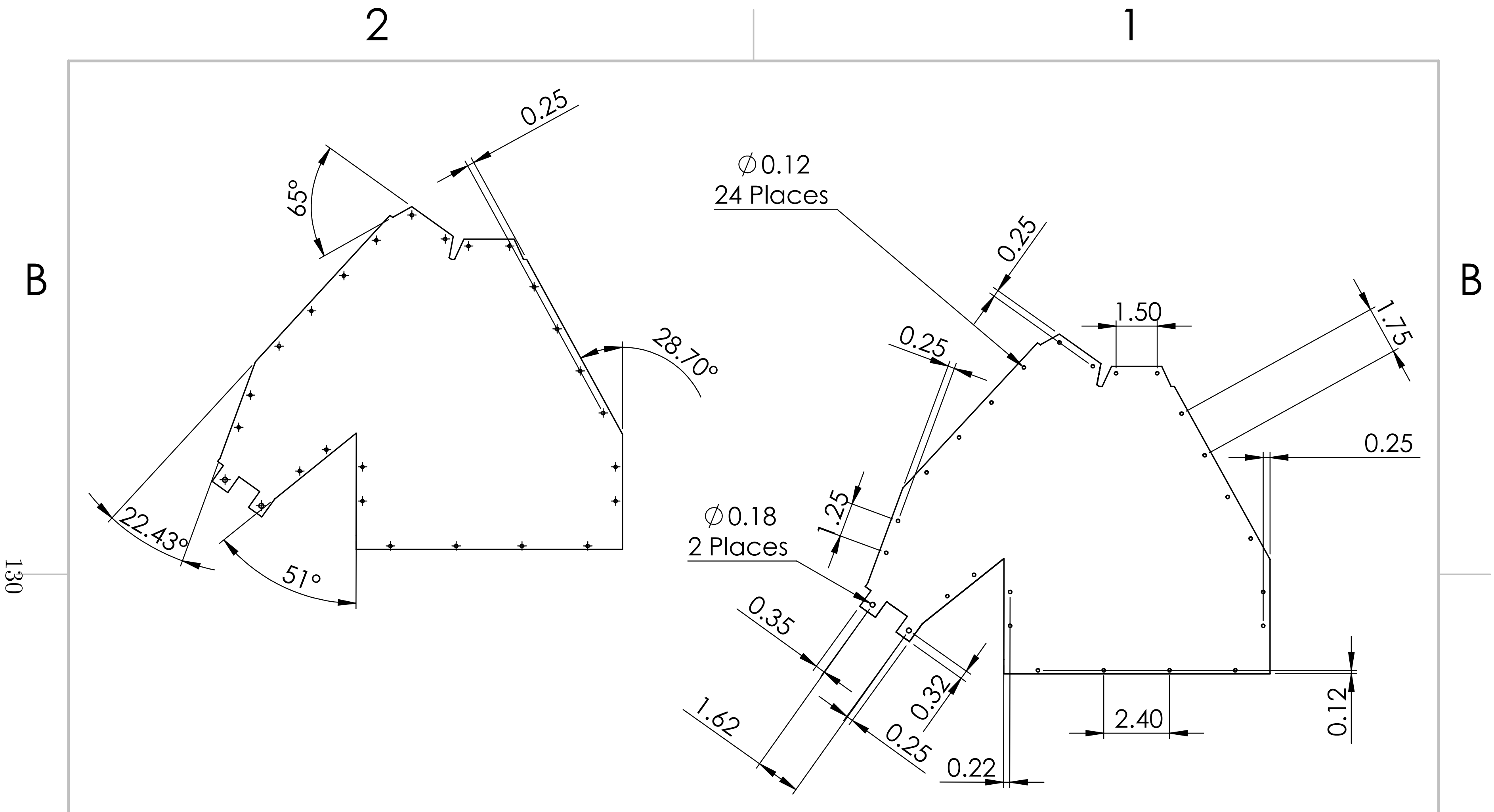

UNLESS OTHERWISE SPECIFIED:		NAME	DATE	Moller Collaboration
DIMENSIONS ARE IN INCHES TOLERANCES: FRACTIONAL ± ANGULAR: MACH ± BEND ± TWO PLACE DECIMAL ± THREE PLACE DECIMAL ±	DRAWN	DKS	1/16/18	TITLE:
	CHECKED			Light Guide Front
	ENG APPR.			
	MFG APPR.			
INTERPRET GEOMETRIC TOLERANCING PER:	Q.A.			
MATERIAL 0.020 ANOLUX MIRO-SILVER REFLECTIVE ALUMINIUM SHEET	COMMENTS:			SIZE A — DWG. NO. 2B — REV 0
				SCALE: 1:5 — WEIGHT: — SHEET 6 OF 16

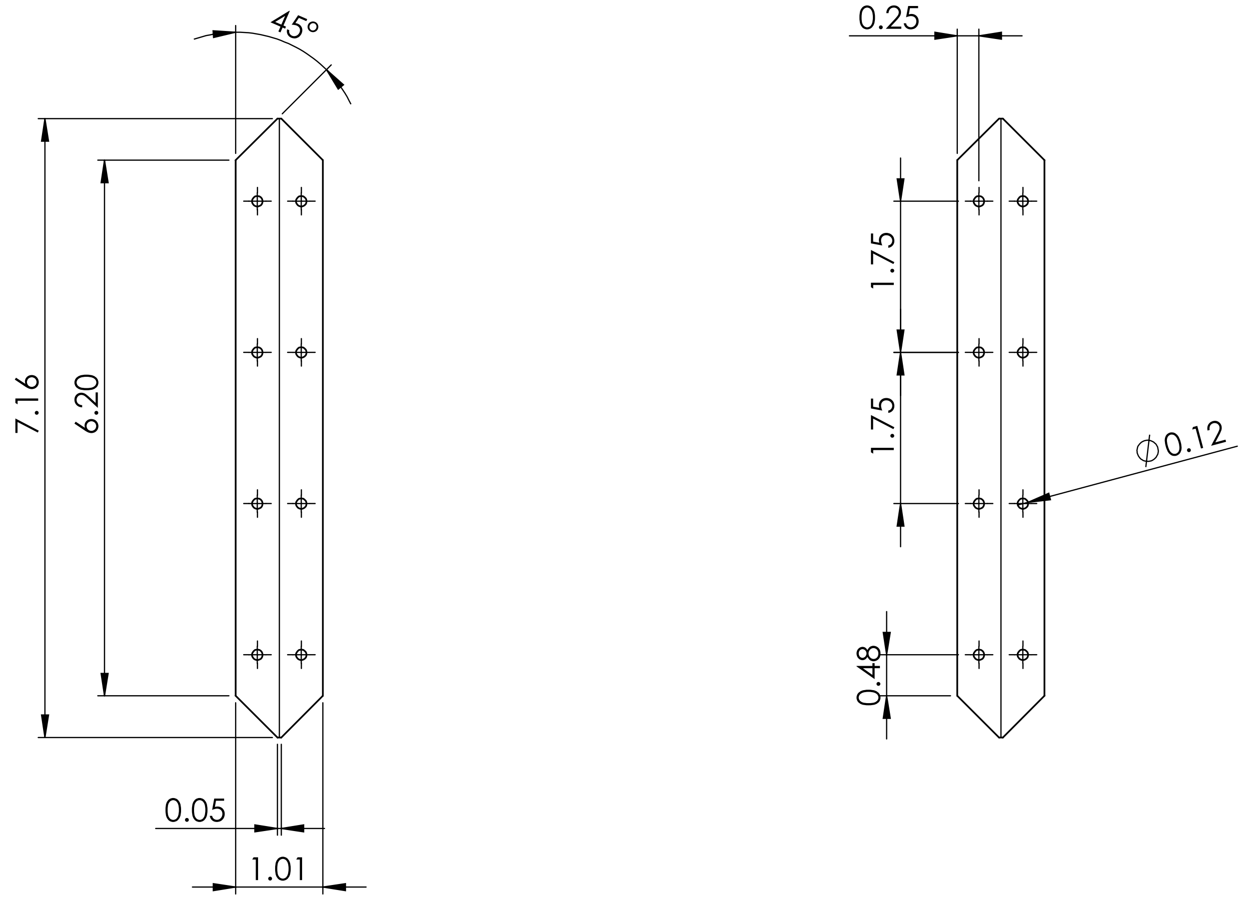

UNLESS OTHERWISE SPECIFIED:		NAME	DATE	Moller Collaboration
DIMENSIONS ARE IN INCHES TOLERANCES: FRACTIONAL ± ANGULAR: MACH ± BEND ± TWO PLACE DECIMAL ± THREE PLACE DECIMAL ±	DRAWN	DKS	1/16/18	TITLE:
	CHECKED			Long Flap
	ENG APPR.			
	MFG APPR.			
INTERPRET GEOMETRIC TOLERANCING PER:	Q.A.			
MATERIAL 0.020 ANOLUX MIRO-SILVER REFLECTIVE ALUMINIUM SHEET	COMMENTS:			SIZE A DWG. NO. 3 REV 0
				SCALE: 1:2 WEIGHT: SHEET 7 OF 16

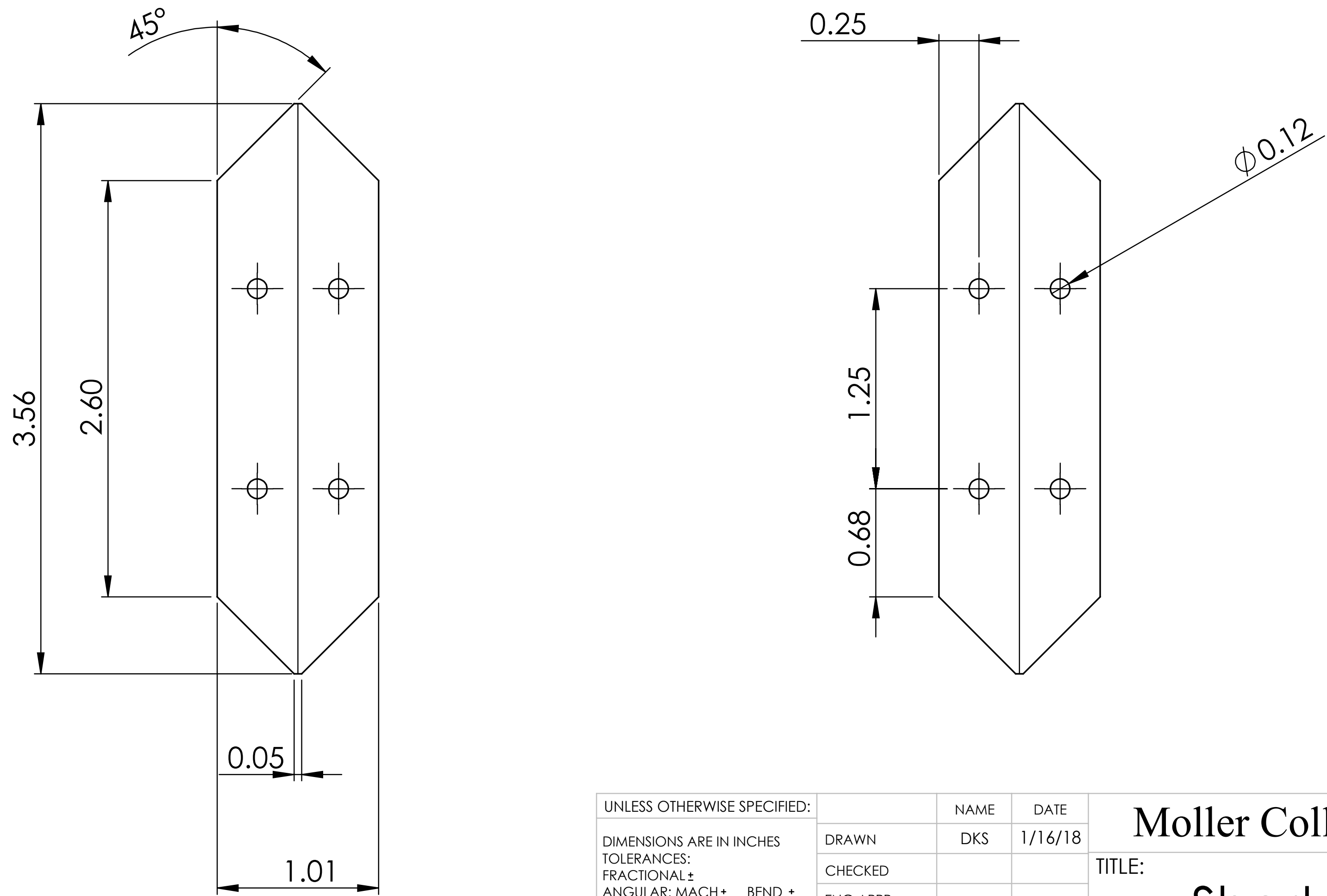

UNLESS OTHERWISE SPECIFIED:		NAME	DATE	Moller Collaboration
DIMENSIONS ARE IN INCHES TOLERANCES: FRACTIONAL ± ANGULAR: MACH ± BEND ± TWO PLACE DECIMAL ± THREE PLACE DECIMAL ±	DRAWN	DKS	1/16/18	TITLE:
	CHECKED			Short Flap
	ENG APPR.			
	MFG APPR.			
INTERPRET GEOMETRIC TOLERANCING PER:	Q.A.			
MATERIAL 0.020 ANOLUX MIRO-SILVER REFLECTIVE ALUMINIUM SHEET	COMMENTS:			SIZE A · DWG. NO. 4 · REV 0
				SCALE: 1:1 · WEIGHT: · SHEET 8 OF 16

Flat Sheet

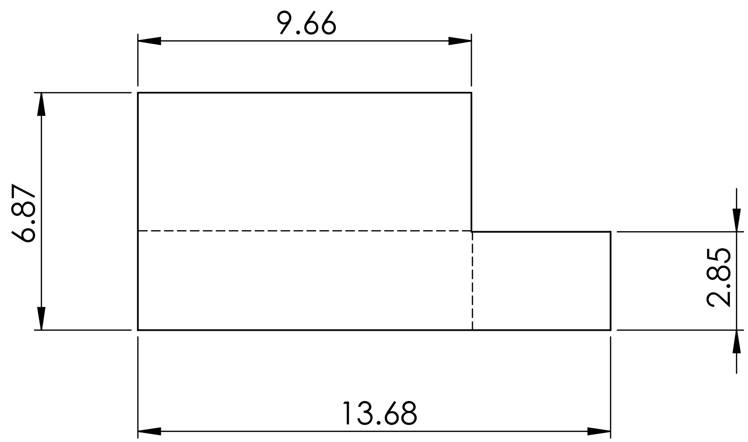

Folded

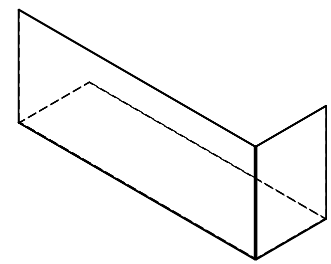

UNLESS OTHERWISE SPECIFIED:		NAME	DATE	Moller Collaboration
DIMENSIONS ARE IN INCHES TOLERANCES: FRACTIONAL ± ANGULAR: MACH ± BEND ± TWO PLACE DECIMAL ± THREE PLACE DECIMAL ±	DRAWN	DKS	1/11/2018	TITLE: Suitcase
	CHECKED			
	ENG APPR.			
	MFG APPR.			
INTERPRET GEOMETRIC TOLERANCING PER:	Q.A.			
MATERIAL 0.020 ANOLUX MIRO-SILVER REFLECTIVE ALUMINIUM SHEET	COMMENTS:			SIZE A · DWG. NO. 5 · REV 0
				SCALE: 1:5 · WEIGHT: · SHEET 9 OF 16

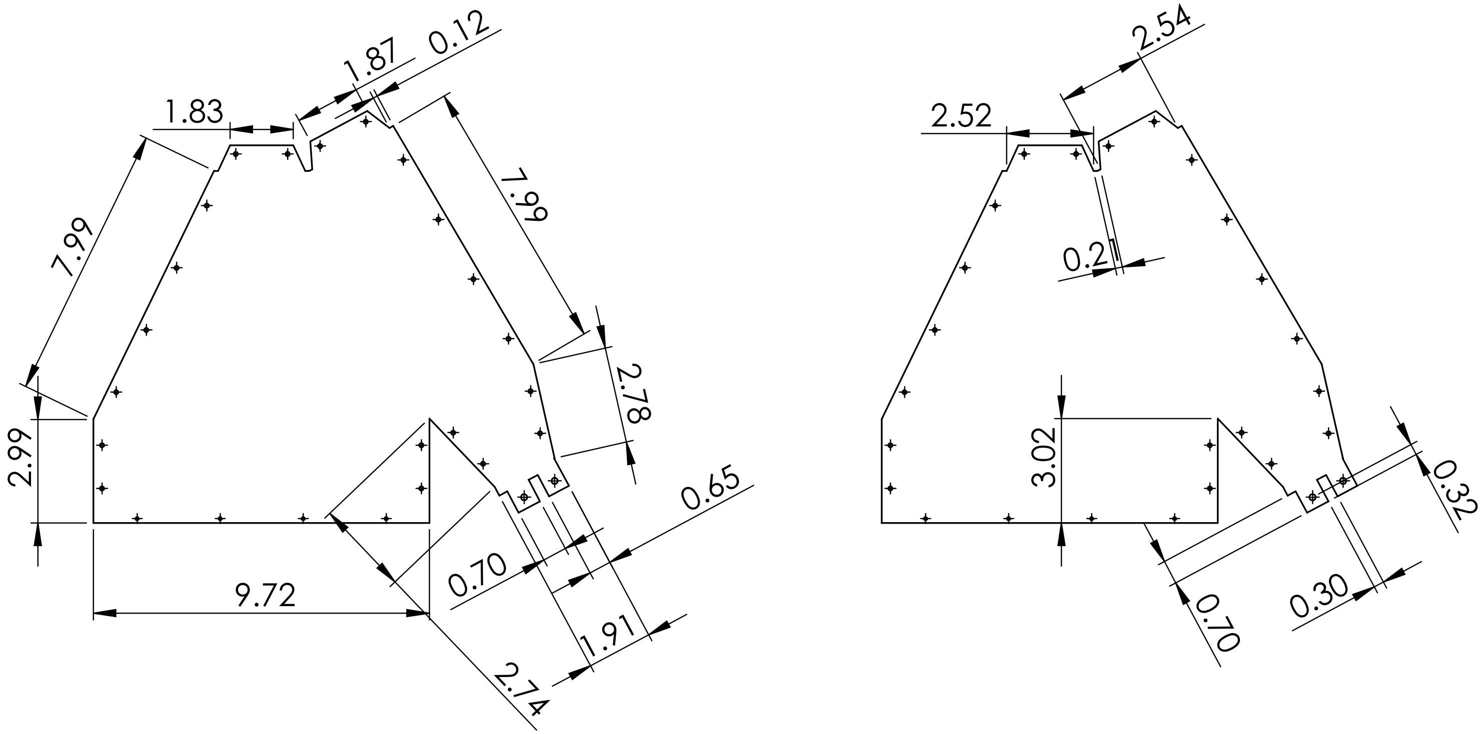

UNLESS OTHERWISE SPECIFIED:		NAME	DATE
DIMENSIONS ARE IN INCHES TOLERANCES: FRACTIONAL ± ANGULAR: MACH ± BEND ± TWO PLACE DECIMAL ± THREE PLACE DECIMAL ±	DRAWN	DKS	2/6/18
	CHECKED		
	ENG APPR.		
	MFG APPR.		
INTERPRET GEOMETRIC TOLERANCING PER:	Q.A.		
MATERIAL 0.020 ANOLUX MIRO-SILVER REFLECTIVE ALUMINIUM SHEET	COMMENTS:		

Moller Collaboration

TITLE:

LG Back Config 1B

SIZE	DWG. NO.	REV
A	6A	0

SCALE: 1:5 WEIGHT: SHEET 10 OF 16

135

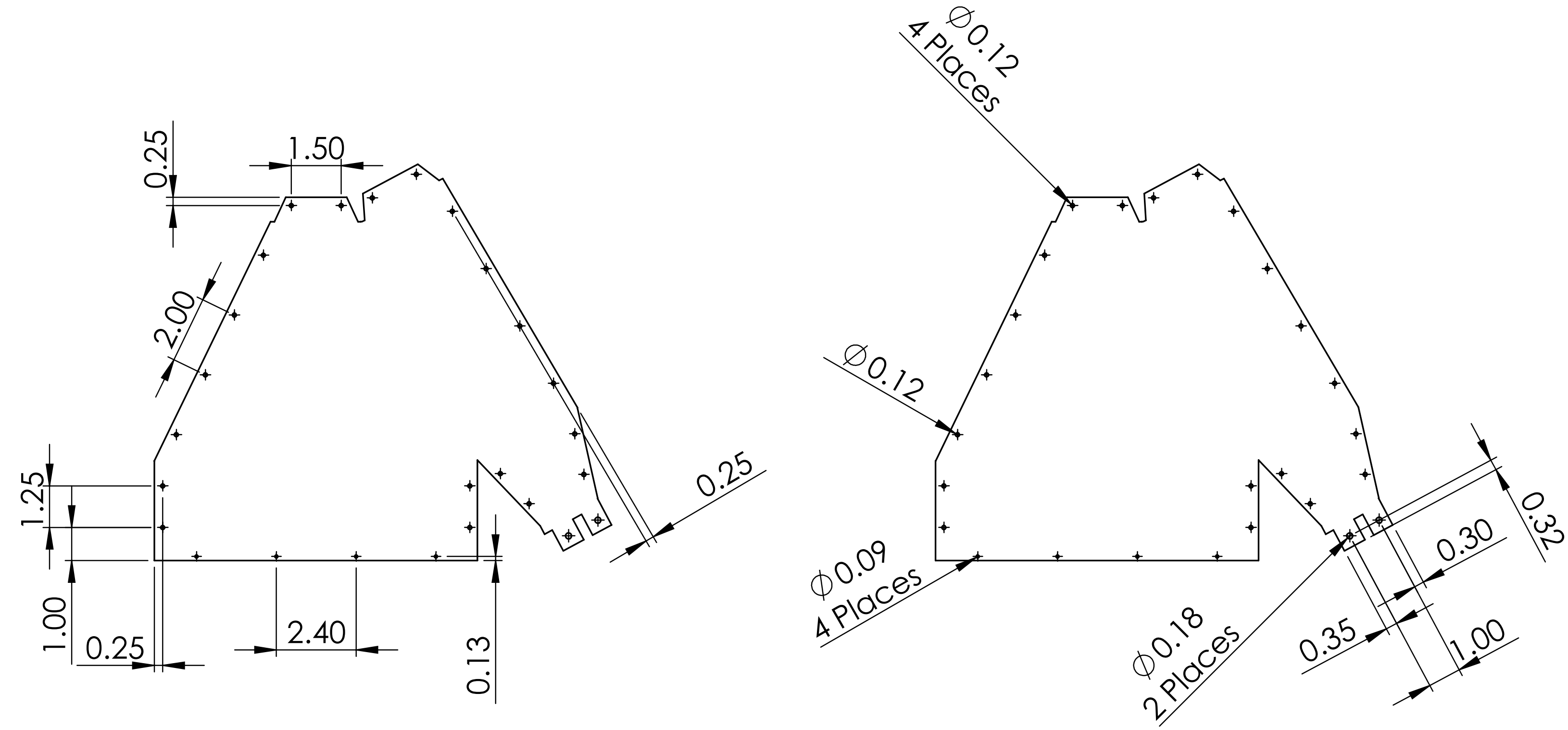

UNLESS OTHERWISE SPECIFIED:		NAME	DATE
DIMENSIONS ARE IN INCHES TOLERANCES: FRACTIONAL± ANGULAR: MACH± BEND ± TWO PLACE DECIMAL ± THREE PLACE DECIMAL ±	DRAWN	DKS	2/6/18
	CHECKED		
	ENG APPR.		
	MFG APPR.		
INTERPRET GEOMETRIC TOLERANCING PER:	Q.A.		
MATERIAL 0.020 ANOLUX MIRO-SILVER REFLECTIVE ALUMINIUM SHEET	COMMENTS:		

Moller Collaboration

TITLE:

LG Back Config 1B

SIZE	DWG. NO.	REV
A	6B	0

SCALE: 1:5 WEIGHT: SHEET 11 OF 16

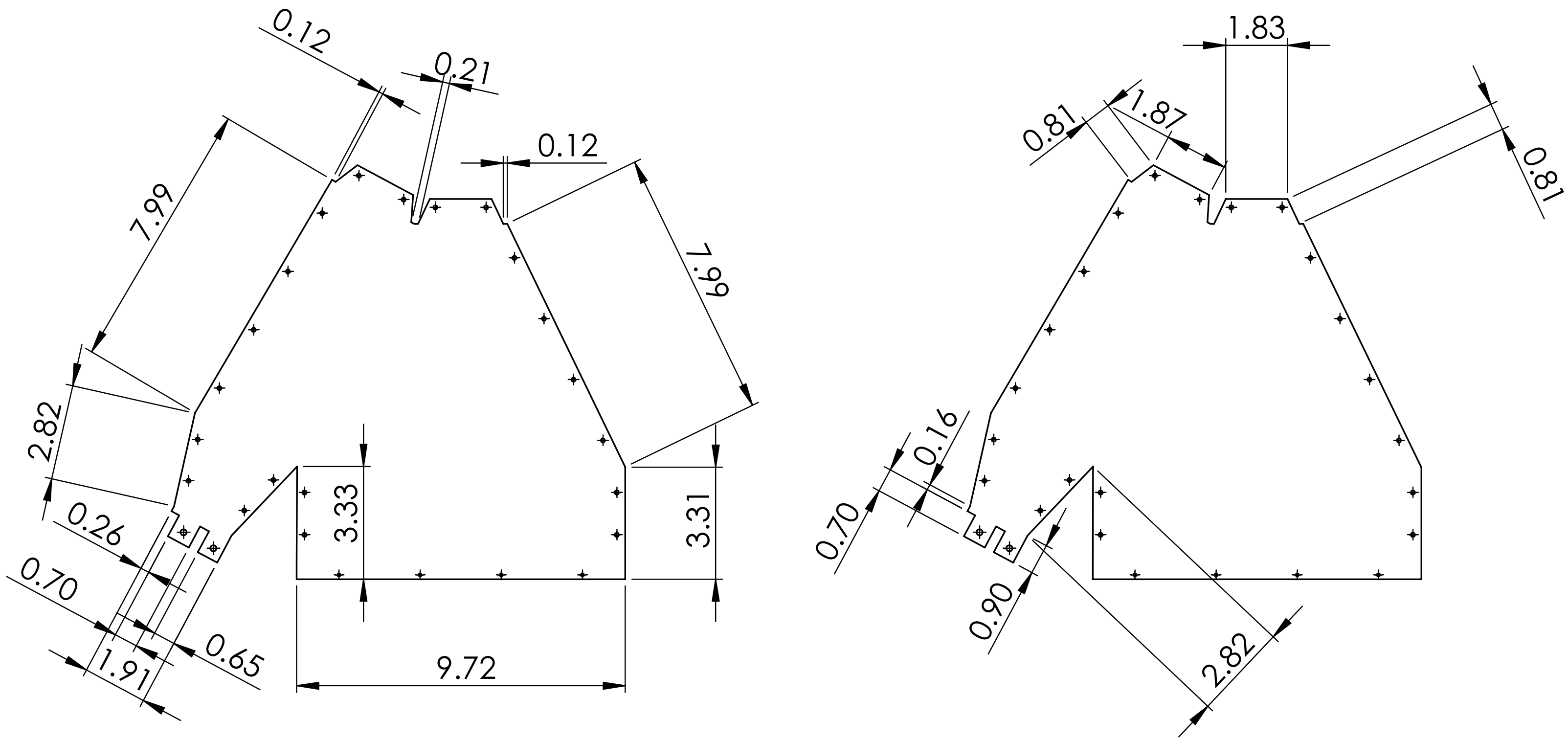

UNLESS OTHERWISE SPECIFIED:

DIMENSIONS ARE IN INCHES
TOLERANCES:
FRACTIONAL ±
ANGULAR: MACH ± BEND ±
TWO PLACE DECIMAL ±
THREE PLACE DECIMAL ±

INTERPRET GEOMETRIC TOLERANCING PER:

MATERIAL
0.020 ANOLUX
MIRO-SILVER REFLECTIVE
ALUMINIUM SHEET

	NAME	DATE
DRAWN	DKS	2/6/18
CHECKED		
ENG APPR.		
MFG APPR.		
Q.A.		

COMMENTS:

Moller Collaboration

TITLE:

LG Front Config1B

SIZE A DWG. NO. 7A REV 0

SCALE: 1:5 WEIGHT: SHEET 12 OF 16

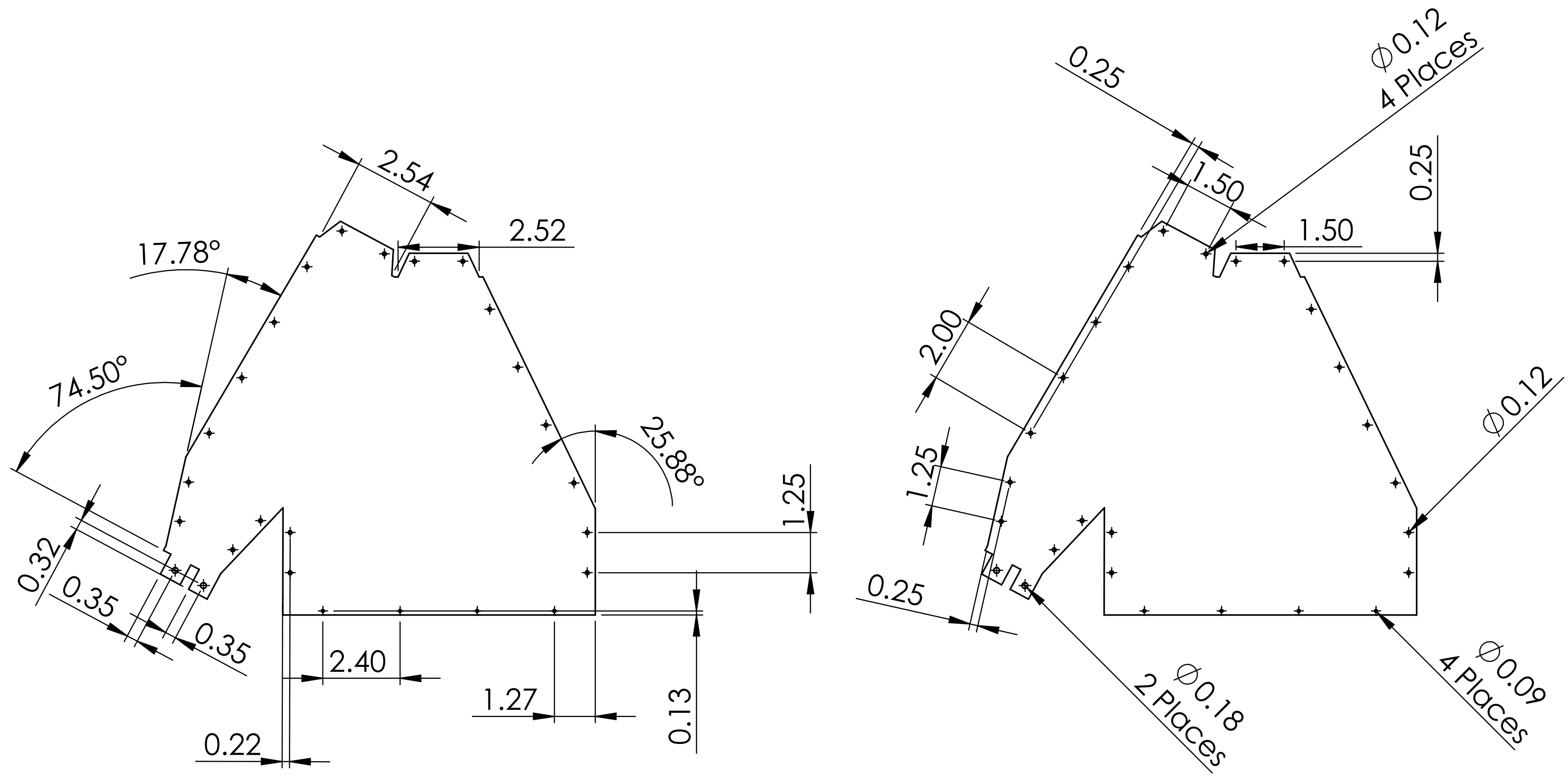

UNLESS OTHERWISE SPECIFIED:		NAME	DATE	Moller Collaboration
DIMENSIONS ARE IN INCHES TOLERANCES: FRACTIONAL± ANGULAR: MACH± BEND ± TWO PLACE DECIMAL ± THREE PLACE DECIMAL ±	DRAWN	DKS	2/6/18	TITLE:
	CHECKED			LG Front Config 1B
	ENG APPR.			
	MFG APPR.			
INTERPRET GEOMETRIC TOLERANCING PER:	Q.A.			
MATERIAL 0.020 ANOLUX MIRO-SILVER REFLECTIVE ALUMINIUM SHEET	COMMENTS:			SIZE A DWG. NO. 7B REV 0
				SCALE: 1:5 WEIGHT: SHEET 13 OF 16

2 1

B B

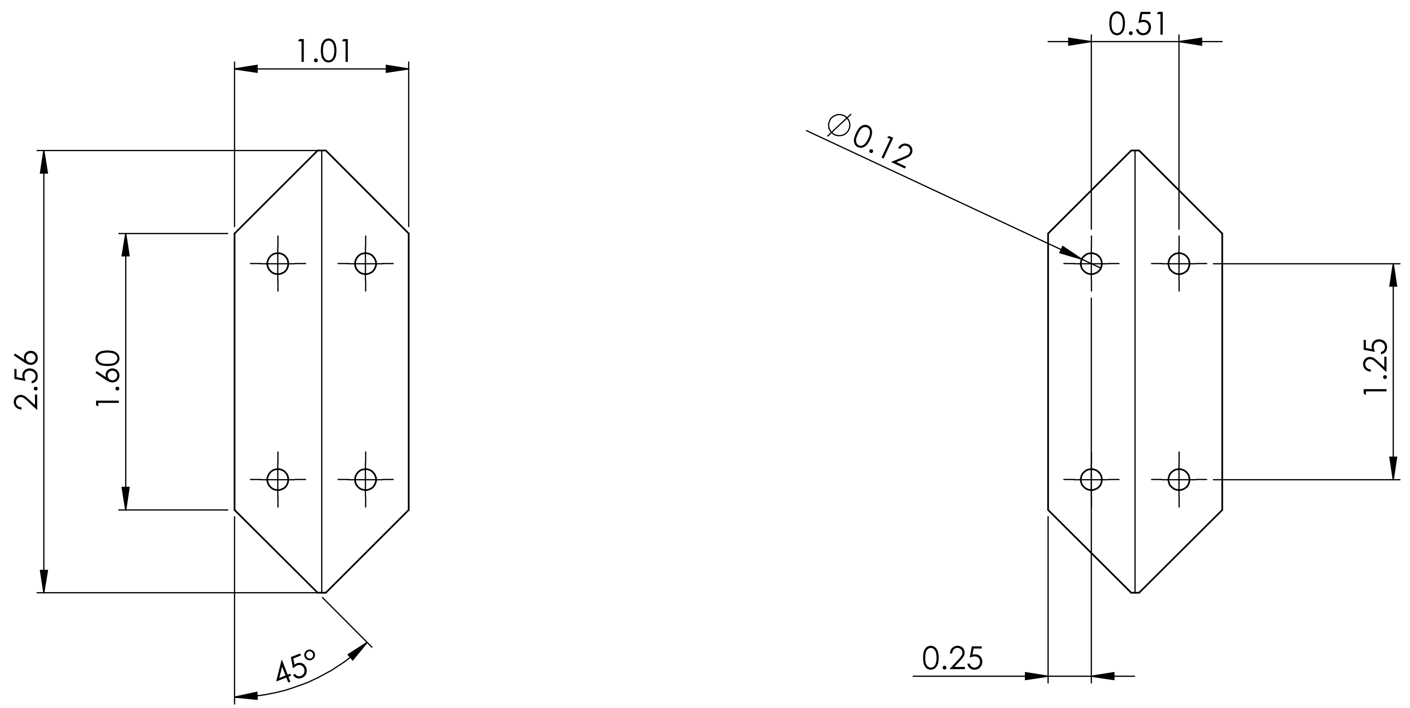

A A

UNLESS OTHERWISE SPECIFIED:

DIMENSIONS ARE IN INCHES
TOLERANCES:
FRACTIONAL±
ANGULAR: MACH± BEND ±
TWO PLACE DECIMAL ±
THREE PLACE DECIMAL ±

INTERPRET GEOMETRIC
TOLERANCING PER:

MATERIAL
0.020 ANOLUX
MIRO-SILVER REFLECTIVE
ALUMINIUM SHEET

	NAME	DATE
DRAWN	DKS	2/6/18
CHECKED		
ENG APPR.		
MFG APPR.		
Q.A.		

COMMENTS:

Moller Collaboration

TITLE:

Short Flap
Config 1B

SIZE A | DWG. NO. 8 | REV 0

SCALE: 1:1 | WEIGHT: | SHEET 14 OF 16

2 1

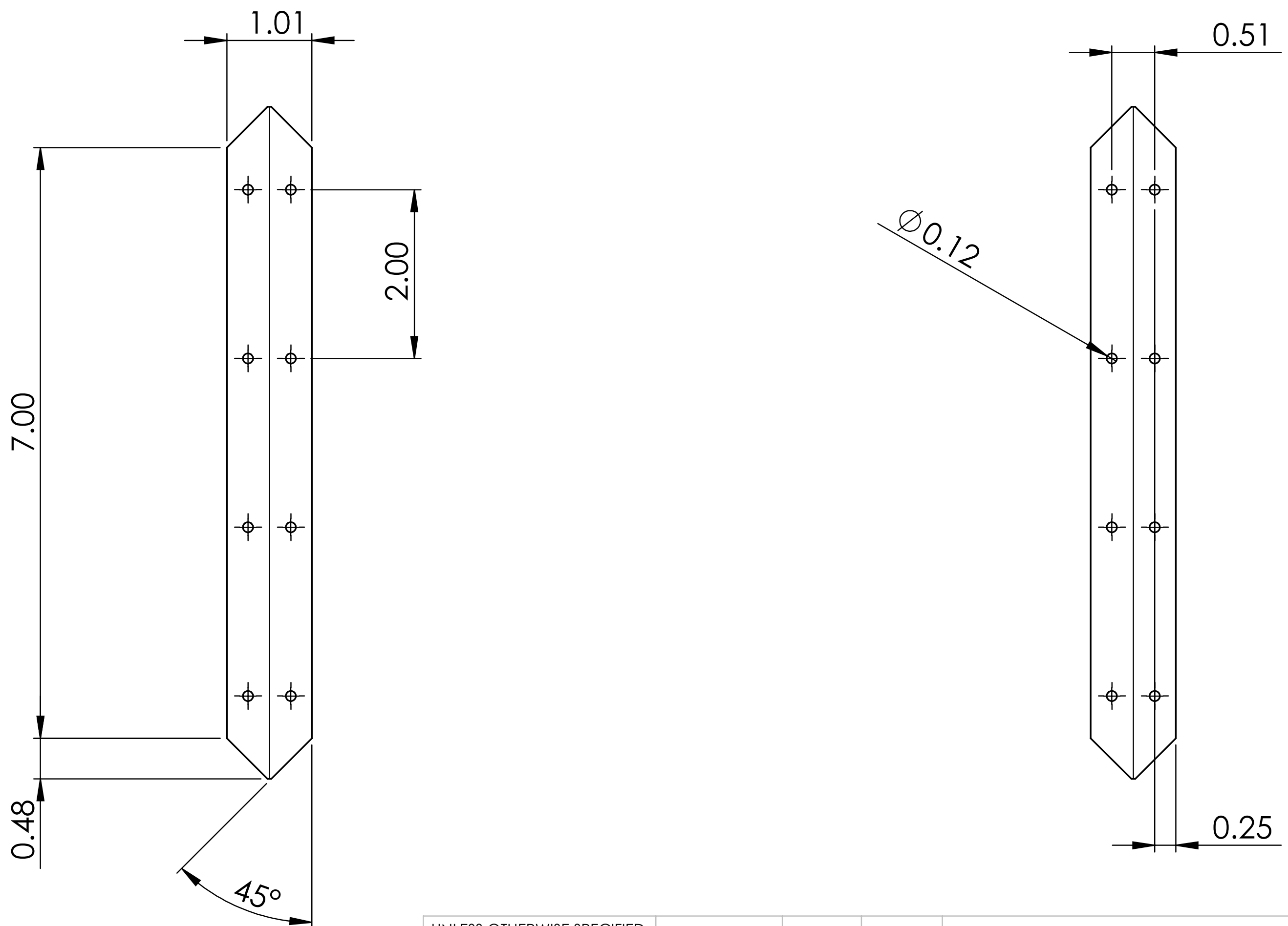

UNLESS OTHERWISE SPECIFIED:		NAME	DATE
DIMENSIONS ARE IN INCHES TOLERANCES: FRACTIONAL ± ANGULAR: MACH ± BEND ± TWO PLACE DECIMAL ± THREE PLACE DECIMAL ±	DRAWN	DKS	2/6/18
	CHECKED		
	ENG APPR.		
	MFG APPR.		
INTERPRET GEOMETRIC TOLERANCING PER:	Q.A.		
MATERIAL 0.020 ANOLUX MIRO-SILVER REFLECTIVE ALUMINIUM SHEET	COMMENTS:		

Moller Collaboration

TITLE:

Long Flap Config 1B

SIZE	DWG. NO.	REV
A	9	0
SCALE: 1:2	WEIGHT:	SHEET 15 OF 16

Flat

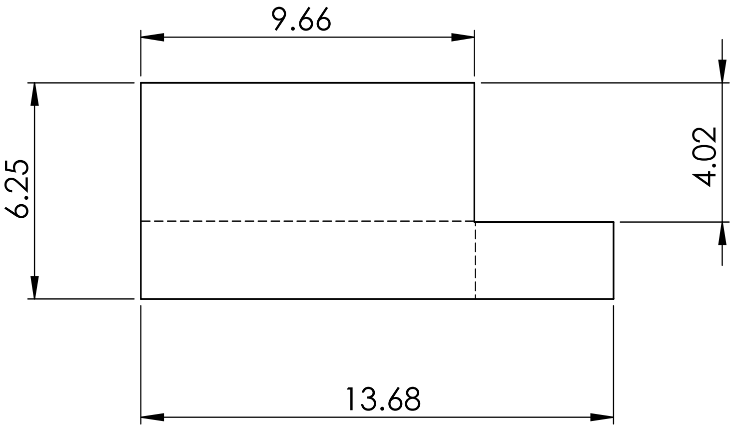

Folded

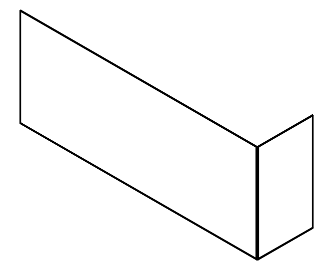

140

UNLESS OTHERWISE SPECIFIED:		NAME	DATE	Moller Collaboration
DIMENSIONS ARE IN INCHES TOLERANCES: FRACTIONAL ± ANGULAR: MACH ± BEND ± TWO PLACE DECIMAL ± THREE PLACE DECIMAL ±	DRAWN	DKS	2/6/18	TITLE:
	CHECKED			Suitcase Config 1B
	ENG APPR.			
	MFG APPR.			
INTERPRET GEOMETRIC TOLERANCING PER:	Q.A.			
MATERIAL 0.020 ANOLUX MIRO-SILVER REFLECTIVE ALUMINIUM SHEET	COMMENTS:			SIZE A · DWG. NO. 10 · REV 0
				SCALE: 1:5 · WEIGHT: · SHEET 16 OF 16

Appendix D

Lateral Shower Development

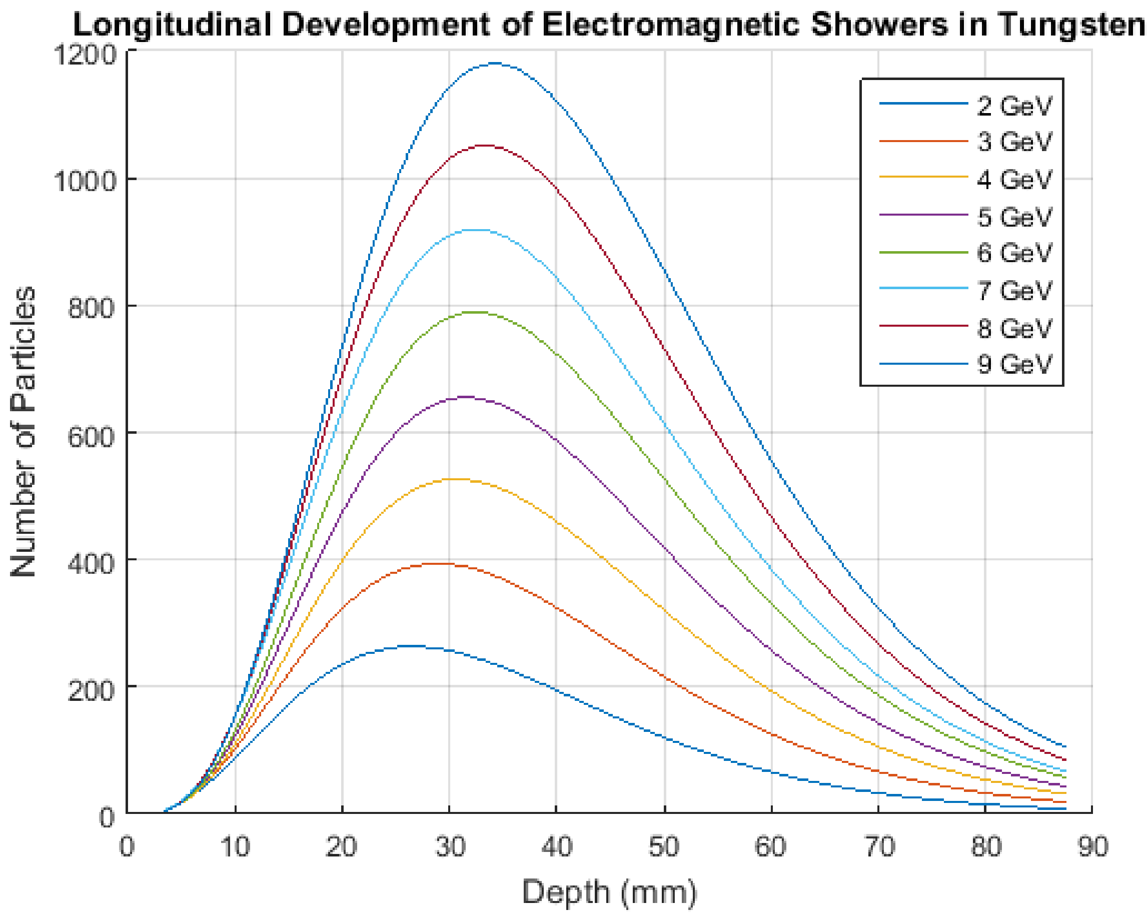

Shower Properties

This script finds the properties of an electromagnetic shower in tungsten. First it plots the depth of the shower max in tungsten and the number of particles at that depth. Next, it picks out these properties at integer energies. It uses these parameters to find the function for the longitudinal development of the EM shower using the function described in Egidio Longo and Ignazio Sestili's 1975 paper in Nuclear Instruments and Methods, volume 128, no.2

Contents

Properties of Shower Max

```
close
clc
clear

E = 2:0.01:9; % Range of energies we are interested in in GeV.

N_max = E/(7.97*10^-3); % Number of particles at shower max. E/E_critical. E_critical= 7.97 MeV

x_max = 5.055*log(N_max); % Depth of shower max in millimeters. x_max = x_0* ln(N_max)/ln(2), x_0 == radiation length.

figure
    plot(E,x_max);
    hold on
    title('Depth of Shower Max')
    xlabel('Energy (GeV)')
    ylabel('Depth (mm)')
    grid on

figure
    semilogx(E,x_max);
    hold on
    title('Depth of Shower Max (semi-log)')
    xlabel('Energy (GeV)')
    ylabel('Depth (mm)')
    grid on

figure
    plot(E,N_max);
    hold on
    title('Number of Particles at Shower Max')
    xlabel('Energy (GeV)')
    ylabel('N')
    grid on


figure
 plot(E,x_max,E,N_max)
 hold on

 title('Properties at Shower Max')
 xlabel('Energy (GeV)')
```

```
legend('Depth of Shower Max (mm)','Number of Particles at Shower Max (N)','location','northwest')
grid on

figure
semilogy(E,x_max,E,N_max)
hold on

title('Properties at Shower Max (semi-log)')
xlabel('Energy (GeV)')
legend('Depth of Shower Max (mm)','Number of Particles at Shower Max (N)','location','northwest')
grid on
```

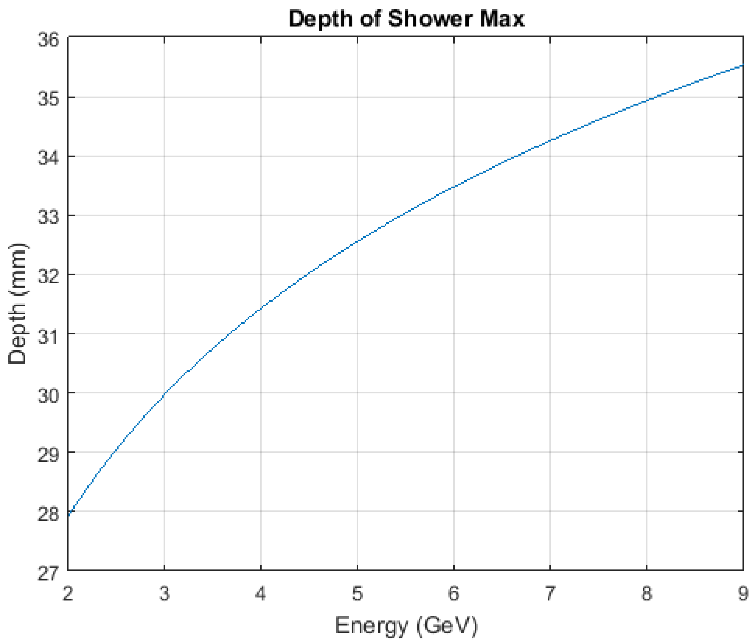
Depth of Shower Max
Depth (mm)
Energy (GeV)
36
35
34
33
32
31
30
29
28
27
2
3
4
5
6
7
8
9

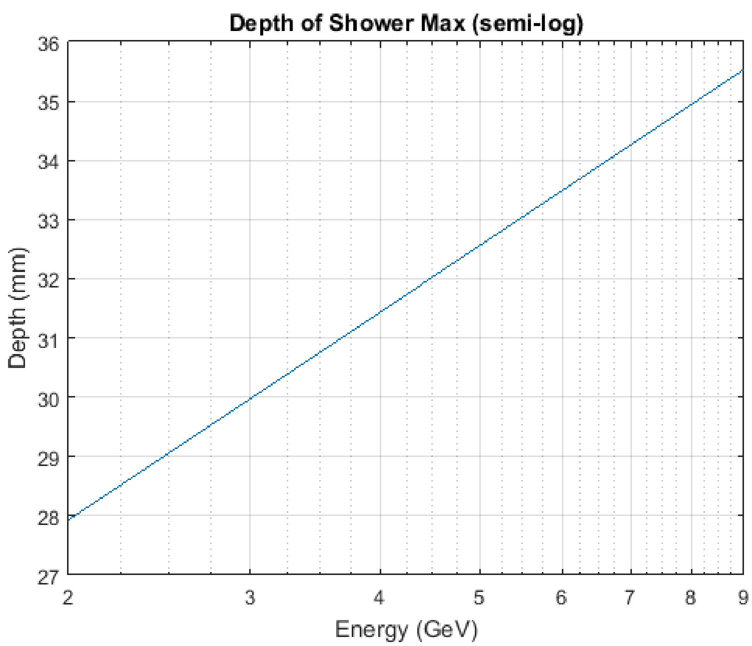
Depth of Shower Max (semi-log)
Depth (mm)
Energy (GeV)
36
35
34
33
32
31
30
29
28
27
2
3
4
5
6
7
8
9

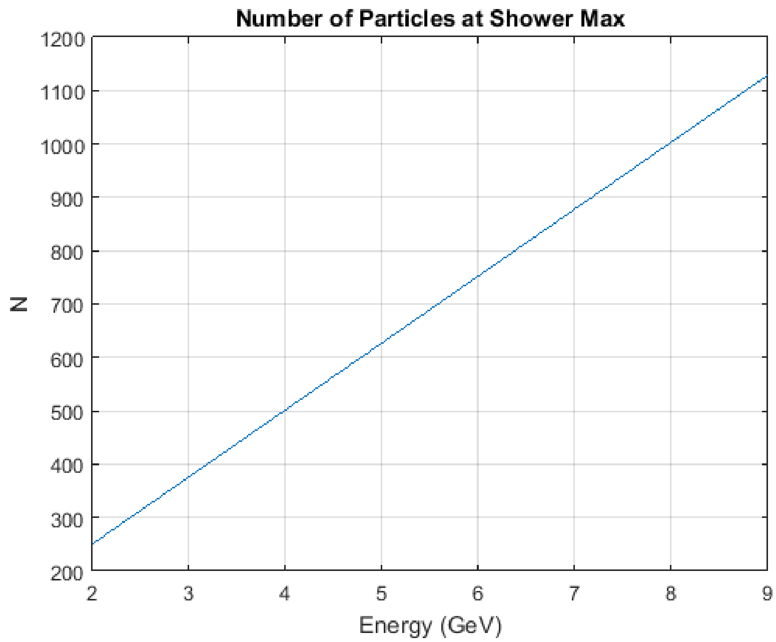
Number of Particles at Shower Max
N
1200
1100
1000
900
800
700
600
500
400
300
200
2
3
4
5
6
7
8
9
Energy (GeV)

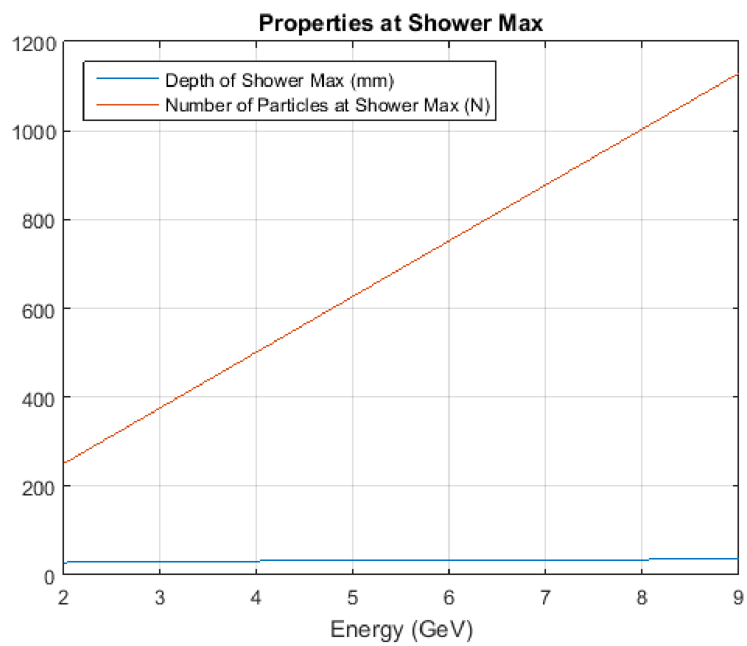
Properties at Shower Max
Depth of Shower Max (mm)
Number of Particles at Shower Max (N)
1200
1000
800
600
400
200
0
2
3
4
5
6
7
8
9
Energy (GeV)

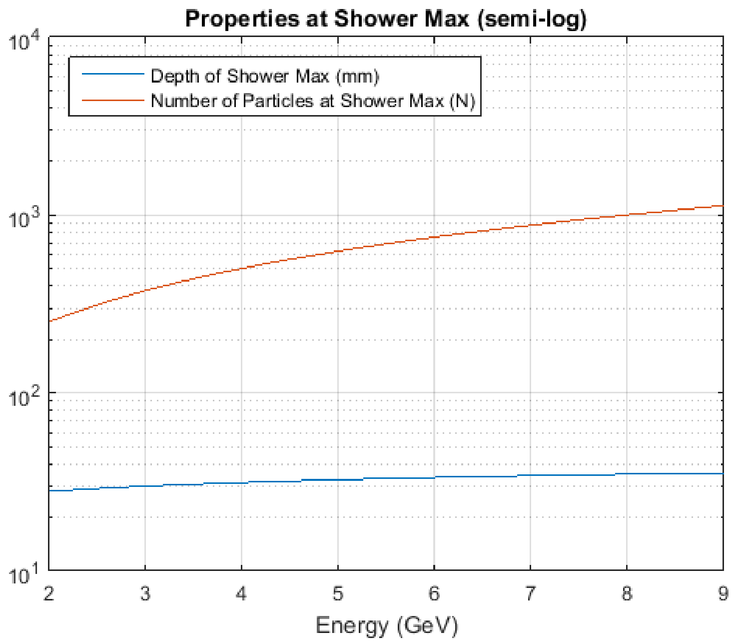

Properties of Shower Max at Integer Energies

```
x_max_integerEnergies=zeros(1,7);
N_max_integerEnergies=zeros(1,7);
E_integer=zeros(1,7);
n=1;
 for i=1:length(E)
     if mod(E(i),1)==0
        x_max_integerEnergies(n)=x_max(i);
        N_max_integerEnergies(n)=N_max(i);
        E_integer(n)=E(i);
        n=n+1;
     end
 end

 E_integer
 x_max_integerEnergies
 N_max_integerEnergies
```

```
E_integer =

     2     3     4     5     6     7     8     9


x_max_integerEnergies =

  Columns 1 through 7

   27.9300   29.9796   31.4338   32.5618   33.4835   34.2627   34.9377

  Column 8

   35.5331


N_max_integerEnergies =
```

```
   1.0e+03 *

  Columns 1 through 7

    0.2509    0.3764    0.5019    0.6274    0.7528    0.8783    1.0038

  Column 8

    1.1292
```

Functions Describing Longitudinal Shower Development

Number of particles with respect to depth is descibed by the equation $N = At^{\alpha}e^{-bt}$, where A, α, and b, are to be determined.

A superficial search

```
t=1:0.1:25; %depth in radiation length
x0=3.504; %radiation length
x=t*x0; %depth in mm
A=9:1:16;
alpha=3:0.5:4.0;
b=0.5;

N=zeros(length(x),length(A),length(alpha),length(b)); % allocate space

for i=1:length(x)
    for j=1:length(A)
        for k=1:length(alpha)
            for l=1:length(b)
                N(i,j,k,l) = A(j)*(x(i)/x0)^(alpha(k))*exp(-b(l)*x(i)/x0); % N=A*t^alpha*exp(-b*t)
            end
        end
    end
end

figure
hold on

clear i
clear j
clear k
clear l

for j=1:length(A)
    for k=1:length(alpha)
        for l=1:length(b)
            semilogy(x,N(:,j,k,l));
        end
    end
end

 title('Possible Longitudinal Shower Development Models')
 xlabel('x (mm)')
 ylabel('N')
 dim = [.5 .55 .3 .3]; %dim = [.2 .5 .3 .3];
 str = 'A=9:1:16; \alpha=3:0.5:4; b=0.5';
 annotation('textbox',dim,'String',str,'FitBoxToText','on');
 grid on

 str2 = '$$ N=A t^\alpha e^{-b t}$$';
text(55,1300,str2,'Interpreter','latex')
```

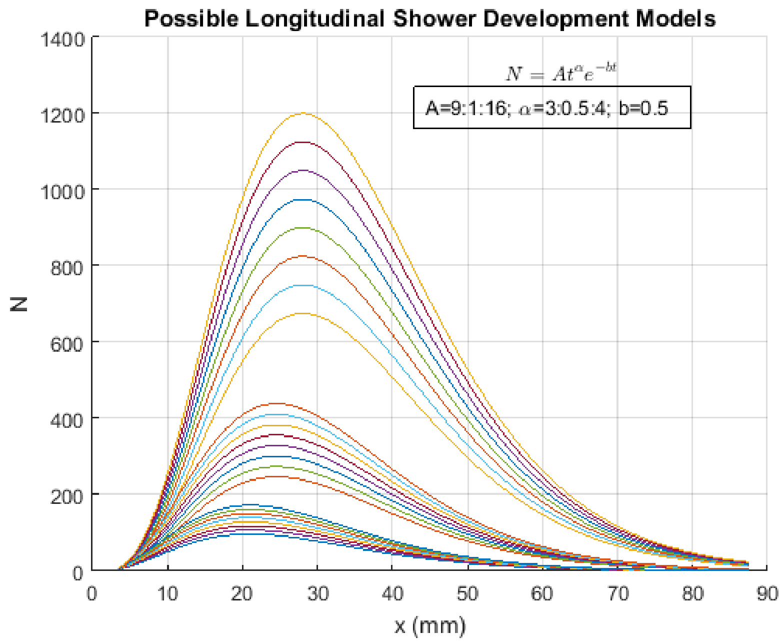

An in depth search

```
clear A
clear alpha
clear b
clear N

A=4:0.05:12;
alpha=1:0.1:5;
b=0.4:0.01:0.6;

N=zeros(length(x),length(A),length(alpha),length(b)); % allocate space

for i=1:length(x)
    for j=1:length(A)
        for k=1:length(alpha)
            for l=1:length(b)
                N(i,j,k,l) = A(j)*(x(i)/x0)^(alpha(k))*exp(-b(l)*x(i)/x0); % N=A*t^alpha*exp(-b*t)
            end
        end
    end
end

clear n


final_A_values=zeros(1,length(x_max_integerEnergies));
final_alpha_values=zeros(1,length(x_max_integerEnergies));
final_b_values=zeros(1,length(x_max_integerEnergies));

for n=1:length(x_max_integerEnergies)


    for j=1:length(A)
        for k=1:length(alpha)
            for l=1:length(b)
                tempN = N(:,j,k,l);
                [NFunctionMax,arrayPositionOfNMax] = max(tempN);
                 if all([NFunctionMax >= 0.95*N_max_integerEnergies(n), NFunctionMax <= 1.05*N_max_integerEnergies(n),
```

```
 x(arrayPositionOfNMax) >= 0.95*x_max_integerEnergies(n), x(arrayPositionOfNMax) <= 1.05*x_max_integerEnergies(n)])
                    final_A_values(n)=A(j);
                    final_alpha_values(n)=alpha(k);
                    final_b_values(n)=b(l);

                end
            end
        end
    end

end
```

Shower Development Results

```
final_A_values
final_alpha_values
final_b_values

figure
hold on

finalNs=zeros(length(E_integer),length(t));

for i=1:length(E_integer)
    finalNs(i,:)= final_A_values(i)*(t.^(final_alpha_values(i))).*exp(-final_b_values(i)*t);
    plot(x,finalNs(i,:))
end


    title('Longitudinal Development of Electromagnetic Showers in Tungsten')
    xlabel('Depth (mm)')
    ylabel('Number of Particles')
    legend('2 GeV','3 GeV','4 GeV','5 GeV','6 GeV','7 GeV','8 GeV','9 GeV','location','northeast')
    grid on


figure
hold on

for i=1:length(E_integer)
    plot(t,finalNs(i,:))
end


    title('Longitudinal Development of Electromagnetic Showers in Tungsten')
    xlabel('t (X_0)')
    ylabel('Number of Particles')
    legend('2 GeV','3 GeV','4 GeV','5 GeV','6 GeV','7 GeV','8 GeV','9 GeV','location','northeast')
    grid on

 figure

for i=1:length(E_integer)
    semilogy(x,finalNs(i,:))
    hold on
end

    title('Longitudinal Development of Electromagnetic Showers in Tungsten (semilog)')
    xlabel('Depth (mm)')
    ylabel('Number of Particles')
    legend('2 GeV','3 GeV','4 GeV','5 GeV','6 GeV','7 GeV','8 GeV','9 GeV','location','northeast')
    grid on

figure
```

```
for i=1:length(E_integer)
    semilogy(t,finalNs(i,:))
    hold on
end

    title('Longitudinal Development of Electromagnetic Showers in Tungsten (semilog)')
    xlabel('t (X_0)')
    ylabel('Number of Particles')
    legend('2 GeV','3 GeV','4 GeV','5 GeV','6 GeV','7 GeV','8 GeV','9 GeV','location','northeast')
    grid on
```

```
final_A_values =

  Columns 1 through 7

   11.0500   10.1000    8.8000    8.8000    8.5000    9.9000    9.0500

  Column 8

    8.1000


final_alpha_values =

  Columns 1 through 7

    3.1000    3.3000    3.5000    3.6000    3.7000    3.7000    3.8000

  Column 8

    3.9000


final_b_values =

  Columns 1 through 7

    0.4100    0.4000    0.4000    0.4000    0.4000    0.4000    0.4000

  Column 8

    0.4000
```

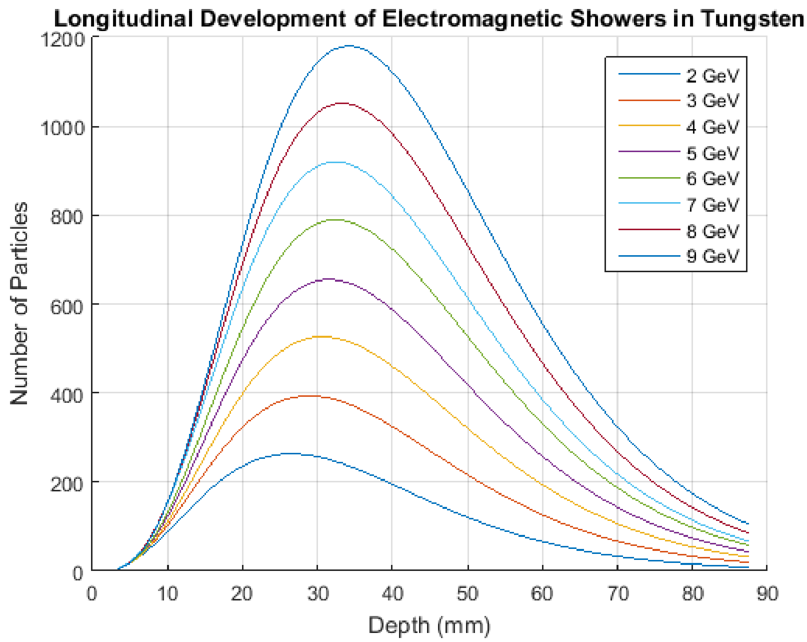
Longitudinal Development of Electromagnetic Showers in Tungsten
Number of Particles
Depth (mm)
2 GeV
3 GeV
4 GeV
5 GeV
6 GeV
7 GeV
8 GeV
9 GeV
0
200
400
600
800
1000
1200
0
10
20
30
40
50
60
70
80
90

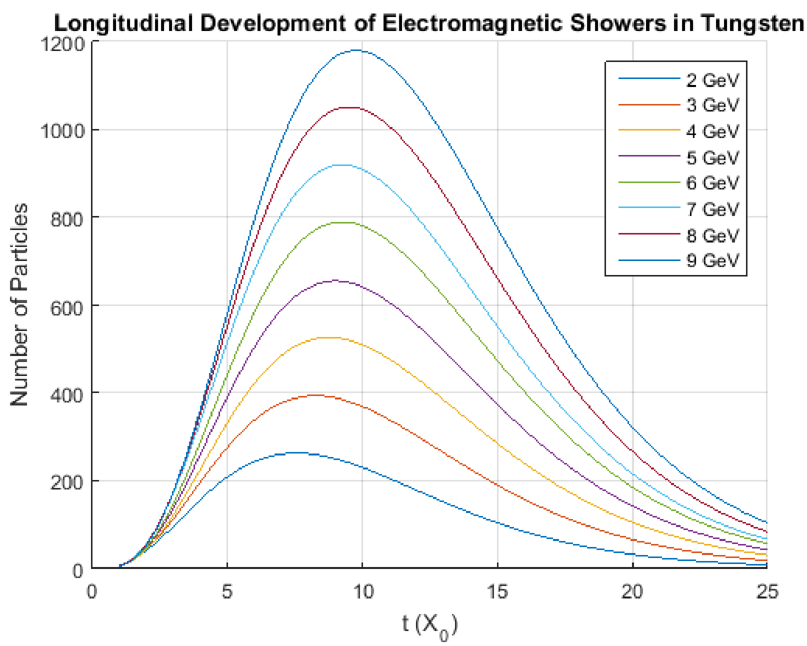
Longitudinal Development of Electromagnetic Showers in Tungsten
Number of Particles
t (X_0)
2 GeV
3 GeV
4 GeV
5 GeV
6 GeV
7 GeV
8 GeV
9 GeV
0
200
400
600
800
1000
1200
0
5
10
15
20
25

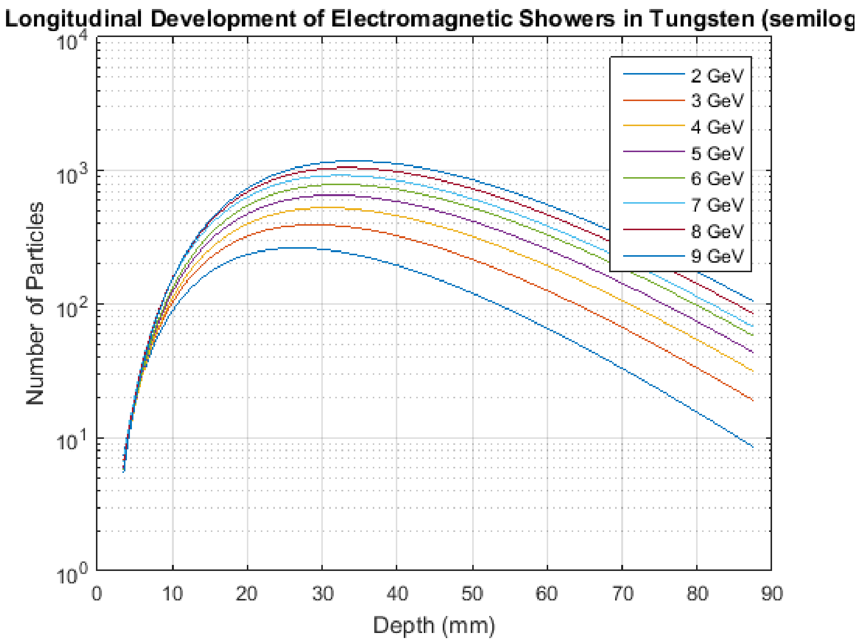

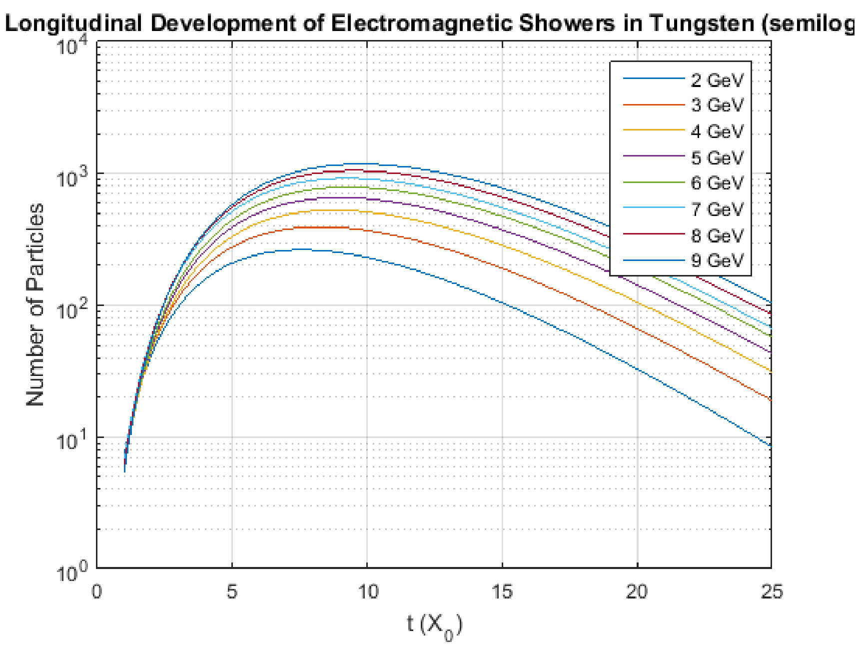

Ratios of Particle Number by Depth

This section looks at the ratio of the number of particles in the shower with respect to depth. Both the regular ration and the ratio of the integrals are considered.

```
ratio_2and3=finalNs(1,:)./finalNs(2,:);
ratio_2and5=finalNs(1,:)./finalNs(4,:);
ratio_2and7=finalNs(1,:)./finalNs(6,:);
ratio_2and8=finalNs(1,:)./finalNs(7,:);

ratio_3and5=finalNs(2,:)./finalNs(4,:);
```

```
ratio_3and7=finalNs(2,:)./finalNs(6,:);
ratio_3and8=finalNs(2,:)./finalNs(7,:);

ratio_5and7=finalNs(4,:)./finalNs(6,:);
ratio_5and8=finalNs(4,:)./finalNs(7,:);

ratio_7and8=finalNs(6,:)./finalNs(7,:);


integral_2GeV=zeros(1,length(x));
integral_3GeV=zeros(1,length(x));
integral_5GeV=zeros(1,length(x));
integral_7GeV=zeros(1,length(x));
integral_8GeV=zeros(1,length(x));


for i=2:1:length(tempN)
    integral_2GeV(i)=integral_2GeV(i-1) + (x(i)-x(i-1))*(finalNs(1,i)+finalNs(1,i-1))/2;
    integral_3GeV(i)=integral_3GeV(i-1) + (x(i)-x(i-1))*(finalNs(2,i)+finalNs(2,i-1))/2;
    integral_5GeV(i)=integral_5GeV(i-1) + (x(i)-x(i-1))*(finalNs(4,i)+finalNs(4,i-1))/2;
    integral_7GeV(i)=integral_7GeV(i-1) + (x(i)-x(i-1))*(finalNs(6,i)+finalNs(6,i-1))/2;
    integral_8GeV(i)=integral_8GeV(i-1) + (x(i)-x(i-1))*(finalNs(1,i)+finalNs(7,i-1))/2;
end

integralRatio_2and = integral_2GeV./integral_8GeV;

figure
hold on

plot(x,ratio_2and3,x,ratio_2and5,x,ratio_2and7,x,ratio_2and8)

    title('Ratio of N for 2GeV and Higher Energies')
    xlabel('x (mm)')
    ylabel('%')
    legend('2Gev & 3GeV','2Gev & 5GeV','2Gev & 7GeV','2Gev & 8GeV','location','northeast')
    grid on

figure
hold on

plot(t,ratio_2and3,t,ratio_2and5,t,ratio_2and7,t,ratio_2and8)

    title('Ratio of N for 2GeV and Higher Energies')
    xlabel('t (X_0)')
    ylabel('%')
    legend('2Gev & 3GeV','2Gev & 5GeV','2Gev & 7GeV','2Gev & 8GeV','location','northeast')
    grid on

 figure
hold on





plot(x,ratio_3and5,x,ratio_3and7,x,ratio_3and8)

    title('Ratio of N for 3GeV and Higher Energies')
    xlabel('x (mm)')
    ylabel('%')
    legend('3Gev & 5GeV','3Gev & 7GeV','3Gev & 8GeV','location','northeast')
    grid on

figure
hold on

plot(t,ratio_3and5,t,ratio_3and7,t,ratio_3and8)
```

```
    title('Ratio of N for 3GeV and Higher Energies')
    xlabel('t (X_0)')
    ylabel('%')
    legend('3Gev & 5GeV','3Gev & 7GeV','3Gev & 8GeV','location','northeast')
    grid on


figure
hold on

plot(x,ratio_5and7,x,ratio_5and8)

    title('Ratio of N for 5GeV and Higher Energies')
    xlabel('x (mm)')
    ylabel('%')
    legend('5Gev & 7GeV','5Gev & 8GeV','location','northeast')
    grid on

figure
hold on

plot(t,ratio_5and7,t,ratio_5and8)

    title('Ratio of N for 5GeV and Higher Energies')
    xlabel('t (X_0)')
    ylabel('%')
    legend('5Gev & 7GeV','5Gev & 8GeV','location','northeast')
    grid on


figure
hold on

plot(x,ratio_7and8)

    title('Ratio of N for 7GeV and 8GeV')
    xlabel('x (mm)')
    ylabel('%')
    legend('7Gev & 8GeV','location','northeast')
    grid on

figure
hold on

plot(t,ratio_7and8)

    title('Ratio of N for 7GeV and 8GeV')
    xlabel('t (X_0)')
    ylabel('%')
    legend('7Gev & 8GeV','location','northeast')
    grid on
```

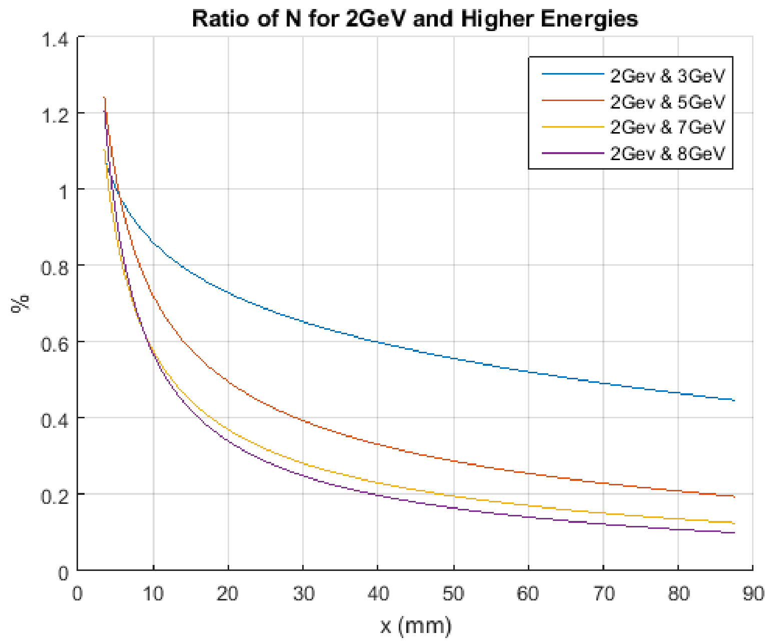
Ratio of N for 2GeV and Higher Energies
2Gev & 3GeV
2Gev & 5GeV
2Gev & 7GeV
2Gev & 8GeV
%
x (mm)
1.4
1.2
1
0.8
0.6
0.4
0.2
0
10
20
30
40
50
60
70
80
90

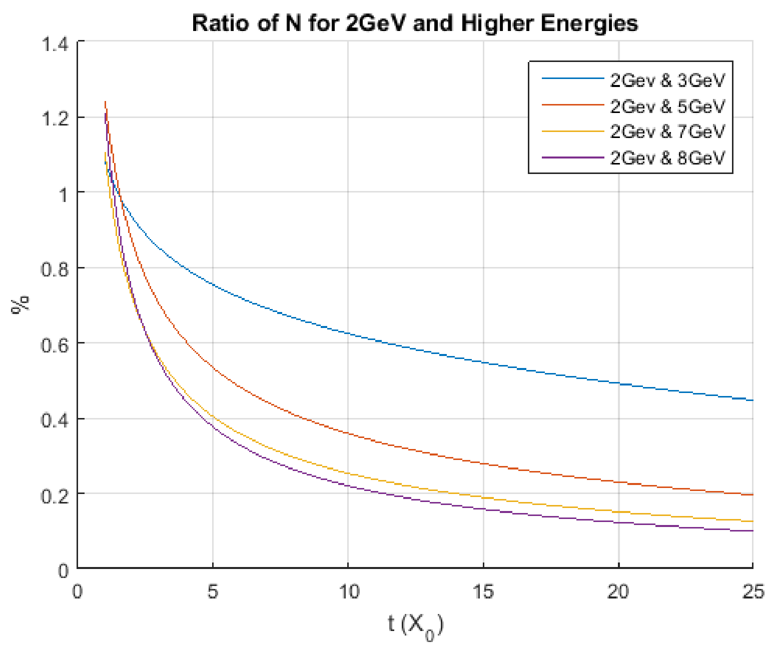
Ratio of N for 2GeV and Higher Energies
2Gev & 3GeV
2Gev & 5GeV
2Gev & 7GeV
2Gev & 8GeV
%
t (X_0)
1.4
1.2
1
0.8
0.6
0.4
0.2
0
5
10
15
20
25

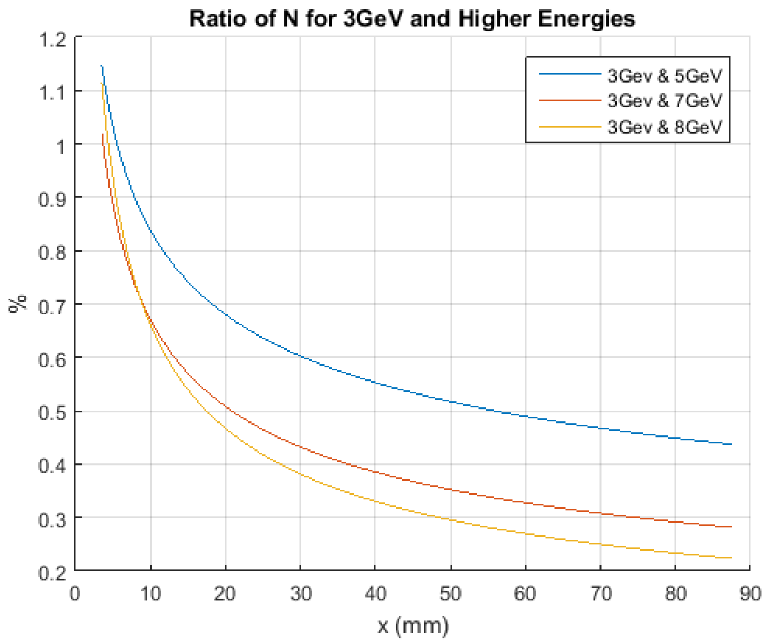
Ratio of N for 3GeV and Higher Energies
3Gev & 5GeV
3Gev & 7GeV
3Gev & 8GeV
%
x (mm)

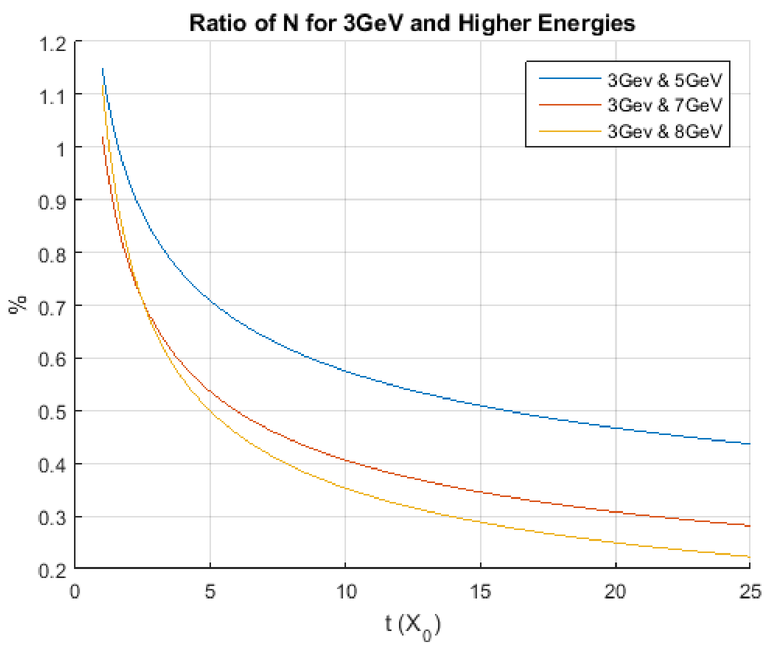
Ratio of N for 3GeV and Higher Energies
3Gev & 5GeV
3Gev & 7GeV
3Gev & 8GeV
%
t (X_0)

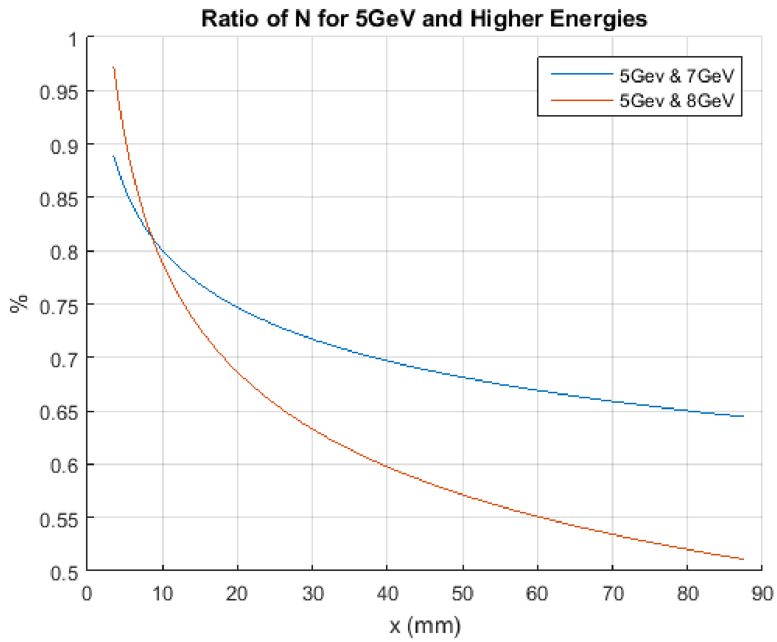
Ratio of N for 5GeV and Higher Energies
5Gev & 7GeV
5Gev & 8GeV
%
x (mm)

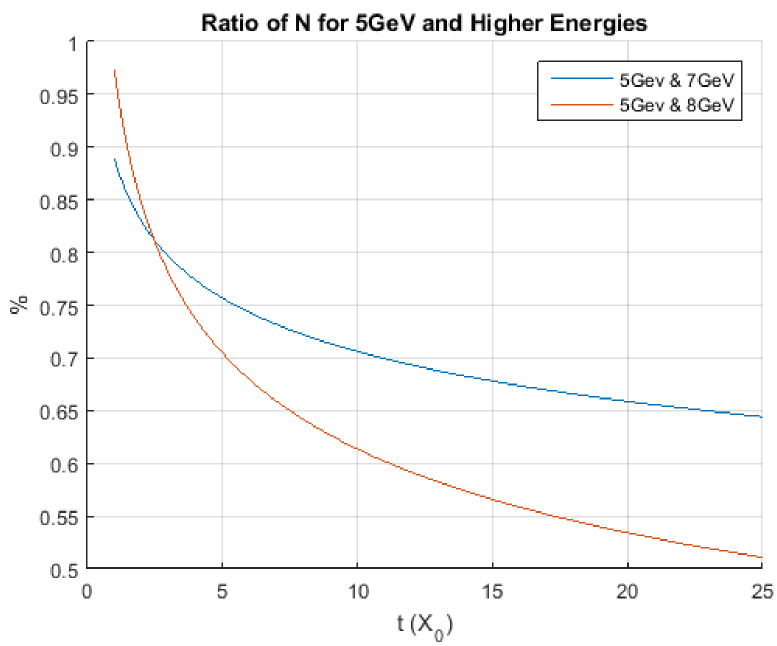
Ratio of N for 5GeV and Higher Energies
5Gev & 7GeV
5Gev & 8GeV
%
t (X0)

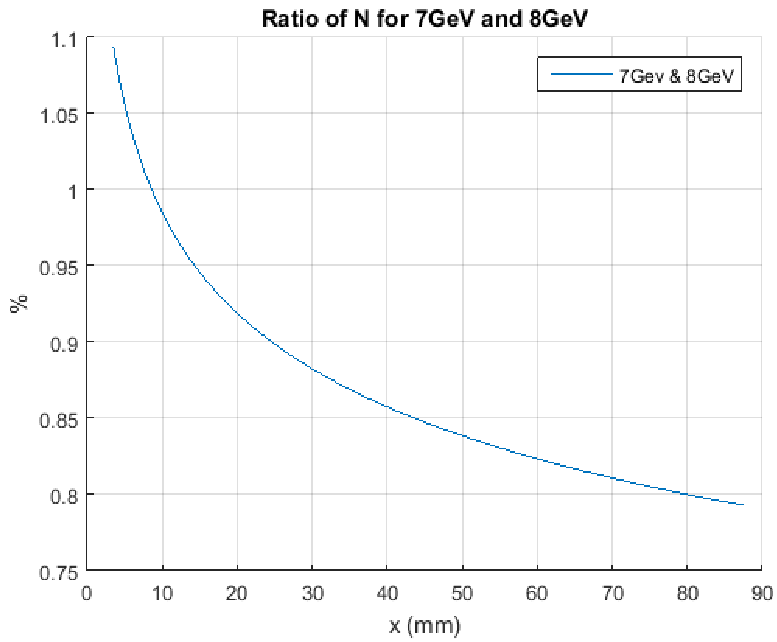

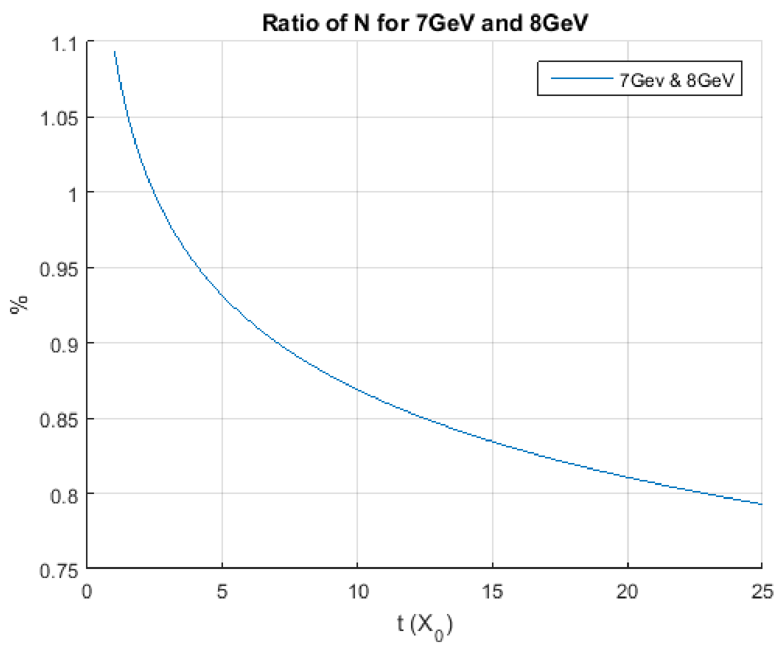

More Comparisons

```
figure
hold on
plotyy(x,ratio_2and3,[x',x'],[finalNs(1,:)',finalNs(2,:)']);
title('Shower Development: 2GeV  vs. 3GeV')
xlabel('x (mm)')
legend('N_2/N_3','N_2','N_3')
grid on
```

```
figure
hold on
plotyy(x,ratio_2and5,[x',x'],[finalNs(1,:)',finalNs(4,:)']);
title('Shower Development: 2GeV  vs. 5GeV')
xlabel('x (mm)')
legend('N_2/N_5','N_2','N_5')
grid on

figure
hold on
plotyy(x,ratio_2and7,[x',x'],[finalNs(1,:)',finalNs(6,:)']);
title('Shower Development: 2GeV  vs. 7GeV')
xlabel('x (mm)')
legend('N_2/N_7','N_2','N_7')
grid on

figure
hold on
plotyy(x,ratio_2and8,[x',x'],[finalNs(1,:)',finalNs(7,:)']);
title('Shower Development: 2GeV  vs. 8GeV')
xlabel('x (mm)')
legend('N_2/N_8','N_2','N_8')
grid on



figure
hold on
plotyy(x,ratio_3and5,[x',x'],[finalNs(2,:)',finalNs(4,:)']);
title('Shower Development: 3GeV  vs. 5GeV')
xlabel('x (mm)')
legend('N_3/N_5','N_3','N_5')
grid on

figure
hold on
plotyy(x,ratio_3and7,[x',x'],[finalNs(2,:)',finalNs(6,:)']);
title('Shower Development: 3GeV  vs. 7GeV')
xlabel('x (mm)')
legend('N_3/N_7','N_3','N_7')
grid on

figure
hold on
plotyy(x,ratio_3and8,[x',x'],[finalNs(2,:)',finalNs(7,:)']);
title('Shower Development: 3GeV  vs. 8GeV')
xlabel('x (mm)')
legend('N_3/N_8','N_3','N_8')
grid on


figure
hold on
plotyy(x,ratio_5and7,[x',x'],[finalNs(4,:)',finalNs(6,:)']);
title('Shower Development: 5GeV  vs. 7GeV')
xlabel('x (mm)')
legend('N_5/N_7','N_5','N_7')
grid on

figure
hold on
plotyy(x,ratio_5and8,[x',x'],[finalNs(4,:)',finalNs(7,:)']);
title('Shower Development: 5GeV  vs. 8GeV')
xlabel('x (mm)')
legend('N_5/N_8','N_5','N_8')
grid on
```

```
figure
hold on
plotyy(x,ratio_7and8,[x',x'],[finalNs(6,:)',finalNs(7,:)']);
title('Shower Development: 7GeV  vs. 8GeV')
xlabel('x (mm)')
legend('N_7/N_8','N_7','N_8')
grid on
```

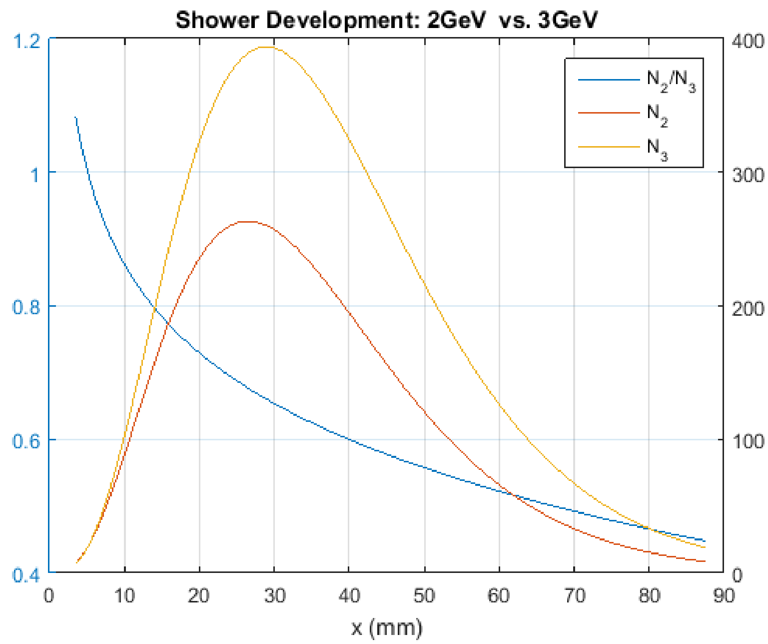

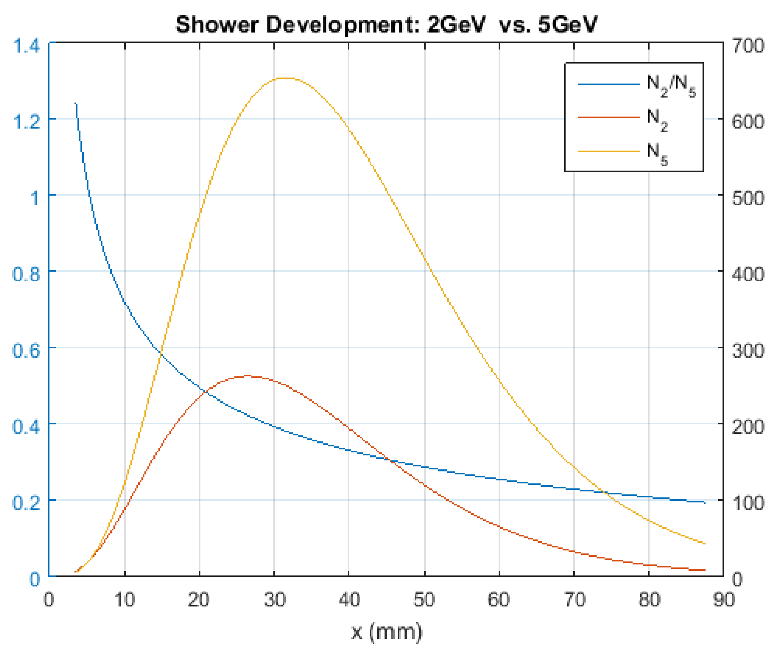

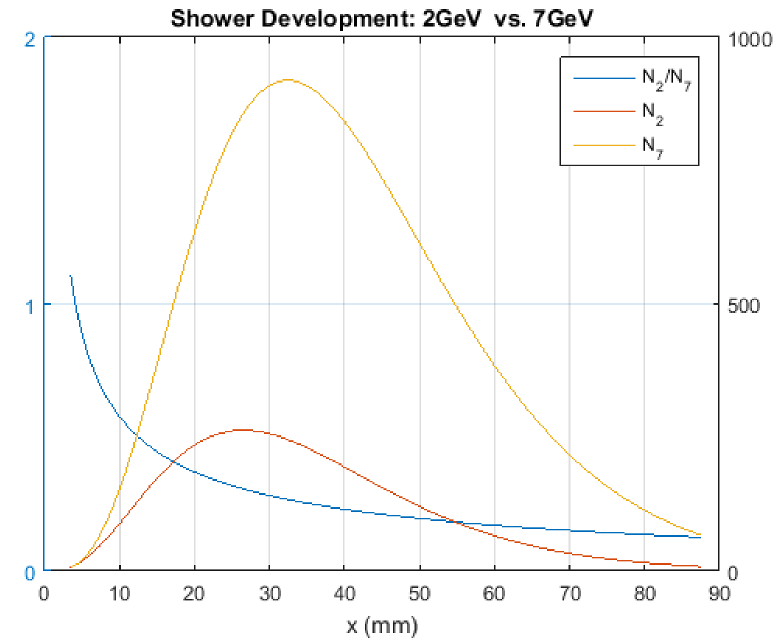
Shower Development: 2GeV vs. 7GeV
N_2/N_7
N_2
N_7
2
1
0
1000
500
0
0
10
20
30
40
50
60
70
80
90
x (mm)

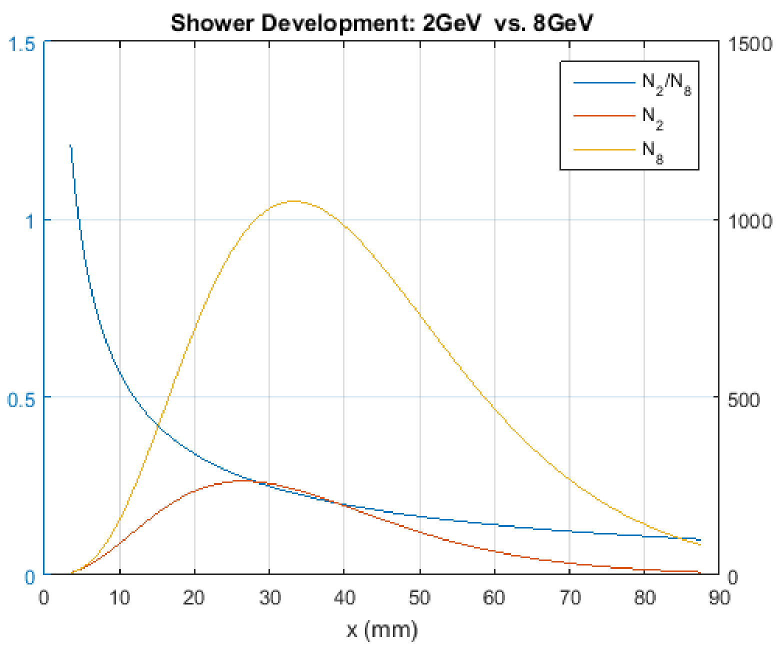
Shower Development: 2GeV vs. 8GeV
N_2/N_8
N_2
N_8
1.5
1
0.5
0
1500
1000
500
0
0
10
20
30
40
50
60
70
80
90
x (mm)

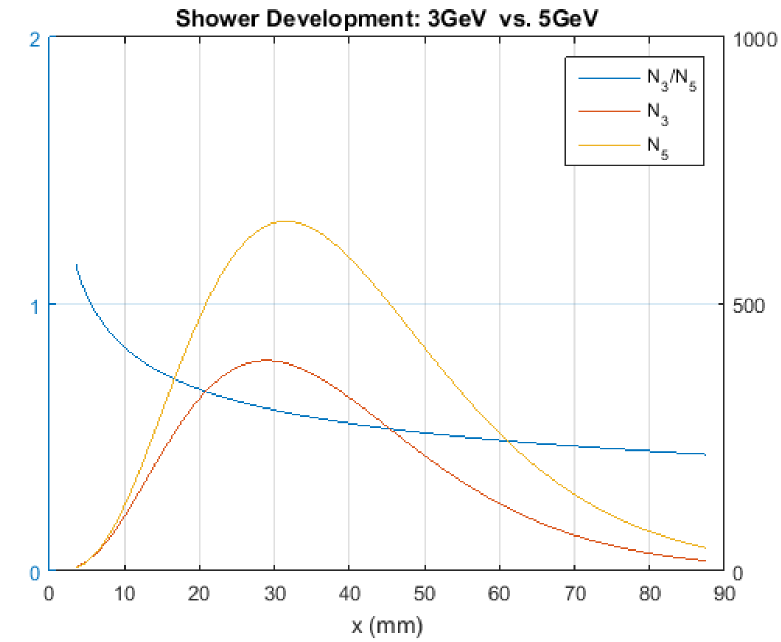
Shower Development: 3GeV vs. 5GeV
2
1
0
1000
500
0
0
10
20
30
40
50
60
70
80
90
x (mm)
N3/N5
N3
N5

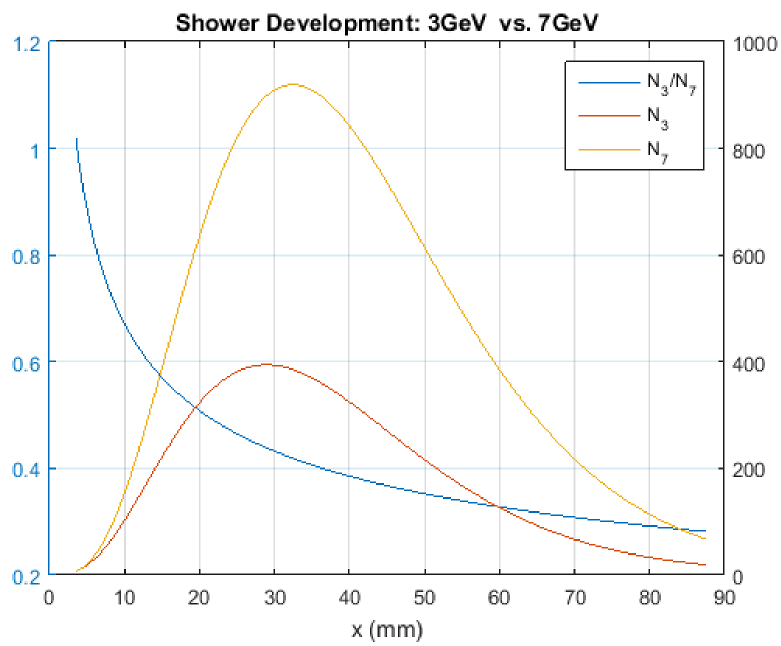
Shower Development: 3GeV vs. 7GeV
1.2
1
0.8
0.6
0.4
0.2
1000
800
600
400
200
0
0
10
20
30
40
50
60
70
80
90
x (mm)
N3/N7
N3
N7

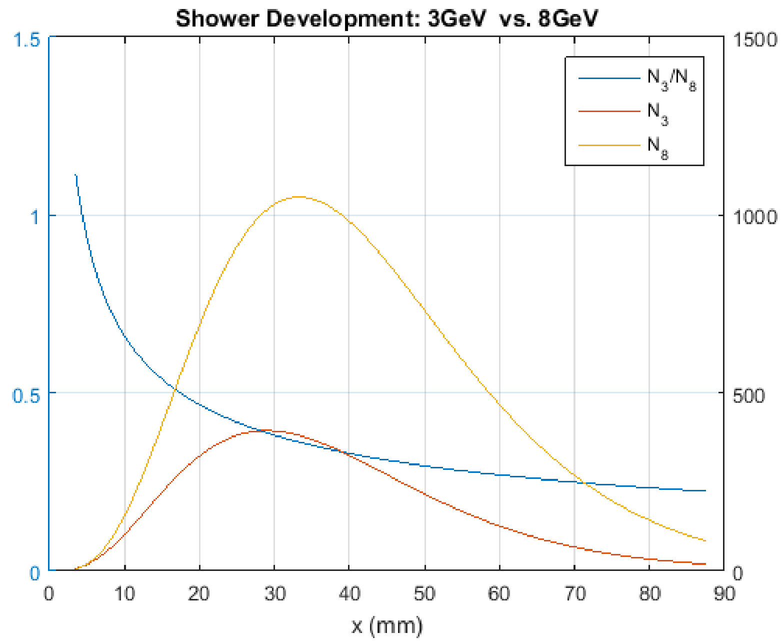
Shower Development: 3GeV vs. 8GeV
1.5
1
0.5
0
1500
1000
500
0
0 10 20 30 40 50 60 70 80 90
x (mm)
N3/N8
N3
N8

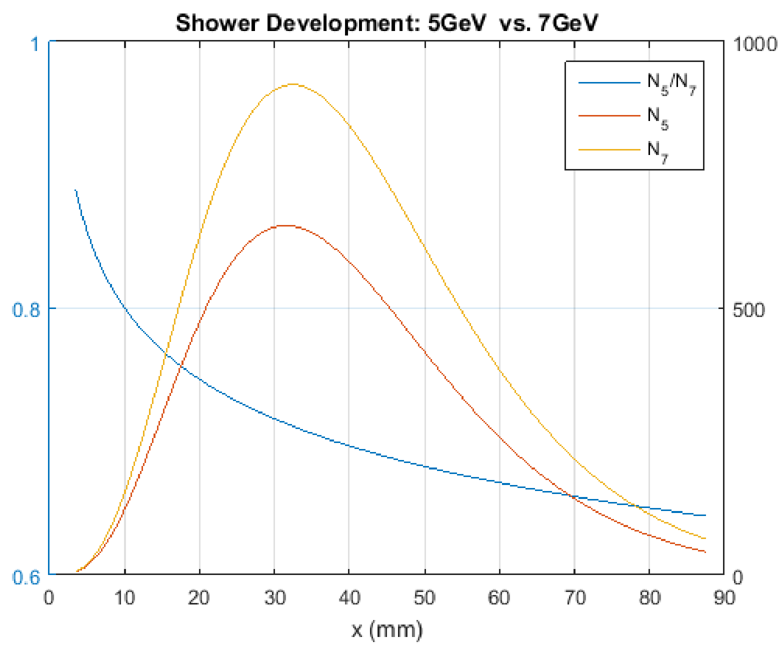
Shower Development: 5GeV vs. 7GeV
1
0.8
0.6
1000
500
0
0 10 20 30 40 50 60 70 80 90
x (mm)
N5/N7
N5
N7

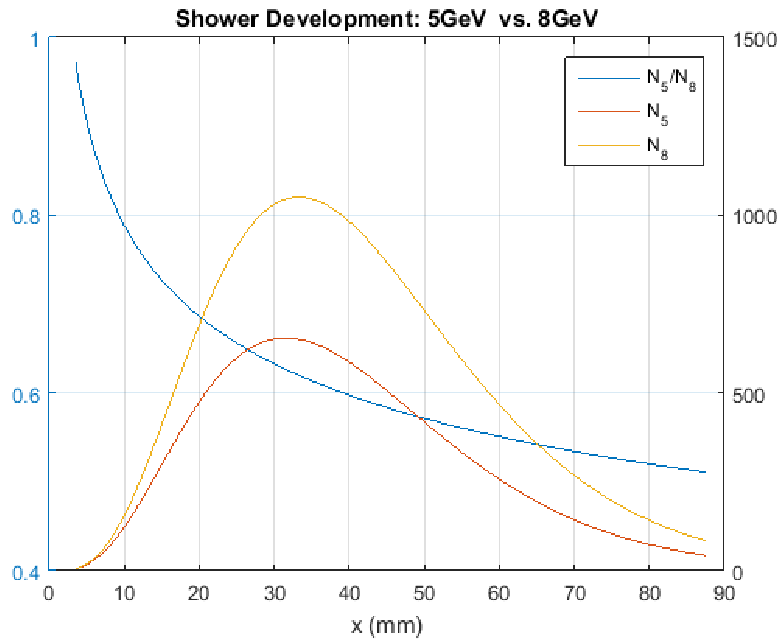

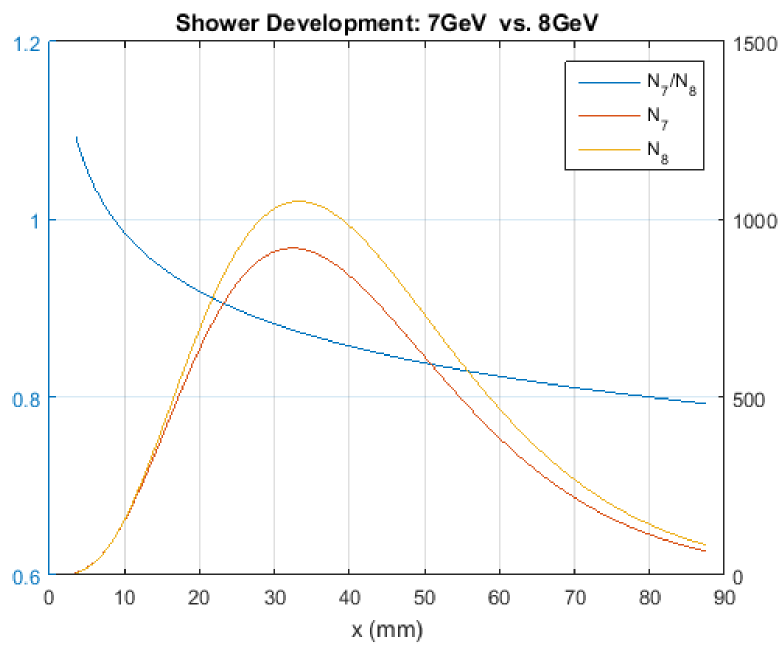

Published with MATLAB® R2015a